

JANUARY 2023

AJNR

VOLUME 44 • PP 1-115

AJNR

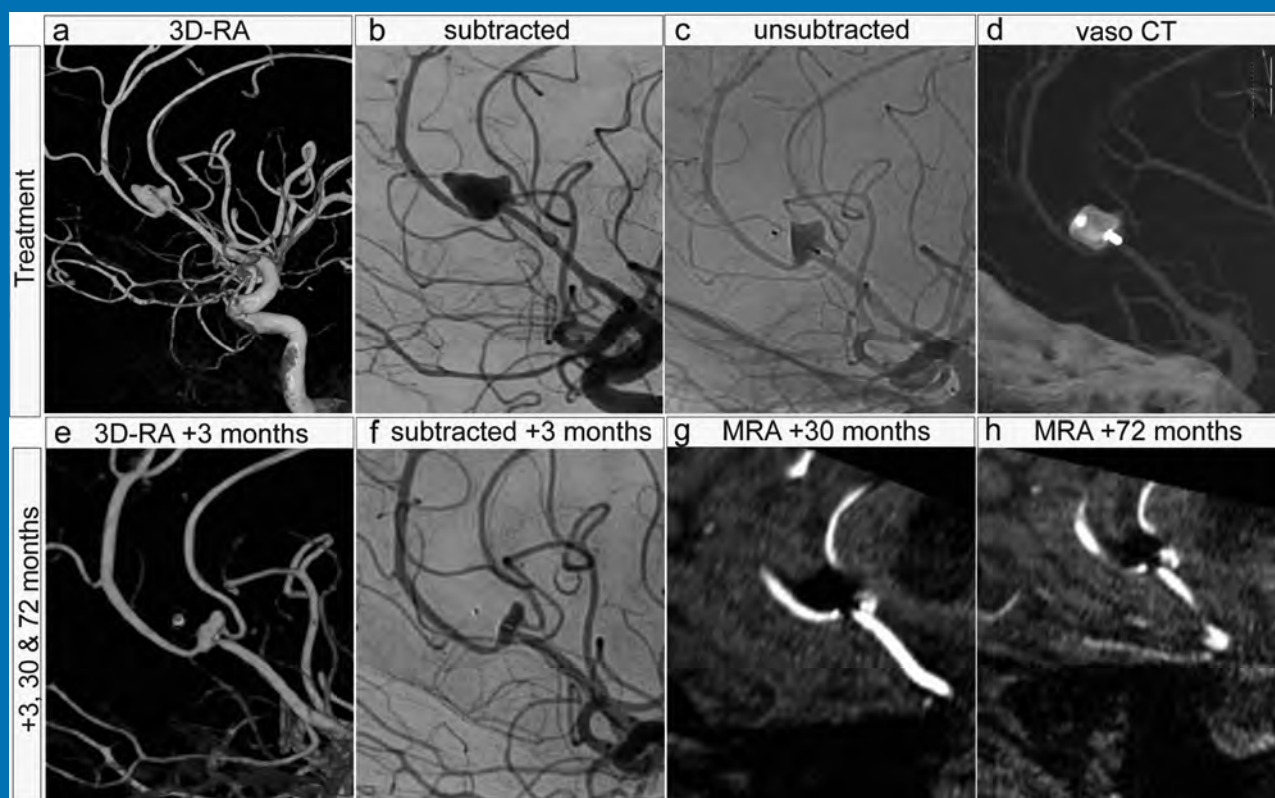
AMERICAN JOURNAL OF NEURORADIOLOGY

JANUARY 2023
VOLUME 44
NUMBER 1
WWW.AJNR.ORG

THE JOURNAL OF DIAGNOSTIC AND
INTERVENTIONAL NEURORADIOLOGY

WEB treatment of ruptured intracranial aneurysms
AI tool for MR brain clinical decision support and protocol selection
Spinal cord sarcoidosis
Quantitative lesion water uptake in ischemic stroke

Official Journal ASNR • ASFNR • ASHNR • ASPNR • ASSR



FRED™ X™

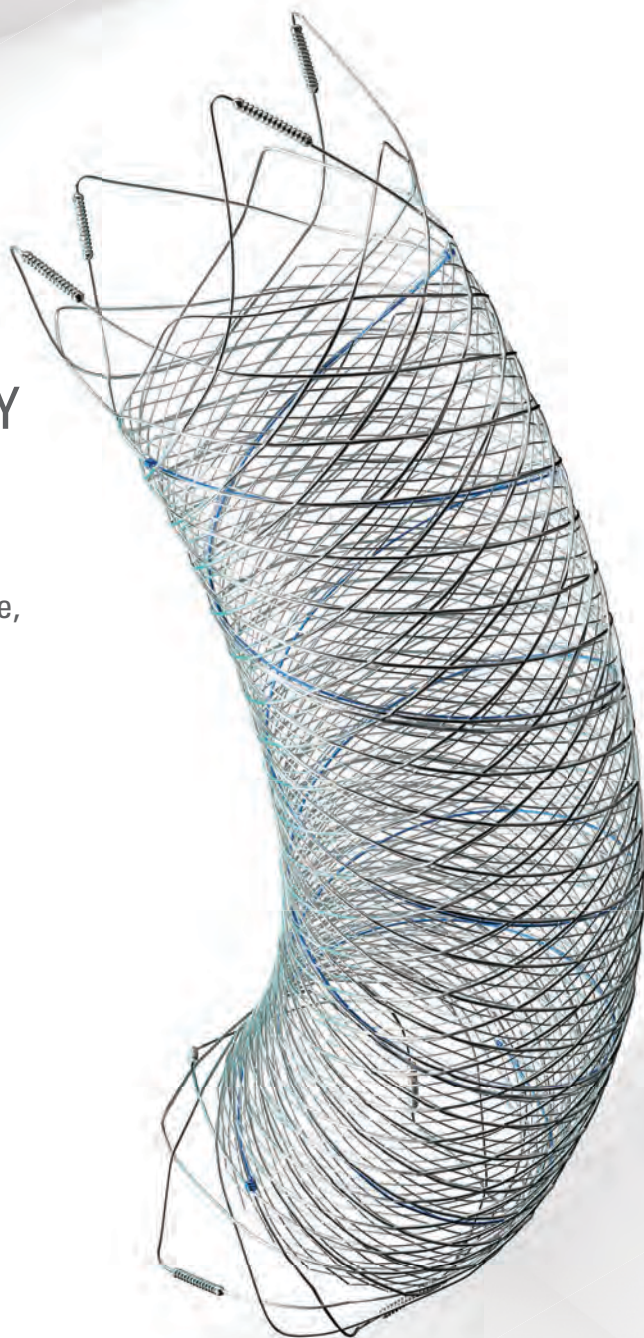
Flow Diverter Stent

THE NEXT ADVANCEMENT IN FLOW DIVERSION TECHNOLOGY

The FRED™ X Flow Diverter features the same precise placement and immediate opening of the FRED™ Device, now with X Technology. X Technology is a covalently bonded, nanoscale surface treatment, designed to:

- **REDUCE MATERIAL THROMBOGENICITY¹**
- **MAINTAIN NATURAL VESSEL HEALING RESPONSE^{2,3,4}**
- **IMPROVE DEVICE DELIVERABILITY AND RESHEATHING¹**

The only FDA PMA approved portfolio with a 0.021" delivery system for smaller device sizes, and no distal lead wire.



For more information, contact your local MicroVention sales representative or visit our website. www.microvention.com



^{*} Data is derived from in vivo and ex vitro testing and may not be representative of clinical performance.

¹ Data on file

² Tanaka M et al. Design of biocompatible and biodegradable polymers based on intermediate water concept. Polymer Journal. 2015;47:114-121.

³ Tanaka M et al. Blood compatible aspects of poly(2-methoxyethylacrylate) (PMEA) – relationship between protein adsorption and platelet adhesion on PMEA surface. Biomaterials. 2000;21:1471-1481.

⁴ Schiel L et al. X Coating™: A new biopassive polymer coating. Canadian Perfusion Canadienne. June 2001;11(2):9.

Indications for Use: The FRED X System is indicated for use in the internal carotid artery from the petrous segment to the terminus for the endovascular treatment of adult patients (22 years of age or older) with wide-necked (neck width 4 mm or dome-to-neck ratio < 2) saccular or fusiform intracranial aneurysms arising from a parent vessel with a diameter 2.0 mm and 5.0 mm.

Rx Only: Federal (United States) law restricts this device to sale by or on the order of a physician. For Healthcare professionals intended use only.

MICROVENTION, FRED and HEADWAY are registered trademarks of MicroVention, Inc. in the United States and other jurisdictions. Stylized X is a trademark of MicroVention, Inc. © 2022 MicroVention, Inc. MM1222 US 03/22

WEB™ 17

Aneurysm Embolization System

LOWER PROFILE



NEW SIZES



MORE ACCESS OPTIONS



INDICATIONS FOR USE:

The WEB Aneurysm Embolization System is intended for the endovascular embolization of ruptured and unruptured intracranial aneurysms and other neurovascular abnormalities such as arteriovenous fistulae (AVF). The WEB Aneurysm Embolization System is also intended for vascular occlusion of blood vessels within the neurovascular system to permanently obstruct blood flow to an aneurysm or other vascular malformation.

POTENTIAL COMPLICATIONS:

Potential complications include but are not limited to the following: hematoma at the site of entry, aneurysm rupture, emboli, vessel perforation, parent artery occlusion, hemorrhage, ischemia, vasospasm, clot formation, device migration or misplacement, premature or difficult device detachment, non-detachment, incomplete aneurysm filling, revascularization, post-embolization syndrome, and neurological deficits including stroke and death. For complete indications, potential complications, warnings, precautions, and instructions, see instructions for use (IFU provided with the device).

VIA 21, 27, 33 - The VIA Microcatheter is intended for the introduction of interventional devices (such as the WEB device/stents/flow diverters) and infusion of diagnostic agents (such as contrast media) into the neuro, peripheral, and coronary vasculature.

VIA 17, 17 Preshaped - The VIA Microcatheter is intended for the introduction of interventional devices (such as the WEB device/stents/flow diverters) and infusion of diagnostic agents (such as contrast media) into the neuro, peripheral, and coronary vasculature.

The VIA Microcatheter is contraindicated for use with liquid embolic materials, such as n-butyl 2-cyanoacrylate or ethylene vinyl alcohol & DMSO (dimethyl sulfoxide).

The device should only be used by physicians who have undergone training in all aspects of the WEB Aneurysm Embolization System procedure as prescribed by the manufacturer.

RX Only: Federal law restricts this device to sale by or on the order of a physician.

For healthcare professional intended use only.



MicroVention Worldwide
Innovator Center

PH +1.714.247.8000

35 Enterprise
Aliso Viejo, CA 92656 USA
MicroVention UK Limited
MicroVention Europe, S.A.R.L.
MicroVention Deutschland GmbH
Website

PH +44 (0) 191 258 6777
PH +33 (1) 39 21 77 46
PH +49 211 210 798-0
microvention.com



WEB™ and VIA™ are registered trademarks
of Sequent Medical, Inc. in the United States.

©2021 MicroVention, Inc. MM1184 WW 11/2021

LIFE IS FULL OF COMPROMISES.
IT'S TIME TO TAKE A STAND.

NO COMPROMISE

HIGH RELAXIVITY, HIGH STABILITY:^{1,2}
I CHOOSE BOTH.

The individual who appears is for illustrative purposes. The person depicted is a model and not a real healthcare professional.
Please see Brief Summary of Prescribing Information including Boxed Warning on adjacent page.

VUEWAY™ (gadopichlenol) solution for injection

Indications

VUEWAY injection is indicated in adults and children aged 2 years and older for use with magnetic resonance imaging (MRI) to detect and visualize lesions with abnormal vascularity in:

- the central nervous system (brain, spine and surrounding tissues),
- the body (head and neck, thorax, abdomen, pelvis, and musculoskeletal system).

IMPORTANT SAFETY INFORMATION

WARNING: NEPHROGENIC SYSTEMIC FIBROSIS (NSF)

Gadolinium-based contrast agents (GBCAs) increase the risk for NSF among patients with impaired elimination of the drugs. Avoid use of GBCAs in these patients unless the diagnostic information is essential and not available with non-contrast MRI or other modalities. NSF may result in fatal or debilitating fibrosis affecting the skin, muscle and internal organs.

- The risk for NSF appears highest among patients with:
 - Chronic, severe kidney disease (GFR < 30 mL/min/1.73 m²), or
 - Acute kidney injury.
- Screen patients for acute kidney injury and other conditions that may reduce renal function. For patients at risk for chronically reduced renal function (e.g. age > 60 years,

hypertension, diabetes), estimate the glomerular filtration rate (GFR) through laboratory testing.

- For patients at highest risk for NSF, do not exceed the recommended VUEWAY dose and allow a sufficient period of time for elimination of the drug from the body prior to any re-administration.

Contraindications

VUEWAY injection is contraindicated in patients with history of hypersensitivity reactions to VUEWAY.

Warnings


Risk of **nephrogenic systemic fibrosis** is increased in patients using GBCA agents that have impaired elimination of the drugs, with the highest risk in patients chronic, severe kidney disease as well as patients with acute kidney injury. Avoid use of GBCAs among these patients unless the diagnostic information is essential and not available with non-contrast MRI or other modalities.

Hypersensitivity reactions, including serious hypersensitivity reactions, could occur during use or shortly following VUEWAY administration. Assess all patients for any history of a reaction to contrast media, bronchial asthma and/or allergic disorders, administer VUEWAY only in situations where trained personnel and therapies are promptly available for the treatment of hypersensitivity reactions, and observe patients for signs and symptoms of hypersensitivity reactions after administration.



IN MRI

INTRODUCING


Vueway™
(gadopiclenol) injection
485.1 mg/mL

HALF THE GADOLINIUM DOSE COMPARED TO OTHER
MACROCYCLIC GBCAs IN APPROVED INDICATIONS.^{1,3-6}
FROM BRACCO, YOUR TRUSTED PARTNER IN MRI.



Gadolinium retention can be for months or years in several organs after administration. The highest concentrations (nanomoles per gram of tissue) have been identified in the bone, followed by other organs (brain, skin, kidney, liver and spleen). Minimize repetitive GBCA imaging studies, particularly closely spaced studies, when possible.

Acute kidney injury requiring dialysis has occurred with the use of GBCAs in patients with chronically reduced renal function. The risk of acute kidney injury may increase with increasing dose of the contrast agent.

Ensure catheter and venous patency before injecting as **extravasation** may occur, and cause tissue irritation.

VUEWAY may **impair the visualization of lesions** seen on non-contrast MRI. Therefore, caution should be exercised when Vueway MRI scans are interpreted without a companion non-contrast MRI scan.

The most common adverse reactions (incidence $\geq 0.5\%$) are injection site pain (0.7%), and headache (0.7%).

You are encouraged to report negative side effects of prescription drugs to the FDA. Visit www.fda.gov/medwatch or call 1-800-FDA-1088.

Please see BRIEF SUMMARY of Prescribing Information for VUEWAY, including BOXED WARNING on Nephrogenic Systemic Fibrosis.

Manufactured for Bracco Diagnostics Inc. by Liebel-Flarsheim Company LLC - Raleigh, NC, USA 27616.

VUEWAY is a trademark of Bracco Imaging S.p.A.

References: 1. Vueway™ (gadopiclenol) Injection Full Prescribing Information. Monroe Twp., NJ: Bracco Diagnostics Inc.; September 2022. 2. Robic C, Port M, Rousseaux O, et al. Physicochemical and Pharmacokinetic Profiles of Gadopiclenol: A New Macrocyyclic Gadolinium Chelate With High T1 Relaxivity. *Invest Radiol.* 2019 Aug;54: 475–484. 3. GADAVIST® (gadobutrol) Injection. Full Prescribing Information. Bayer HealthCare Pharmaceuticals Inc. Whippany, NJ; April 2022. 4. DOTAREM® (gadoterate meglumine) Injection. Full Prescribing Information. Guerbet LLC. Princeton, NJ; April 2022. 5. CLARISCAN™ (gadoterate meglumine) injection for intravenous use. Full Prescribing Information. GE Healthcare. Marlborough, MA; February 2020. 6. ProHance® (Gadoteridol) Injection. Full Prescribing Information and Patient Medication Guide. Monroe Twp., NJ: Bracco Diagnostics Inc.; December 2020.

Bracco Diagnostics Inc.
259 Prospect Plains Road, Building H
Monroe Township, NJ 08831 USA
Phone: 609-514-2200
Toll Free: 1-877-272-2269 (U.S. only)
Fax: 609-514-2446
© 2022 Bracco Diagnostics Inc.
All Rights Reserved. US-VW-2200012 10/22

VISIT
VUEWAY.COM
FOR MORE
INFORMATION



Vueway™ (gadopiclenol) injection, for intravenous use

BRIEF SUMMARY: Please see package insert of full prescribing information.

WARNING: NEPHROGENIC SYSTEMIC FIBROSIS (NSF)

Gadolinium-based contrast agents (GBCAs) increase the risk for NSF among patients with impaired elimination of the drugs. Avoid use of GBCAs in these patients unless the diagnostic information is essential and not available with non-contrast MRI or other modalities. NSF may result in fatal or debilitating fibrosis affecting the skin, muscle and internal organs.

- The risk for NSF appears highest among patients with:
 - Chronic, severe kidney disease (GFR < 30 mL/min/1.73 m²), or
 - Acute kidney injury.
- Screen patients for acute kidney injury and other conditions that may reduce renal function. For patients at risk for chronically reduced renal function (e.g. age > 60 years, hypertension, diabetes), estimate the glomerular filtration rate (GFR) through laboratory testing.
- For patients at highest risk for NSF, do not exceed the recommended Vueway dose and allow a sufficient period of time for elimination of the drug from the body prior to any re-administration [see Warnings and Precautions (5.1) in the full Prescribing Information].

INDICATIONS AND USAGE

Vueway™ (gadopiclenol) is a gadolinium-based contrast agent indicated in adult and pediatric patients aged 2 years and older for use with magnetic resonance imaging (MRI) to detect and visualize lesions with abnormal vascularity in:

- the central nervous system (brain, spine, and associated tissues),
- the body (head and neck, thorax, abdomen, pelvis, and musculoskeletal system).

CONTRAINDICATIONS

Vueway is contraindicated in patients with history of hypersensitivity reactions to gadopicholol.

WARNINGS AND PRECAUTIONS

Nephrogenic Systemic Fibrosis Gadolinium-based contrast agents (GBCAs) increase the risk for nephrogenic systemic fibrosis (NSF) among patients with impaired elimination of the drugs. Avoid use of GBCAs among these patients unless the diagnostic information is essential and not available with non-contrast MRI or other modalities. The GBCA-associated NSF risk appears highest for patients with chronic, severe kidney disease (GFR < 30 mL/min/1.73 m²) as well as patients with acute kidney injury. The risk appears lower for patients with chronic, moderate kidney disease (GFR 30-59 mL/min/1.73 m²) and little, if any, for patients with chronic, mild kidney disease (GFR 60-89 mL/min/1.73 m²). NSF may result in fatal or debilitating fibrosis affecting the skin, muscle, and internal organs. Report any diagnosis of NSF following Vueway administration to Bracco Diagnostics Inc. (1-800-257-5181) or FDA (1-800-FDA-1088 or www.fda.gov/medwatch).

Screen patients for acute kidney injury and other conditions that may reduce renal function. Features of acute kidney injury consist of rapid (over hours to days) and usually reversible decrease in kidney function, commonly in the setting of surgery, severe infection, injury or drug-induced kidney toxicity. Serum creatinine levels and estimated GFR may not reliably assess renal function in the setting of acute kidney injury. For patients at risk for chronically reduced renal function (e.g., age > 60 years, diabetes mellitus or chronic hypertension), estimate the GFR through laboratory testing.

Among the factors that may increase the risk for NSF are repeated or higher than recommended doses of a GBCA and the degree of renal impairment at the time of exposure. Record the specific GBCA and the dose administered to a patient. For patients at highest risk for NSF, do not exceed the recommended Vueway dose and allow a sufficient period of time for elimination of the drug prior to re-administration. For patients receiving hemodialysis, physicians may consider the prompt initiation of hemodialysis following the administration of a GBCA in order to enhance the contrast agent's elimination [see Use in Specific Populations (8.6) and Clinical Pharmacology (12.3) in the full Prescribing Information]. The usefulness of hemodialysis in the prevention of NSF is unknown.

Hypersensitivity Reactions With GBCAs, serious hypersensitivity reactions have occurred. In most cases, initial symptoms occurred within minutes of GBCA administration and resolved with prompt emergency treatment.

- Before Vueway administration, assess all patients for any history of a reaction to contrast media, bronchial asthma and/or allergic disorders. These patients may have an increased risk for a hypersensitivity reaction to Vueway.
- Vueway is contraindicated in patients with history of hypersensitivity reactions to Vueway [see Contraindications (4) in the full Prescribing Information].
- Administer Vueway only in situations where trained personnel and therapies are promptly available for the treatment of hypersensitivity reactions, including personnel trained in resuscitation.
- During and following Vueway administration, observe patients for signs and symptoms of hypersensitivity reactions.

Gadolinium Retention Gadolinium is retained for months or years in several organs. The highest concentrations (nanomoles per gram of tissue) have been identified in the bone, followed by other organs (e.g. brain, skin, kidney, liver, and spleen). The duration of retention also varies by tissue and is longest in bone. Linear GBCAs cause more retention than macrocyclic GBCAs. At equivalent doses, gadolinium retention varies among the linear agents with gadodiamide causing greater retention than other linear agents such as gadoxetate disodium, and gadobenate dimeglumine. Retention is lowest and similar

among the macrocyclic GBCAs such as gadoterate meglumine, gadobutrol, gadoteridol, and gadopicholol.

Consequences of gadolinium retention in the brain have not been established. Pathologic and clinical consequences of GBCA administration and retention in skin and other organs have been established in patients with impaired renal function [see Warnings and Precautions (5.1) in the full Prescribing Information]. There are rare reports of pathologic skin changes in patients with normal renal function. Adverse events involving multiple organ systems have been reported in patients with normal renal function without an established causal link to gadolinium.

While clinical consequences of gadolinium retention have not been established in patients with normal renal function, certain patients might be at higher risk. These include patients requiring multiple lifetime doses, pregnant and pediatric patients, and patients with inflammatory conditions. Consider the retention characteristics of the agent when choosing a GBCA for these patients. Minimize repetitive GBCA imaging studies, particularly closely spaced studies, when possible.

Acute Kidney Injury In patients with chronically reduced renal function, acute kidney injury requiring dialysis has occurred with the use of GBCAs. The risk of acute kidney injury may increase with increasing dose of the contrast agent. Do not exceed the recommended dose.

Extravasation and Injection Site Reactions Injection site reactions such as injection site pain have been reported in the clinical studies with Vueway [see Adverse Reactions (6.1) in the full Prescribing Information]. Extravasation during Vueway administration may result in tissue irritation [see Nonclinical Toxicology (13.2) in the full Prescribing Information]. Ensure catheter and venous patency before the injection of Vueway.

Interference with Visualization of Lesions Visible with Non-Contrast MRI As with any GBCA, Vueway may impair the visualization of lesions seen on non-contrast MRI. Therefore, caution should be exercised when Vueway MRI scans are interpreted without a companion non-contrast MRI scan.

ADVERSE REACTIONS

The following serious adverse reactions are discussed elsewhere in labeling:

- Nephrogenic Systemic Fibrosis [see Warnings and Precautions (5.1) in the full Prescribing Information]
- Hypersensitivity Reactions [see Contraindications (4) and Warnings and Precautions (5.2) in the full Prescribing Information]

Clinical Trials Experience Because clinical trials are conducted under widely varying conditions, adverse reaction rates observed in the clinical trials of a drug cannot be directly compared to rates in the clinical trials of another drug and may not reflect the rates observed in clinical practice.

The safety of Vueway was evaluated in 1,047 patients who received Vueway at doses ranging from 0.025 mmol/kg (one half the recommended dose) to 0.3 mmol/kg (six times the recommended dose). A total of 708 patients received the recommended dose of 0.05 mmol/kg. Among patients who received the recommended dose, the average age was 51 years (range 2 years to 88 years) and 56% were female. The ethnic distribution was 79% White, 10% Asian, 7% American Indian or Alaska native, 2% Black, and 2% patients of other or unspecified ethnic groups.

Overall, approximately 4.7% of subjects receiving the labeled dose reported one or more adverse reactions.

Table 1 lists adverse reactions that occurred in > 0.2% of patients who received 0.05 mmol/kg Vueway.

TABLE 1. ADVERSE REACTIONS REPORTED IN > 0.2% OF PATIENTS RECEIVING VUEWAY IN CLINICAL TRIALS	
Adverse Reaction	Vueway 0.05 mmol/kg (n=708) (%)
Injection site pain	0.7
Headache	0.7
Nausea	0.4
Injection site warmth	0.4
Injection site coldness	0.3
Dizziness	0.3
Local swelling	0.3

Adverse reactions that occurred with a frequency < 0.2% in patients who received 0.05 mmol/kg Vueway included: maculopapular rash, vomiting, worsened renal impairment, feeling hot, pyrexia, oral paresthesia, dysgeusia, diarrhea, pruritus, allergic dermatitis, erythema, injection site paresthesia, Cystatin C increase, and blood creatinine increase.

Adverse Reactions in Pediatric Patients

One study with a single dose of Vueway (0.05 mmol/kg) was conducted in 80 pediatric patients aged 2 years to 17 years, including 60 patients who underwent a central nervous system (CNS) MRI and 20 patients who underwent a body MRI. One adverse reaction (maculopapular rash of moderate severity) in one patient (1.3%) was reported in the CNS cohort.

USE IN SPECIFIC POPULATIONS

Pregnancy Risk Summary There are no available data on Vueway use in pregnant women to evaluate for a drug-associated risk of major birth defects, miscarriage or other adverse maternal or fetal outcomes. GBCAs cross the human placenta and result in fetal exposure and gadolinium retention. The available human data on GBCA exposure during pregnancy and adverse fetal outcomes are limited and inconclusive [see Data]. In animal reproduction studies, there were no adverse developmental effects observed in rats or rabbits with intravenous administration of Vueway during organogenesis [see Data]. Because of the potential risks of gadolinium to the fetus, use Vueway only if imaging is essential during pregnancy and cannot be delayed. The estimated background risk of major birth defects and miscarriage for the indicated population(s) are unknown. All pregnancies have a background risk of birth defect, loss, or other adverse outcomes. In the U.S. general population, the estimated background risk of major birth defects and miscarriage in clinically recognized pregnancies is 2% to 4% and 15% to 20% respectively. Data Human Data Contrast enhancement is visualized in the placenta and fetal tissues after maternal GBCA administration. Cohort studies and case reports on exposure to GBCAs during pregnancy have not reported a clear association between GBCAs and adverse effects in the exposed neonates. However, a retrospective cohort study comparing pregnant women who had a GBCA MRI to pregnant women who did not have an MRI reported a higher occurrence of stillbirths and neonatal deaths in the group receiving GBCA MRI. Limitations of this study include a lack of comparison with non-contrast MRI and lack of information about the maternal indication for MRI. Overall, these data preclude

a reliable evaluation of the potential risk of adverse fetal outcomes with the use of GBCAs in pregnancy.

Animal Data Gadolinium Retention: GBCAs administered to pregnant non-human primates (0.1 mmol/kg on gestational days 85 and 135) result in measurable gadolinium concentration in the offspring in bone, brain, skin, liver, kidney, and spleen for at least 7 months. GBCAs administered to pregnant mice (2 mmol/kg daily on gestational days 16 through 19) result in measurable gadolinium concentrations in the pups in bone, brain, kidney, liver, blood, muscle, and spleen at one-month postnatal age.

Reproductive Toxicology: Animal reproduction studies conducted with gadopicholol showed some signs of maternal toxicity in rats at 10 mmol/kg and rabbits at 5 mmol/kg (corresponding to 52 times and 57 times the recommended human dose, respectively). This maternal toxicity was characterized in both species by swelling, decreased activity, and lower gestation weight gain and food consumption.

No effect on embryo-fetal development was observed in rats at 10 mmol/kg (corresponding to 52 times the recommended human dose). In rabbits, a lower mean fetal body weight was observed at 5 mmol/kg (corresponding to 57 times the recommended human dose) and this was attributed as a consequence of the lower gestation weight gain.

Lactation Risk Summary There are no data on the presence of gadopicholol in human milk, the effects on the breastfed infant, or the effects on milk production. However, published lactation data on other GBCAs indicate that 0.01% to 0.04% of the maternal gadolinium dose is excreted in breast milk. Additionally, there is limited GBCA gastrointestinal absorption in the breast-fed infant. Gadopicholol is present in rat milk. When a drug is present in animal milk, it is likely that the drug will be present in human milk [see Data]. The developmental and health benefits of breastfeeding should be considered along with the mother's clinical need for Vueway and any potential adverse effects on the breastfed infant from Vueway or from the underlying maternal condition. Data In lactating rats receiving single intravenous injection of [¹⁵³Gd]-gadopiclenol, 0.3% and 0.2% of the total administered radioactivity was transferred to the pups via maternal milk at 6 hours and 24 hours after administration, respectively. Furthermore, in nursing rat pups, oral absorption of gadopicholol was 3.6%.

Pediatric Use The safety and effectiveness of Vueway for use with MRI to detect and visualize lesions with abnormal vascularity in the CNS (brain, spine, and associated tissues), and the body (head and neck, thorax, abdomen, pelvis, and musculoskeletal system) have been established in pediatric patients aged 2 years and older.

Use of Vueway in this age group is supported by evidence from adequate and well-controlled studies in adults with additional pharmacokinetic and safety data from an open-label, uncontrolled, multicenter, single dose study of Vueway (0.05 mmol/kg) in 80 pediatric patients aged 2 to 17 years. The 80 patients consisted of 60 patients who underwent a CNS MRI and 20 patients who underwent a body MRI [see Adverse Reactions (6.1) and Clinical Pharmacology (12.3) in the full Prescribing Information].

The safety and effectiveness of Vueway have not been established in pediatric patients younger than 2 years of age.

Geriatric Use Of the total number of Vueway-treated patients in clinical studies, 270 (26%) patients were 65 years of age and over, while 62 (6%) patients were 75 years of age and over. No overall differences in safety or efficacy were observed between these subjects and younger subjects.

This drug is known to be substantially excreted by the kidney, and the risk of adverse reactions to this drug may be greater in patients with impaired renal function. Because elderly patients are more likely to have decreased renal function, it may be useful to monitor renal function.

Renal Impairment In patients with renal impairment, the exposure of gadopicholol is increased compared to patients with normal renal function. This may increase the risk of adverse reactions such as nephrogenic systemic fibrosis (NSF). Avoid use of GBCAs among these patients unless the diagnostic information is essential and not available with non-contrast MRI or other modalities. No dose adjustment of Vueway is recommended for patients with renal impairment. Vueway can be removed from the body by hemodialysis [see Warnings and Precautions (5.1, 5.3, 5.4) and Clinical Pharmacology (12.3) in the full Prescribing Information].

OVERDOSAGE

Among subjects who received a single 0.3 mmol/kg intravenous dose of gadopicholol (6 times the recommended dose of Vueway), headache and nausea were the most frequently reported adverse reactions. Gadopicholol can be removed from the body by hemodialysis [see Clinical Pharmacology (12.3) in the full Prescribing Information].

PATIENT COUNSELING INFORMATION Advise the patient to read the FDA-approved patient labeling (Medication Guide).

Nephrogenic Systemic Fibrosis Inform the patient that Vueway may increase the risk for NSF among patients with impaired elimination of the drugs and that NSF may result in fatal or debilitating fibrosis affecting the skin, muscle and internal organs.

Instruct the patients to contact their physician if they develop signs or symptoms of NSF following Vueway administration, such as burning, itching, swelling, scaling, hardening and tightening of the skin; red or dark patches on the skin; stiffness in joints with trouble moving, bending or straightening the arms, hands, legs or feet; pain in the hip bones or ribs; or muscle weakness [see Warnings and Precautions (5.1) in the full Prescribing Information].

Gadolinium Retention Advise patients that gadolinium is retained for months or years in brain, bone, skin, and other organs following Vueway administration even in patients with normal renal function. The clinical consequences of retention are unknown. Retention depends on multiple factors and is greater following administration of linear GBCAs than following administration of macrocyclic GBCAs [see Warnings and Precautions (5.3) in the full Prescribing Information].

Injection Site Reactions Inform the patient that Vueway may cause reactions along the venous injection site, such as mild and transient burning or pain or feeling of warmth or coldness at the injection site [see Warnings and Precautions (5.5) in the full Prescribing Information].

Pregnancy Advise pregnant women of the potential risk of fetal exposure to Vueway [see Use in Specific Populations (8.1) in the full Prescribing Information].

Rx only

US Patent No. 10,973,934
Manufactured for Bracco Diagnostics Inc. by Liebel-Flarsheim Company LLC - Raleigh, NC, USA 27616.
Toll Free: 1-877-272-2269 (U.S. only)
Revised November 2022

CALL FOR AJNR EDITORIAL FELLOWSHIP CANDIDATES

2023 Candidate Information and Requirements

ASNR and AJNR are pleased once again to join efforts with other imaging-related journals that have training programs on editorial aspects of publishing for trainees or junior staff (<5 years on staff), including Radiology (Olmsted fellowship), AJR (Figley and Rogers fellowships), JACR (Bruce J. Hillman fellowship), and Radiologia.

GOALS

- Increase interest in editorial and publication-related activities in younger individuals.
- Increase understanding and participation in the AJNR review process.
- Incorporate into AJNR's Editorial Board younger individuals who have previous experience in the review and publication process.
- Fill a specific need in neuroradiology not offered by other similar fellowships.
- Increase the relationship between "new" generation of neuroradiologists and more established individuals.
- Increase visibility of AJNR among younger neuroradiologists.

ACTIVITIES OF THE FELLOWSHIP

- Serve as Editorial Fellow for one year. This individual will be listed on the masthead as such.
- Review at least one manuscript per month for 12 months. Evaluate all review articles submitted to AJNR.
- Learn how electronic manuscript review systems work.
- Be involved in the final decision of selected manuscripts together with the Editor-in-Chief.
- Participate in all monthly Senior Editor telephone conference calls.
- Participate in 2 virtual meetings of the Editorial Board.
- Evaluate progress and adjust program to specific needs in annual meeting or telephone conference with the Editor-in-Chief.
- Embark on an editorial scientific or bibliometric project that will lead to the submission of an article to AJNR or another appropriate journal as determined by the Editor-in-Chief. This project will be presented by the Editorial Fellow at the ASNR annual meeting. The Foundation of the ASNR will provide \$2000 funding for this activity.
- Recruit trainees as reviewers as determined by the Editor-in-Chief.
- Serve as Guest Editor for an issue of AJNR's News Digest with a timely topic.

QUALIFICATIONS

- Be a fellow in neuroradiology from North America, including Canada (this may be extended to include other countries).
- Be a junior faculty neuroradiology member (< 5 years) in either an academic or private environment.
- Be an "in-training" or member of ASNR in any other category.

APPLICATION

- Include a short letter of intent with statement of goals and desired research project. CV must be included.
- Include a letter of recommendation from the Division Chief or fellowship program director. A statement of protected time to perform the functions outlined is desirable.
- Applications will be evaluated by AJNR's Senior Editors prior to the ASNR annual meeting. The name of the selected individual will be announced at the meeting.
- Applications should be received by March 1, 2023 and sent to Ms. Karen Halm, AJNR Managing Editor, electronically at khalm@asnr.org.



The ASNR Career Center

The Go-To Job Site for Neuroradiology Employers and Job Seekers

For Job Seekers

- Access to an expanded network of jobs via the National Healthcare Career Network
- Confidential resume posting
- Professional online profile

For Employers

- Employer resources to help you recruit top talent
- Multiple pricing options, including free Fellowship listings
- Resume search

Start here: careers.asnr.org

EDITOR-IN-CHIEF

Jeffrey S. Ross, MD

Professor of Radiology, Department of Radiology,
Mayo Clinic College of Medicine, Phoenix, AZ

SENIOR EDITORS

Harry J. Cloft, MD, PhD

Professor of Radiology and Neurosurgery,
Department of Radiology, Mayo Clinic College of
Medicine, Rochester, MN

Christopher G. Filippi, MD

Professor and Alice Ettinger-Jack R. Dreyfuss
Chair of Radiology,
Tufts University School of Medicine,
Radiologist-in-Chief
Tufts University Medical Center, Boston, MA

Thierry A.G.M. Huisman, MD, PD, FICIS, FACR

Radiologist-in-Chief and Chair of Radiology, Texas
Children's Hospital,
Professor of Radiology, Pediatrics, Neurosurgery,
and OBGYN, Baylor College of Medicine,
Houston, TX

Yvonne W. Lui, MD

Associate Professor of Radiology,
Chief of Neuroradiology,
New York University School of Medicine,
New York, NY

C.D. Phillips, MD, FACR

Professor of Radiology, Weill Cornell Medical
College, Director of Head and Neck Imaging,
New York-Presbyterian Hospital, New York, NY

Lubdhra M. Shah, MD, MS

Professor of Radiology and Director of Spine
Imaging, University of Utah Department of
Radiology and Imaging Sciences, Salt Lake City, UT

STATISTICAL SENIOR EDITOR

Bryan A. Comstock, MS

Senior Biostatistician,
Department of Biostatistics,
University of Washington, Seattle, WA

ARTIFICIAL INTELLIGENCE DEPUTY EDITOR

Peter D. Chang, MD

Assistant Professor-in-Residence,
Departments of Radiological Sciences,
Computer Sciences, and Pathology,
Director, Center for Artificial Intelligence in
Diagnostic Medicine (CAIDM),
University of California, Irvine, Irvine, CA

EDITORIAL BOARD

Ashley H. Aiken, *Atlanta, GA*

Matthew D. Alexander, *Salt Lake City, UT*

Lea M. Alhilali, *Phoenix, AZ*

Jason W. Allen, *Atlanta, GA*

Mohammed A. Almekhlafi, *Calgary, Alberta, Canada*

Niranjan Balu, *Seattle, WA*

Matthew J. Barkovich, *San Francisco, CA*

Joachim Berkefeld, *Frankfurt, Germany*

Karen Buch, *Boston, MA*

Judah Burns, *New York, NY*

Danielle Byrne, *Dublin, Ireland*

Federico Cagnazzo, *Montpellier, France*

Gloria C. Chiang, *New York, NY*

Daniel Chow, *Irvine, CA*

Kars C.J. Compagne, *Rotterdam, The Netherlands*

Yonghong Ding, *Rochester, MN*

Birgit Ertl-Wagner, *Toronto, Ontario, Canada*

Aaron Field, *Madison, WI*

Nils D. Forkert, *Calgary, Alberta, Canada*

Frank Gaillard, *Melbourne, Australia*

Joseph J. Gemmete, *Ann Arbor, Michigan*

Brent Griffith, *Detroit, MI*

Michael J. Hoch, *Philadelphia, PA*

Joseph M. Hoxworth, *Phoenix, AZ*

Raymond Y. Huang, *Boston, MA*

Susie Y. Huang, *Boston, MA*

Ferdinand K. Hui, *Honolulu, HI*

Christof Karmonik, *Houston, TX*

Gregor Kasprian, *Vienna, Austria*

Timothy J. Kaufmann, *Rochester, MN*

Hillary R. Kelly, *Boston, MA*

Toshibumi Kinoshita, *Akita, Japan*

Ioannis Koktzoğlu, *Evanston, IL*

Stephen F. Kralik, *Houston, TX*

Luke Ledbetter, *Los Angeles, CA*

Franklin A. Marden, *Chicago, IL*

Markus A. Möhlenbruch, *Heidelberg, Germany*

Mahmud Mossa-Basha, *Morrisville, NC*

Renato Hoffmann Nunes, *Sao Paulo, Brazil*

Sam Payabvash, *New Haven, CT*

Johannes A.R. Pfaff, *Salzburg, Austria*

Eike I. Piechowiak, *Bern, Switzerland*

Laurent Pierot, *Reims, France*

Alexander R. Podgorsak, *Chicago, IL*

Eytan Raz, *New York, NY*

Jeff Rudie, *San Diego, CA*

Paul M. Ruggieri, *Cleveland, OH*

Fatih Seker, *Heidelberg, Germany*

Maksim Shapiro, *New York, NY*

Timothy Shepherd, *New York, NY*

Mark S. Shiroishi, *Los Angeles, CA*

Neetu Soni, *Rochester, NY*

Ashok Srinivasan, *Ann Arbor, MI*

Jason F. Talbott, *San Francisco, CA*

Anderanik Tomasian, *Los Angeles, CA*

Fabio Triulzi, *Milan, Italy*

Arastoo Vossough, *Philadelphia, PA*

Richard Watts, *New Haven, CT*

Elysa Widjaja, *Toronto, Ontario, Canada*

Ronald Wolf, *Philadelphia, Pennsylvania*

Shuang Xia, *Tianjin, China*

Leonard Yeo, *Singapore*

Woong Yoon, *Gwangju, South Korea*

David M. Yousem, *Evergreen, CO*

Carlos Zamora, *Chapel Hill, NC*

Chengcheng Zhu, *Seattle, WA*

EDITORIAL FELLOW

Alexandre Boutet, *Toronto, Ontario, Canada*

SPECIAL CONSULTANTS TO THE EDITOR

AJNR Blog Editor

Neil Lall, *Denver, CO*

Case of the Month Editor

Nicholas Stence, *Aurora, CO*

Case of the Week Editors

Matylda Machnowska, *Toronto, Ontario, Canada*

Anvita Pauranik, *Calgary, Alberta, Canada*

Vinil Shah, *San Francisco, CA*

Classic Case Editor

Sandy Cheng-Yu Chen, *Taipei, Taiwan*

Health Care and Socioeconomics Editor

Pina C. Sanelli, *New York, NY*

Physics Editor

Greg Zaharchuk, *Stanford, CA*

Podcast Editor

Kevin Hiatt, *Winston-Salem, NC*

Twitter Editor

Jacob Ormsby, *Albuquerque, NM*

Official Journal:

American Society of Neuroradiology

American Society of Functional Neuroradiology

American Society of Head and Neck Radiology

American Society of Pediatric Neuroradiology

American Society of Spine Radiology

Founding Editor
Juan M. Taveras

Editors Emeriti
Mauricio Castillo, Robert I. Grossman,
Michael S. Huckabee, Robert M. Quencer

Managing Editor
Karen Halm

Assistant Managing Editor
Laura Wilhelm

Executive Director, ASNR
Mary Beth Hepp

AJNR *go green*

***AJNR* urges American Society of Neuroradiology members to reduce their environmental footprint by voluntarily suspending their print subscription.**

The savings in paper, printing, transportation, and postage directly fund new electronic enhancements and expanded content.

The digital edition of *AJNR* presents the print version in its entirety, along with extra features including:

- Publication Preview
- Case Collection
- Podcasts
- The *AJNR* News Digest
- The *AJNR* Blog

It also reaches subscribers much faster than print. An electronic table of contents will be sent directly to your mailbox to notify you as soon as it publishes.

Readers can search, reference, and bookmark current and archived content 24 hours a day on www.ajnr.org.

















ASNR members who wish to opt out of print can do so by using the *AJNR* Go Green link on the *AJNR* Website (<http://www.ajnr.org/content/subscriber-help-and-services>). Just type your name in the email form to stop print and spare our ecosystem.

AJNR

AMERICAN JOURNAL OF NEURORADIOLOGY

JANUARY 2023
VOLUME 44
NUMBER 1
WWW.AJNR.ORG

Publication Preview at www.ajnr.org features articles released in advance of print.
Visit www.ajnrblog.org to comment on AJNR content and chat with colleagues
and AJNR's News Digest at <http://ajnrndigest.org> to read the stories behind the
latest research in neuroimaging.

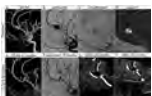
- 1 **PERSPECTIVES** *M. Hauben*
- REVIEW ARTICLE**
- 2  **The Monro-Kellie Doctrine: A Review and Call for Revision** *J.C. Benson, et al.* **ADULT BRAIN**
- EDITORIAL**
- 7 **The No Surprises Act: What Neuroradiologists Should Know**
T.H. Nguyen, et al.
- GENERAL CONTENTS**
- 11   **An Artificial Intelligence Tool for Clinical Decision Support and Protocol Selection for Brain MRI** *K.A. Wong, et al.* **ADULT BRAIN**
- 17   **Artificial Intelligence–Assisted Evaluation of the Spatial Relationship between Brain Arteriovenous Malformations and the Corticospinal Tract to Predict Postsurgical Motor Defects** *Y. Jiao, et al.* **ADULT BRAIN**
- 26  **FLAIR Vascular Hyperintensities as a Surrogate of Collaterals in Acute Stroke: DWI Matters** *L. Legrand, et al.* **ADULT BRAIN**
- 33    **Automated Estimation of Quantitative Lesion Water Uptake as a Prognostic Biomarker for Patients with Ischemic Stroke and Large-Vessel Occlusion** *S.S. Lu, et al.* **ADULT BRAIN**
- 40  **Topological Structural Brain Connectivity Alterations in Aspartylglucosaminuria: A Case-Control Study** *U. Roine, et al.* **ADULT BRAIN FUNCTIONAL**
- 47   **Viz.ai Implementation of Stroke Augmented Intelligence and Communications Platform to Improve Indicators and Outcomes for a Comprehensive Stroke Center and Network** *M.E. Figurelle, et al.* **INTERVENTIONAL ADULT BRAIN**
- 54  **Association between Infarct Location and Hemorrhagic Transformation of Acute Ischemic Stroke following Successful Recanalization after Mechanical Thrombectomy** *H. Ni, et al.* **INTERVENTIONAL ADULT BRAIN**
- 60  **WEB Treatment of Ruptured Intracranial Aneurysms: Long-Term Follow-up of a Single-Center Cohort of 100 Patients** *H. Kortman, et al.* **INTERVENTIONAL**
- 65   **Association of Left Vertebral Artery Hypoplasia with Posterior Circulation Stroke and the Functional Outcome of Patients with Atrial Fibrillation–Related Cardioembolic Stroke** *J.-H. Bae, et al.* **EXTRACRANIAL VASCULAR**

AJNR (Am J Neuroradiol ISSN 0195–6108) is a journal published monthly, owned and published by the American Society of Neuroradiology (ASNR), 820 Jorie Boulevard, Oak Brook, IL 60523. Annual dues for the ASNR include approximately 19% for a journal subscription. The journal is printed by Intellicor Communications, 330 Eden Road, Lancaster, PA 17601; Periodicals postage paid at Oak Brook, IL and additional mailing offices. Printed in the U.S.A. POSTMASTER: Please send address changes to American Journal of Neuroradiology, P.O. Box 3000, Denver, NJ 07834, U.S.A. Subscription rates: nonmember \$452 (\$530 foreign) print and online, \$320 online only; institutions \$520 (\$594 foreign) print and basic online, \$1029 (\$1103 foreign) print and extended online, \$380 online only (basic), \$825 online only (extended); single copies are \$35 each (\$40 foreign). Indexed by PubMed/MEDLINE, BIOSIS Previews, Current Contents (Clinical Medicine and Life Sciences), EMBASE, Google Scholar, HighWire Press, Q-Sensei, RefSeek, Science Citation Index, SCI Expanded, ReadCube, and Semantic Scholar. Copyright © American Society of Neuroradiology.

- 70 Retrospective Analysis of the Association of a Small Vestibular Aqueeduct with Cochleovestibular Symptoms in a Large, Single-Center Cohort Undergoing CT *K. Bouhadjer, et al.* **HEAD & NECK**
-  74 Dynamic Contrast-Enhanced MRI Parameters and Normalized ADC Values Could Aid Differentiation of Skull Base Osteomyelitis from Nasopharyngeal Cancer *A. Baba, et al.* **HEAD & NECK FUNCTIONAL**
- 79 Subtle Malformation of the Cochlear Apex and Genetic Abnormalities: Beyond the “Thorny” Cochlea *F. D’Arco, et al.* **HEAD & NECK**
-  82 Development of Gestational Age–Based Fetal Brain and Intracranial Volume Reference Norms Using Deep Learning *C.B.N. Tran, et al.* **PEDIATRICS**
- 91 Dilated Optic Nerve Sheath in Mucopolysaccharidosis I: Common and Not Necessarily High Intracranial Pressure *S. Huang, et al.* **PEDIATRICS**
- 95 Enhancing Annular Fissures and High-Intensity Zones: Pain, Internal Derangement, and Anesthetic Response at Provocation Lumbar Discography *W.S. Bartynski, et al.* **SPINE**
-   105 Spinal Cord Sarcoidosis Occurring at Sites of Spondylotic Stenosis, Mimicking Spondylotic Myelopathy: A Case Series and Review of the Literature *R.M. Kurtz, et al.* **SPINE**
- 111 The Dominant Anterior Thoracic Artery of the Spinal Cord *J.E. Small, et al.* **SPINE**
- 115 **35 YEARS AGO IN AJNR**
- ONLINE FEATURES**
- E1 **ERRATUM**
- LETTERS**
- E2 Regarding “Emergency Department Visits for Chronic Subdural Hematomas within 30 Days after Surgical Evacuation with and without Middle Meningeal Artery Embolization” *L. Wang*
- E3 *Reply* *L. Scherschinski, et al.*
- E4 MRI Monitoring of Anti-Alzheimer Therapy Amyloid-Related Imaging Abnormalities: Due Diligence or Overkill? *P.F. Høiland-Carlsen, et al.*
- E6 *Reply* *P.M. Cogswell, et al.*
- E7 Response to “Flow Diversion in the Treatment of Intracranial Aneurysms: A Pragmatic Randomized Care Trial” *J. de Winkel, et al.*
- E9 *Reply* *T.E. Darsaut, et al.*

BOOK REVIEWS *R.M. Quencer, Section Editor*

Please visit www.ajnrblog.org to read and comment on Book Reviews.



Treatment of a pericallosal aneurysm with a WEB-SL 6X4 from Kortman et al, in this issue.



Indicates Editor's Choices selection



Indicates Fellows' Journal Club selection



Indicates open access to non-subscribers at www.ajnr.org



Indicates article with supplemental online data



Indicates article with supplemental online video



Evidence-Based Medicine Level 1



Evidence-Based Medicine Level 2



Simplify the MOC Process



Manage your CME Credits Online

CMEgateway.org

Available to Members of Participating Societies

American Board of Radiology (ABR)
American College of Radiology (ACR)
American Roentgen Ray Society (ARRS)
American Society of Neuroradiology (ASNR)
Commission on Accreditation of Medical
Physics Educational Programs, Inc. (CAMPEP)
Radiological Society of North America (RSNA)
Society of Interventional Radiology (SIR)
SNM
The Society for Pediatric Radiology (SPR)

It's Easy and Free!

Log on to CME Gateway to:

- View or print reports of your CME credits from multiple societies from a single access point.
- Print an aggregated report or certificate from each participating organization.
- Link to SAMs and other tools to help with maintenance of certification.

American Board of Radiology (ABR) participation!

By activating ABR in your organizational profile, your MOC-fulfilling CME and SAM credits can be transferred to your own personalized database on the ABR Web site.

Sign Up Today!

go to CMEgateway.org

In Planning for Brain Metastases Treatment, Imaging may be the Missing Link in Cost Containment¹

When faced with a patient presenting with metastatic brain cancer, determining whether to use up-front stereotactic radiosurgery (SRS) vs. first treating with whole brain radiotherapy (WBRT) is a significant clinical decision.

WBRT: The whole story on cognitive impairment

While whole brain radiotherapy (WBRT) has been the main treatment option for many years, experts agree that it often results in cognitive deterioration and a negative impact on quality of life. This mental decline has a devastating impact on patients and their families and adds ongoing costs for the healthcare systems managing these symptoms.

Using WBRT instead of SRS in some patients is estimated to decrease the total costs of brain metastasis management, though with increased toxicity.

SRS: Fewer side effects but greater risk of missed tumors

The cost of upfront SRS is the greatest contributor to cost of brain metastasis management.¹ SRS is often more expensive than WBRT. What's more, multiple applications of SRS can increase the cost of treatment greatly.

Stereotactic radiosurgery (SRS) has far fewer side effects, but upfront use of SRS is expensive and can carry the risk of missed tumors, requiring repeat procedures such as salvage SRS.¹

Number of lesions and lesion size are key factors to be considered when determining the treatment plan for these patients. It follows that increased diagnostic information and accuracy could be beneficial in directing the proper therapy and improving overall long-term patient outcomes and containing costs. Getting the diagnosis right the first time is crucial to ensure proper treatment begins quickly, and high cost/high stakes procedures such as SRS need precise surgical planning.

What does optimal visualization mean for outcomes and cost?

For surgical planning with SRS, radiologists need the best visualization achievable to accurately count the number and size of the lesions. These metrics are the key predictors of the need for SRS,¹ WBRT, or a combination of both.

By selecting the ideal contrast agent and equipment protocols, neuroradiologists can identify the proximate numbers of metastases for upfront treatment and reduced salvage treatment occurrences.

The role of radiology

As medical care for oncology patients continues to evolve, it will be increasingly important to assess the cost of various interventions given the often-limited life expectancy of cancer patients, the rising costs of cancer therapy, and the increasing prevalence of cancer in an aging population.

Through seeing all the tumors and tumor borders as clearly as technology allows, radiology can play a part in ensuring that proper treatment can begin quickly,

while containing costs through optimized patient care. Efforts to carefully manage treatment approaches require improvements in protocol design, contrast administration in imaging, and utilizing multimodal imaging approaches.

In this era of precision medicine, radiology departments' contribution to this improved standard of care will have significant short and long-term implications by reducing cost of care, providing a more proximate diagnosis, and ensuring optimal patient outcomes. ■



Getting the diagnosis right the first time is crucial to ensure proper treatment begins quickly.

Reference: 1. Shenker, R. F., McTyre, E. R., Taksler, D et al. Analysis of the drivers of cost of management when patients with brain metastases are treated with upfront radiosurgery. *Clin Neurol Neurosurg.* 2019 Jan;176:10-14.



For more information on MRI contrast agents, precision medicine, and reducing cost of care please visit bracco.com

© 2022 Bracco Diagnostics Inc.

I am a global citizen.

I am patient-centered care.

I am committed to health equity.

I am a teacher.

I am a life-long learner.

I am determined.

I am curious.

I am a collaborative team player.

I am a volunteer.

I am ASNR.

Don't miss out on the tools, resources and relationships you've come to rely on. Log in and renew your ASNR membership today! www.asnr.org



Title: Manhattan Approach Span of Ed Koch Queensboro Bridge and Roosevelt Island Tram. The Manhattan approach span of the Ed Koch Queensboro Bridge is a major artery for automotive corpuscles entering and leaving Manhattan Island in New York City. Its terminus on the Manhattan side is an urban anatomic hilum with circulatory branches to various parts of the city. It is also a terminal for the Roosevelt Island Aerial Tram, the first commuter aerial tram in the United States. Seen here sliding outbound above the frenzy on its way to Roosevelt Island in the East River, is one of its two antiparallel traveling cabins. Since the tram's opening in 1976, over 26 million people have taken this eye-popping ride.

Manfred Hauben, MD, MPH, Pfizer Inc and NYU Langone Health, New York City

The Monro-Kellie Doctrine: A Review and Call for Revision

J.C. Benson, A.A. Madhavan, J.K. Cutsforth-Gregory, D.R. Johnson, and C.M. Carr



ABSTRACT

SUMMARY: The Monro-Kellie doctrine is a well-accepted principle of intracranial hemodynamics. It has undergone few consequential revisions since it was established. Its principle is straightforward: The combined volume of neuronal tissue, blood, and CSF is constant. To maintain homeostatic intracranial pressure, any increase or decrease in one of these elements leads to a reciprocal and opposite change in the others. The Monro-Kellie doctrine assumes a rigid, unadaptable calvaria. Recent studies have disproven this assumption. The skull expands and grows in response to pathologic changes in intracranial pressure. In this review, we outline what is known about calvarial changes in the setting of pressure dysregulation and suggest a revision to the Monro-Kellie doctrine that includes an adaptable skull as a fourth component.

ABBREVIATIONS: IIH = idiopathic intracranial hypertension; SIH = spontaneous intracranial hypotension

The Monro-Kellie doctrine has been a fundamental principle of neurophysiology for >200 years. Its hypothesis is based on simple reasoning: Within a rigid calvarial vault, the total volume of brain, CSF, and blood is constant. Any change in one of these elements results in an opposing compensatory response by the other 2 components.¹ On neuroimaging, the effects of this doctrine are ubiquitous: Encephalomalacia leads to ex vacuo dilation of an adjacent ventricle, an edematous and enlarged brain compresses ventricles and vessels, and CSF hypovolemia results in pituitary and venous engorgement.

Multiple studies, however, now suggest that the Monro-Kellie doctrine is due for further examination, particularly in the setting of abnormal intracranial pressure. Both increased and decreased intracranial pressure exerts downstream effects on the calvaria. Increased pressure leads to calvarial thinning and pitting,² while decreased pressure leads to development of layering hyperostosis along the inner table of the skull.³ These findings have substantial implications, both in terms of how we think of the Monro-Kellie doctrine and potentially how pathologies of intracranial pressure are identified and treated. In light of these findings, we review the history of the Monro-Kellie hypothesis and describe mounting

evidence of a nonrigid, adaptable calvaria in the setting of pathologically elevated or reduced CSF pressure.

BACKGROUND

The Monro-Kellie doctrine underwent many early changes before achieving its current form. Alexander Monro, a Scottish doctor of impressive medical lineage, first proposed that a rigid skull contained an incompressible brain and a constant amount of blood; ie, a steady input of arterial blood led to a compensatory output in venous blood.⁴ In 1824, his student George Killie de Leith provided postmortem evidence of this theory. Neither, however, mentioned CSF.⁵ Around the same time, John Ambercrombie made similar observations in animals; some early citations of this theorem were entitled the “Monro-Abercrombie doctrine.”⁶

George Burrows first included CSF in this model, and it was not until 1926 that Harvey Cushing⁷ neatly summarized the Monro-Kellie doctrine as it is generally known today. According to Cushing, the “three elements” (blood, nervous tissue, and fluid) in the skull “must always remain the same in bulk...any increase in blood volume, for example, can only take place at the expense of one of the other elements.” Cushing considered the responsiveness of any reciprocal action to be prompt, “These changes all take place rapidly—a matter of minutes.”⁷

Of course, self-evident exceptions to this rule abound. A foreign body may enter the calvarial vault, displacing or decreasing all 3 native intracranial components. Many types of intracranial masses are not composed of brain, CSF, or blood (eg, abscesses, metastases, and granulation tissue). These exceptions do not

Received August 27, 2022; accepted after revision October 5.

From the Departments of Radiology (J.C.B., A.A.M., D.R.J., C.M.C.) and Neurology (J.K.C.-G.), Mayo Clinic, Rochester, Minnesota.

Please address correspondence to John C. Benson, MD, Department of Radiology, Mayo Clinic, 723 6th St. SW, Rochester, MN 55902; e-mail: benson.john3@mayo.edu

Indicates open access to non-subscribers at www.ajnr.org

<http://dx.doi.org/10.3174/ajnr.A7721>

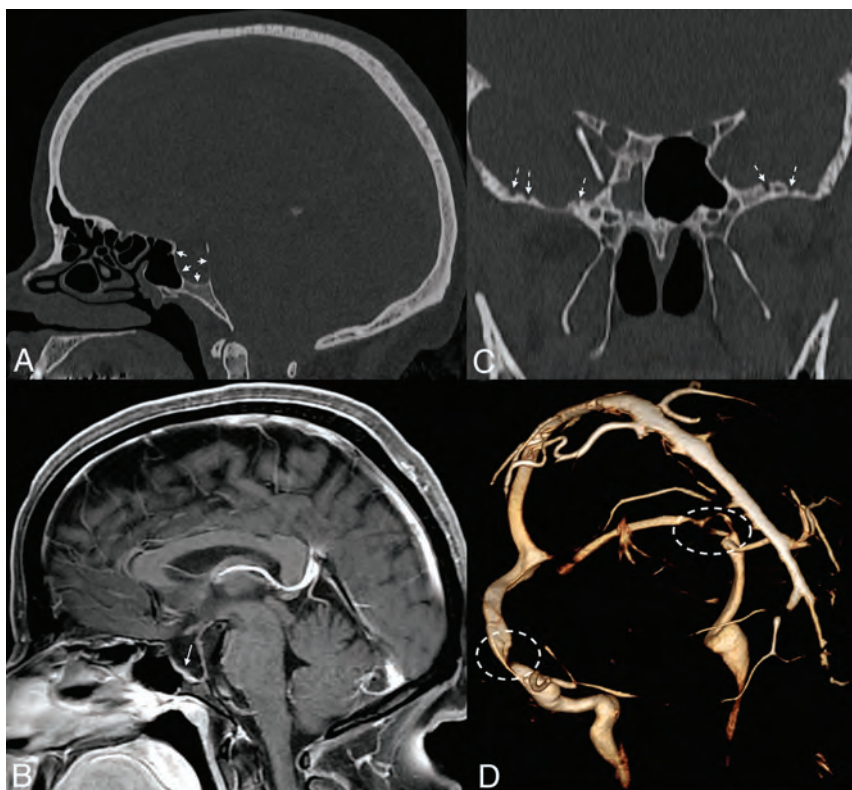


FIG 1. Sella expansion and skull base pitting in IIH. Sagittal CT image (A) in a 38-year-old woman with pseudotumor cerebri demonstrates marked expansion of the osseous walls of the sella (*short solid arrows*), with frank dehiscence posteriorly. Corresponding sagittal MR image (B) shows flattening of the pituitary tissue along the floor of the sella (*long solid arrow*). Prominent pitting is also noted along the anterior margins of both middle cranial fossae (*dashed arrows*, C). 3D reconstruction image of an MRV (D) demonstrates smooth tapering of the bilateral transverse sinuses (*dashed ovals*), compatible with IIH.

require a revision of the doctrine because they neither challenge the underlying mechanism on which the Monro-Kellie doctrine is built nor change the primary assumption of a fixed-volume skull.

Our understanding of intracranial pressure dynamics has become more nuanced since the inception of the doctrine. It is now known, for example, that blood plays a much greater role in dictating intracranial pressure than CSF. The total intracranial in- and outflow of blood is approximately 700 mL/min, occupying 100–130 mL of intracranial volume at any time. CSF, conversely, is produced at only 0.35 mL/min, with a total volume of about 75 mL.⁵ The cardiac cycle also dynamically influences intracranial pressure, with variations in arterial input during systolic and diastolic flow resulting in pulsatile brain movement, brain expansion and contraction, and intraventricular CSF flow.⁸

Although our understanding of intracranial pressure has become more refined, the Monro-Kellie doctrine has notably not been adjusted or revised. A few prior studies have proposed minor updates regarding concepts such as tissue elasticity and compliance⁹ and the dynamic nature of intracranial arterial and venous vascularity.⁵ None of these proposals have strayed far from the tenets of the doctrine: 1) The 3 major constituents that play a role in intracranial pressure homeostasis are blood, CSF, and brain parenchyma, and 2) the calvaria is rigid and has a fixed volume.

The closest proposed revision came from Mascarenhas et al,⁶ who performed a set of postmortem experiments in which they expanded a rubber balloon in a skull while measuring skull deformation. The results indicated that deformation was noted during increases and decreases in internal pressure. The authors consequently contended that the Monro-Kellie doctrine was, therefore, invalid because it failed to acknowledge such deformational changes in the skull.

Now there is convincing evidence of a more chronic type of elasticity of the calvaria in response to increases and decreases in intracranial pressure. Unlike the experiments of Mascarenhas et al,⁶ however, this elasticity manifests as changes in the thickness and shape of the calvarium, rather than transient deformations. Both types of changes represent adaptivity of the skull to expand or contract the calvarial vault in response to CSF pressure abnormalities. Below, we review in detail what is currently known about such calvarial changes.

Intracranial Hypertension

Intracranial hypertension was first described in 1893 by Heinrich Quincke, a disease he labeled “meningitis serosa”

attributed to alterations in CSF secretions.¹⁰ In 1904, Max Nonne first used the term pseudotumor cerebri (“false brain tumor”) to describe this syndrome. Nonne’s intent was to propose a state of elevated intracranial pressure that was distinct from that related to cerebral tumors: intercranial hypertension that followed a less sinister course.¹¹ John Foley¹² later offered the term “benign intracranial hypertension.”

These labels have become outdated. First, several other etiologies of increased intracranial pressure have become known. Such cases are referred to as secondary intracranial hypertension, reserving the term “primary pseudotumor cerebri” (also known as idiopathic intracranial hypertension [IIH]) for cases of cryptogenic elevated intracranial pressure. Next, the vision loss associated with IIH has made the label “benign” inappropriate.¹³

The etiologic mechanism for IIH remains unknown. Theories generally fall into the categories of altered CSF hydrodynamics or hindrances to venous outflow.¹⁴ The disorder represents a dysfunction in the homeostatic regulatory role of the Monro-Kellie doctrine; the increase in ≥ 1 intracranial component is insufficiently balanced by a corresponding decrease in the others.¹⁵

On imaging, numerous sequelae of IIH have been well-established. The pituitary gland is typically flattened along the floor of the sella, thought to be related to downward herniation of an arachnoid through the diaphragma sella. Ventricles are often

slitlike.¹⁶ Many findings have been reported in the orbits: flattening of the posterior sclera, distention of the perioptic subarachnoid space, tortuosity of the optic nerves, and intraocular protrusion of the optic nerve.¹⁷ Most important, lateral transverse sinus stenosis is also common, likely mediated by and contributing to increased intracranial pressure.¹⁸

Recent studies have demonstrated that remodeling of the calvaria is common in the setting of chronic pseudotumor cerebri. In such patients, the elevated intracranial pressure can lead to enlargement of the sella turcica (Fig 1),¹⁹ as well as prominent arachnoid pits and/or arachnoid granulations.² Meningoceles are also common, typically forming in the temporal bone (Fig 2).²⁰ As Bialer et al²⁰ noted, these findings are all biomechanically similar in that they increase the volume of the subarachnoid space, thereby at least conceptually decreasing intracranial pressure. Skull base erosion and meningocele formation can lead to the development of CSF leaks.²¹ In some cases, encephaloceles in these locations may also lead to epilepsy.²²

Beyond distinct areas of pitting, the skull itself becomes thinned in IIH. A case-control study by Barke et al²³ found both skull base thickness ($P < .001$) and calvarial width ($P = .024$) to be significantly smaller in patients with IIH than in controls. Rabbani et al²⁴ confirmed such findings, noting that while advancing age was typically associated with increased calvarial thickness, increased age portended calvarial thinning in patients with IIH. These calvarial changes are in opposition to the conventional understanding of the Monro-Kellie doctrine.

Except for CSF leaks and rare cases of epilepsy related to encephaloceles, little remains known about the clinical relevance of

calvarial expansion and/or thinning in the setting of IIH. To date, no studies have shown that these calvarial changes affect patient outcomes. Still, IIH remains an evolving field. As our knowledge of this disorder continues to grow, it is possible that calvarial changes among some patients with IIH could affect treatment strategies or could be used as a prognostic marker.

Intracranial Hypotension

Spontaneous intracranial hypotension (SIH) is related to CSF volume depletion. Although CSF leaks may be secondary to trauma and iatrogenic causes such as surgery or lumbar punctures, intracranial hypotension by fiat is due to spontaneous spinal CSF leaks.²⁵ Like IIH, the intracranial sequelae of intracranial hypotension have been well-described on imaging.

Even more so than intracranial hypertension, most of the intracranial sequelae of SIH can be explained by the conventional understanding of the Monro-Kellie doctrine. For example, the relative dearth of CSF results in pituitary enlargement (ie, opposite to IIH) and expansion of the dural venous sinuses.^{26,27} The dura engorges, leading to diffuse dural thickening and enhancement.²⁸ In some patients, subdural fluid collections, either hygromas or hematomas, develop over the cerebral convexities.²⁹ On the basis of the presence or absence of these findings, one can reliably predict the likelihood of a patient having SIH.²⁹ Ultimately, SIH represents a disorder in which autoregulatory mechanisms are insufficient to compensate for the CSF loss, and other imaging abnormalities reflect this breakdown. Specifically, the brain begins to sag inferiorly, with effacement of the suprasellar and prepontine cisterns and decreased mamillopontine distance.²⁹

Despite the number of changes observed, most of the compensatory changes in SIH are related to hyperemia; other than the pituitary gland, the brain parenchyma is relatively unable to expand in response to CSF depletion.³⁰ The same is true following treatment. Once a leak has been repaired, intracranial CSF volume has been shown to increase significantly over its hypotensive baseline. The brain volume in the posttreatment setting, in contrast, remains the same.^{17,31} Thus, the main compensatory action following CSF leak repair is a reciprocal reduction of intracranial blood volume.

It is only recently that we have become aware of calvarial changes in the setting of SIH. Johnson et al³² first showed that patients with SIH were often observed to have a thickened calvaria, often with a characteristic layered hyperostotic growth pattern along the inner table of the skull. In the setting of long-standing SIH, the authors opined, calvarial growth served as an additional compensatory mechanism for the depleted intracranial CSF volume. Babcock et al³ confirmed such findings

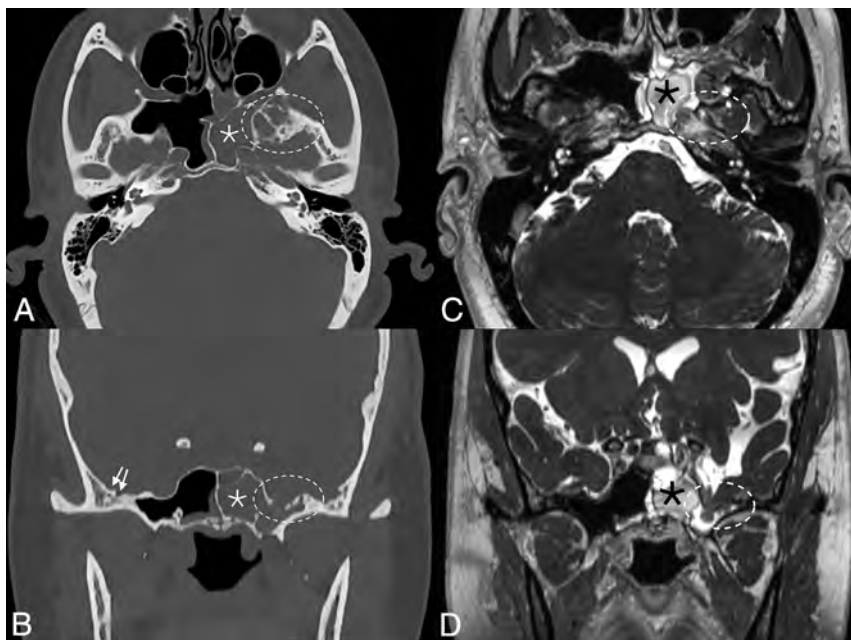


FIG 2. Skull pitting, meningoceles, and CSF leak in a patient who presented with rhinorrhea. Axial and coronal CT images (A and B) demonstrate substantial pitting along the anteromedial aspect of the left middle cranial fossa (dashed ovals, A and B), with complete opacification of the left sphenoid sinus (asterisks), concerning for a CSF leak. Milder pitting is noted on the right (solid arrows). Corresponding MR imaging (C and D) confirms a meningocele protruding into the left sphenoid sinus (dashed ovals, C and D). MRV (not shown) noted smooth tapered stenoses involving both transverse sinuses, and the patient was ultimately diagnosed with pseudotumor cerebri.

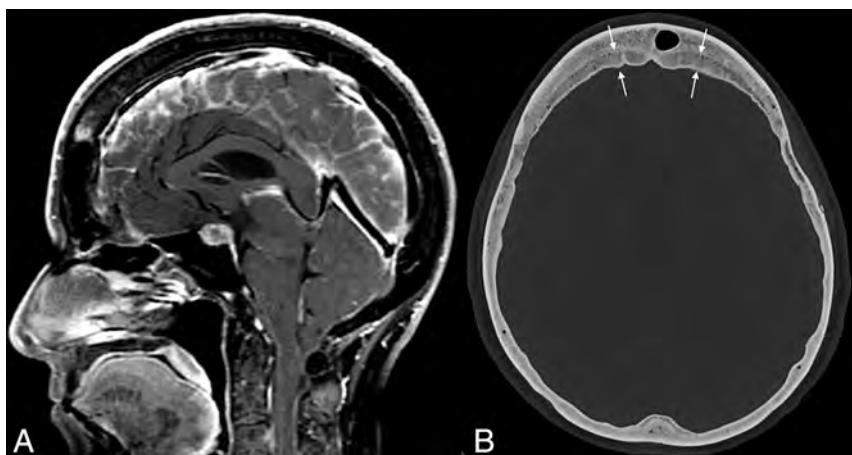


FIG 3. Example of layered calvarial thickening in a patient with SIH. Sagittal MR images (A) demonstrate classic findings of SIH, including pituitary enlargement, brain sag, and dural venous sinus engorgement. Axial CT image (B) in the same patient shows thickening of the bifrontal calvaria with characteristic layering related to preferential growth along the inner table of the skull (between straight arrows).

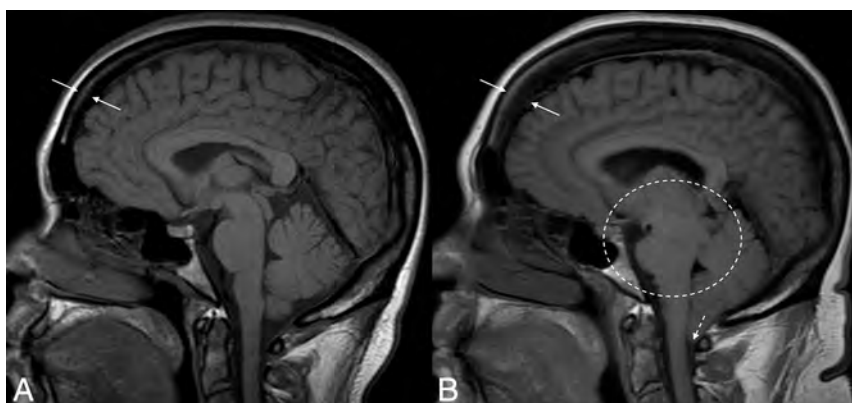


FIG 4. Hyperostosis related to a CSF leak. Sagittal T1-weight images before (A) and after (B) the development and diagnosis of SIH, with 16 years between examinations. Multiple classic findings of SIH are seen, including brain sag (dashed oval) and herniation of the cerebellar tonsils through the foramen magnum (dashed arrow). The patient also developed substantial frontal-predominant calvarial hyperostosis (between solid arrows), particularly along the inner table of the skull.

in a case-control study, noting that layered hyperostosis was present in 32% of patients with SIH but in only 5% of controls ($P < .001$; OR = 11.58) (Fig 3). Most important, the study of Babcock et al found no significant difference in the prevalence of diffuse (nonlayered) hyperostosis between groups ($P = .465$). Thus, the “layer cake” type of hyperostosis is much more indicative of intracranial hypotension (Fig 4). Although the expected location of this layer cake appearance was not discussed in detail in either publication, it is possible that these findings tend to be frontal-predominant, similar to benign hyperostosis frontalis interna. Specifically, the representative examples in the article by Babcock et al seem to suggest that such findings are at least prone to more substantial development along the frontal bone.

A similar phenomenon, termed “hyperostosis cranii ex vacuo” has been described in chronic shunting of pediatric hydrocephalus.^{33,34} In this condition, there is prominent growth of histologically lamellar bone, with scattered foci of woven bone.³³ This

growth, Moseley et al³⁵ noted, is primarily the inner table of the calvaria. Thus, the findings are analogous to the layer cake appearance seen in adult patients with SIH. The increased inner-to-outer table measurement is important because it helps distinguish these calvarial changes from those related to expansion of the diploic space (eg, sickle cell disease or thalassemia).³³

The clinical implications of these calvarial findings are currently unknown. There are, however, some potential effects that have been considered. The presence of layer cake hyperostosis in patients with SIH, for example, leads to a decrease in the volume of the calvarial vault. Conceptually, this could reduce the ability to normalize brain sag following CSF leak repair—that is, calvarial hyperostosis could impede the ability of brain to “un-sag” by acting as an unyielding intracranial barrier. Similarly, patients with SIH with layer cake skull changes might be at higher risk of rebound hypertension after leak repair because the tightened intracranial space could potentially lead to greater mass effect on the transverse sinuses. For now, these hypotheses remain conceptual in nature, though studies on these topics are ongoing.

Call For Revision

Altogether, studies have convincingly shown demonstrable changes in the calvaria in the setting of pathologic conditions of intracranial pressure. The skull expands in response to ITH and grows inward along its inner table in response

to SIH. Skeptics might argue that these changes are outside the realm of the Monro-Kellie doctrine because they represent adaptive changes in response to a breakdown of pressure homeostasis. It is clear, however, that the concept of a rigid calvaria, a fundamental tenet upon which the doctrine is based, has been disproven multiple times. We should add a fourth component to the Monro-Kellie hypothesis: a nonrigid calvaria that adjusts, albeit slowly, to changes in intracranial pressure.






Disclosure forms provided by the authors are available with the full text and PDF of this article at www.ajnr.org.

REFERENCES

1. Mokri B. The Monro-Kellie hypothesis: applications in CSF volume depletion. *Neurology* 2001;56:1746–48 CrossRef Medline
2. Rosenberg KI, Banik R. Pseudotumor cerebri syndrome associated with giant arachnoid granulation. *J Neuroophthalmol* 2013;33:417–19 CrossRef Medline

3. Babcock JC, Johnson DR, Benson JC, et al. **Diffuse calvarial hyperostosis and spontaneous intracranial hypotension: a case-control study.** *AJNR Am J Neuroradiol* 2022;43:978–83 CrossRef Medline
4. Wu OC, Manjila S, Malakooti N, et al. **The remarkable medical lineage of the Monro family: contributions of Alexander primus, secundus, and tertius.** *J Neurosurg* 2012;116:1337–46 CrossRef Medline
5. Wilson MH. **Monro-Kellie 2.0: The dynamic vascular and venous pathophysiological components of intracranial pressure.** *J Cereb Blood Flow Metab* 2016;36:1338–50 CrossRef Medline
6. Mascarenhas S, Vilela GH, Carlotti C, et al. **The new ICP minimally invasive method shows that the Monro-Kellie doctrine is not valid.** *Acta Neurochir Suppl* 2012;114:117–20 CrossRef Medline
7. Cushing H. *Studies in intracranial physiology & surgery: the third circulation, the hypophysis, the gliomas.* Humphrey Milford, Oxford University; 1926
8. Greitz D, Wirestam R, Franck A, et al. **Pulsatile brain movement and associated hydrodynamics studied by magnetic resonance phase imaging: the Monro-Kellie doctrine revisited.** *Neuroradiology* 1992;34:370–80 CrossRef Medline
9. Kalisvaart AC, Wilkinson CM, Gu S, et al. **An update to the Monro-Kellie doctrine to reflect tissue compliance after severe ischemic and hemorrhagic stroke.** *Sci Rep* 2020;10:22013 CrossRef Medline
10. Johnston I. **The historical development of the pseudotumor concept.** *Neurosurg Focus* 2001;11:E2 CrossRef Medline
11. Juhász J, Hensler J, Jansen O. **MRI-findings in idiopathic intracranial hypertension (pseudotumor cerebri).** *Rofo* 2021;193:1269–76 CrossRef Medline
12. Foley J. **Benign forms of intracranial hypertension; toxic and otitic hydrocephalus.** *Brain* 1955;78:1–41 CrossRef Medline
13. Friedman DI, Liu GT, Digre KB. **Revised diagnostic criteria for the pseudotumor cerebri syndrome in adults and children.** *Neurology* 2013;81:1159–65 CrossRef Medline
14. Degnan AJ, Levy LM. **Pseudotumor cerebri: brief review of clinical syndrome and imaging findings.** *AJNR Am J Neuroradiol* 2011;32:1986–93 CrossRef Medline
15. Ozkal B, Ozen O. **The effect of intracerebral structure volumes on idiopathic intracranial hypertension.** *Neuroreport* 2021;32:16–22 CrossRef Medline
16. George AE. **Idiopathic intracranial hypertension: pathogenesis and the role of MR imaging.** *Radiology* 1989;170:21–22 CrossRef Medline
17. Brodsky MC, Vaphiades M. **Magnetic resonance imaging in pseudotumor cerebri.** *Ophthalmology* 1998;105:1686–93 CrossRef Medline
18. Morris PP, Lachman N, Black DF, et al. **Increased curvature of the tentorium cerebelli in idiopathic intracranial hypertension.** *AJNR Am J Neuroradiol* 2017;38:1789–93 CrossRef Medline
19. Kyung S Eun E, Botelho JV, Horton JC. **Enlargement of the sella turcica in pseudotumor cerebri.** *J Neurosurg* 2014;120:538–42 CrossRef Medline
20. Bialer OY, Rueda MP, Bruce BB, et al. **Meningoceles in idiopathic intracranial hypertension.** *AJR Am J Roentgenol* 2014;202:608–13 CrossRef Medline
21. Pérez MA, Bialer OY, Bruce BB, et al. **Primary spontaneous cerebrospinal fluid leaks and idiopathic intracranial hypertension.** *J Neuroophthalmol* 2013;33:330–37 CrossRef Medline
22. Thottiyil JJ, Prasad A, Dutta DJ, et al. **Temporal lobe encephalocele with epilepsy in a young female: an atypical presentation of idiopathic intracranial hypertension.** *Neurol India* 2022;70:1618–21 CrossRef Medline
23. Barke M, Castro HM, Adesina OO, et al. **Thinning of the skull base and calvarial thickness in patients with idiopathic intracranial hypertension.** *J Neuroophthalmol* 2022;42:192–98 CrossRef Medline
24. Rabbani CC, Patel JM, Nag A, et al. **Association of intracranial hypertension with calvarial and skull base thinning.** *Otol Neurotol* 2019;40:e619–26 CrossRef Medline
25. Schievink WI. **Spontaneous spinal cerebrospinal fluid leaks and intracranial hypotension.** *JAMA* 2006;295:2286–96 CrossRef Medline
26. Leung GK, Ho J, Pu JK. **Pituitary enlargement in spontaneous intracranial hypotension—a diagnostic pitfall.** *Acta Neurochir (Wien)* 2011;153:2445–46 CrossRef Medline
27. Bond KM, Benson JC, Cutsforth-Gregory JK, et al. **Spontaneous intracranial hypotension: atypical radiologic appearances, imaging mimickers, and clinical look-alikes.** *AJNR Am J Neuroradiol* 2020;41:1339–47 CrossRef Medline
28. Antony J, Hacking C, Jeffree RL. **Pachymeningeal enhancement—a comprehensive review of literature.** *Neurosurg Rev* 2015;38:649–59 CrossRef Medline
29. Dobrocky T, Grunder L, Breiding PS, et al. **Assessing spinal cerebrospinal fluid leaks in spontaneous intracranial hypotension with a scoring system based on brain magnetic resonance imaging findings.** *JAMA Neurol* 2019;76:580–87 CrossRef Medline
30. Huang YM, Davidsson L. **Sagging brain development after lumbar puncture agrees with Monro-Kellie hypothesis.** *J Neurol* 2013;260:920–22 CrossRef Medline
31. Dobrocky T, Rebsamen M, Rummel C, et al. **Monro-Kellie hypothesis: increase of ventricular CSF volume after surgical closure of a spinal dural leak in patients with spontaneous intracranial hypotension.** *AJNR Am J Neuroradiol* 2020;41:2055–61 CrossRef Medline
32. Johnson DR, Carr CM, Luetmer PH, et al. **Diffuse calvarial hyperostosis in patients with spontaneous intracranial hypotension.** *World Neurosurg* 2021;146:e848–53 CrossRef Medline
33. Di Preta JA, Powers JM, Hicks DG. **Hyperostosis cranii ex vacuo: a rare complication of shunting for hydrocephalus.** *Hum Pathol* 1994;25:545–47 CrossRef Medline
34. Lucey BP, March GP, Hutchins GM. **Marked calvarial thickening and dural changes following chronic ventricular shunting for shaken baby syndrome.** *Arch Pathol Lab Med* 2003;127:94–97 CrossRef Medline
35. Moseley JE, Rabinowitz JG, Dziadiw R. **Hyperostosis cranii ex vacuo.** *Radiology* 1966;87:1105–07 CrossRef Medline

The No Surprises Act: What Neuroradiologists Should Know

 T.H. Nguyen,  R.E. Heller, K. Keysor,  J.M. Milburn,  E.Y. Rula, R. Spangler, and  J.A. Hirsch

The No Surprises Act (NSA) is the first federal law to address surprise medical billing and became effective as of January 2022. This law prohibits balance billing to patients who receive unexpected out-of-network care and limits patient payments to their in-network cost-sharing (coinsurance, copay, or deductible). The remaining balance is determined through negotiations between insurers and providers. If negotiations are unsuccessful, these parties enter an arbitration process termed independent dispute resolution (IDR). Many neuroradiologists and neurointerventionalists are involved in care that may be subject to the NSA, such as stroke or trauma work-ups from the emergency department, and, thus, should be aware of the implications.

While the patient protections of this law are commendable, the IDR process is problematic because it uses a benchmark-like approach to determine disputed payments, favoring insurers. In IDR, payment determinations are largely based on the median in-network contracted rate of a health plan, termed the qualifying payment amount (QPA). Because of how the QPA is calculated, this amount may often be lower than typical contract rates for the services. The federal arbitration process is thus likely to lower payments from insurers for out-of-network emergency care as well as increase costs to physician groups requiring arbitration. Moreover, if insurers can pay lower prices for out-of-network care, they are less incentivized to maintain robust provider networks and have greater leverage in network contract negotiations. Therefore, while the NSA pertains to out-of-network emergency care, it is anticipated to also disrupt in-network contracts and good faith contract negotiations.

Background

Personal health care costs, especially unexpected medical bills, are a major concern among Americans, even for those with health insurance.¹ An important-but-often misunderstood issue is unanticipated out-of-network costs. If a person with private health insurance receives care from an out-of-network provider, his or her health plan typically pays at least a portion of the bill. The patient is then billed for the remaining amount, which can be much greater than expected. This practice is known as balance billing, and an unexpected balance bill is called a “surprise bill.”² The term surprise billing is a misnomer because the practice actually reflects a surprise gap in insurance coverage.³

The NSA is a federal law that went into effect in 2022 to address surprise medical billing. The name “No Surprises Act” places emphasis on balance billing and unfortunately does not

also highlight surprise gaps in coverage. The NSA prohibits balance billing to patients in specific situations. Relevant to hospital-based specialties like radiology, the NSA covers out-of-network emergency care or nonemergency care delivered by out-of-network providers at an in-network facility. The NSA is considered a minimum standard, which means it applies if a state does not already have laws meeting minimum standards for protections against balance billing. The NSA does not apply to services payable by Medicare, Medicaid, the Children’s Health Insurance Program (CHIP), or TRICARE Health Insurance because each of these programs already largely prohibit balance billing.

Many neuroradiologists and neurointerventionalists are involved in care that may be subject to the NSA, such as stroke or trauma work-ups from the emergency department. With the NSA effective as of January 2022, practices should be aware of the situations in which the law applies, how insurers may act, and how to navigate out-of-network disputes. In this article, we also discuss aspects of the law that can be problematic for radiology practices and anticipated disruptions to in-network contracts as an insidious adverse effect.

Key Features of the NSA

Under the NSA, patient payment for unexpected out-of-network care is generally limited to in-network cost-sharing (coinsurance, copay, or deductible).⁴ The remaining out-of-network balance is determined through negotiations between insurers and providers. If negotiations are unsuccessful, these parties enter an arbitration process, termed IDR.⁵

IDR uses third-party arbiters to settle disputed out-of-network payments between insurers and providers. In this process, the insurer and provider each propose a payment amount, and an arbiter selects one of the proposals as the final payment. The law provides a list of factors for the arbiter to consider in making the determination, of which the QPA is the first mentioned. The QPA is the median in-network contracted rate of a health plan (as of January 31, 2019) for a certain service in a particular geographic area. Additional criteria mentioned in the law include the training level of the physician, the complexity of care, and the previously contracted rate, among other factors. Information that cannot be considered in the IDR includes billed charges and public payor (eg, Medicare) reimbursement rates, which usually represent the highest and lowest payments, respectively. More detailed information about the IDR process can be found on the Centers for Medicare & Medicaid Services Web site (<https://www.cms.gov/>).⁵

Why the QPA Is Problematic

Rulemaking by the government has attempted to establish the QPA as an appropriate out-of-network payment amount. The government asserts that the QPA reflects rates achieved through typical contract negotiations and should therefore be a reasonable out-of-network rate.⁴ However, the QPA calculation methodology does not reflect real-world economics. Instead of establishing the median in-network rate at the claims level, it is set at the contract level. This is an important distinction because contracted rates from providers who do not perform a service (and thus may not carefully negotiate

Dr Hirsch’s work was supported, in part, by a grant from the Neiman Health Policy Institute.
<http://dx.doi.org/10.3174/ajnr.A7739>

that rate) are given the same weight in the QPA calculation as rates from providers who do frequently provide that service.

For example, a radiology practice with a robust neurointerventional section performs thousands of cerebral angiograms each year. This practice will value reimbursement for cerebral angiograms in network negotiations. In contrast, a group that rarely bills for cerebral angiograms may not focus on this rate during their contract negotiations because it will not significantly affect their revenue. The contracted rate from each of these practices is given equal weight when calculating the QPA. This calculation methodology may skew the QPA below the typical contracted rate of providers that generally perform the examination. This concern is more than hypothetical: A study found that more than half of surveyed primary care providers had contracted rates for advanced medical imaging examinations.⁶ The government seems to acknowledge this problem of “ghost rates” and attempts to address the issue, though the end result remains to be seen.⁷ Also of concern, when there are not at least 3 contracts from which to calculate the median (once subsegmented by procedures, provider, group, geography, and so forth), there is leeway for the insurer to modify the calculation.⁸ This leeway provides an opportunity for insurers to influence the QPA value.

Before passage of the NSA, there was a great deal of debate about how to settle out-of-network payment disputes between insurers and providers. Ultimately, the law settled on an approach rooted in negotiation and arbitration. The arbitration process is intended to protect good faith contract negotiations. With arbitration, each party submits a proposed payment and evidence supporting that amount. The arbiter then selects an offer, by using “baseball style” rules, in which 1 of the 2 offers must be selected; the arbiter cannot split the difference. Baseball style arbitration promotes reasonability among participants because an unreasonable offer will be rejected (unless the other offer happens to be more unreasonable). As opposed to good faith negotiations with an arbitration backstop, insurers generally favor a benchmarking process to determine payment. This entails establishing a fixed rate for a service,³ such as use of the QPA. By establishing a reimbursement ceiling, the benchmark approach can disrupt good faith contract negotiations.

Between passage of the NSA in December 2020 and the start date of January 1, 2022, the government established the policies of the law through a series of interim final rules (IFRs). The first IFR, released in July 2021, clarified situations in which the ban on surprise billing would apply and detailed the process for determining the QPA.⁹ In September 2021, the second IFR was released outlining the federal IDR process. In this rule, arbiters were directed to presume that the QPA is the appropriate IDR payment amount unless there is credible information that demonstrates why the appropriate payment is materially different from the QPA.⁸ This action essentially established the QPA as the main determinant of reimbursement.

Implications for Radiology Groups

The implications of the NSA for medical practices including radiology are substantial.

While the NSA pertains to out-of-network care, it can influence in-network contracting. If in-network practices are reimbursed at a

rate higher than the QPA, insurers can opt not to renew contracts and instead deal with them as out-of-network providers. Given the many benefits of network contracting for medical practices, including timely payment and a less costly revenue cycle process, many practices may have to accept the reduced rates to stay in-network. The Congressional Budget Office and the Joint Committee on Taxation estimated that legislation using a median in-network benchmark rate would cause in-network rates to drop 15%–20% on average at the national level.¹⁰ This result is because insurers would likely reduce rates for providers with higher contracted payments, while those with lower contracted payments would demand an increased rate (assuming a frictionless environment, in which groups that are below the median rate can actually go out of network to achieve higher rates if negotiations fail). The reality is that due to economics and hospital requirements, many medical practices do not have that luxury.

As proof of this threat, shortly after the second IFR, which benchmarked out-of-network payments to the QPA, was released, a large commercial insurance company in North Carolina sent letters to dozens of their in-network medical practices with take-it-or-leave-it offers. The practices were told that they must accept a substantial rate reduction or their contracts would be terminated and they would be pushed out of network.¹¹ Although the intent of the NSA was to end surprise out-of-network billing, these letters were sent exclusively to in-network practices. There is no evidence that the groups targeted in North Carolina ever participated in surprise billing. Furthermore, while a goal of the NSA was promotion of network contracting, a result of this benchmark approach was network disruption, as seen in North Carolina.

An insidious aspect of the benchmark approach using the QPA is that it disincentivizes health plans from maintaining robust provider networks. Smaller provider networks decrease the in-network patient population of a practice and limit patient access to physicians in nonemergent settings. Proponents of the benchmark approach argue that providers previously avoided being in-network to profit from surprise billing.¹² The claim specifically mentions radiology. In fact, there is no evidence that radiology practices chose to stay out of network to use surprise billing as a revenue-generating strategy.³ Furthermore, it seems that a major health insurance company used undisclosed connections with a researcher to promote its narrative and frame the debate as the fault of provider groups.¹⁰

Insurers have financial advantages in the IDR process. By pursuing IDR, insurers can delay payments and retain profits. Medical practices, on the other hand, may struggle with cash flow as a consequence of delayed payments.³ Insurers also have more financial resources than most radiology practices, so the IDR arbitration fees and increased legal or administrative work will be more burdensome to practices. Increased costs and delayed payments may impair the ability of a practice to staff facilities and deliver quality services. These costs also take up resources that could be used to improve patient care. Together, the process adds additional cost to the system and perhaps to the detriment of patient care.

Increased consolidation in health care may be another inadvertent consequence of the NSA.¹³ Larger practices, with the advantages of scale, may have greater success with insurers. For

example, if a large radiology group develops in-house resources for successful IDR, insurers may find it more efficient to contract reasonably with them and reserve their aggressive tactics for smaller groups with fewer resources. A recent court case in Nevada demonstrated that health insurers may systematically underpay even large provider organizations; however, such groups can successfully fight back in court.¹⁴

Legal Challenges and Evolution of the NSA

The interim final rule in September 2021 placed the QPA above all other criteria in IDR and created a de facto benchmark for determining IDR payments unless it can be proved that the QPA is materially different from an appropriate payment rate. In law, this practice is referred to as a “rebuttable presumption.” Because this was contrary to both the words and spirit of the law, the move prompted more than a half dozen lawsuits, including from the American College of Radiology.^{15,16}

In February 2022, the judge in a lawsuit brought by the Texas Medical Association ruled that the creation of a rebuttable presumption was inappropriate and vacated that section of the rule.¹⁷ The federal government filed an appeal in this lawsuit but later placed this on hold and revised its final rule to comply with the Texas court ruling.¹⁸ In August 2022, the government released the final rule on the IDR process, including updates to comply with the Texas lawsuit decision. While the rule acknowledged that the QPA could not be a rebuttable presumption, it nonetheless highlighted the significance of the QPA in IDR determination. Specifically, the rule instructs arbiters to first consider the QPA and then consider additional credible information.¹⁹

The implication of the August final rule is that the QPA has outsized importance. Not only are arbiters instructed to first consider the QPA, the rule also specifies that if the arbiter assigns weight to non-QPA additional information, he or she must explain in writing why this information is not already accounted for by the QPA. For example, if a radiology group submits information regarding the level of training and experience of the neuroradiologist who provided the care (which is a criterion described in the law and rule), the arbiter would have to deem this irrelevant if he or she believes that this information was already considered in the QPA calculation. Because this approach of placing the QPA above the other criteria is contrary to the law, in September 2022, the Texas Medical Association filed a second lawsuit.²⁰

CONCLUSIONS

Brain and spine imaging are frequently performed in emergency departments, and radiologists do not know or consider a patient’s insurance status when interpreting these scans. It is expected that many neuroimaging studies may be out of network and subject to the NSA arbitration process to receive reimbursement. Because insurers are disincentivized to maintain robust provider networks if they can pay lower prices for out-of-network care through IDR, neuroradiologists will increasingly encounter out-of-network patients. A narrower network will also decrease the in-network population for routine outpatient imaging.

Physicians’ efforts to re-establish a balanced law continue to emphasize patient protections. While the patient protections of the NSA are notable, it is easy to overlook the concerning

implications of the arbitration process.^{1,11} The QPA calculation and arbitration process can have substantial effects on radiology practices and the patients we serve. These complex challenges may be addressed in future rulemaking, underscoring the importance of awareness and advocacy.

Until those changes can be implemented, radiology practices may benefit from having a designated expert to handle out-of-network payment negotiations and navigate the IDR process. It may be tempting to decrease out-of-network cases by expanding network contracts, but this recourse might not always be worthwhile or possible. We have already seen an insurer attempt to force rate reductions on practices to remain in-network.¹¹

These new out-of-network complexities and insurer tactics to unilaterally reduce physician reimbursement are a concern to practices and the patients they serve. Future research may focus on how access to care is impacted by implementation of the law. In the meantime, we advise practices to be aware of the law and insurer actions and emphasize the importance of physician advocacy.

Disclosure forms provided by the authors are available with the full text and PDF of this article at www.ajnr.org.

REFERENCES

1. Kirzinger A, Wu B, Muñana C, et al. **Health Tracking Poll: Late Summer 2018: The Election, Pre-Existing Conditions, and Surprises on Medical Bills.** Kaiser Family Foundation. September 5, 2018. <https://www.kff.org/health-costs/poll-finding/kaiser-health-tracking-poll-late-summer-2018-the-election-pre-existing-conditions-and-surprises-on-medical-bills/>. Accessed January 16, 2022
2. Centers for Medicare & Medicaid Services. **What You Need to Know about the Biden-Harris Administration’s Actions to Prevent Surprise Billing.** July 1, 2021. <https://www.cms.gov/newsroom/fact-sheets/what-you-need-know-about-biden-harris-administrations-actions-prevent-surprise-billing>. Accessed January 3, 2022
3. Heller RE 3rd, Gaines E, Parti N, et al. **Federal out-of-network balance billing legislation: context and implications for radiology practices.** *Radiology* 2021;300:506–11 CrossRef Medline
4. U.S. Department of Health and Human Services. **Federal Independent Dispute Resolution (IDR) Process Guidance for Certified IDR Entities.** February 11, 2022. <https://www.hhs.gov/guidance/sites/default/files/hhs-guidance-documents/Technical-Assistance-IDR-Entities-August-2022.pdf>. Accessed June 2, 2022
5. Centers for Medicare & Medicaid Services. **No Surprises Act: overview of rules & fact sheets.** August 29, 2022. <https://www.cms.gov/nosurprises/Policies-and-Resources/Overview-of-rules-fact-sheets>. Accessed January 3, 2022
6. Avalere Health. **PCP Contracting Practices and Qualified Payment Amount Calculation under the No Surprises Act.** August 2, 2022. https://www.acr.org/-/media/ACR/Files/Advocacy/2022-8-15-Avalere-QPA-Whitepaper_Final.pdf Published. Accessed September 1, 2022
7. Department of Labor. **FAQs About Affordable Care Act and Consolidated Appropriations Act, 2021 Implementation Part 55.** August 19, 2022. <https://www.dol.gov/sites/dolgov/files/EBSA/about-ebsa/our-activities/resource-center/faqs/aca-part-55.pdf>. Accessed August 23, 2022
8. Personnel Management Office, the Internal Revenue Service. **Requirements Related to Surprise Billing; Part II.** October 7 2021 <https://www.govinfo.gov/content/pkg/FR-2021-10-07/pdf/2021-21441.pdf>. Published 8/07/2021. Accessed November 15, 2021
9. Personnel Management Office, Internal Revenue Service. **Requirements Related to Surprise Billing; Part I.** July 13, 2021. <https://www.federalregister.gov/documents/2021/07/13/2021-14379/requirements-related-to-surprise-billing-part-i>. Accessed August 21, 2021

10. Adams R. **UnitedHealthcare guided Yale's groundbreaking surprise billing study.** *The Intercept*. August 10, 2021. <https://theintercept.com/2021/08/10/unitedhealthcare-yale-surprise-billing-study/>. Accessed January 5, 2022
11. Werner M. **Re: Necessity to amend rate agreement, response needed before November 21, 2021.** November 5, 2021. https://www.documentcloud.org/documents/21116581-20211105-bcbsnc-rate-reduction-notice_redacted?responsive=1&title=1. Accessed August 25, 2022
12. Appleby J. **Here's what the new ban on surprise medical billing means for you.** *NPR*. December 30, 2021. <https://www.npr.org/sections/health-shots/2021/10/14/1045828215/ban-on-surprise-medical-bills>. Accessed January 3, 2022
13. The White House. **Fact Sheet: Executive Order on Promoting Competition in the American Economy.** July 9, 2021. <https://www.whitehouse.gov/briefing-room/statements-releases/2021/07/09/fact-sheet-executive-order-on-promoting-competition-in-the-american-economy/>. Published 7/09/2021. Accessed August 21, 2021
14. Pierson B. **UnitedHealthcare underpaid TeamHealth provides: Nevada jury.** *Reuters*. November 11, 2021. <https://www.reuters.com/legal/litigation/unitedhealthcare-underpaid-teamhealth-provides-nevada-jury-2021-11-30/>. Accessed January 20, 2022
15. California Medical Association. **Lawsuits filed over No Surprises Act.** December 21, 2021. <https://www.cmadocs.org/newsroom/news/view/ArticleId/49618/Lawsuits-filed-over-No-Surprises-Act>. Accessed January 5, 2022
16. American Medical Association. **AMA and AHA file lawsuit over No Surprises Act final rule.** December 9, 2021. <https://www.ama-assn.org/press-center/press-releases/ama-and-aha-file-lawsuit-over-no-surprises-act-final-rule>. Accessed January 8, 2022
17. Keith K. **Health Care Providers Fight Arbitration Rule in No Surprises Act.** *The Commonwealth Fund*. March 17, 2022. <https://www.commonwealthfund.org/blog/2022/health-care-providers-fight-arbitration-rule-no-surprises-act>. Accessed March 20, 2022
18. Department of Labor. **Memorandum Regarding Continuing Surprise Billing Protections for Consumers.** February 28, 2022. <https://www.dol.gov/agencies/ebsa/laws-and-regulations/laws/no-surprises-act/memorandum-regarding-continuing-surprise-billing-protections-for-consumers>. Published 2/28/2022. Accessed June 26, 2022
19. Internal Revenue Service, the Employee Benefits Security Administration, and the Health and Human Services Department. **Requirements Related to Surprise Billing: Final Rules.** August 26, 2022. <https://www.federalregister.gov/documents/2022/08/26/2022-18202/requirements-related-to-surprise-billing>. Accessed August 30, 2022
20. Goldman M. **Texas Medical Association files another surprise billing lawsuit.** *Modern Healthcare*. September 22, 2022. <https://www.modernhealthcare.com/legal/surprise-billing-lawsuit-texas-doctors>. Accessed October 10, 2022

An Artificial Intelligence Tool for Clinical Decision Support and Protocol Selection for Brain MRI

 K.A. Wong,  A. Hatef,  J.L. Ryu,  X.V. Nguyen,  M.S. Makary, and  L.M. Prevedello



ABSTRACT

BACKGROUND AND PURPOSE: Protocolling, the process of determining the most appropriate acquisition parameters for an imaging study, is time-consuming and produces variable results depending on the performing physician. The purpose of this study was to assess the potential of an artificial intelligence–based semiautomated tool in reducing the workload and decreasing unwarranted variation in the protocolling process.

MATERIALS AND METHODS: We collected 19,721 MR imaging brain examinations at a large academic medical center. Criterion standard labels were created using physician consensus. A model based on the Long Short-Term Memory network was trained to predict the most appropriate protocol for any imaging request. The model was modified into a clinical decision support tool in which high-confidence predictions, determined by the values the model assigns to each possible choice, produced the best protocol automatically and low confidence predictions provided a shortened list of protocol choices for review.

RESULTS: The model achieved 90.5% accuracy in predicting the criterion standard labels and demonstrated higher agreement than the original protocol assignments, which achieved 85.9% accuracy ($\kappa = 0.84$ versus 0.72, P value $< .001$). As a clinical decision support tool, the model automatically assigned 70% of protocols with 97.3% accuracy and, for the remaining 30% of examinations, achieved 94.7% accuracy when providing the top 2 protocols.

CONCLUSIONS: Our model achieved high accuracy on a standard based on physician consensus. It showed promise as a clinical decision support tool to reduce the workload by automating the protocolling of a sizeable portion of examinations while maintaining high accuracy for the remaining examinations.

ABBREVIATIONS: AI = artificial intelligence; CDS = clinical decision support; SRS = stereotactic radiosurgery; LSTM = Long Short-Term Memory

During protocolling of cross-sectional study requests, radiologists review the study indication and the patient's medical history to determine the examination needed and subsequently set study parameters to best answer the ordering provider's specific clinical question. Protocolling decreases the waste of medical resources, minimizes risks to patients (eg, unnecessary exposure to radiation and/or contrast), and reduces patient inconvenience (eg, callbacks for additional imaging). Time spent on protocolling can vary from a few minutes to several hours a day. Schemmel et al¹ reported that protocolling occupied 6.2% of the workday of a

neuroradiology fellow and contributed to frequent interruptions from image interpretation. While protocolling is an important job of radiologists, it is time-consuming and can benefit from greater automation.

Despite the existence of standardized rules such as the American College of Radiology Appropriateness Criteria,² radiologists often disagree about which protocol is best for a particular study.³ Preferences among radiologists can vary considerably depending on training level and experience and may lead to suboptimal protocol selection. Boland et al³ advocated the standardization of protocolling to improve efficiency and patient safety. Artificial intelligence (AI) can potentially increase both the efficiency and standardization of the process.

The goals of this study were to determine the degree of variability of historical protocol selection relative to a criterion standard based on radiologist consensus and to compare the performance of an AI-based solution against this criterion standard. We also sought to evaluate the automated algorithm as a clinical decision support (CDS) tool by using techniques described previously by

Received March 7, 2022; accepted after revision October 15.

From the Department of Radiology (K.A.W., A.H., J.L.R., X.V.N., M.S.M., L.M.P.), The Ohio State University College of Medicine, Columbus, Ohio; Tri-County Radiologists (A.H.), Newark, Ohio; and ProScan Imaging (J.L.R.), Columbus, Ohio.

Please address correspondence to Luciano Prevedello, MD, MPH, Department of Radiology, The Ohio State University College of Medicine, 395 W 12th Ave, Columbus, OH 43210; e-mail: Luciano.Prevedello@osumc.edu



Indicates article with online supplemental data.

<http://dx.doi.org/10.3174/ajnr.A7736>

Table 1: Label frequencies of the training/validation and test sets^a

	Training/Validation Set	Original Test Set before Protocol Review	Final Test Set after Adjudication
MR imaging brain without/with contrast	11,543 (68.4%)	1274 (67.9%)	1156 (6.2%)
MR imaging brain for MS	2235 (13.2%)	242 (12.9%)	251 (13.4%)
MR imaging tumor	963 (5.7%)	113 (6.0%)	149 (7.9%)
MR imaging brain meningioma follow-up	653 (3.9%)	81 (4.3%)	117 (6.2%)
MR imaging brain dedicated seizure with contrast	519 (3.1%)	65 (3.5%)	65 (3.5%)
MR imaging stealth/Stryker/mask/presurgical planning	436 (2.6%)	43 (2.3%)	45 (2.4%)
MR imaging for gamma knife, brain lab, and SRS	332 (2.0%)	41 (2.2%)	58 (3.1%)
MR imaging cranial nerves III–VI without/with contrast	201 (1.2%)	17 (0.9%)	35 (1.9%)
Total	16,882	1876	1876

^a Data are No. (%).

Kalra et al,⁴ in which cases deemed straightforward were automatically protocolled and more complex studies were sent to radiologists to make the final decision.

MATERIALS AND METHODS

Data Set Collection and Preparation

Brain MR imaging was chosen as the focus of this study for its large number of protocol options. After securing approval with a waiver of informed consent from the institutional review board (The Ohio State University Wexner Medical Center), we obtained a de-identified data set containing all brain MR imaging with and without contrast examinations performed at our institution from January 2015 to January 2017. Each examination included order diagnoses, reason for the examination, order comments, and final assigned protocol. The original data set contained a total of 19,721 examinations. Because our patient population consists almost exclusively of adult patients, no pediatric brain MR imaging protocol was included.

Of the 32 protocols available for this examination in our database, several were specific to research studies or very uncommon clinical scenarios. To focus on common clinical protocols, we narrowed our evaluation to protocols with frequencies of at least 1%, which yielded 9 protocols. A total of 18,758 examinations were included (95.1% of the total). The protocols, in order of frequency, were the following: 1) MR imaging brain without/with contrast; 2) MR imaging brain for MS; 3) MR imaging tumor; 4) MR imaging meningioma follow-up; 5) MR imaging brain–dedicated seizure with contrast; 6) MR imaging stealth/Stryker/mask/presurgical planning; 7) MR imaging brain for gamma knife, brain lab, and stereotactic radiosurgery (SRS); 8) MR imaging cranial nerves III–VI without/with contrast; and 9) MR imaging for brain metastasis. The MR imaging brain without/with contrast and MR imaging for brain metastasis protocols differed only in that perfusion imaging is included in the MR imaging for brain metastasis protocol if the patient reports prior radiation treatment to the technologist. Because the decision to include perfusion is not made at the time of protocoling and MR imaging for brain metastasis was the least common protocol in our data set (1% of all studies), we combined the MR imaging brain without/with contrast and MR imaging for brain metastasis protocols into 1 class. The number of examinations assigned to each protocol is shown in Table 1. Additional details regarding the specific parameters and sequences used in each protocol and a complete list of protocols is shown in the Online Supplemental Data.

The examinations were randomized and divided into a training/validation set containing 16,882 examinations (90%) and a test set containing 1876 examinations (10%). Examinations in the test set were manually protocolled by 2 diagnostic radiology residents (postgraduate year 3 and postgraduate year 2 at the time of review). The residents were blinded to the final protocol assignment but were provided with procedure descriptions (general study ordered, eg, MR imaging brain with and without contrast), coded order diagnosis, reason for examination, order information, order comments, and authorizing provider and department. Criterion standard labels were prepared for the test set by comparing the protocols chosen by the residents. For examinations on which the residents agreed, the resident's protocol choice was taken to be the criterion standard label for the examination. Examinations in which the residents disagreed (207 of 1876 examinations) were reviewed by a board-certified fellowship-trained neuroradiologist, and his protocol choice was taken to be the criterion standard label. Label frequencies of the training/validation set, original test set before protocol review, and final test set after adjudication are available in Table 1.

Word Embeddings and Vocabulary

Word embeddings come from the idea that the meaning of a word can be represented as an array of numbers, or a vector.⁵ Words with similar meanings should correspond to vectors, or embeddings, that lie close together in space. In this work, we used BioWordVec (<https://github.com/ncbi-nlp/BioWordVec>), a set of biomedical-specific word embeddings derived from descriptor terms of medical subject headings and PubMed titles and abstracts.⁶ Its vocabulary contains 2.3 million distinct tokens, of which we used a subset as described later.

Data Preprocessing

For each example in the training/validation set, all associated data, including order diagnoses, reason for the examination, and comments, were concatenated into a single string of text. The text was converted to lowercase. Hyphens were retained, but all other punctuation was removed. Numbers were removed, including ages, dates, and diagnosis codes. Text was split into tokens via whitespace. Tokens from the training/validation set were matched with terms in the BioWordVec vocabulary. Tokens that failed to match (1006 of 7953 unique tokens) were manually reviewed and mapped to a similar term in the BioWordVec vocabulary. The final vocabulary comprised 7102 distinct terms.

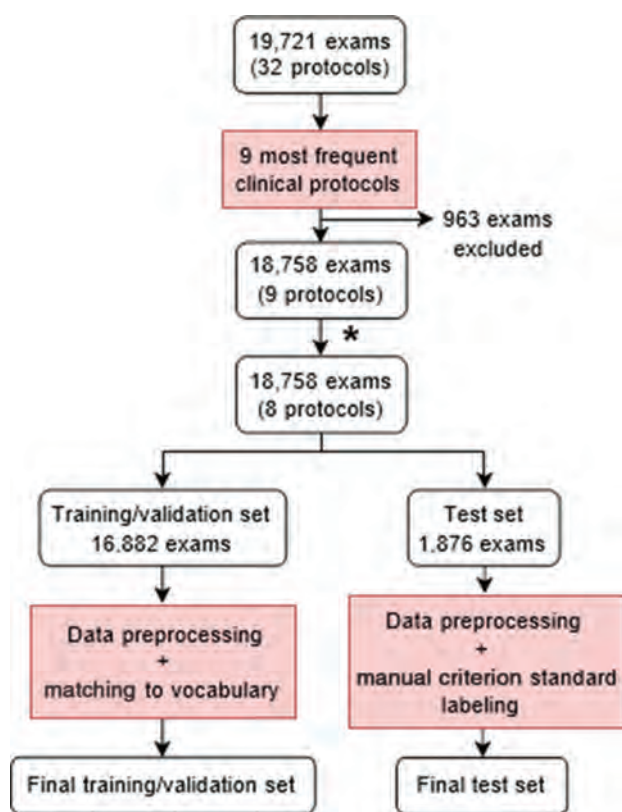


FIG 1. Flow chart describing preparation of training/validation and test sets. The asterisk indicates that due to its infrequency within the data set (1%) and its similarities with the MR imaging brain without/with contrast protocol, the MR imaging for brain metastasis protocol was combined with the MR imaging brain without/with contrast protocol, reducing the total number of protocols from 9 to 8.

Examples in the test set underwent similar preprocessing, but unmatched tokens were not manually reviewed and were instead mapped to the unknown term token. Examinations in the training/validation set contained an average of 25.4 (SD, 19.4) tokens, and those in the test set contained an average of 24.7 (SD, 18.2) tokens. An overview of the data preparation process can be found in Fig 1.

Natural Language-Processing Model

The Long Short-Term Memory (LSTM) network (<https://colah.github.io/posts/2015-08-Understanding-LSTMs/>) was used for the text-classification task. The LSTM is a type of recurrent neural network that uses multiplicative gates to update an internal state, allowing it to retain information during long input sequences.⁷ LSTMs have been shown to perform well on several text-classification benchmarks, particularly when pretrained as a language model and fine-tuned as a text classifier.⁸

To pretrain the LSTM, we assigned a language model around the LSTM to perform an autoregressive sentence-completion task. An embedding layer populated with BioWordVec pretrained word embeddings was placed before the LSTM to match input tokens with their corresponding embeddings. These embeddings were fed into a single bidirectional LSTM layer with a hidden size of 256. Outputs from the LSTM were passed through a fully-connected

layer with output the size of the vocabulary to predict the next token. During training, the training/validation set was randomly split into training (80%) and validation (20%) sets. The language model was trained across 10 epochs of the training set using cross-entropy loss.

Next, the LSTM was fine-tuned on the classification task of predicting the most appropriate imaging protocol of 8 possible choices. Weights from the language model were copied to the classifier model before training, and the last layer was replaced with a fully-connected layer with an output size of 8. Again, the training/validation set was randomly split into training (80%) and validation (20%) sets. Class weights for the training/validation set were computed so that the weight of each class was proportional to the inverse of its prevalence. These class weights were used in the calculation of cross-entropy loss to scale the loss for each class so that loss associated with rarer classes would have greater impact on the weights of the model than loss associated with more prevalent classes. This process allowed the model to compensate for imbalanced class distribution. The classifier model was trained across 5 epochs of the training set and evaluated on the test set with criterion standard labels.

Hyperparameter tuning was performed using a grid search, and optimal values were found to be a batch size of 64, a learning rate of 10^{-7} , an LSTM hidden size of 256, and the number of LSTM layers at 1. See the Online Supplemental Data for an overview of the network architectures. The code used to train and evaluate the model can be found at <https://github.com/kwong22/protocol-brain-mri>.

CDS Tool

Inspired by the work of Kalra et al,⁴ we evaluated the performance of our classifier model as a CDS tool. After receiving input, the model outputs a probability for each possible class. Usually, the class with the greatest probability is chosen as the predicted class. Kalra et al proposed that a threshold be set so that whenever the model produces an output in which the greatest class probability is greater than or equal to the threshold (high confidence), the model enters “automatic” mode and produces the 1 class with the greatest probability. If no probability in the output reaches the threshold (low confidence), the model enters the CDS mode and yields the 3 classes with the greatest probabilities. We applied this idea to our model by testing different thresholds and the number of suggestions for CDS mode.

Tools and Libraries

All code was written in Python (Version 3.8.11; <http://www.python.org>). Word embeddings were loaded using the Gensim library (<https://radimrehurek.com/gensim/>).⁹ Machine learning was performed using PyTorch (<https://pytorch.org/>).¹⁰ The Cohen κ score for interrater reliability was calculated using the scikit-learn library (<https://scikit-learn.org/stable/index.html>).¹¹ The McNemar test of homogeneity was performed using the Statsmodels library (<https://www.statsmodels.org/v0.10.1/>).¹² Model predictions were interpreted using the PyTorch Captum library (<https://github.com/pytorch/captum>)¹³ with the Integrated Gradients method.¹⁴

Table 2: Performance of the classifier model^a

Labels	Weighted Precision	Weighted Recall (Accuracy)	Weighted F1 Score
Criterion standard labels	0.908	0.905	0.905
Original protocol assignments	0.872	0.841	0.850

^aPrecision, recall, and F1 score were calculated for each class, and weighted averages of these metrics were computed using class frequencies as weights. The weighted F1 score represents the average of F1 scores weighted by class frequency.

Actual	WO/W	1061	15	39	10	17	2	0	12
	MS	6	244	0	0	0	0	0	1
	TUMOR	28	0	115	2	1	0	3	0
	MENINGIOMA	4	0	0	113	0	0	0	0
	SEIZURE	1	1	0	0	63	0	0	0
	STEALTH	2	0	1	1	0	40	0	1
	GAMMA	5	0	6	1	0	0	45	1
	CN	15	0	0	3	0	0	0	17
		WO/W	MS	TUMOR	MENINGIOMA	SEIZURE	STEALTH	GAMMA	CN
		Predicted							

FIG 2. Confusion matrix for the LSTM classifier model. Criterion standard labels are on the y-axis. Labels predicted by the model are on the x-axis. Numbers represent the number of examinations in the test set. WO/W indicates MR imaging brain without/with contrast; MS, MR imaging brain for MS; TUMOR, MR imaging tumor; MENINGIOMA, MR imaging brain meningioma follow-up; SEIZURE, MR imaging brain dedicated seizure with contrast; STEALTH, MR imaging stealth/Stryker/mask/pre-surgical planning; GAMMA, MR imaging for gamma knife, brain lab, and SRS; CN, MR imaging cranial nerves III–VI without/with contrast.

Table 3: Contingency table comparing performances of the classifier model and the original protocol assignments on the criterion standard labels^a

	Incorrectly Predicted by Original Assignments	Correctly Predicted by Original Assignments
Incorrectly predicted by model	80	98
Correctly predicted by model	185	1513

^aNumbers represent number of examinations in the test set that were incorrectly/correctly classified by the model and incorrectly/correctly classified by the original protocol assignments. The McNemar test of homogeneity statistic is 26.13; *P* value < .001.

RESULTS

The model achieved weighted F1 scores of 0.905 when predicting the criterion standard labels and 0.850 when predicting the original protocol assignments (Table 2). When predicting the criterion standard labels, the model demonstrated strong performance on 6 of 8 classes, with F1 scores for the top 6 classes ranging from 0.849 to 0.955 (Online Supplemental Data). The 2 classes in which the model performed worst were MR imaging tumor and MR imaging cranial nerves protocols, which had F1 scores of 0.742 and 0.507, respectively. The confusion matrix can be found

in Fig 2. Examples of correct and incorrect model predictions and their associated interpretations via the Integrated Gradients method can be found in the Online Supplemental Data.

The Cohen κ score, a measure of interrater agreement, between the output of the model and the criterion standard labels was 0.842, whereas the interrater agreement between the original protocol assignments and the criterion standard labels was 0.719. In predicting the criterion standard labels, the model (90.5% accuracy) performed significantly better than the original protocol assignments (85.9% accuracy) according to the McNemar test of marginal homogeneity (McNemar χ^2 statistic of 26.13, *P* value < .001) (Table 3).

To evaluate the model as a CDS tool, we varied 2 parameters: the confidence threshold that delineates the automation and CDS modes of the model, and the number of classes (*k*) returned by the CDS mode (Online Supplemental Data). On the lower extreme, with the threshold at 0.5 and *k* at 2, the model demonstrated a weighted recall of 0.925 in the automation mode (applied to 95% of examinations), 0.835 in the CDS mode (applied to the remaining 5% of examinations), and an overall weighted F1 score of 0.921. At the higher extreme, setting the threshold to 0.9 and *k* to 4 resulted in a weighted recall of 0.982 in the automation mode (applied to 48% of examinations), 0.997 in the CDS mode (applied to the remaining 52% of examinations), and an overall weighted F1 score of 0.990.

DISCUSSION

Protocolling decisions made by different radiologists can vary considerably, and previous work has argued for standardization to reduce suboptimal protocol

choices³ associated with unnecessary imaging, increased cost, and patient dissatisfaction. AI, with its ability to analyze large amounts of data and automate tasks in a consistent manner, has the potential to not only increase the accuracy and efficiency of the protocolling process but also to decrease variability. In this study, we compared the performance of the original protocol assignment with that of an AI tool relative to a criterion standard reference based on radiologist consensus. Our AI model showed greater agreement with the criterion standard labels compared with the original protocol assignments, supporting the idea that AI tools

can decrease variability in protocol selection for advanced imaging modalities.

Prior studies have demonstrated the effectiveness of AI in the automation of study protocolling. Brown and Marotta¹⁵ used various machine learning classifiers to select the most appropriate protocol from 13 classes and achieved a recall of 0.83 with a random forest classifier. Kalra et al⁴ evaluated a deep neural network as a CDS tool for protocolling and found that their algorithm protocollered 69% of studies with a weighted recall of 0.951 and, for the remaining 31% of studies, suggested the correct protocol from 3 choices with a weighted recall of 0.915. Our AI model demonstrated an overall strong performance on our criterion standard labels, with high precision (0.908) and recall (0.905).

However, the performance of our model was suboptimal in some categories, particularly MR imaging tumor and cranial nerve protocols. The MR imaging tumor protocol had a low sensitivity of 0.772, indicating a large number of false-negatives, predominantly when the model instead predicted the MR imaging brain without/with contrast protocol. This outcome seems reasonable given that these 2 protocols share the same foundation protocol, differing only in the use of perfusion imaging for MR imaging tumor. The model performed especially poorly on the MR imaging cranial nerves protocol, with a sensitivity of 0.486 and a positive predictive value of 0.531. MR imaging cranial nerves was the second least common protocol in the original data set, suggesting that the poor performance of the model on this class may be due to the lack of data for this class. Further research is needed to determine whether a larger data set would improve performance.

Review of the classification errors of the model revealed that the model learned to associate certain highly predictive terms with protocols, for instance, “gbm” (glioblastoma) for MR imaging tumor; “gamma knife” and “radiation” for MR imaging for gamma knife, brain lab, and SRS; and “facial” for MR imaging cranial nerves. Examinations that mentioned “weakness,” “paresthesia,” and “numbness” were often classified by the model as MR imaging for MS, and “seizure” was often associated with MR imaging dedicated seizure. However, when these highly predictive terms were combined in 1 indication (eg, “possible gbm progression presenting with seizures” or “right facial numbness”), the confidence level of the model decreased, as shown in the Online Supplemental Data. Further research is needed to assess whether a combination of AI and string search methods would benefit performance.

We also evaluated a CDS tool with the goal of reducing the manual workload and increasing protocolling accuracy. The idea behind this tool is that the model will evaluate every study before it reaches any human reviewers. High-confidence predictions result in automatic protocol assignments, while low-confidence predictions present a shortened list of suggested protocols to the appropriate radiologist. The confidence threshold should be low enough that a large portion of examinations are evaluated confidently and automatically by the model, resulting in a noticeable workload reduction for radiologists, and high enough that the model automatically evaluates only examinations about which it is truly confident, ensuring high performance. In addition, *k*, the number of suggested protocols provided by the model in the

CDS mode, should be small enough that the model adequately narrows the range of possibilities and large enough that the optimal protocol choice is almost always included in the suggestions.

Setting our model to protocol all studies in the automation mode results in 90.5% accuracy, but accuracy can be further increased by directing examinations with low-confidence predictions to the CDS mode, in which reviewers are provided a list of *k* protocols from which to choose. Varying *k* from 2 to 4 resulted in accuracies of the CDS mode ranging from 83.5% to 99.7%. A small list of protocols that almost always includes the most appropriate protocol could serve as a definitive resource for reviewers. Increasing the confidence threshold from 0.5 to 0.9 increased the accuracy of automation mode from 92.5% to 98.2% (Online Supplemental Data). However, in doing so, the percentage of studies protocollered automatically fell from 95% to 48%. Thus, this tool can decrease the protocolling workload by a factor of 2 (if 48% of studies are protocollered automatically), with even greater reductions possible depending on the user’s tolerance for automated protocolling errors. This observation illustrates a practical concept in clinical AI implementation in that the AI tool does not need to perform perfectly to improve radiology workflow.

It is difficult to directly compare our tool with that of Kalra et al⁴ because our project scopes differ considerably. While we focused exclusively on brain MR imaging studies, Kalra et al included multiple body regions and imaging modalities. In addition, our model selected from 8 protocol choices, while theirs selected from 108. To adapt our model to make a fair comparison, we selected the minimum *k* for the CDS mode (*k* = 2) and a confidence threshold (threshold = 0.8) to match the 69% rate of high-confidence predictions reported by Kalra et al. With these settings, our model automatically evaluated 70% of examinations with an accuracy of 97.3%; for the remaining 30% of examinations, it included the optimal protocol choice in the top 2 suggestions 94.7% of the time. Compared with the CDS tool created by Kalra et al, our tool achieved higher accuracy in both the automation mode (97.3% versus 95.1%) and the CDS mode (94.7% versus 91.1%).

This study was limited by a relatively low number of cases in certain classes, such as the MR imaging cranial nerves protocol, leading to poor performance by the model. Additional data may increase performance on these classes. Another limitation was the lack of criterion standard labeling of the training data. Because the model was trained on the original assigned protocols, it may have been limited by the variability inherent in those protocol choices. If criterion standard labels were available for the training data, model performance may improve.

In addition, the information provided to the residents and to the attending physician during creation of the criterion standard labels was limited. Key information that would be available through the patient chart, including provider notes, laboratory values, prior imaging examinations, and provider-to-provider communication, was not included in our data set. Future research should investigate how AI performs in a more complex environment that accounts for current patient status and additional information in the electronic medical record.

Furthermore, this study included a limited number of protocol choices. Indeed, only the most frequent protocols were selected,

which simplified the task substantially. Inclusion of more protocols, as will be necessary for real-world applications, will require additional data and model training. Note that imaging study requests and available protocol choices differ among institutions, so clinicians hoping to use our tool will need to retrain it on data from their own institutions for more tailored results.

Finally, the scope of this study was small in that it focused solely on brain MR imaging studies. This focus restricts the ability of the study to generalize to other imaging domains. However, creating a single algorithm to protocol all radiology studies may be impractical. Having separate algorithms for different study types may enable the algorithms to acquire domain-specific knowledge and assign protocols more accurately, just as ours did for brain MR imaging examinations.

CONCLUSIONS

Our AI-based model achieved high accuracy (90.5%) on a reference standard based on physician consensus and has the potential to decrease variability in protocolling by serving as a reliable reference for radiologists during the protocolling process. In addition, our model showed promise as a CDS tool to reduce the workload by automating the protocolling of 70% of examinations with 97.3% accuracy while maintaining 94.7% accuracy for the remaining 30% of examinations when providing the top 2 protocols.

Disclosure forms provided by the authors are available with the full text and PDF of this article at www.ajnr.org.

REFERENCES

1. Schemmel A, Lee M, Hanley T, et al. **Radiology workflow disruptors: a detailed analysis.** *J Am Coll Radiology* 2016;13:1210–14 CrossRef Medline
2. American College of Radiology. **ACR Appropriateness Criteria Overview.** <https://www.acr.org/Clinical-Resources/ACR-Appropriateness-Criteria/Overview>. Accessed May 4, 2021
3. Boland GW, Duszak R, Kalra M. **Protocol design and optimization.** *J Am Coll Radiol* 2014;11:440–41 CrossRef Medline
4. Kalra A, Chakraborty A, Fine B, et al. **Machine learning for automation of radiology protocols for quality and efficiency improvement.** *J Am Coll Radiol* 2020;17:1149–58 CrossRef Medline
5. Harris ZS. **Distributional structure.** *WORD* 1954;10:146–62 CrossRef
6. Zhang Y, Chen Q, Yang Z, et al. **BioWordVec, improving biomedical word embeddings with subword information and MeSH.** *Sci Data* 2019;6:52 CrossRef Medline
7. Hochreiter S, Schmidhuber J. **Long Short-Term Memory.** *Neural Comput* 1997;9:1735–80 CrossRef Medline
8. Howard J, Ruder S. **Universal language model fine-tuning for text classification.** May 23, 2018. *ArXiv180106146 Cs Stat* <http://arxiv.org/abs/1801.06146>. Accessed April 8, 2021
9. Rehurek R, Sojka P. **Software framework for topic modelling with large corpora.** In: *Proceedings of the LREC 2010 Workshop on New Challenges for NLP Frameworks*, Valletta, Malta. May 22, 2010:45–50
10. Paszke A, Gross S, Massa F, et al. **PyTorch: an imperative style, high-performance deep learning library.** In: *Proceedings of the 33rd Conference on Neural Information Processing Systems (NeurIPS 2019)*, Vancouver, Canada. December 8–14, 2019
11. Pedregosa F, Varoquaux G, Gramfort A, et al. **Scikit-learn: machine learning in Python.** *J Mach Learn Res* 2011;12:2825–30
12. Seabold S, Perktold J. **Statsmodels: econometric and statistical modeling with Python.** In: *Proceedings of the 9th Python in Science Conference (SciPy 2010)*, Austin, Texas. June 28 to July 3, 2010 CrossRef
13. Kokhlikyan N, Miglani V, Martin M, et al. **Captum: a unified and generic model interpretability library for PyTorch.** *ArXiv200907896 Cs Stat*. September 16, 2020. <http://arxiv.org/abs/2009.07896>. Accessed February 12, 2022
14. Sundararajan M, Taly A, Yan Q. **Axiomatic attribution for deep networks.** *ArXiv170301365*. June 12, 2017. <http://arxiv.org/abs/1703.01365>. Accessed February 12, 2022
15. Brown AD, Marotta TR. **A natural language processing-based model to automate MRI brain protocol selection and prioritization.** *Acad Radiol* 2017;24:160–66 CrossRef Medline

Artificial Intelligence–Assisted Evaluation of the Spatial Relationship between Brain Arteriovenous Malformations and the Corticospinal Tract to Predict Postsurgical Motor Defects

Y. Jiao, J. Zhang, X. Yang, T. Zhan, Z. Wu, Y. Li, S. Zhao, H. Li, J. Weng, R. Huo, J. Wang, H. Xu, Y. Sun, S. Wang, and Y. Cao



ABSTRACT

BACKGROUND AND PURPOSE: Preoperative evaluation of brain AVMs is crucial for the selection of surgical candidates. Our goal was to use artificial intelligence to predict postsurgical motor defects in patients with brain AVMs involving motor-related areas.

MATERIALS AND METHODS: Eighty-three patients who underwent microsurgical resection of brain AVMs involving motor-related areas were retrospectively reviewed. Four artificial intelligence–based indicators were calculated with artificial intelligence on TOF-MRA and DTI, including $FN_{5mm/50mm}$ (the proportion of fiber numbers within 5–50mm from the lesion border), $FN_{10mm/50mm}$ (the same but within 10–50mm), $FP_{5mm/50mm}$ (the proportion of fiber voxel points within 5–50mm from the lesion border), and $FP_{10mm/50mm}$ (the same but within 10–50mm). The association between the variables and long-term postsurgical motor defects was analyzed using univariate and multivariate analyses. Least absolute shrinkage and selection operator regression with the Pearson correlation coefficient was used to select the optimal features to develop the machine learning model to predict postsurgical motor defects. The area under the curve was calculated to evaluate the predictive performance.

RESULTS: In patients with and without postsurgical motor defects, the mean $FN_{5mm/50mm}$, $FN_{10mm/50mm}$, $FP_{5mm/50mm}$, and $FP_{10mm/50mm}$ were 0.24 (SD, 0.24) and 0.03 (SD, 0.06), 0.37 (SD, 0.27) and 0.06 (SD, 0.08), 0.06 (SD, 0.10) and 0.01 (SD, 0.02), and 0.10 (SD, 0.12) and 0.02 (SD, 0.05), respectively. Univariate and multivariate logistic analyses identified $FN_{10mm/50mm}$ as an independent risk factor for long-term postsurgical motor defects ($P = .002$). $FN_{10mm/50mm}$ achieved a mean area under the curve of 0.86 (SD, 0.08). The mean area under the curve of the machine learning model consisting of $FN_{10mm/50mm}$, diffuseness, and the Spetzler-Martin score was 0.88 (SD, 0.07).

CONCLUSIONS: The artificial intelligence–based indicator, $FN_{10mm/50mm}$, can reflect the lesion-fiber spatial relationship and act as a dominant predictor for postsurgical motor defects in patients with brain AVMs involving motor-related areas.

ABBREVIATIONS: AI = artificial intelligence; AUC = area under the curve; BAVM = brain AVM; CST = corticospinal tract; EuDX = Euler Delta Crossing; FN = fiber number; FP = proportion of fiber voxel points; HDVL = hemorrhagic presentation, diffuseness, deep venous drainage, and lesion-to-eloquence distance; LASSO = least absolute shrinkage and selection operator; LCD = lesion-to-corticospinal tract distance; LR = logistic regression; M-AVM = brain AVM involving motor-related areas; MDs = motor defects; ML = machine learning; ROC = receiver operating characteristic; S-M = Spetzler-Martin grading; XGBoost = Extreme Gradient Boosting

Brain AVMs (BAVMs) are congenital vascular dysplasias of the CNS that cause cerebral hemorrhage.¹ Radical resection by microsurgery to eliminate abnormal vascular masses is an

important curative treatment for BAVMs.² However, surgical management of BAVMs, particularly involving eloquent areas, may lead to serious neurologic defects and a poor prognosis.^{3,4} Preoperative evaluation for BAVMs to identify proper surgical candidates is crucial for reducing the risk of postsurgical defects.⁵

Received March 18, 2022; accepted after revision November 7.

From the Department of Neurosurgery (Y.J., J.Z., S.Z., H.L., J. Weng, R.H., J. Wang, H.X., Y.S., S.W., Y.C.), Beijing Tiantan Hospital, Capital Medical University, Beijing, China; and China National Clinical Research Center for Neurological Diseases (Y.J., J.Z., X.Y., T.Z., Z.W., Y.L., S.Z., H.L., J. Weng, R.H., J. Wang, H.X., Y.S., S.W., Y.C.), Beijing, China.

This study was supported by the National Natural Science Foundation of China (grant No. 81901175; principal investigator, Yuming Jiao), the National Key Research and Development Program of China during the 14th Five-Year Plan Period (grant No. 2021YFC2501102; principal investigator, Yong Cao), and the Beijing Advanced Innovation Center for Big Data-Based Precision Medicine (grant No. PXM2020_014226_000066).

Please address correspondence to Yong Cao, MD, Department of Neurosurgery, Beijing Tiantan Hospital, Capital Medical University, 119 South Fourth Ring Rd West, Fengtai District, Beijing, 100071, China; e-mail: caoyong@bjtth.org

Indicates open access to non-subscribers at www.ajnr.org

Indicates article with online supplemental data.

<http://dx.doi.org/10.3174/ajnr.A7735>

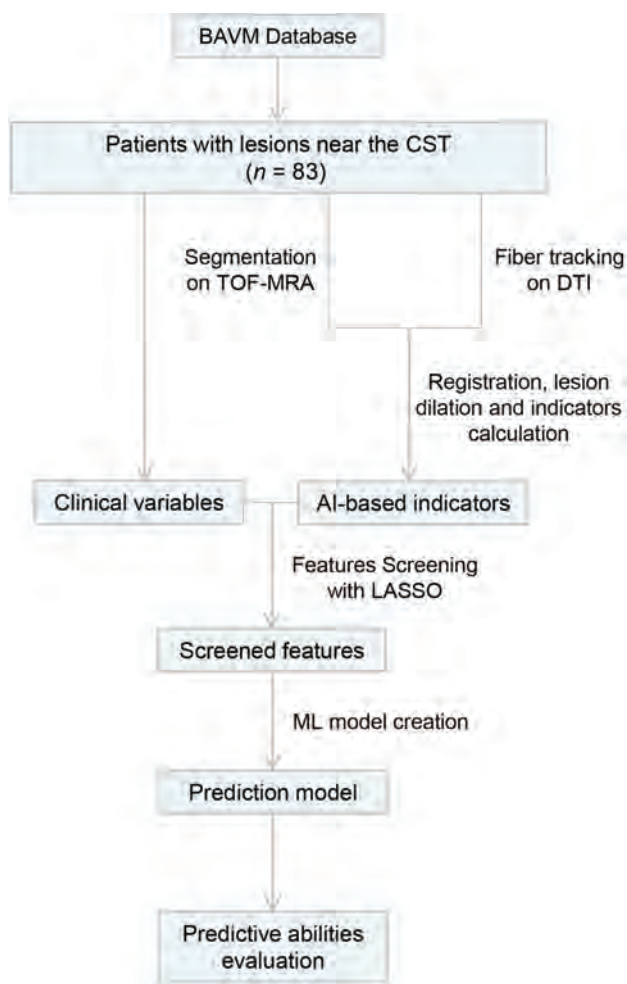


FIG 1. Flow diagram of patient selection, AI-based indicator calculation, ML model development, and predictive ability evaluation. AI-based indicators include $FN_{5mm/50mm}$, $FN_{10mm/50mm}$, $FP_{5mm/50mm}$, and $FP_{10mm/50mm}$. Clinical variables include age, sex, side, lobe, size, deep perforating artery supply, deep venous drainage, hemorrhage, seizure, and S-M grading score. LASSO indicates least absolute shrinkage and selection operator.

In our previous studies using fMRI and DTI, lesion-to-corticospinal tract distance (LCD) was used to evaluate the relationship between white fibers and lesions, which has proved to be an important predictive factor for postsurgical motor defects (MDs) in BAVMs involving motor-related areas (M-AVMs).^{6,7}

However, because BAVM lesions and the corticospinal tract (CST) are both stereoscopic objects, LCD obviously has some limitations in describing the spatial relationship between them. First, LCD is measured on the basis of a 2D plane and is a measurement that is too simple and crude to describe the complicated 3D spatial relationship between CST and BAVM lesions.^{8,9} Second, LCD is measured manually, which may lead to relatively inaccurate and subjective measurements.¹⁰ Finally, as a basic step of LCD calculation, fiber tracking skills may have confounding bias, which might vary with the operators' different levels of clinical experience or in different clinical centers.¹¹

Artificial intelligence (AI) technology, with its powerful processing and analysis ability, is emerging to develop a predictive model for clinical prognosis.¹² AI-based tools have the capability

of overcoming the shortcomings of manual evaluation, such as time-consuming workflows and substantial clinical experience requirements.¹³ Meanwhile, AI also has great potential in calculating the sophisticated 3D spatial relationship between stereoscopic objects.^{14,15} Whether exploiting AI technology to evaluate BAVMs has a better ability to predict postoperative motor function in M-AVMs remains unknown.

In this study, 83 patients who underwent microsurgical resection of M-AVMs were retrospectively reviewed. Four AI technology-based indicators were calculated followed by a machine learning (ML) model to predict the long-term postsurgical MDs of patients. Our study indicated that AI technology is an excellent method for predicting postoperative motor function in patients with M-AVMs.

MATERIALS AND METHODS

Patients

All patients were retrospectively reviewed from our BAVM database of a prospective clinical trial (ClinicalTrials.gov Identifier: NCT02868008) conducted between July 2015 and December 2020. Inclusion criteria were the following: 1) The lesions were near the CST (LCDs were <10 mm based on DTI tractography), 2) patients underwent microsurgical resection of the BAVMs, 3) patients were followed up for 6 months with complete information of motor function, and 4) patients' TOF-MRA and DTI data were acquired before microsurgery. The exclusion criteria included the following: 1) poor-quality neuroimaging, 2) atypical BAVM images after stereotactic radiosurgery or interventional therapy, and 3) incomplete imaging or follow-up data. The standard of postsurgical MDs was defined as patients not recovering to the level of being able to carry out all their usual activities ($mRS > 2$) 6 months after microsurgery as previously reported.^{5,16} Finally, 83 patients with BAVM lesions near the CST who underwent microsurgery were enrolled. The study was reviewed and approved by the ethics committee of the Beijing Tiantan Hospital Affiliated with Capital Medical University (approval No. KY2016-031-01). Before the study, the patients were informed about the design of the study, and each participant provided his or her informed consent. The design and all procedures adhered to the latest version of the Helsinki Declaration. The flow diagram of patient selection, AI-based indicator calculation, model development, and predictive ability evaluation is shown in Fig 1.

Baseline Data

The clinical factors including patients' age, sex, hemorrhage, and seizure information were collected from the prospectively collected database and the electronic medical records system by a neurosurgeon (J. Zhang). The variables such as BAVM size, lobe, diffuseness, deep venous drainage, deep perforating artery supply, Spetzler-Martin (S-M) score, and hemorrhagic presentation, diffuseness, deep venous drainage, and lesion-to-eloquence distance (HDVL) score were determined with consensus by 2 experienced neurosurgeons (H. Li and J. Weng) from preoperative angiograms, traditional MR imaging scans, and TOF-MRA images.⁵⁻⁷ As described in our previous study, the LCD was defined as the nearest distance from the BAVM lesions to the CST. The LCD_{Manual} , serving only as an inclusion criterion (LCD_{Manual}

<10 mm), was measured with consensus by 2 experienced neurosurgeons (H. Li and Y. Jiao) on the iPlan 3.0 workstation (Brainlab). Sections for measurement were manually selected where the tracked CST appeared to be nearest to the margin of the lesions on the TOF-MRA images fused with fMRI and DTI.¹⁷ Meanwhile, the lesion-to-corticospinal tract distance measured by the AI method (LCD_{AI}) was used for developing a predictive model. Distances of any 2 points between the surface of the segmented lesions and tracked CSTs were measured by matrix operations. The minimum value among the distances was the nearest LCD_{AI}.

MR Image Acquisition

The MR images were obtained using a 3T MR imaging scanner (Magnetom Trio; Siemens). The sagittal T1 anatomic image acquired was a gradient-echo sequence: TR = 2300 ms, TE = 2.98 ms, section thickness = 1 mm, slices = 176, FOV = 256 mm, flip angle = 9°, matrix = 64 × 64, voxel size = 1 × 1 × 1 mm³, and bandwidth = 240 kHz. Axial TOF-MRA was performed using a 3D TOF gradient-echo acquisition sequence: TR = 22 ms, TE = 3.86 ms, section thickness = 1 mm, slices = 36 × 4, FOV = 220 × 220 mm², flip angle = 120°, and matrix = 512 × 512. DTI was performed using the DWI-EPI technique: TR = 6100 ms, TE 93 = ms, section thickness = 3 mm, slices = 45, FOV = 230 × 230 mm², and matrix = 128 × 128 with a motion-probing gradient in 30 orientations.^{6,7}

Lesion Segmentation, Fiber Tracking, Registration, and Lesion Dilation

Lesion Segmentation Assisted by AI. In the segmentation phase, we used the U-Net model proposed in our previous study to delineate BAVM lesions automatically. Before we trained the model, all AVM lesions on the TOF-MRA images were manually labeled with lesion masks by 3 neuroradiologists (H. Li, J. Wang, and J. Zhang) as the ground truth references according to their signal, shape, course, texture, and so forth. The manually labeled images were used to train and test the U-Net model. In the process of developing the U-Net segmentation model, we set the number of training epochs as 300 and evaluate the model after each epoch with a Dice score. The criterion used to stop the iteration was no more than a 0.5% increase of the Dice score in 50 consecutive epochs. The results of AI segmentation were checked and verified by 2 neurosurgeons (H. Li and J. Wang). Finally, the Dice score of the model reached 0.80. In addition, the goal of our study was to build a fully AI-based automatic prediction model for convenient clinical application: inputting the raw imaging data into the model without the time-consuming manual segmentation by neurosurgeons and directly going to the prediction of the prognosis. Therefore, in the present study, we used the U-Net model for segmentation rather than using manual segmentation. The details of the segmentation method were described in our previous work.¹⁸

Fiber Tracking. Fiber tracking was based on DTI, which could reflect the anisotropy of the diffusion motion of water molecules. The Constant Solid Angle model and the Euler Delta Crossing (EuDX) algorithm were used to track the fibers on DTI with the Python Library Dipy (<https://github.com/dipy>).^{19,20} The Constant

Solid Angle model was used to obtain the orientation distribution function of each voxel on DTI scans. The orientation distribution function was used to express the probability of the fiber distribution in finite directions per voxel.²¹ The EuDX algorithm used the obtained orientation distribution function to connect the directions of these voxels with the highest probabilities to form a complete fiber tract. The results of AI fiber tracking were checked and verified by neurosurgeons (H. Li and J. Wang).

Registration Assisted by AI. In this study, the registration method included affine registration and deformable registration; the objectives of using these methods were to find a coordinate transformation and to bring the 2 images as close as possible. The difference between affine registration and deformable registration was that the affine registration performed a linear transform operation and each voxel of the image had the same transformation, so the 2 images had the same size and position after affine registration.²²

Affine registration can be expressed as

$$\begin{bmatrix} x_A \\ y_A \\ z_A \\ 1 \end{bmatrix} = T_A \begin{bmatrix} x \\ y \\ z \\ 1 \end{bmatrix} = \begin{bmatrix} A_{1,1} & A_{1,2} & A_{1,3} & A_{1,4} \\ A_{2,1} & A_{2,2} & A_{2,3} & A_{2,4} \\ A_{3,1} & A_{3,2} & A_{3,3} & A_{3,4} \\ 0 & 0 & 0 & 1 \end{bmatrix} \begin{bmatrix} x \\ y \\ z \\ 1 \end{bmatrix}.$$

T_A is a 4 × 4 matrix that represents linear transformation in affine registration. (X, y, z) is the coordinate of a voxel in an image. (x_A, y_A, z_A) is the coordinate of a voxel in an image after affine registration.

On the other hand, deformable registration performed nonlinear transformations for which each voxel of the image had its own transformation direction, so the 2 images had the same shape and texture after deformable registration.²³ The whole process is represented as follows:

$$\begin{bmatrix} x_F \\ y_F \\ z_F \end{bmatrix} = \begin{bmatrix} \Delta X \\ \Delta Y \\ \Delta Z \end{bmatrix} + \begin{bmatrix} x_A \\ y_A \\ z_A \end{bmatrix}.$$

$\Delta X, \Delta Y, \Delta Z$ indicates the offset in each dimension of each voxel. (x_F, y_F, z_F) is the coordinate of a pixel in an image after deformable registration. The nonlinear transformation operation was performed on the coordinates (x_A, y_A, z_A) after affine registration.

To obtain T_A and ($\Delta X, \Delta Y, \Delta Z$), we used U-Net neural networks to build a model for the 2 registration processes.²⁴ In the affine registration model, the decoder was designed as a fully connected neural network, and the output was a 3 × 4 matrix. In the deformable registration model, the output was a 3-channel matrix, and each channel was represented as ($\Delta X, \Delta Y, \Delta Z$). To achieve end-to-end training, we added interpolation operations into the neural network model for which the output of the network was a registered image. In addition, our study could train the affine registration and deformable registration in a cascade by which the images input into the model could undergo both affine and deformable registration.

The registration method was used to complete the functional segmentation of the medical images. The ICBM-152 (<https://>

nist.mni.mcgill.ca/icbm-152-nonlinear-atlases-2009/), which has detailed anatomic structural segmentation, was used as an atlas.^{25,26} We first extracted all the data for fibers of patients in DTI scans through the Constant Solid Angle model and the EuDX algorithm. We performed affine registration and deformable registration operations on the patients' DTI scans with the atlas, and the patients' anatomic structural segmentation data were obtained. Then, we found ROIs, the anterior half of the lower pons on the ipsilateral side and precentral gyrus, related to motor function in the patients' anatomic structural segmentation.²⁷ The fibers between the 2 ROIs were extracted from the patients' DTI scans; these were the CST of the patient. When we combined the results of segmentation and fiber tracking on the patients' DTI scans, the fibers related to motor function could be distinguished from all the fibers. Finally, the CST tracked on DTI scans was registered to TOF-MRA scans with BAVM segmentation by affine registration so that the AI-based indicators reflecting the spatial relationship of the CST and lesion could be calculated (Fig 2).

Lesion Dilation. To evaluate the spatial relationship, we performed a dilation operation on the lesion mask segmented by the U-Net model to obtain the AI-based indicators. The dilation operation was implemented using affine transformation. The centroid position (x_c, y_c, z_c) of the lesion mask was calculated, and the position was used as the center of the affine transformation. Then, all the parameters related to the times of dilation in the affine transformation matrix were calculated. We recorded the size of each voxel in an image as x_v, y_v, z_v , which represented the size of each voxel in 3 dimensions. If the size of the area where the lesion was located was (h, w, d) and we wanted to dilate the lesion by β mm, the dilated lesion was in an $(h + 2*\beta/x_v, w + 2*\beta/y_v, d + 2*\beta/z_v)$ -sized area—that is, the voxels $\beta/x_v, \beta/y_v$, and β/z_v were expanded at both ends of the region. Therefore, the lesions were dilated $((h + 2*\beta/x_v)/h, (w + 2*\beta/y_v)/w, (d + 2*\beta/z_v)/d)$ times in each dimension.

The affine transformation matrix was expressed as

$$D = \begin{bmatrix} \frac{h + 2*\beta/x_v}{h} & 0 & 0 & 0 \\ 0 & \frac{w + 2*\beta/y_v}{w} & 0 & 0 \\ 0 & 0 & \frac{d + 2*\beta/z_v}{d} & 0 \\ 0 & 0 & 0 & 1 \end{bmatrix}.$$

The dilation operation can be expressed as

$$\begin{bmatrix} x' \\ y' \\ z' \\ 1 \end{bmatrix} = D \begin{bmatrix} x - x_c \\ y - y_c \\ z - z_c \\ 1 \end{bmatrix} + \begin{bmatrix} x_c \\ y_c \\ z_c \\ 0 \end{bmatrix}.$$

AI-Based Indicator Calculations in Patients with M-AVMs

In this study, 4 AI-based indicators were proposed to predict postsurgical MDs, including fiber number (FN)_{5mm/50mm}, FN_{10mm/50mm}, and proportion of fiber voxel points (FP)_{5mm/50mm} and FP_{10mm/50mm}. FN_{5mm/50mm} and FN_{10mm/50mm} indicated the

proportion of fiber numbers from 5 to 50mm and from 10 to 50mm from the lesion border, respectively. FP_{5mm/50mm} and FP_{10mm/50mm} indicate the proportion of fiber voxel points from 5 to 50mm and from 10 to 50mm from the lesion border, respectively. The 4 indicators may reflect the lesion-to-fiber spatial relationship and the degree of potential CST damage caused by BAVM lesions. These indicators were automatically calculated by AI algorithm-assisted methods based on the results of lesion segmentation, fiber tracking, registration, and lesion dilation. In the process of indicator calculations, we used the method of lesion dilation to illustrate the distances of 5 mm, 10 mm, and 50mm from the borders of the lesion (Fig 3).

Development of a Machine Learning Model

In our study, we used the least absolute shrinkage and selection operator (LASSO) regression with the Pearson correlation coefficient to select the optimal features to develop the ML model among clinical features (including age, sex, lobe, size, deep perforating artery supply, deep venous drainage, diffuseness, hemorrhage, seizure, S-M score, LCD_{AI}, and AI-based features (including FN_{5mm/50mm}, FN_{10mm/50mm}, FP_{5mm/50mm}, and FP_{10mm/50mm})).

The aim of this process was to minimize the prediction error, determined by the following equation:

$$\operatorname{argmin}_{\beta} \|Y - X\beta\|^2 \text{ subject to } \|\beta\| = \sum_{j=0}^d \beta_j \leq t,$$

where β_j is the regression coefficient of variables selected and t is the L1-norm of the regression coefficient that controls the degree of penalty.²⁸ The impact of the penalty function was that coefficient estimates with a small contribution to the model were forced to be exactly zero.

On the basis of LASSO regression, a nomogram was built to provide a quantitative tool for clinical use. Additionally, different ML algorithms were used to build the model to find the best algorithm, including logistic regression (LR), random forest, Extreme Gradient Boosting (XGBoost) (<https://www.geeksforgeeks.org/xgboost/>), and support vector machine.

In this study, nested cross-validation comprising an outer cross-validation loop and an inner cross-validation loop was used for model optimization and evaluation. In the outer cross-validation loop, the data set was split into 10 equally sized folds based on k-fold stratified cross-validation. For each cross-validation iteration, 9 folds of data were used as the training set and 1 was used as the testing set. The training set was used as input in the inner cross-validation loop and was split into 5 folds (4 were used for training and 1 was used for validation) for feature selection and hyperparameter optimization.²⁹ The nested cross-validation was randomly repeated 50 times, and 50 different experimental results were obtained to ensure the robustness and stability of the model. The mean areas under the curve (AUCs) of the models built by different algorithms were compared to find the best performing algorithm to build the ML model.

Statistical Analysis

Statistical analyses were performed with SPSS, Version 20.0.0 (IBM). Nomograms, calibration plots, and decision curves were

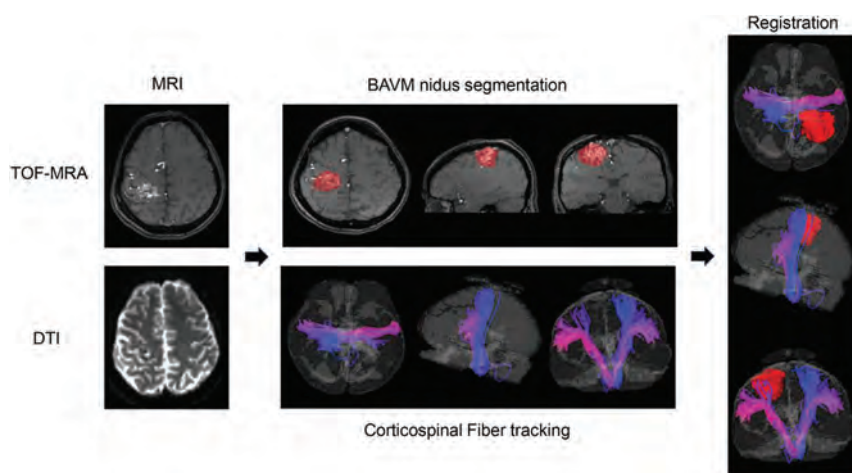


FIG 2. The workflow of segmentation, fiber tracking, and registration. Segmentation and fiber tracking were performed by the algorithm independently on TOF-MRA and DTI scans. The CSTs tracked on DTI scans were registered to TOF-MRA with BAVM segmentation to calculate the AI-based indicators.

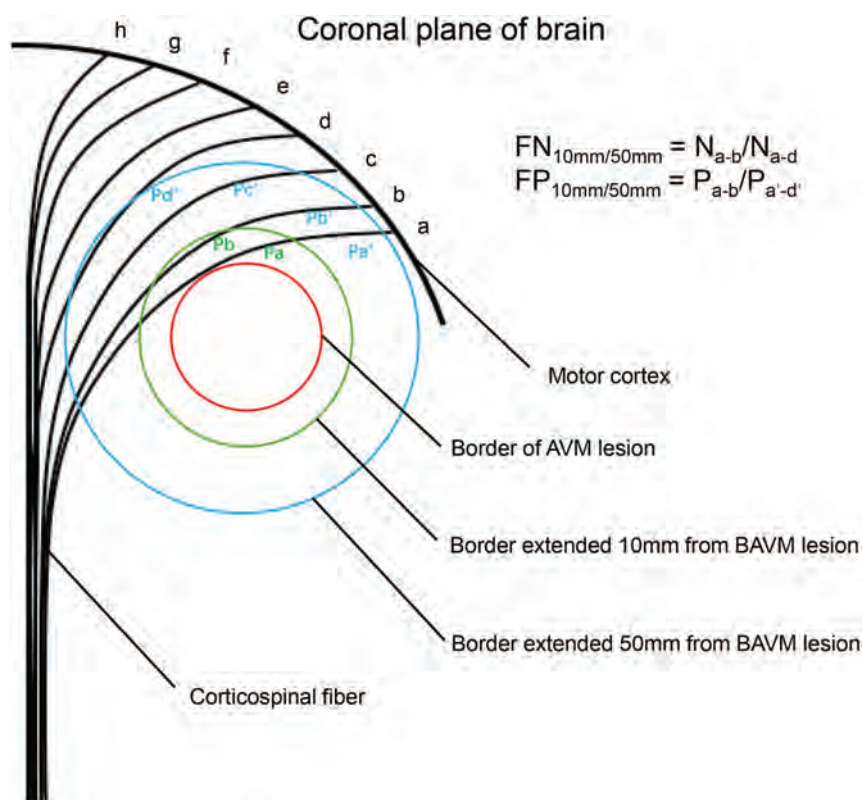


FIG 3. Schematic diagram of AI-based indicator calculation. The letters a–h indicate CSTs. The red, green, and blue circles indicate the borders of the BAVM lesion and the border with radii extended by the dilation algorithm to 10 and 50mm from the lesion, respectively. Letters a–b indicate CSTs within 10mm of the border of the BAVM lesion. Letters a–d indicate CSTs within 50mm from the border of the BAVM lesion. N_{a-b} and N_{a-d} indicate the number of fibers between a and b and between a and d, respectively. P_{a-b} and P_{a-d} indicate the sum of voxel points of fibers between a and b and between a and d, respectively.

generated using R statistical and computing software, Version R-4.0.5 (<http://www.r-project.org>). Receiver operating characteristic (ROC) plots were generated using Python, Version 3.6.0. The association between the variables and postsurgical MDs was

analyzed using univariate and multivariate analyses. The AUCs of different ML algorithms were compared to select the optimum algorithm with the highest AUC to build the ML model. The AUCs were calculated to compare the predictive ability of the AI-based indicator and ML model with reported predictive methods (LCD_{AI}, S-M score, and HDVL score).^{7,30} The DeLong test was performed to compare the AUC between FN_{10mm/50mm} and other predictive methods. The accuracy, specificity, sensitivity, precision, and F1 score of different predictive methods were calculated to evaluate their predictive abilities. A calibration plot was used to graphically represent the agreement between the probability predicted by the nomogram and the actual probability of postsurgical MDs. The Brier Score of the calibration plot was calculated to evaluate the predictive ability of the nomogram. All statistical tests were 2-sided with a significance level of $P < .05$.

RESULTS

Clinical Characteristics

A total of 83 surgically treated patients with M-AVM were included in this study. Among all the patients, there were 53 (62.4%) male and 30 (37.6%) female patients, with a mean age of 30.2 (SD, 11.5) years. The mean lesion diameter was 35.1 (SD, 11.4) mm. A deep perforating artery supply was present in 22 patients (26.5%), and deep venous drainage was present in 7 (8.4%) patients. Twenty-five (30.1%) patients had diffuse lesions, and 58 patients (69.9%) had compact lesions. Thirty-three (39.8%) and 41 (49.4%) patients had preoperative hemorrhages and seizures, respectively. The mean LCD_{AI} was 4.3 (SD, 5.1) mm. More general information on the patients is shown in Table 1. After a mean follow-up of 6 months, 26 (31.3%) patients had long-term postsurgical MDs.

Calculation of AI-Based Indicators

In patients with and without postsurgical MDs, the mean FN_{5mm/50mm} was 0.24 (SD, 0.24) and 0.03 (SD, 0.06), the mean FN_{10mm/50mm} was 0.37 (SD, 0.27) and 0.06 (SD, 0.08), the mean FP_{5mm/50mm} was 0.06 (SD, 0.10) and 0.01 (SD, 0.02), and the mean FP_{10mm/50mm} was 0.10 (SD, 0.12) and

Table 1: Baseline characteristics of patients with BAVM

	Total Patients (n = 83)
Age (mean) (yr)	30.2 (SD, 11.5)
Sex (No.) (%)	
Male	53 (62.4)
Female	30 (37.6)
Lobe (No.) (%)	
Frontal	37 (44.6)
Temporal	18 (21.7)
Parietal	18 (21.7)
Occipital	8 (9.6)
Insula	2 (2.4)
Size (mean) (mm)	35.1 (SD, 11.4)
Deep perforating artery supply (No.) (%)	22 (26.5)
Deep venous drainage (No.) (%)	7 (8.4)
Diffuse nidus (No.) (%)	25 (30.1)
LCD _{AI} (mean) (mm)	4.3 (SD, 5.1)
Hemorrhage (No.) (%)	33 (39.8)
Seizure (No.) (%)	41 (49.4)
S-M score (No.) (%)	2.4 (SD, 0.9)

Table 2: Values of the calculated AI-based indicators

	Postsurgical MDs	
	Yes	No
FN _{5mm/50mm} (mean)	0.24 (SD, 0.24)	0.03 (SD, 0.06)
FN _{10mm/50mm} (mean)	0.37 (SD, 0.27)	0.06 (SD, 0.08)
FP _{5mm/50mm} (mean)	0.06 (SD, 0.10)	0.01 (SD, 0.02)
FP _{10mm/50mm} (mean)	0.10 (SD, 0.12)	0.02 (SD, 0.05)

0.02 (SD, 0.05), respectively (Table 2). The values of the AI-based indicators are detailed in the Online Supplemental Data.

Risk Factors for Postsurgical MDs

According to the univariate analysis, significant differences in size ($P = .006$), deep perforating artery supply ($P = .031$), deep venous drainage ($P = .032$), diffuse nidus ($P = .009$), LCD_{AI} ($P = .011$), S-M score ($P = .007$), FN_{5mm/50mm} ($P = .001$), FN_{10mm/50mm} ($P < .001$), FP_{5mm/50mm} ($P = .003$), and FP_{10mm/50mm} ($P < .001$) were found between the patient cohorts with and without postoperative MDs. No significant difference was found in the other factors. According to the multivariate analysis, FN_{10mm/50mm} ($P = .002$) was significantly associated with an increased risk of MDs. No significant difference was found in the other factors (Online Supplemental Data).

Development of the ML Model and Nomogram

FN_{10mm/50mm}, the S-M score, and diffuseness were selected by LASSO regression to establish the ML model. The Pearson coefficient between any 2 of these factors was < 0.35 (Fig 4A). The AUCs of LR, random forest, XGBoost, and support vector machine algorithms in prediction were 0.88 (SD, 0.07), 0.86 (SD, 0.07), 0.86 (SD, 0.07), and 0.77 (SD, 0.12), respectively. The LR with the highest AUC of 0.88 (SD, 0.07) was selected as the algorithm for the ML model (Fig 4B). The ML model resulted in $\text{Log}[p(x)/1-p(x)] = -3.516 + (10.046 \times \text{FN}_{10\text{mm}/50\text{mm}}) + (0.279 \times \text{S-M score}) + (1.203 \times \text{Diffuseness})$, where $p(x)$ was the probability of postsurgical MDs. The AUC of the ML model achieved 0.88 (SD, 0.07) with a specificity of 0.74 at a high sensitivity of 0.92 for prediction (Online Supplemental Data).

A nomogram was created combining FN_{10mm/50mm}, the S-M score, and diffuseness based on LASSO regression (Online Supplemental Data). The graphic preliminary score for each of the 3 factors was summed to generate the total score, which indicates the probability of postsurgical MDs. The calibration curve with a Brier Score of 0.131 showed excellent agreement between the predicted probabilities of the nomogram and the observed probabilities for postsurgical MDs (Online Supplemental Data).

Comparison of Different Predictive Methods

The AUC of FN_{10mm/50mm} was 0.86 (SD, 0.08), which was statistically higher than that of LCD_{AI} (0.75 [SD, 0.08], $P = .032$), the S-M score (0.61 [SD, 0.07], $P = .011$), and the HDVL score (0.78 [SD, 0.06], $P = .045$) (Fig 4C). Furthermore, the ML model had a mean AUC of 0.88 (SD, 0.07), slightly improved by 0.02 compared with FN_{10mm/50mm} (Fig 4D). The difference was not significant ($P = .48$). Details of the AUC, accuracy, sensitivity, specificity, precision, recall, and F1 score of different predictive methods are shown in the Online Supplemental Data.

DISCUSSION

To the best of our knowledge, there is no satisfactory method that is able to accurately reflect the 3D spatial relationship between BAVM lesions and the CST to predict postsurgical motor function. In this study, we proposed a novel indicator, FN_{10mm/50mm}, acquired by AI, which has excellent performance for predicting postsurgical MDs. Meanwhile, an ML model consisting of FN_{10mm/50mm}, the S-M score, and diffuseness was developed, having better prediction performance.

Currently, AI is widely used to develop a predictive model for clinical prognosis because of its irreplaceable advantages.¹² First, AI has the ability to analyze diverse data types (eg, demographic data, imaging data, and doctors' free-text notes) and incorporate them into predictions for prognosis.¹³ Second, AI can alleviate the subjectivity and need for expertise in the interpretation of medical images and clinical evaluation. Oermann et al³¹ used an ML model to predict outcomes after radiosurgery for BAVMs and achieved good performance. Third, AI is able to reconstruct the complex geometry of stereoscopic objects captured through sophisticated imaging instruments and calculate the quantitative indicators reflecting their spatial relationship that go beyond those measured by human readers.^{14,15} In this study, we used the FN_{10mm/50mm} automatically calculated by AI to indicate the potential for CST damage due to surgery, which could reflect the spatial relationship of the 3D orientation of the CST and the border of the BAVM lesion. Furthermore, an ML model consisting of FN_{10mm/50mm}, diffuseness, and S-M grading was also developed for prognosis prediction and achieved a better performance.

The distances of 5 and 10 mm were chosen as variables on the basis of our previous studies.^{6,17} In our previous study, we found that for the BAVMs involving the eloquent areas, the LCDs of 5 and 10 mm were the cutoff values for predicting postoperative dysfunction.^{6,17} It suggested that the fibers within 5 or 10 mm from the border of AVM lesions may be most likely to be injured during the resection of AVMs.^{6,17} Meanwhile, according to the anatomic evaluation, for the recruited AVMs adjacent to CSTs

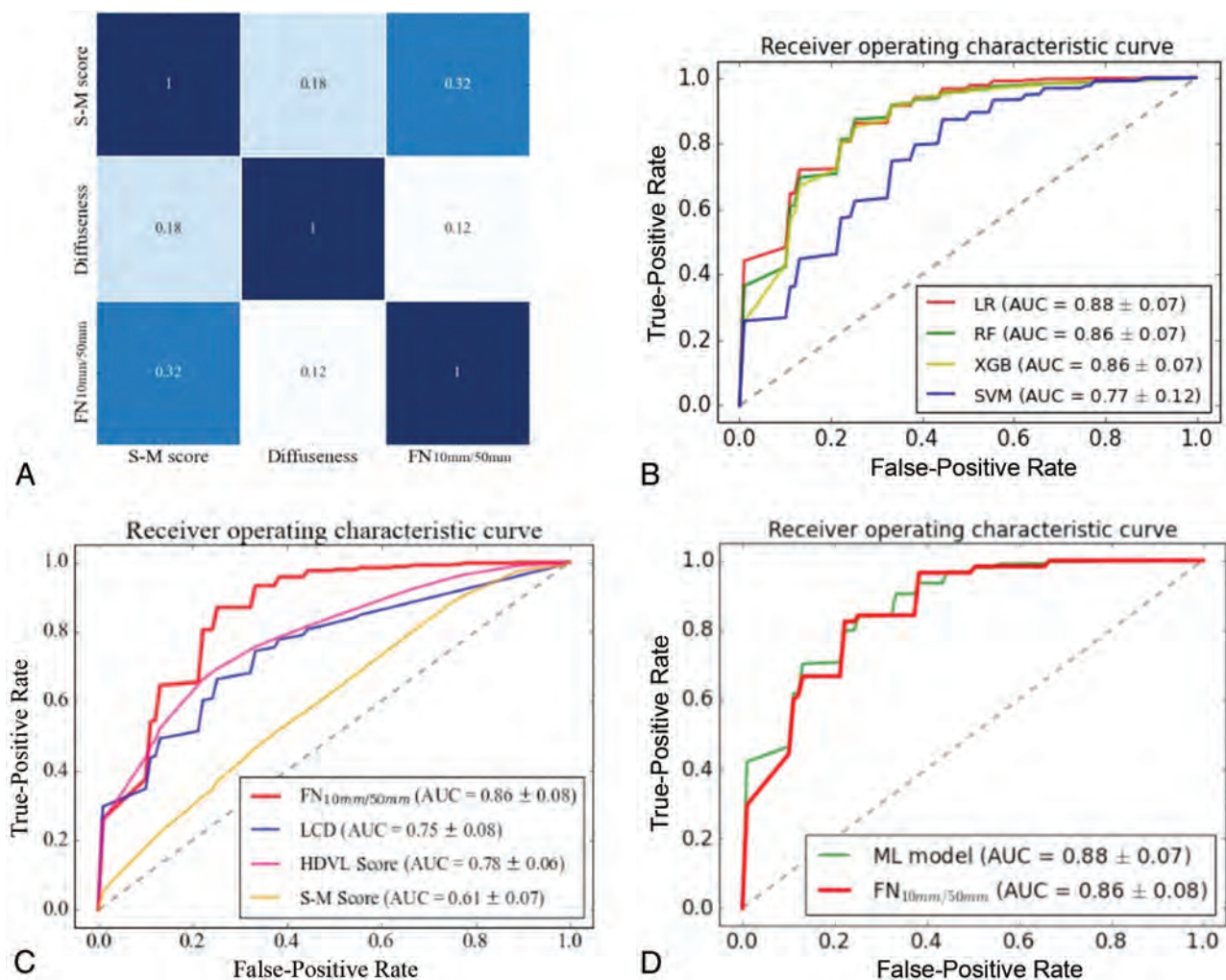


FIG 4. Results of feature screening of the ML model and different predictive methods in predicting postsurgical MDs. A, Result of feature screening with LASSO. The $FN_{10mm/50mm}$, diffuseness, and S-M score were selected for ML model building. The values in every square indicate the Pearson coefficient between every 2 features. B, ROC curves of different algorithms for the ML model in prediction. C, ROC curves of $FN_{10mm/50mm}$, LCD_{AI} , S-M score, and HDVL score in prediction. D, ROC curves of $FN_{10mm/50mm}$ and the ML model in prediction. RF indicates random forest; SVM, support vector machine; XGB, XGBoost.

(the shortest distance between AVM lesions and CSTs of $\leq 10mm$), a range of 50mm from the boundary of AVM lesions may include all CST fibers. Therefore, we used 5 mm/50mm and 10 mm/50mm to reflect the potentially injured fiber proportion of CSTs in surgery. In addition, consistent with our previous study, we used the mRS score at 6 months after microsurgery to define the postoperative MDs ($mRS > 2$).^{5,32} Patients' visual or language deficits were also taken into consideration when grading the mRS.³³

Most interesting, our results showed that the proportion of potentially affected fiber numbers was more effective than the proportion of potentially affected voxel points in predicting long-term postsurgical MDs. This finding suggested that once the CSTs were injured at 1 point, they affected the whole length of the CSTs. We speculated that this situation might be related to the characteristics of nerve axons. According to previous reports, the interruption of axon anatomic continuity will destroy the function of the whole nerve fiber, resulting in partial or total loss of its functions due to the degeneration of nerve fibers distal

to the lesion and eventual death of axotomized neurons.³⁴ This outcome means that neural fibers have less plasticity.³⁵ Therefore, neurosurgeons should be more cautious and alert when crossing a section perpendicular to CSTs in an operation to reduce the possibility of postsurgical MDs.

Our study presents novelty in the algorithm: First, we proposed a method of automatically tracking WM fibers on DTL.³⁶ DTI has been indicated as the only noninvasive way to display WM tracts in vivo and has a unique advantage in identifying and estimating neural fibers at the subcortical level.^{37,38} However, in clinical work, the differences in fiber tracking techniques in diverse clinical centers and the experiences of diverse clinicians may lead to a divergence in the accuracy of fiber tracking among different clinicians.⁸⁻¹¹ In this study, the Constant Solid Angle model and the EuDX algorithm were used to track the CST automatically; this approach could reduce the bias of identification and improve the accuracy and efficiency of fiber tracking in different clinical centers.^{21,39} Second, for our registration method, compared with traditional registration methods, we used a neural

network to perform both affine and deformable registration in a cascade. The deep learning-based registration has higher accuracy and shorter execution time than conventional registration methods.^{40,41} Third, the lesion-dilation operation in our study was implemented using affine transformation, which can accurately control the expansion of the lesions at any distance in all directions. Finally, the LR algorithm with L2 regularization was used for model establishment. The algorithm also unified the LASSO characteristics and ridge characteristics to generate sparse weights to eliminate irrelevant features, possibly preventing overfitting and improving the generalization of the model.⁴²

Our study had several limitations. First, it was conducted in a single center with a limited number of patients due to a relatively small number of this kind of surgery performed. Second, due to its retrospective nature, it may be difficult to avoid information bias, selection bias, and confounding factors. Third, the automated segmentations and fiber tracking may have some errors because of the unclear boundary of AVM lesions themselves, rough surface of the manually section-by-section labeled lesions, and so forth. The model will be trained with more cases to minimize these errors in our following study. Finally, although internal cross-validation was performed, further external validation studies including more patients and from other centers are needed.

CONCLUSIONS

Surgical treatment for M-AVMs is challenging for neurosurgeons. An accurate prediction of the possibility of postsurgical MDs would help guide neurosurgeons in the selection of surgical candidates. In this study, a new AI-based indicator $FN_{10mm/50mm}$ and a corresponding ML model are proposed that both benefit from the assistance of AI techniques. This approach will have potential in the development of predictive software and to assist doctors with different levels of clinical experience in various clinical centers, providing more precise consultation to patients with M-AVM.

ACKNOWLEDGMENTS

We would like to acknowledge the support of Dr Feng Su from the Academy for Advanced Interdisciplinary Studies at Peking University in the study design and article revision. We also thank the professional statistician Anxin Wang from the China National Clinical Research Center for Neurologic Diseases for statistical assistance.

Disclosure forms provided by the authors are available with the full text and PDF of this article at www.ajnr.org.

REFERENCES

- Solomon RA, Connolly ES Jr. **Arteriovenous malformations of the brain.** *N Engl J Med* 2017;376:1859–66 CrossRef Medline
- Lawton MT. **The role of AVM microsurgery in the aftermath of a randomized trial of unruptured brain arteriovenous malformations.** *AJNR Am J Neuroradiol* 2015;36:617–19 CrossRef Medline
- Wang M, Jiao Y, Zeng C, et al. **Chinese Cerebrovascular Neurosurgery Society and Chinese Interventional & Hybrid Operation Society, of Chinese Stroke Association clinical practice guidelines for management of brain arteriovenous malformations in eloquent areas.** *Front Neurol* 2021;12:651663 CrossRef Medline
- Davidson AS, Morgan MK. **How safe is arteriovenous malformation surgery? A prospective, observational study of surgery as first-line treatment for brain arteriovenous malformations.** *Neurosurgery* 2010;66:498–504 CrossRef Medline
- Jiao Y, Li H, Fu W, et al. **Classification of brain arteriovenous malformations located in motor-related areas based on location and anterior choroidal artery feeding.** *Stroke Vasc Neurol* 2021;6:441–48 CrossRef Medline
- Lin F, Zhao B, Wu J, et al. **Risk factors for worsened muscle strength after the surgical treatment of arteriovenous malformations of the eloquent motor area.** *J Neurosurg* 2016;125:289–98 CrossRef Medline
- Jiao Y, Lin F, Wu J, et al. **A supplementary grading scale combining lesion-to-eloquence distance for predicting surgical outcomes of patients with brain arteriovenous malformations.** *J Neurosurg* 2018;128:530–40 CrossRef Medline
- Maier-Hein KH, Neher PF, Houde JC, et al. **The challenge of mapping the human connectome based on diffusion tractography.** *Nat Commun* 2017;8:1349 CrossRef Medline
- Jbabdi S, Johansen-Berg H. **Tractography: where do we go from here?** *Brain Connect* 2011;1:169–83 CrossRef Medline
- Campbell JS, Pike GB. **Potential and limitations of diffusion MRI tractography for the study of language.** *Brain Lang* 2014;131:65–73 CrossRef Medline
- Rheault F, Poulin P, Valcourt Caron A, et al. **Common misconceptions, hidden biases and modern challenges of dMRI tractography.** *J Neural Eng* 2020;17:011001 CrossRef Medline
- Huang S, Yang J, Fong S, et al. **Artificial intelligence in cancer diagnosis and prognosis: Opportunities and challenges.** *Cancer Lett* 2020;471:61–71 CrossRef Medline
- Rudie JD, Rauschecker AM, Bryan RN, et al. **Emerging applications of artificial intelligence in neuro-oncology.** *Radiology* 2019;290:607–18 CrossRef Medline
- Wang M, Shen LQ, Pasquale LR, et al. **An artificial intelligence approach to assess spatial patterns of retinal nerve fiber layer thickness maps in glaucoma.** *Transl Vis Sci Technol* 2020;9:41 CrossRef Medline
- Gonzalez Izard S, Sanchez Torres R, Alonso Plaza O, et al. **Nextmed: automatic imaging segmentation, 3D reconstruction, and 3D model visualization platform using augmented and virtual reality.** *Sensors (Basel)* 2020;20:2962 CrossRef Medline
- Banks JL, Marotta CA. **Outcomes validity and reliability of the modified Rankin Scale: implications for stroke clinical trials—a literature review and synthesis.** *Stroke* 2007;38:1091–96 CrossRef Medline
- Jiao Y, Lin F, Wu J, et al. **Risk factors for neurological deficits after surgical treatment of brain arteriovenous malformations supplied by deep perforating arteries.** *Neurosurg Rev* 2018;41:255–65 CrossRef Medline
- Jiao Y, Zhang JZ, Zhao Q, et al. **Machine learning-enabled determination of diffuseness of brain arteriovenous malformations from magnetic resonance angiography.** *Transl Stroke Res* 2022;13:939–48 CrossRef Medline
- Garyfallidis E, Brett M, Amirbekian B, et al; Dipy Contributors. **Dipy, a library for the analysis of diffusion MRI data.** *Front Neuroinform* 2014;8:8 CrossRef Medline
- Garyfallidis E, Brett M, Tsias V, et al. **Identification of corresponding tracks in diffusion MRI tractographies.** In: *Proceedings of the Annual Meeting of the International Society of Magnetic Resonance in Medicine*, Stockholm, Sweden. May 1–7, 2010
- Aganj I, Lenglet C, Sapiro G. **ODF reconstruction in Q-ball imaging with solid angle consideration.** *Proc IEEE Int Symp Biomed Imaging* 2009;2009:1398–401 CrossRef Medline
- Chee E, Wu ZJ. **Airnet: self-supervised affine registration for 3D medical images using neural networks.** 2018. <https://arxiv.org/abs/1810.02583v1>. Accessed January 10, 2021
- Shen Z, Vialard FX, Niethammer MJ. **Region-specific diffeomorphic metric mapping.** *Adv Neural Inf Process Syst* 2019;32:1098–110 Medline

24. Lee B, Yamanakkanavar N, Choi JY. **Automatic segmentation of brain MRI using a novel patch-wise U-NET deep architecture.** *PLoS One* 2020;15:e0236493 CrossRef Medline
25. Fonov V, Evans AC, Botteron K, et al; Brain Development Cooperative Group. **Unbiased average age-appropriate atlases for pediatric studies.** *Neuroimage* 2011;54:313–27 CrossRef Medline
26. Fonov VS, Evans AG, McKinstry RC, et al. **Unbiased nonlinear average age-appropriate brain templates from birth to adulthood.** *Neuroimage* 2009;47:S102 CrossRef
27. Collins D, Zijdenbos A, Baaré W, et al. ANIMAL+INSECT: improved cortical structure segmentation. *Lecture Notes in Computer Science* 1999;1613:210–23
28. Tibshirani RM. **Regression shrinkage and selection via the lasso.** *J R Stat Soc Series B Stat Methodol* 1996;58:267–88 CrossRef
29. Krstajic D, Buturovic LJ, Leahy DE, et al. **Cross-validation pitfalls when selecting and assessing regression and classification models.** *J Cheminform* 2014;6:10 CrossRef Medline
30. Spetzler R, Martin N. **A proposed grading system for arteriovenous malformations.** *J Neurosurg* 1986;65:476–83 CrossRef Medline
31. Oermann EK, Rubinsteyn A, Ding D, et al. **Using a machine learning approach to predict outcomes after radiosurgery for cerebral arteriovenous malformations.** *Sci Rep* 2016;6:21161 CrossRef Medline
32. van Swieten J, Koudstaal P, Visser M, et al. **Interobserver agreement for the assessment of handicap in stroke patients.** *Stroke* 1988;19:604–07 CrossRef Medline
33. Mascitelli JR, Yoon S, Cole TS, et al. **Does eloquence subtype influence outcome following arteriovenous malformation surgery?** *J Neurosurg* 2018;131:876–83 CrossRef Medline
34. Navarro X, Vivó M, Valero-Cabré A. **Neural plasticity after peripheral nerve injury and regeneration.** *Prog Neurobiol* 2007;82:163–201 CrossRef Medline
35. Lundborg G. **A 25-year perspective of peripheral nerve surgery: evolving neuroscientific concepts and clinical significance.** *J Hand Surg Am* 2000;25:391–414 CrossRef Medline
36. Jiao Y, Lin F, Wu J, et al. **Plasticity in language cortex and white matter tracts after resection of dominant inferior parietal lobule arteriovenous malformations: a combined fMRI and DTI study.** *J Neurosurg* 2020;134:953–60 CrossRef Medline
37. Ciccarelli O, Catani M, Johansen-Berg H, et al. **Diffusion-based tractography in neurological disorders: concepts, applications, and future developments.** *Lancet Neurol* 2008;7:715–27 CrossRef Medline
38. Lin F, Wu J, Zhao B, et al. **Preoperative functional findings and surgical outcomes in patients with motor cortical arteriovenous malformation.** *World Neurosurg* 2016;85:273–81 CrossRef Medline
39. Bihan DL, Mangin J, Poupon C, et al. **Diffusion tensor imaging: concepts and applications.** *J Magn Reson Imaging* 2001;13:534–46 CrossRef Medline
40. de Vos BD, Berendsen FF, Viergever MA, et al. **A deep learning framework for unsupervised affine and deformable image registration.** *Med Image Anal* 2019;52:128–43 CrossRef Medline
41. Zhu Z, Cao Y, Qin C, et al. **Joint affine and deformable three-dimensional networks for brain MRI registration.** *Med Phys* 2021;48:1182–96 CrossRef Medline
42. Owen A. **A robust hybrid of lasso and ridge regression.** *Prediction and Discovery* 2007;443:59–72 CrossRef

FLAIR Vascular Hyperintensities as a Surrogate of Collaterals in Acute Stroke: DWI Matters

L. Legrand, A. Le Berre, P. Seners, J. Benzakoun, W. Ben Hassen, S. Lion, G. Boulouis, J.-P. Cottier, V. Costalat, S. Bracad, Y. Berthezene, C. Ozsancak, C. Provost, O. Naggara, J.-C. Baron, G. Turc, and C. Oppenheim, On behalf of the PREDICT-RECANAL Collaborators



ABSTRACT

BACKGROUND AND PURPOSE: FLAIR vascular hyperintensities are thought to represent leptomeningeal collaterals in acute ischemic stroke. However, whether all-FLAIR vascular hyperintensities or FLAIR vascular hyperintensities–DWI mismatch, ie, FLAIR vascular hyperintensities beyond the DWI lesion, best reflects collaterals remains debated. We aimed to compare the value of FLAIR vascular hyperintensities–DWI mismatch versus all-FLAIR vascular hyperintensities for collateral assessment using PWI-derived collateral flow maps as a reference.

MATERIALS AND METHODS: We retrospectively reviewed the registries of 6 large stroke centers and included all patients with acute stroke with anterior circulation large-vessel occlusion who underwent MR imaging with PWI before thrombectomy. Collateral status was graded from 1 to 4 on PWI-derived collateral flow maps and dichotomized into good (grades 3–4) and poor (grades 1–2). The extent of all-FLAIR vascular hyperintensities and FLAIR vascular hyperintensities–DWI mismatch was assessed on the 7 cortical ASPECTS regions, ranging from 0 (absence) to 7 (extensive), and associations with good collaterals were compared using receiver operating characteristic curves.

RESULTS: Of the 209 included patients, 133 (64%) and 76 (36%) had good and poor collaterals, respectively. All-FLAIR vascular hyperintensity extent was similar between collateral groups ($P = .76$). Conversely, FLAIR vascular hyperintensities–DWI mismatch extent was significantly higher in patients with good compared with poor collaterals ($P < .001$). The area under the curve was 0.80 (95% CI, 0.74–0.87) for FLAIR vascular hyperintensities–DWI mismatch and 0.52 (95% CI, 0.44–0.60) for all-FLAIR vascular hyperintensities ($P < .001$ for the comparison), to predict good collaterals. Variables independently associated with good collaterals were smaller DWI lesion volume ($P < .001$) and larger FLAIR vascular hyperintensities–DWI mismatch ($P = .02$).

CONCLUSIONS: In acute ischemic stroke with large-vessel occlusion, the extent of FLAIR vascular hyperintensities does not reliably reflect collateral status unless one accounts for DWI.

ABBREVIATIONS: AIS = acute ischemic stroke; ASITN/SIR = American Society of Interventional and Therapeutic Neuroradiology/Society of Interventional Radiology; FVH = FLAIR vascular hyperintensities; HIR = hypoperfusion intensity ratio; IQR = interquartile range; IVT = IV thrombolysis; LVO = large-vessel occlusion; MT = mechanical thrombectomy; ROC = receiver operating characteristic; Tmax = time-to-maximum

Neuroimaging is critical for the diagnosis and triage for treatment of patients with acute ischemic stroke (AIS) due to


Received July 29, 2022; accepted after revision October 27.

From the Institute of Psychiatry and Neuroscience of Paris (LL, A.L.B., J.B., W.B.H., C.P., O.N., J.-C.B., G.T., C. Oppenheim), Université Paris Cité, Institut National de la Santé et de la Recherche Médicale U1266, Fédération Hospitalo-Universitaire NeuroVasc, Paris, France; Departments of Neuroradiology (LL, A.L.B., J.B., W.B.H., C.P., O.N., C. Oppenheim) and Neurology (J.-C.B., G.T.), Groupe Hospitalier Universitaire-Paris Psychiatrie et Neurosciences, Sainte-Anne Hospital, Paris, France; Department of Neurology (P.S.), Hôpital Fondation Rothschild, Paris, France; Edmus Services (S.L.), Fondation Edmus, Lyon, France; Department of Diagnostic and Interventional Neuroradiology (G.B., J.-P.C.), Bretonneau Hospital, University of Tours, Institut National de la Santé et de la Recherche Médicale 1253 iBrain, Tours, France; Department of Interventional Neuroradiology (V.C.), Centre Hospitalier Régional Universitaire Gui de Chauliac, Montpellier, France; Department of Diagnostic and Interventional Neuroradiology (S.B.), University Hospital of Nancy, Institut National de la Santé et de la Recherche Médicale U947, Nancy, France; Department of Neuroradiology (Y.B.), Hospices Civils de Lyon, Lyon, France; and Department of Neurology (C. Ozsancak), Orleans Hospital, Orleans, France.

large-vessel occlusion (LVO). Collateral status before treatment is an important determinant of tissue fate and response to treatment.^{1,2} Incorporation of collateral flow status into clinical decision-making may help determine eligibility for mechanical thrombectomy (MT),³ particularly in the delayed time window.⁴

Collateral grading on DSA is considered the criterion standard. It is based on both the extent and delay of retrograde perfusion, as per the American Society of Interventional and Therapeutic Neuroradiology/Society of Interventional Radiology (ASITN/SIR)

Please address correspondence to Laurence Legrand, MD, Department of Neuroradiology, Sainte-Anne Hospital, 1 rue Cabanis, 75014 Paris, France; e-mail: l.legrand@ghu-paris.fr

 Indicates article with online supplemental data.
<http://dx.doi.org/10.3174/ajnr.A7733>

score.^{5,6} This score has been adapted to collateral flow maps derived from PWI source data. These collateral flow maps have been validated against DSA, and provide greater parenchymal detail.^{2,7}

Besides this advanced MR imaging technique for direct collateral flow imaging,^{2,7} routine MR images without contrast injection potentially provide valuable information regarding collateral status. On the FLAIR sequence, intracranial arteries normally appear dark due to the loss of signal intensity from the movement of blood. In case of an arterial occlusion, intracranial arteries become brighter, presumably because of the slow retrograde flow through leptomeningeal channels.⁸ These FLAIR vascular hyperintensities (FVH) are defined as focal, tubular, or serpentine hyperintensities in the subarachnoid space relative to CSF,⁹ corresponding to a typical arterial course. Although FVH have been proposed as a surrogate marker of collateral status,⁹ the relation between FVH and collateral status remains incompletely understood.^{10,11} Actually, FVH may not only represent retrograde collateral flow but also reflect slow anterograde flow or even stationary blood.

Collateral grading based on FVH commonly considers the extent of all FVH (all-FVH) in the affected territory; however, this lacks information regarding brain parenchyma, in contrast to both the ASITN/SIR DSA criterion standard and the PWI-derived collateral flow map-based grading scores. Critically, in the latter scores, parenchymal defect is a key item for distinguishing poor from good collaterals. Thus, the extent of all-FVH without consideration of the brain parenchyma may imperfectly reflect collateral adequacy. In contrast, assessing the presence of FVH beyond the DWI lesion, the so-called “FVH-DWI mismatch,” considers only the FVH associated with the at-risk but not yet irreversibly damaged tissue.¹² Accordingly, the FVH-DWI mismatch has been previously used as an alternative to the PWI-DWI mismatch to assess the at-risk tissue^{12,13} and identify patients most likely to benefit from intravenous thrombolysis (IVT)¹⁴ or MT.^{15,16}

On the basis of the above rationale, we hypothesized that the FVH-DWI mismatch is a better surrogate of collateral status than considering all-FVH. To test this hypothesis, we compared the value of the FVH-DWI mismatch versus all-FVH for collateral assessment using PWI-derived collateral flow maps as references.

MATERIALS AND METHODS

Study Design and Inclusion Criteria

All patients in the present study were included in a previous study that reported that good collaterals independently predict post-IVT recanalization before MT.¹ In accordance with French legislation, each patient was informed of his or her participation in the latter study and was offered the possibility to withdraw. Because the study implied retrospective analysis of anonymized data collected as part of routine care, formal approval by an ethics committee was not required. This manuscript was prepared according to the Standards for Reporting Diagnostic Accuracy (STARD) statement.¹⁷ Data from 6 French stroke centers that perform PWI as part of routine admission imaging (Sainte-Anne [Paris], Hospices Civils [Lyon], Orléans, Tours, Montpellier, and Nancy University hospitals), extracted from a large French multicenter registry

(PREDICT-RECANAL) of consecutive patients with LVO stroke referred for MT after IVT,¹⁸ were reviewed. Of note, the PWI data were not a basis for decision-making routinely, except in borderline cases.

The following inclusion criteria were used for this study: 1) acute stroke with LVO of the anterior circulation treated with IVT and referred for MT between May 2015 (when MT became routine care in these centers) and March 2017; and 2) pre-IVT MR imaging including DWI, FLAIR, T2*, MRA, and dynamic susceptibility contrast PWI to compute collateral flow maps (see below).

Data Acquisition

The following variables were extracted from the registries: age, sex, vascular risk factors, NIHSS score on admission, time between symptom onset and the start of MR imaging (onset-to-MR imaging time), and time between symptom onset and the start of IVT (onset-to-IVT time).

In line with French recommendations,¹⁹ MR imaging is implemented as first-line imaging in candidates for reperfusion therapy in all centers of the present study. Per inclusion criteria, the stroke MR imaging protocol included DWI, T2*, TOF-MRA, and dynamic susceptibility contrast PWI. FLAIR sequences were those routinely used in each center and were not standardized. The list of the main parameters of FLAIR sequences is presented in the Online Supplemental Data (all 2D FLAIR sequences).

A stroke neurologist (P.S. with 7 years of experience in stroke MR imaging) reviewed the pre-IVT imaging of all included patients. We collected the following variables: 1) occlusion site, according to 3 categories (intracranial ICA T or L occlusion and M1 and M2 segments of the MCA); 2) DWI lesion volume, semi-automatically segmented using Olea Sphere (Olea Medical) after applying a threshold of $620 \times 10^{-6} \text{ mm}^2/\text{s}$ on ADC maps,²⁰ with manual correction whenever necessary; and 3) hypoperfusion volumes, with time-to-maximum (Tmax) >4-, >6- and >10-second volumes, automatically segmented from PWI using Olea Sphere, with manual correction whenever necessary.²¹ Mismatch ratio was considered as a continuous variable and defined as $\text{Tmax} > 6\text{-second volume}/\text{DWI volume}$.²² It was further dichotomized using a 1.8 cutoff (PWI-DWI mismatch profile: $\text{Tmax} > 6\text{-second volume} > 1.8 \times \text{DWI volume}$).²³ The hypoperfusion intensity ratio (HIR) was defined as $\text{Tmax} > 10\text{-second}/\text{Tmax} > 6\text{-second volume}$. The HIR reflects the proportion of severely hypoperfused tissue and is another surrogate for collaterals.²⁴

PWI Collateral Flow Map Generation and Grading

The PWI acquisition parameters used in each participating center have been previously detailed.¹ The collateral grading method used here is similar to that described in Kim et al.² Briefly, this method uses the PWI raw data set and subtracts the baseline pre-bolus image from each frame of the raw perfusion data to automatically generate 3 sets of maps covering the MCA territory (early phase map, mid phase map, and late phase map, corresponding to the arterial, capillary, and venous phases of angiography, respectively) from which collaterals are visually graded from 1 to 4 on the basis of the ASITN/SIR angiographic classification,^{5,6}

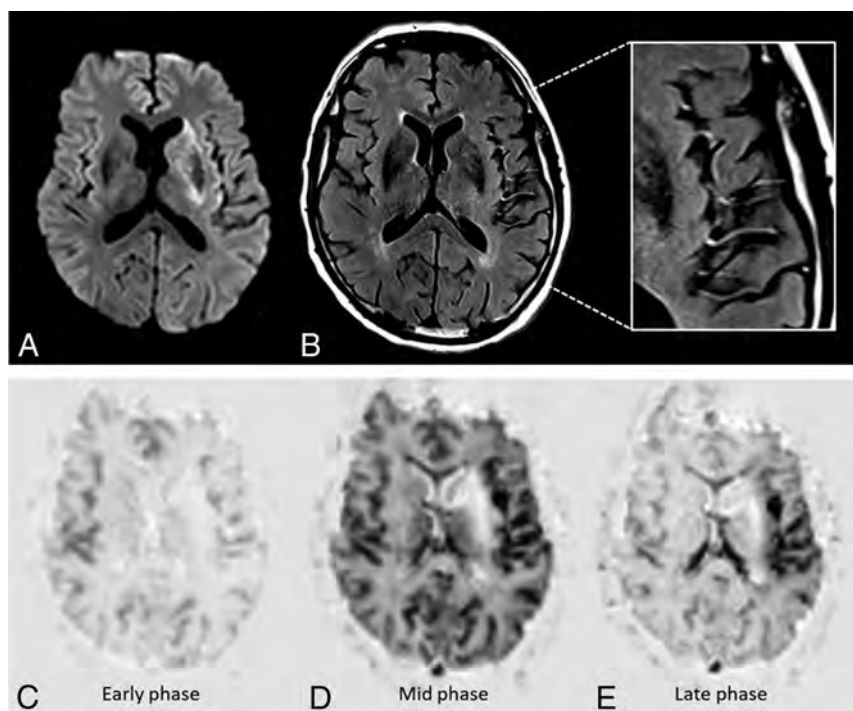


FIG 1. Illustrative case of good collaterals. MR imaging of a patient around 60 years of age obtained 108 minutes after stroke onset. Hyperintense lesions in the left MCA territory on admission DWI (A) and FVH on admission FLAIR (B), with FVH_{ASPECTS} of 5 and FVH-DWI mismatch_{ASPECTS} of 4. Grade 4 collaterals on early phase (C), mid phase (D), and late phase (E) of collateral flow maps (subtracted dynamic susceptibility contrast perfusion imaging). Note complete and rapid (from mid phase) collateral blood flow to the vascular bed in the entire ischemic territory by retrograde perfusion.

relying on the extension and the delay of retrograde perfusion: grade 1 (no or slow collaterals to the periphery of the ischemic site with persistence of some of the defect), grade 2 (rapid collaterals to the periphery of the ischemic site with persistence of some of the defect), grade 3 (collaterals with slow but complete angiographic blood flow of the ischemic bed by the late venous phase), and grade 4 (complete and rapid collateral blood flow to the vascular bed in the entire ischemic territory by retrograde perfusion).^{1,2,7} This technique has previously been validated against DSA² and was used here as reference for collateral assessment. Of note, the reproducibility of collateral grading on PWI collateral flow maps was previously assessed in a random subset ($n = 100$); the weighted κ value for interrater agreement was 0.85 (95% CI, 0.76–0.93).¹

Extent of FVH-DWI Mismatch and of All-FVH

FVH were defined as focal, tubular, or serpentine hyperintensities in the subarachnoid space relative to CSF,⁹ corresponding to a typical arterial course. On the basis of the 7 cortical ASPECTS regions,²⁵ DWI and FLAIR sequences were rated for the presence or absence of DWI lesions and FVH by 1 radiologist (A.L.B. with 5 years of experience), blinded to the collateral grade. This rating allowed us to compute FVH_{ASPECTS} ranging from 0 (no FVH) to 7 (FVH abutting all cortical ASPECTS regions)^{26,27} and FVH-DWI mismatch_{ASPECTS} ranging from 0 (no FVH-DWI mismatch) to 7 (FVH-DWI mismatch in all cortical ASPECTS areas).¹² To assess reproducibility, an experienced neuroradiologist (L.L. with

8 years of experience) independently reviewed a random subset ($n = 100$) of the sample. Figures 1 and 2 illustrate good and poor collaterals, respectively.

Statistical Analysis

Categorical variables were described as number (percentage) and were compared using the χ^2 or Fisher exact test. Continuous variables were described as means or median (interquartile range [IQR]) and compared using the Student t test or Mann-Whitney U test, as appropriate. The intraclass correlation coefficient was used to assess interobserver agreement for FVH_{ASPECTS} and FVH-DWI mismatch_{ASPECTS}. Correlations between collateral grades (1–4) and pre-specified variables of interest (NIHSS, DWI lesion volume, PWI-DWI mismatch profile, and HIR) were assessed using the Spearman (ρ) coefficient. Associations between the dichotomized collateral status and FVH-DWI mismatch_{ASPECTS} or FVH_{ASPECTS} were assessed in univariable ordinal logistic regression and described as the common OR and its 95% CI, after verifying the assumption of proportional odds. Baseline variables at a level of $P < .20$ were candidates for inclusion in a mul-

tivariable binary logistic regression model, with good collaterals as the dependent variable. Variable selection was performed backwards using a stepwise approach, whereby candidate variables entered the model at $P < .20$ and were retained only if they remained associated at $P < .05$ with the dependent variable. Covariates were assessed for collinearity and interaction effects. To determine the predictive ability of FVH-DWI mismatch and all-FVH to assess collateral status, we calculated the area under the receiver operating characteristic (ROC) curve (ie, c-statistics). Statistical analyses were performed using SAS 9.4 (SAS Institute) and SPSS 19.0 (IBM). Two-tailed $P < .05$ was considered statistically significant.

RESULTS

Patient Characteristics, Collateral Grade, and Other Variables

Of the 224 patients reported in the princeps study,¹ 15 were excluded because MR imaging was not available ($n = 4$), lacked the FLAIR sequence ($n = 8$), or was affected by severe movement artifacts ($n = 3$), leaving 209 patients for the final analysis. Excluded patients were similar to included patients in terms of age ($P = .21$), sex ($P = .46$), NIHSS score ($P = .40$), occlusion site ($P = .14$), and collateral grade ($P = .41$). The baseline characteristics of included patients are presented in the Table. Grade 1 (poor) collaterals were present in 5 (2%); grade 2, in 71 (34%); grade 3, in 108 (52%); and grade 4 (excellent), in 25 (12%)

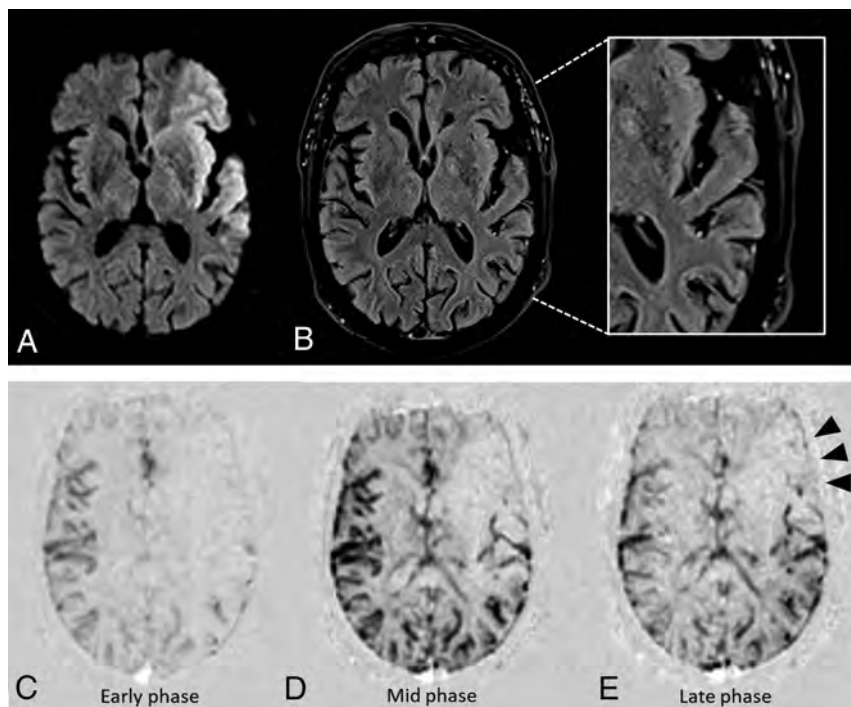


FIG 2. Illustrative case of poor collaterals. MR imaging of a patient around 70 years of age obtained 83 minutes after stroke onset. Hyperintense lesions in the left MCA territory on admission DWI (A) and FVH on admission FLAIR (B), with $FVH_{ASPECTS}$ of 6 and FVH-DWI mismatch $_{ASPECTS}$ of 1. Grade 2 collaterals on early phase (C), mid phase (D), and late phase (E) of collateral flow maps (subtracted dynamic susceptibility contrast perfusion imaging). Note rapid collaterals to the periphery of ischemic site with persistence of some of the defect (arrowheads).

patients. Given the small number of patients with grade 1 and 4 collaterals, grades 1–2 (poor collaterals) and grades 3–4 (good collaterals) were merged for subsequent analyses. A higher collateral grade was associated, as expected, with lower admission NIHSS scores ($\rho = -0.29$, $P < .001$), smaller DWI lesions ($\rho = -0.61$, $P < .001$), more frequent PWI-DWI mismatch profiles (96% versus 81%, $P < .001$), and lower HIR ($\rho = -0.57$, $P < .001$).

Extent of FVH-DWI Mismatch and of All-FVH

Interobserver agreement for $FVH_{ASPECTS}$ and FVH-DWI mismatch $_{ASPECTS}$ was good, with intraclass correlation coefficients of 0.83 (95% CI, 0.75–0.89) for $FVH_{ASPECTS}$, in line with previous studies,^{26,27} and 0.89 (95% CI, 0.84–0.92) for FVH-DWI mismatch $_{ASPECTS}$. FVH-DWI mismatch $_{ASPECTS}$ was significantly larger in patients with good compared with poor collaterals (median: 4 [IQR, 3–5] versus 2 [IQR, 0–2.75], $P < .001$). Conversely, $FVH_{ASPECTS}$ was similar between the 2 groups (median: 5 [IQR, 4–5.5] in the good collaterals group versus 5 [IQR, 4–5] in the poor collaterals group, $P = .76$, Table). The common OR for good collaterals was 1.75 (95% CI, 1.48–2.06, $P < .001$) for the FVH-DWI mismatch and 1.00 (95% CI, 0.80–1.25, $P = .98$) for all-FVH. The area under the ROC curve to predict good collaterals was 0.80 (95% CI, 0.74–0.87) for FVH-DWI mismatch and 0.52 (95% CI, 0.44–0.60) for all-FVH ($P < .001$ for the comparison) (Fig 3). The cut-point of FVH-DWI mismatch $_{ASPECTS}$,

maximizing the sum of sensitivity and specificity, was ≥ 3 . By means of this cut-point, FVH-DWI mismatch $_{ASPECTS}$ identified good collaterals with a sensitivity of 80% (95% CI, 72%–86%), specificity of 75% (95% CI, 64%–84%), a positive predictive value of 85% (95% CI, 77%–90%), and a negative predictive value of 68% (95% CI, 57%–77%). We verified post hoc that the results were similar by using the HIR instead of the PWI-derived collateral flow maps as an alternative surrogate for collaterals: HIR was dichotomized on the basis of its median value (0.43) into low (ie, good collaterals) versus high (ie, poor collaterals) subgroups. The area under the ROC curves to predict low HIR was 0.75 (95% CI, 0.68–0.81) for FVH-DWI mismatch and 0.53 (95% CI, 0.45–0.61) for all-FVH ($P < .001$ for the comparison). We also studied post hoc the correlations between $FVH_{ASPECTS}$ /FVH-DWI mismatch $_{ASPECTS}$ and perfusion deficits using Spearman (ρ) coefficients (Online Supplemental Data). The extent of all-FVH was associated with larger perfusion abnormalities (irrespective of the severity of the hypoperfusion). In contrast, the extent of the FVH-DWI mismatch was not correlated with

$T_{max} > 4$ -second and $T_{max} > 6$ -second volumes but was negatively correlated with $T_{max} > 10$ -second volume and HIR, consistent with FVH-DWI mismatch reflecting good collaterals.

Multivariable Analysis

By means of good collaterals as the dependent variable, the multivariable model included 205 patients (132 with good collaterals and 73 without, after exclusion of 4 patients without PWI volumes). Variables included in the multivariable model were NIHSS score, DWI volume, $T_{max} > 6$ -second volume, and FVH-DWI mismatch $_{ASPECTS}$. Because of the collinearity among all PWI-derived metrics, only the $T_{max} > 6$ -second volume was entered in the model. Variables that remained independently associated with good collaterals were DWI volume (adjusted OR, 0.91; 95% CI, 0.87–0.94; $P < .001$) and FVH-DWI mismatch $_{ASPECTS}$ (adjusted OR, 1.33; 95% CI, 1.04–1.70; $P = .02$); ie, patients with good collaterals had smaller DWI lesion volume and larger FVH-DWI mismatch.

DISCUSSION

In this large, multicentric population of patients with AIS referred for MT, we found, in line with our hypothesis, that the FVH-DWI mismatch is a reliable surrogate of collateral status and a better one than all-FVH. These findings emphasize the importance of taking into account the DWI lesion whenever FVH are used as a surrogate of collateral status.

Baseline characteristics of the population and univariate relationships with collateral grade^a

	Whole Cohort (n = 209)	Good Collaterals (Grades 3 and 4) (n = 133)	Poor Collaterals (Grades 1 and 2) (n = 76)	P Value
Patient characteristics				
Age (yr)	72 (61–80)	72 (61–81)	71 (60–80)	.39
Men	118 (56)	73 (55)	45 (59)	.54
Hypertension	118 (56)	80 (60)	38 (50)	.16
Diabetes mellitus	32 (15)	23 (17)	9 (12)	.29
Current smoking	26 (12)	15 (11)	11 (14)	.50
Pre-IVT characteristics				
NIHSS score	16 (9–19.5)	14 (7–18)	17 (14–21)	<.001
Onset-to-IVT time (min)	160 (130–193.5)	158 (127–195)	161 (135–186)	.67
Pre-IVT MRI				
Onset-to-MRI time (min)	123 (96–154)	122 (94–159)	124 (101–154)	.74
Occlusion site				.26
ICA-T/L	36 (17)	22 (17)	14 (18)	
M1	124 (60)	75 (56)	49 (65)	
M2	49 (23)	36 (27)	13 (17)	
DWI volume (mL)	12 (5–25)	8 (2–13)	33 (16–54)	<.001
PWI volumes (mL)				
Tmax > 4 s	133 (83–187)	119 (70–168)	176 (114–209)	<.001
Tmax > 6 s	83 (44–127)	64 (35–108)	119 (71–166)	<.001
Tmax > 10 s	31 (13–63)	18 (8–44)	61 (34–95)	<.001
HIR	0.43 (0.30–0.53)	0.36 (0.22–0.45)	0.53 (0.46–0.62)	<.001
PWI-DWI mismatch profile	186 (91%)	127 (96%)	59 (81%)	<.001
Mismatch ratio	5.6 (3.0–11.1)	8.2 (4.4–18.7)	3.2 (2.0–5.0)	.001
FVH-DWI mismatch _{ASPECTS}	3 (2–5)	4 (3–5)	2 (0–2.75)	<.001
FVH _{ASPECTS}	5 (4–5)	5 (4–5.5)	5 (4–5)	.76

Note:—HIR indicates Tmax > 10-second/Tmax > 6-second volume; ICA-T/L, ICA T or L occlusion; Mismatch ratio, Tmax > 6-second volume/DWI volume; PWI-DWI mismatch profile, Tmax > 6-second volume > 1.8 × DWI volume.

^a Categorical variables are expressed as number (%), and continuous variables, as median (IQR). Four patients had missing PWI volume data (1 patient with good collaterals and 3 patients with poor collaterals).

Collaterals play a major role in stroke pathophysiology.²⁸ These alternative vascular channels maintain perfusion to the ischemic tissue distal to the arterial occlusion, to a degree that depends on their strength. Accordingly, collateral status is a key determinant of the speed of core growth before recanalization² and may be used for decision-making as a major treatment effect modifier.⁴ Although DSA remains the reference to assess collateral status, it is invasive; furthermore, exploration of all 4 arterial axes during MT is not systematically performed to save time, thereby hampering a comprehensive analysis of collaterals. Moreover, interobserver agreement of ASITN/SIR collateral grading on DSA has been reported by some to be poor.²⁹ Finally, DSA provides information on collaterals once the patient is in the catheterization lab, which has a limited impact on the endovascular treatment workflow.

One strength of our study is the use of PWI for collateral assessment, as also reported by others.^{1,2,7,30} Contrary to DSA, grading on PWI-derived collateral flow maps has an almost perfect interobserver agreement.^{1,30} Moreover, PWI is performed within minutes of FLAIR, thereby providing information on collaterals almost simultaneous with FVH visualization. On the downside, PWI is not consistently part of acute stroke MR imaging because it requires additional scanning time, contrast agent administration and dedicated software. Thus, a straightforward pretreatment surrogate of collateral status would be useful in the clinical setting. This surrogate should be easily extractable from standard sequences whenever MR imaging is

used for patient triage and should be directly assessable before patient transfer to the catheterization lab. FVH are such a promising candidate.

Our findings are consistent with accumulating evidence that FVH are a marker of adequate collaterality¹⁰ and, furthermore, that FVH beyond and those facing the DWI lesion have a different clinical significance,³¹ as recently highlighted in a study-level meta-analysis including 36 cohort studies involving >3500 patients.³² Studies that separately analyzed the FVH beyond versus those facing the DWI lesion found that the FVH pattern, not their sole extent or number, could serve as an imaging-selection criterion for endovascular therapy.^{31,33} Our study is the first to directly compare the 2 main methods of FVH assessment for collateral assessment in the same population. To this end, we used the same scoring approach based on ASPECTS regions for both all-FVH and FVH-DWI mismatch and found that good collaterals were associated solely with FVH-DWI mismatch extent. This finding relied on PWI-derived collateral flow maps to estimate collateral status and was confirmed post hoc using HIR as alternative collateral surrogate. Our finding is consistent with those in previous studies reporting that patients with an FVH-DWI mismatch have higher ASITN/SIR scores, ie, better collaterals than those without an FVH-DWI mismatch.^{34,35} These studies, however, considered the FVH-DWI mismatch as a binary variable compared with an ordinal one as used here. Samples used were small and overlapping, and interobserver reproducibility of collateral assessment on DSA was lacking.

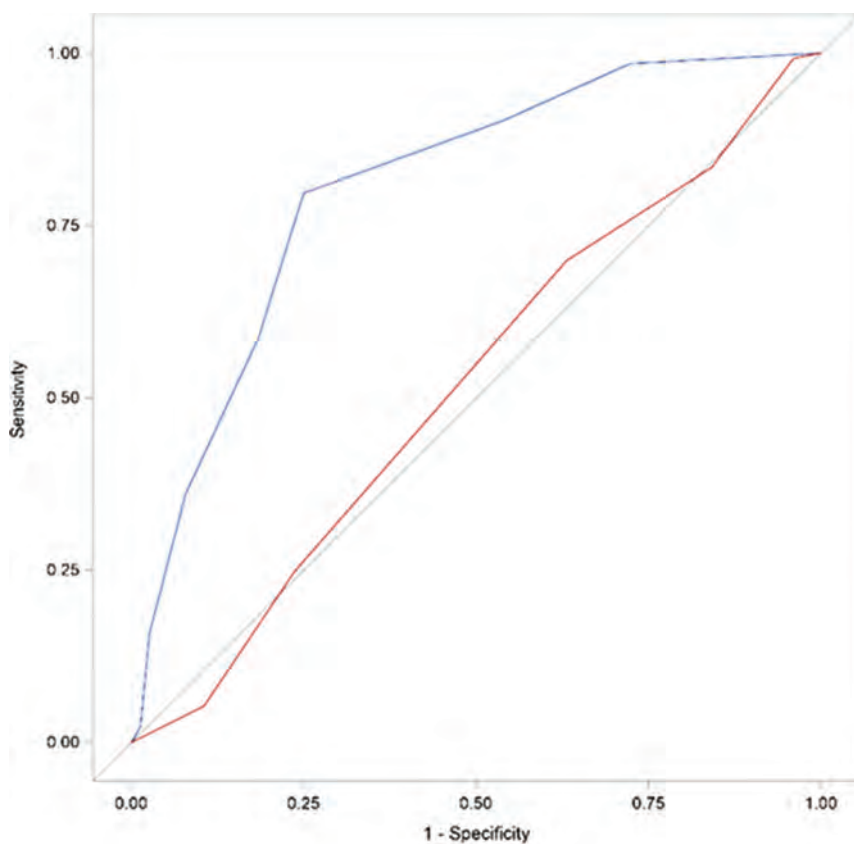


FIG 3. ROC curves of FVH-DWI mismatch_{ASPECTS} (blue) and FVH_{ASPECTS} (red) to predict good (grades 3–4) collaterals. The area under the ROC curve was higher for FVH-DWI mismatch_{ASPECTS} (0.80; 95% CI, 0.74–0.87) than for FVH_{ASPECTS} (0.52; 95% CI, 0.44–0.60), $P < .001$ for comparison.

Here we found no significant association between all-FVH extent and collateral grade, in contrast to some previous studies using DSA as a reference.^{36,37} However, the DSA-based studies used small samples, did not report interobserver reproducibility of DSA-based collateral assessment, and found no association between extensive all-FVH and smaller infarct size, which seems inconsistent. Using HIR rather than DSA before the MT era, a study found that all-FVH extent was associated with good collaterals.²⁶ However, the FVH-DWI mismatch was not assessed in this monocenter study. Our multicenter study suggests that in patients referred for MT, the latter is a much better surrogate of collaterals than all-FVH. A score based on FVH-only might be more sensitive to data heterogeneity than a score based on the FVH-DWI mismatch, given that DWI lesion visibility is more straightforward than FVH, which are influenced by FLAIR parameters.³⁸

Overall, the FVH facing and those beyond the DWI lesion may not share the same pathophysiology. In support, all-FVH had no prognostic value in 2 previous studies;^{31,39} furthermore, the presence of FVH within the DWI lesion was associated with subsequent hemorrhagic transformation.³¹ Considering this previous work together with our present findings, it would appear that all-FVH, though still widely used in recent prognostic studies,^{27,40} do not reliably reflect the collateral status in MT candidates and may, instead, represent variable degrees of perfusion abnormalities.

Our study has limitations. First, the multicenter registry used here was not designed for our analysis. Second, because our study

included patients who underwent PWI, a selection bias cannot be excluded. However, patients excluded because of absent or poor-quality PWI did not differ from included patients in terms of age, NIHSS scores, and occlusion site.¹ Third, MR images were mainly obtained within 4 hours of stroke onset, and results might differ at later time points when information on collaterals might be more useful for treatment decisions.^{10,11} Fourth, some patients were excluded because of FLAIR artifacts; however, this exclusion concerned <2% of the total sample. Fifth, although ratings of FVH_{ASPECTS} and FVH-DWI mismatch_{ASPECTS} remain subjective, interobserver agreement was good. Last, there were differences in FLAIR and DWI sequences among centers, which could have influenced the assessment of the FVH-DWI mismatch. Nevertheless, the prevalence of the FVH-DWI mismatch was similar across magnetic field strengths and manufacturers in a previous cohort,¹⁵ suggesting that it may be applied regardless of the MR imaging unit.

CONCLUSIONS

On the basis of a large multicenter population of patients with AIS and LVO who underwent MR imaging before MT, we show that the extent of the FVH-DWI mismatch is a good surrogate for collateral status and better than all-FVH. These findings support our hypothesis that the DWI lesion should be considered whenever FVH are used as surrogates for collaterals in this setting.

ACKNOWLEDGMENTS

We thank Fatemehsadat Arzanforoosh for the collection of the technical parameters for FLAIR sequences in the participating centers.

Disclosure forms provided by the authors are available with the full text and PDF of this article at www.ajnr.org.

REFERENCES

1. Seners P, Roca P, Legrand L, et al. **Better collaterals are independently associated with post-thrombolysis recanalization before thrombectomy.** *Stroke* 2019;50:867–72 CrossRef Medline
2. Kim SJ, Son JP, Ryoo S, et al. **A novel magnetic resonance imaging approach to collateral flow imaging in ischemic stroke.** *Ann Neurol* 2014;76:356–69 CrossRef Medline
3. Powers WJ, Rabinstein AA, Ackerson T, et al. **Guidelines for the Early Management of Patients with Acute Ischemic Stroke: 2019 Update to the 2018 Guidelines for the Early Management of Acute Ischemic Stroke—A Guideline for Healthcare Professionals From the American Heart Association/American Stroke Association.** *Stroke* 2019;50:e344–418 CrossRef Medline

4. Goyal M, Demchuk AM, Menon BK, et al; ESCAPE Trial Investigators. **Randomized assessment of rapid endovascular treatment of ischemic stroke.** *N Engl J Med* 2015;372:1019–30 CrossRef Medline
5. Higashida RT, Furlan AJ, Roberts H, et al; Technology Assessment Committee of the Society of Interventional Radiology. **Trial design and reporting standards for intra-arterial cerebral thrombolysis for acute ischemic stroke.** *Stroke* 2003;34:e109–37 CrossRef Medline
6. Zaidat OO, Yoo AJ, Khatri P, et al; STIR Thrombolysis in Cerebral Infarction (TICI) Task Force. **Recommendations on angiographic revascularization grading standards for acute ischemic stroke: a consensus statement.** *Stroke* 2013;44:2650–63 CrossRef Medline
7. Campbell BC, Christensen S, Tress BM, et al; EPITHET Investigators. **Failure of collateral blood flow is associated with infarct growth in ischemic stroke.** *J Cereb Blood Flow Metab* 2013;33:1168–72 CrossRef Medline
8. Sanossian N, Saver JL, Alger JR, et al. **Angiography reveals that fluid-attenuated inversion recovery vascular hyperintensities are due to slow flow, not thrombus.** *AJNR Am J Neuroradiol* 2009;30:564–68 CrossRef Medline
9. Azizyan A, Sanossian N, Mogensen MA, et al. **Fluid-attenuated inversion recovery vascular hyperintensities: an important imaging marker for cerebrovascular disease.** *AJNR Am J Neuroradiol* 2011;32:1771–75 CrossRef Medline
10. Lee KY, Kim JW, Park M, et al. **Interpretation of fluid-attenuated inversion recovery vascular hyperintensity in stroke.** *J Neuroradiol* 2022;49:258–66 CrossRef Medline
11. Zeng L, Chen J, Liao H, et al. **Fluid-attenuated inversion recovery vascular hyperintensity in cerebrovascular disease: a review for radiologists and clinicians.** *Front Aging Neurosci* 2021;13:790626 CrossRef Medline
12. Legrand L, Tisserand M, Turc G, et al. **Do FLAIR vascular hyperintensities beyond the DWI lesion represent the ischemic penumbra?** *AJNR Am J Neuroradiol* 2015;36:269–74 CrossRef Medline
13. Reyes D, Simpkins AN, Hitomi E, et al. **Estimating perfusion deficits in acute stroke patients without perfusion imaging.** *Stroke* 2022;53:3439–45 CrossRef Medline
14. Legrand L, Tisserand M, Turc G, et al. **Fluid-attenuated inversion recovery vascular hyperintensities-diffusion-weighted imaging mismatch identifies acute stroke patients most likely to benefit from recanalization.** *Stroke* 2016;47:424–27 CrossRef Medline
15. Legrand L, Turc G, Edjlali M, et al; THRACE Investigators. **Benefit from revascularization after thrombectomy according to FLAIR vascular hyperintensities-DWI mismatch.** *Eur Radiol* 2019;29:5567–76 CrossRef Medline
16. Wang Y, Zhou Z, Ding S. **FLAIR vascular hyperintensity-DWI mismatch most likely to benefit from recanalization and good outcome after stroke.** *Medicine (Baltimore)* 2020;99:e18665 CrossRef Medline
17. Bossuyt PM, Reitsma JB, Bruns DE, et al; STARD Group. **STARD 2015: an updated list of essential items for reporting diagnostic accuracy studies.** *BMJ* 2015;351:h5527 CrossRef Medline
18. Seners P, Turc G, Naggara O, et al; PREDICT-RECANAL Collaborators. **Post-thrombolysis recanalization in stroke referrals for thrombectomy: incidence, predictors, and prediction scores.** *Stroke* 2018;49:2975–82 CrossRef Medline
19. Haute Autorité de Santé. **Stroke: early management (alert, prehospital phase, initial hospital phase, indications for thrombolysis).** *Clinical Practice Guidelines*, 2009. https://www.has-sante.fr/upload/docs/application/pdf/2010-03/stroke_early_management_-_guidelines_-_english_version.pdf. Accessed June 29, 2022
20. Purushotham A, Campbell BC, Straka M, et al. **Apparent diffusion coefficient threshold for delineation of ischemic core.** *Int J Stroke* 2015;10:348–53 CrossRef Medline
21. Seners P, Turc G, Lion S, et al. **Relationships between brain perfusion and early recanalization after intravenous thrombolysis for acute stroke with large vessel occlusion.** *J Cereb Blood Flow Metab* 2020;40:667–77 CrossRef Medline
22. Campbell BCV, Majoie C, Albers GW, et al; HERMES Collaborators. **Penumbra imaging and functional outcome in patients with anterior circulation ischaemic stroke treated with endovascular thrombectomy versus medical therapy: a meta-analysis of individual patient-level data.** *Lancet Neurol* 2019;18:46–55 CrossRef Medline
23. Albers GW, Marks MP, Kemp S, et al; DEFUSE 3 Investigators. **Thrombectomy for stroke at 6 to 16 hours with selection by perfusion imaging.** *N Engl J Med* 2018;378:708–18 CrossRef Medline
24. Olivot JM, Mlynash M, Inoue M, et al; DEFUSE 2 Investigators. **Hypoperfusion intensity ratio predicts infarct progression and functional outcome in the DEFUSE 2 cohort.** *Stroke* 2014;45:1018–23 CrossRef Medline
25. Barber PA, Demchuk AM, Zhang J, et al. **Validity and reliability of a quantitative computed tomography score in predicting outcome of hyperacute stroke before thrombolytic therapy : ASPECTS Study Group—Alberta Stroke Programme Early CT Score.** *Lancet* 2000;355:1670–74 CrossRef Medline
26. Mahdjoub E, Turc G, Legrand L, et al. **Do fluid-attenuated inversion recovery vascular hyperintensities represent good collaterals before reperfusion therapy?** *AJNR Am J Neuroradiol* 2018;39:77–83 CrossRef Medline
27. Lyu JH, Zhang SH, Wang XY, et al. **FLAIR vessel hyperintensities predict functional outcomes in patients with acute ischemic stroke treated with medical therapy.** *Eur Radiol* 2022;32:5436–45 CrossRef Medline
28. Liebeskind DS. **Collateral circulation.** *Stroke* 2003;34:2279–84 CrossRef Medline
29. Ben Hassen W, Malley C, Boulouis G, et al. **Inter- and intraobserver reliability for angiographic leptomeningeal collateral flow assessment by the American Society of Interventional and Therapeutic Neuroradiology/Society of Interventional Radiology (ASITN/SIR) scale.** *J Neurointerv Surg* 2019;11:338–41 CrossRef Medline
30. Son JP, Lee MJ, Kim SJ, et al. **Impact of slow blood filling via collaterals on infarct growth: comparison of mismatch and collateral status.** *J Stroke* 2017;19:88–96 CrossRef Medline
31. Liu D, Scalzo F, Rao NM, et al. **Fluid-attenuated inversion recovery vascular hyperintensity topography, novel imaging marker for revascularization in middle cerebral artery occlusion.** *Stroke* 2016;47:2763–69 CrossRef Medline
32. Zhou Z, Malavera A, Yoshimura S, et al. **Clinical prognosis of FLAIR hyperintense arteries in ischaemic stroke patients: a systematic review and meta-analysis.** *J Neurol Neurosurg Psychiatry* 2020;91:475–82 CrossRef Medline
33. Maruyama D, Yamada T, Murakami M, et al. **FLAIR vascular hyperintensity with DWI for regional collateral flow and tissue fate in recanalized acute middle cerebral artery occlusion.** *Eur J Radiol* 2021;135:109490 CrossRef Medline
34. Zhou SB, Zhang XM, Gao Y, et al. **Diffusion-weighted imaging volume and diffusion-weighted imaging volume growth in acute stroke: associations with fluid-attenuated inversion recovery hyperintensities-diffusion-weighted imaging mismatch and functional outcome.** *Neuroreport* 2019;30:875–81 CrossRef Medline
35. Jiang L, Peng M, Geng W, et al. **FLAIR hyperintensities-DWI mismatch in acute stroke: associations with DWI volume and functional outcome.** *Brain Imaging Behav* 2020;14:1230–37 CrossRef Medline
36. Nave AH, Kufner A, Bucke P, et al. **Hyperintense vessels, collateralization, and functional outcome in patients with stroke receiving endovascular treatment.** *Stroke* 2018;49:675–81 CrossRef Medline
37. Jiang L, Chen YC, Zhang H, et al. **FLAIR vascular hyperintensity in acute stroke is associated with collateralization and functional outcome.** *Eur Radiol* 2019;29:4879–88 CrossRef Medline
38. Ahn SJ, Lee KY, Ahn SS, et al. **Can FLAIR hyperintense vessel (FHV) signs be influenced by varying MR parameters and flow velocities? A flow phantom analysis.** *Acta Radiol* 2016;57:580–86 CrossRef Medline
39. Schellinger PD, Chalela JA, Kang DW, et al. **Diagnostic and prognostic value of early MR imaging vessel signs in hyperacute stroke patients imaged <3 hours and treated with recombinant tissue plasminogen activator.** *AJNR Am J Neuroradiol* 2005;26:618–24 Medline
40. Derraz I, Pou M, Labreuche J, et al; ASTER and the THRACE Trials Investigators. **Clot burden score and collateral status and their impact on functional outcome in acute ischemic stroke.** *AJNR Am J Neuroradiol* 2021;42:42–48 CrossRef Medline

Automated Estimation of Quantitative Lesion Water Uptake as a Prognostic Biomarker for Patients with Ischemic Stroke and Large-Vessel Occlusion

S.S. Lu, R.R. Wu, Y.Z. Cao, X.Q. Xu, Z.Y. Jia, H.B. Shi, S. Liu, and F.Y. Wu



ABSTRACT

BACKGROUND AND PURPOSE: Net water uptake is qualified as an imaging marker of brain edema. We aimed to investigate the ability of net water uptake to predict 90-day functional outcome in patients with acute ischemic stroke and large-vessel occlusion.

MATERIALS AND METHODS: A total of 295 consecutive patients were retrospectively enrolled. Automated ASPECTS-net water uptake was calculated on the admission CT. The relationship between ASPECTS-net water uptake and 90-day neurologic outcome was assessed. The independent predictors of favorable outcome (mRS score ≤ 2) were assessed using multivariate logistic regression analysis and receiver operating characteristic curves and stratified by the ASPECTS.

RESULTS: Favorable 90-day outcomes were observed in 156 (52.9%) patients. ASPECTS-net water uptake (OR, 0.79; 95% CI, 0.70–0.90), NIHSS scores (OR, 0.91; 95% CI, 0.87–0.96), age (OR, 0.96; 95% CI, 0.94–0.99), and vessel recanalization (OR, 7.78; 95% CI, 3.96–15.29) were independently associated with favorable outcomes at 90 days (all, $P < .01$). A lower ASPECTS-net water uptake independently predicted a good prognosis, even in the subgroup of patients with low ASPECTS (≤ 5) ($P < .05$). An outcome-prediction model based on these variables yielded an area under the receiver operating characteristic curve of 0.856 (95% CI, 0.814–0.899; sensitivity, 76.3%; specificity, 81.3%).

CONCLUSIONS: ASPECTS-net water uptake could independently predict 90-day neurologic outcomes in patients with acute ischemic stroke and large-vessel occlusion. Integrating ASPECTS-net water uptake with clinical models could improve the efficiency of outcome stratification.

ABBREVIATIONS: AIS = acute ischemic stroke; AUC = area under the curve; IQR = interquartile range; LVO = large-vessel occlusion; MT = mechanical thrombectomy; mTICI = modified TICI; NWU = net water uptake; ROC = receiver operating characteristic

With the development of tPA and mechanical thrombectomy (MT), there has been a remarkable improvement in the functional outcome of patients with acute ischemic stroke (AIS). In particular, the recent successes of the Clinical Mismatch in the Triage of Wake Up and Late Presenting Strokes Undergoing Neurointervention with Trevo (DAWN) and Endovascular Therapy Following Imaging Evaluation for Ischemic Stroke 3 (DEFUSE-3) trials have demonstrated the benefit of MT for

patients with AIS with large-vessel occlusion (LVO) who presented within 6–24 hours after symptom onset.^{1,2} The trials used strict eligibility criteria based on advanced imaging with CTP or MR imaging for patient selection.³ However, perfusion imaging is not widely available in emergency settings due to technical and software requirements. Moreover, vendor software, institutional methods, and thresholds vary widely, causing a controversy over stroke imaging.^{4,5} The use of fixed thresholds to distinguish core and penumbra for the processing of perfusion imaging is not optimal because tissue viability after AIS is time-dependent and has substantial intrasubject variability.^{6,7}

Recent studies found that NCCT yielded no significant difference in clinical and safety outcomes compared with CTP or MR imaging for selecting eligible patients.^{8–10} NCCT was considered potentially more sensitive than relative CBF for the detection of irreversible injury in the extended time window.¹¹ Net water uptake (NWU) is a recently introduced NCCT-based parameter that can be used as a pathophysiologic imaging marker of brain edema and an individualized indicator of “tissue clock” in patients with AIS.¹² An early elevated level of NWU in ischemic

Received August 23, 2022; accepted after revision November 11.

From the Departments of Radiology (S.S.L., R.R.W., X.Q.X., F.Y.W.) and Interventional Radiology (Y.Z.C., Z.Y.J., H.B.S., S.L.), The First Affiliated Hospital of Nanjing Medical University, Nanjing, Jiangsu Province, China.

Drs Shan-Shan Lu and Rong-Rong Wu contributed equally to this work.

This work was supported by the National Natural Science Foundation of China (grant No. 82171907 to Shan-Shan Lu and grant No. 81971613 to Hai-Bin Shi).

Please address correspondence to Fei-Yun Wu, MD, Department of Radiology, The First Affiliated Hospital of Nanjing Medical University, No. 300 Guangzhou Rd, Gulou District, Nanjing, Jiangsu Province, China; e-mail: wfy_njmu@163.com

Indicates open access to non-subscribers at www.ajnr.org

Indicates article with online supplemental data.

<http://dx.doi.org/10.3174/ajnr.A7741>

lesions was associated with the development of malignant edema, malignant infarction, hemorrhagic transformation, and poor clinical outcomes.¹²⁻¹⁵

We hypothesized that besides quantifying infarction by spatial extension (ASPECTS), NWU could provide a second imaging dimension for characterizing the pathophysiology of ischemic lesions¹⁶ and predict the clinical outcome of individual patients with AIS. We tested this hypothesis by calculating the NWU using an automated ASPECTS-based method (ASPECTS-NWU) and investigating the performance of baseline ASPECTS-NWU as an imaging predictor of the 90-day functional outcome in patients with AIS and LVO. We also performed a subgroup analysis of patients with low ASPECTS (≤ 5).

MATERIALS AND METHODS

Patient Inclusion

This retrospective study was reviewed and approved by the local institutional review board. The need to obtain patient informed consent was waived. From October 2019 to January 2022, consecutive patients with AIS due to LVO admitted to our stroke center were retrospectively reviewed. The detailed inclusion criteria were as follows: 1) patients older than 18 years of age; 2) AIS due to LVO of the ICA and/or the M1 or M2 segment of the MCA; 3) stroke-onset time or last-seen-well time to admission of ≤ 24 hours; 4) NCCT performed at admission; and 5) good image quality of NCCT without significant motion artifacts. The exclusion criteria were as follows: 1) patients with posterior circulation stroke; 2) unavailable segmentation from ASPECTS software; 3) segmentation error of ASPECTS software due to midline deviation or incorrect posture; 4) previous intracranial hemorrhage, brain surgery, or large territorial lesion; 5) incomplete medical records of clinical characteristics; and 6) baseline mRS score of > 2 .

Clinical Characteristics

The clinical characteristics were obtained from the electronic medical records, including demographic information (age, sex) and stroke and treatment characteristics, including stroke-onset or last-seen-well time to admission time, site of large-artery occlusion, NIHSS score at admission (NIHSS_{admission}), treatment methods (intravenous thrombolysis, mechanical thrombectomy, bridging therapy, and standard medical therapy), and vessel recanalization. The mRS scores at 90 days were dichotomized into favorable outcome (mRS score 0–2, no or slight disability and able to perform complex activities of daily living) and unfavorable outcomes (mRS score 3–4, disabled and dependent on others for activities of daily living; mRS 5–6, bedridden or dead).

Image Acquisition and Protocols

All patients with AIS underwent stroke protocol imaging on a 128-section multidetector CT scanner (Optima CT660; GE Healthcare) with the following parameters—NCCT: collimation, 16×1.25 mm; rotation time, 1.0 seconds; FOV, 250 mm; tube voltage, 120 kV (peak); tube current, 250 mAs; and 5.0-mm section reconstruction. CTP images were obtained using a periodic spiral approach (4D adaptive spiral mode; 100 kV[p]; 200 mAs; rotation time, 0.4 seconds; and pitch value, 0.984). The protocol included 30 consecutive spiral scans of the brain (z-axis, 80 mm; 2-second delay; and 1.7-

second temporal resolution) after injection of 50 mL of contrast medium (iopromide, Ultravist 370; Bayer Schering Pharma) at a flow rate of 5 mL/s followed by administration of 30 mL of saline. The peak arterial phase of CTP data was selected on the basis of the arterial input function curve, and single-phase CTA was reconstructed with a section thickness of 0.625 mm for every 1 mm.

Image Analysis

Calculation of ASPECTS-NWU. An automated software tool (Rapid ASPECTS, iSchemaView) was used to calculate an ASPECTS as well as the ASPECTS-NWU. The software performs a series of operations to generate an automated ASPECTS evaluation, which has been described in detail previously.¹⁷ The mean Hounsfield unit (HU) value was calculated for each predefined ASPECTS region. Each ASPECTS region was classified as either normal or abnormal using a machine learning–based algorithm. ASPECTS regions involved in the ischemic brain lesion were demonstrated in red on the output map. Then, the relative difference in mean HU values between each affected ASPECTS region in the ischemic hemisphere (HU_{ischemic}) and the contralateral normal hemisphere (HU_{normal}) was computed and presented as the percentage HU difference using the following formula:¹⁸

$$\text{ASPECTS-NWU (\%)} = [1 - (\text{HU}_{\text{ischemic}}/\text{HU}_{\text{normal}})] \times 100\%.$$

All affected ASPECTS regions were verified by a senior neuro-radiologist (with 26 years of neuroradiology experience) to avoid inaccurate segmentation or identification of the ASPECTS regions.

Evaluation of Vessel Recanalization. For the patients who underwent MT, the extent of recanalization was evaluated according to the modified TICI (mTICI) scale on the basis of postprocedural DSA by a neurointerventionalist (with 13 years of experience). Good recanalization was defined as an mTICI score of $\geq 2b$. For patients who underwent only intravenous thrombolysis or standard medical therapy, vessel recanalization was evaluated on the basis of the follow-up CTA or MRA by a neuro-radiologist (with 10 years of experience) who was blinded to all the clinical information.

Statistical Analysis

Continuous variables were presented as means (SD) or medians with an interquartile range (IQR) of the 25th–75th percentile. Categorical data were presented as numbers and corresponding percentages. The Kolmogorov-Smirnov test was used to assess the normality of data distribution. The correlation between ASPECTS-NWU and stroke-onset time was evaluated using a linear relation and a nonlinear logarithmic relation. Differences in clinical and imaging characteristics between patients with favorable and unfavorable outcomes were compared using the independent *t* test or Mann-Whitney *U* test for continuous variables and the χ^2 test or Fisher exact test for categorical variables, as appropriate. Variables with significant *P* values ($P < .05$) on univariable analysis were entered into the multivariable logistic regression analysis.

Multivariable analysis was performed using the backward method to identify the independent predictors of a 90-day favorable outcome (mRS score, ≤ 2). Odds ratios with 95% confidence intervals were calculated. Receiver operating characteristic (ROC) curve analysis was used to assess the performance of different clinical and/or imaging models for predicting a favorable outcome

at 90 days. The Youden index was used to calculate the optimal cutoff point, and the sensitivity and specificity were calculated on the basis of the best cutoff values. All tests were 2-tailed, and α was set at the .05 level. The statistical analyses were performed using the commercial software SPSS (Version 20.0; IBM) and MedCalc for Windows (Version 12.3.0; MedCalc Software).

RESULTS

Patient Characteristics

A total of 295 patients (171 men; mean age, 71.0 years) who fulfilled the inclusion criteria were included. The flowchart of patient

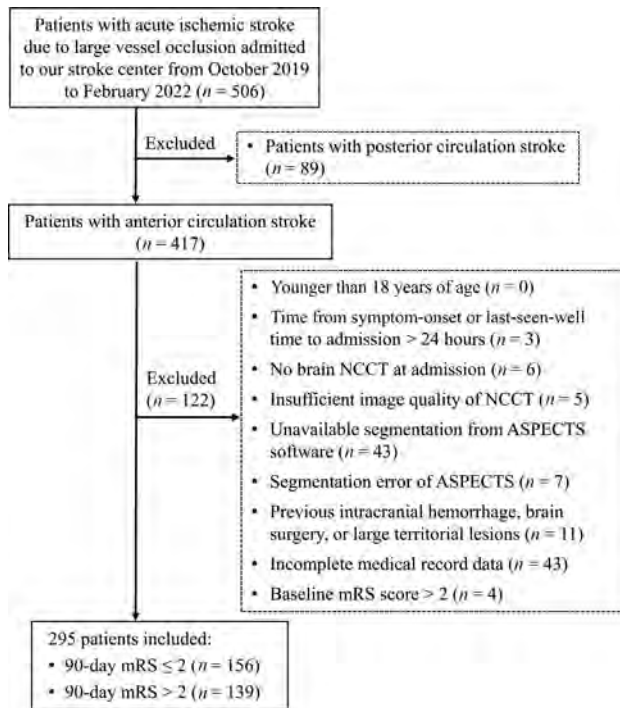


FIG 1. Flow chart for patient selection.

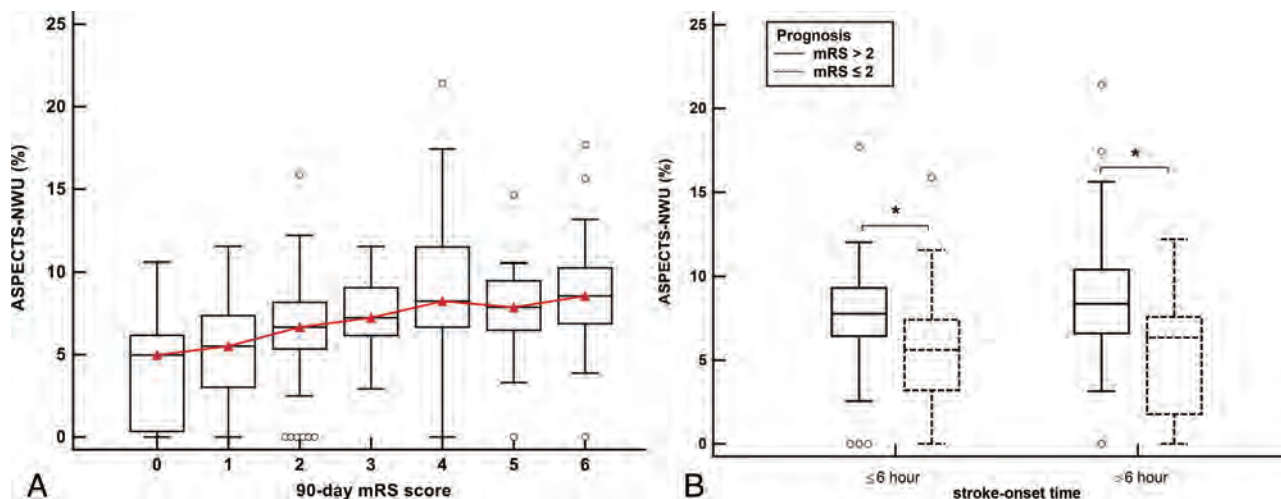


FIG 2. A, Differences in ASPECTS-NWU between patients with an mRS score of 0–6 at 90 days. The value of ASPECTS-NWU significantly correlates with the 90-day mRS scores ($r = 0.451$, $P < .001$). B, Boxplots display differences in ASPECTS-NWU between patients with favorable prognosis (mRS ≤ 2) and patients with poor prognosis (mRS > 2). Significantly lower values of ASPECTS-NWU can be observed in patients with good prognosis when compared to those with poor prognosis, regardless of the 6-hour time window. The asterisks indicate $P < .001$.

selection is shown in Fig 1. There were 186 and 109 patients within the 6-hour and 6- to 24-hour time windows, respectively. The median stroke-onset time was 270 minutes (IQR, 143–432 minutes). The median ASPECTS and ASPECTS-NWU was 7 (IQR, 6–9) and 6.83% (IQR, 5.04%–8.76%). These patients had large-artery occlusions involving the MCA M1 segment ($n = 196$), MCA M2 segment ($n = 54$), ICA ($n = 16$), or ICA combined with the MCA M1 ($n = 29$). In total, 216 patients (73.3%) underwent MT. Vessel recanalization was achieved in 184 of 295 (62.4%) patients.

Favorable outcomes at 90 days were observed in 156 patients (52.9%). The univariable analyses showed that patients with favorable outcomes were younger (69.0 versus 73.0 years) and had lower NIHSS scores (11 versus 16), lower ASPECTS-NWU (5.73% versus 8.00%), higher ASPECTS (8 versus 6) at admission, and a higher percentage of vessel recanalization after therapy (75.6% versus 47.5%) compared with those with unfavorable outcomes (all $P < .001$). The detailed clinical and imaging characteristics stratified by 90-day functional outcomes are listed in the Online Supplemental Data.

Association between ASPECTS-NWU and Prognosis Stratified by Time Window

A significant nonlinear logarithmic correlation was identified among all patients between ASPECTS-NWU and stroke-onset time ($r = 0.139$, $P = .017$). ASPECTS-NWU significantly correlated with the mRS scores at 90 days ($r = 0.451$, $P < .001$) as shown in Fig 2A. A lower ASPECTS-NWU was more consistently observed in patients with good prognoses than in those with poor prognoses, regardless of the time window (both, $P < .001$; Fig 2B).

Independent Predictors of Favorable Outcome

Multivariable logistic regression using backward selection revealed that age (OR, 0.96; 95% CI, 0.94–0.99; $P = .007$), NIHSS_{admission} (OR, 0.91; 95% CI, 0.87–0.96; $P < .001$), ASPECTS-NWU (OR, 0.79; 95% CI, 0.70–0.90; $P < .001$), and vessel recanalization (OR, 7.78; 95% CI, 3.96–15.29; $P < .001$) were independently associated

Table 1: Independent clinical and imaging predictors for a 90-day favorable outcome

Variables	Univariable Analyses		Multivariable Analyses	
	OR (95% CI)	P Value	OR (95% CI)	P Value
Age	0.97 (0.95–0.99)	<.001	0.96 (0.94–0.99)	.007
Male sex	1.62 (1.01–2.58)	.043	1.56 (0.84–2.91)	.159
NIHSS _{admission}	0.89 (0.86–0.92)	<.001	0.91 (0.87–0.96)	<.001
ASPECTS	1.52 (1.33–1.73)	<.001	1.18 (0.98–1.43)	.086
ASPECTS-NWU	0.75 (0.68–0.82)	<.001	0.79 (0.70–0.90)	<.001
Vessel recanalization	3.44 (2.10–5.63)	<.001	7.78 (3.96–15.29)	<.001

Table 2: Predication models for a 90-day favorable outcome^a

Prediction Models	AUC	Sensitivity	Specificity
Age + NIHSS	0.727 (0.670–0.784)	45.5 (37.5–53.7)	90.7 (84.5–94.9)
NWU	0.737 (0.681–0.793)	57.7 (49.5–65.6)	78.4 (70.6–84.9)
Age + NIHSS + NWU	0.794 (0.744–0.845)	76.3 (68.8–82.7)	71.9 (63.7–79.2)
Age + NIHSS + NWU + Recanalization	0.856 (0.814–0.899)	76.3 (68.8–82.7)	81.3 (73.8–87.4)

^a Data in parentheses are 95% confidence intervals.

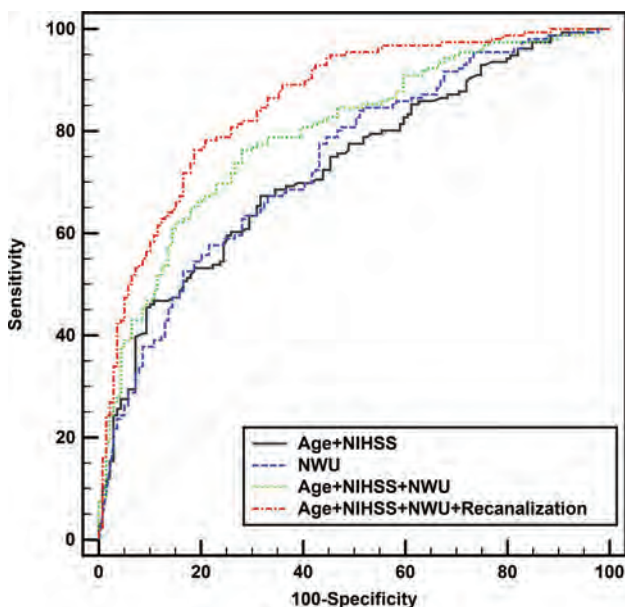


FIG 3. ROC curves for ASPECTS-NWU, age, and NIHSS_{admission} and their combinations with vessel recanalization for predicting a favorable prognosis (mRS \leq 2) at 90 days. The discrimination power is significantly higher when ASPECTS-NWU is combined with the clinical model (age and NIHSS) and is further improved when vessel recanalization is added.

with a favorable outcome at 90 days (Table 1). The area under the ROC curve of ASPECTS-NWU for the prediction of favorable outcomes was 0.737 (95% CI, 0.681–0.793), with a sensitivity of 57.7% and specificity of 78.4% at the optimal cutoff value of 6.32%. When ASPECTS-NWU was combined with the clinical model (NIHSS_{admission} and age), the area under the curve (AUC) was significantly increased to 0.794 (95% CI, 0.744–0.845; sensitivity, 76.3%; specificity, 71.9%; $P < .001$). When vessel recanalization was added, the AUC was further improved to 0.856 (95% CI, 0.814–0.899; sensitivity, 76.3%; specificity, 81.3%; $P < .001$; Table 2 and Fig 3). Two representative cases are shown in the Online Supplemental Data.

Subgroup Analysis for Patients with Low ASPECTS (≤ 5)

In the subgroup of patients with low ASPECTS of ≤ 5 ($n = 68$), 52 (76.5%) patients underwent MT, and 18 (34.6%) achieved a good neurologic outcome at 90 days. Lower mean ASPECTS-NWU values (8.44 [SD, 1.44]) were observed in patients with a good outcome compared with those with a poor outcome (10.15 [SD, 3.12]; $P = .003$). ASPECTS-NWU was consistently an independent negative predictor (OR, 0.56; 95% CI, 0.34–0.92; $P = .022$) of the 90-day neurologic outcome (Online Supplemental Data). The AUC of ASPECTS-NWU to predict a favorable outcome was 0.673 (95% CI, 0.542–0.805), with a sensitivity of 88.9% and a specificity of 48.0% at the optimal cutoff value of 9.86% in patients with low ASPECTS. A representative case is shown in Fig 4.

DISCUSSION

In the current study, we investigated the utility of ASPECTS-NWU as a quantitative imaging marker of 90-day clinical outcome in patients with AIS with LVO. Our results revealed that a lower ASPECTS-NWU at admission was consistently associated with a good prognosis at 90 days, regardless of the stroke-onset time. ASPECTS-NWU was an independent predictor of neurologic outcomes at 90 days, even in the subgroup of patients with a low ASPECTS of ≤ 5 . The combination of ASPECTS-NWU and clinical variables yielded a good performance for stratifying the neurologic outcome at 90 days.

The efficacy of treatment on functional outcome in AIS is highly time-dependent. The concepts of ischemic core and penumbra have long been considered the key decision driver for AIS treatment and were used to guide patient selection in the extended time window.³ However, considering the differences in patients and tissue characteristics, it seems neither reliable nor reasonable to apply a single universal CTP core threshold across all time points from stroke onset.^{5,19} Some researchers have suggested that the threshold-derived CTP may overestimate the ischemic core (ghost core), especially in the early time window, which may potentially deny treatment to patients who might still benefit from reperfusion.^{6,7,20} Moreover, the software for CTP processing is not available in many centers, even comprehensive stroke centers. Therefore, it is desirable to develop practical and easy-to-implement imaging biomarkers that correlate with the time-dependent tissue viability and functional outcome after treatment.

Recently, NWU has been described as a quantitative imaging biomarker of ischemic lesion edema on NCCT and an individual indicator of tissue clock in patients with AIS.^{12,21,22} An elevated NWU in ischemic lesions indicates more severe ischemic damage to brain tissue.^{13,23,24} Nawabi et al¹² reported that early elevated lesion water uptake in acute stroke predicted a poor outcome despite successful recanalization in a patient group with a stroke-onset time of < 6 hours. Brooks et al²⁵ also found that NWU

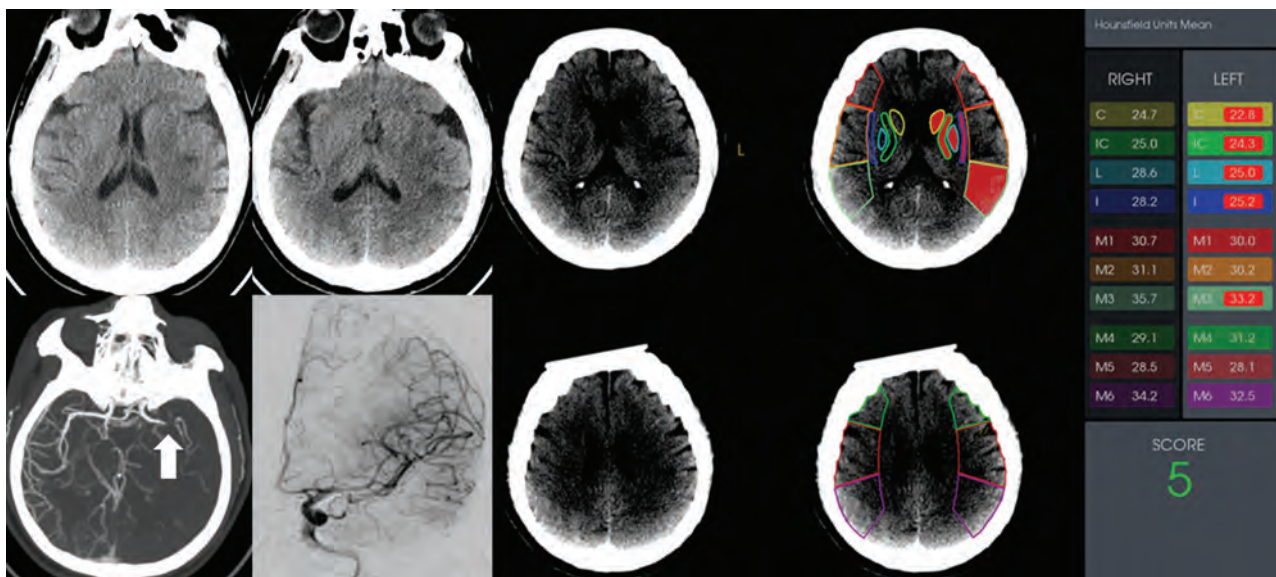


FIG 4. A patient with acute ischemic stroke due to occlusion of the M1 segment of the left MCA. This patient had an NIHSS score of 15 at admission and a low ASPECTS of 5. The mean value of ASPECTS-NWU at admission CT was 8.2%. Complete revascularization (mTICI grade 3) was achieved after mechanical thrombectomy. This patient had a favorable outcome, with an mRS score of 1 at 90 days. C indicates caudate nucleus; IC, internal capsule; L, lenticular nucleus; I, insula.

and NIHSS were independently associated with the outcomes after adjusting for the degree of recanalization and ASPECTS for patients in the extended time window. In line with their findings, we found that the level of ASPECTS-NWU in ischemic lesions may mediate treatment effects and was independently associated with functional outcome, in addition to the traditional clinical variables (such as age and NIHSS). A combination of ASPECTS-NWU with NIHSS_{admission}, age, and vessel recanalization could achieve an AUC of 0.856, sensitivity of 76.3%, and specificity of 81.3% for the outcome stratification. Our sample size was larger than in previous studies. Moreover, the calculation of ASPECTS-NWU was based on an automated software-based analysis without the requirement of CTP, which may be a simple, rapid, and practical method for clinical use.

Individual variability exists in edema progression after stroke onset, especially among patients in the extended time window. Several previous studies have confirmed that ASPECTS-NWU may serve as a reliable indicator of lesion age in acute stroke^{18,26,27}, of which a linear correlation between stroke onset time and ASPECTS-NWU was reported by Cheng et al.¹⁸ Consistent with their results, we observed a lower ASPECTS-NWU in patients with a stroke-onset time of ≤ 6 hours compared with those in the extended time window. However, in contrast to their results, we found a significant nonlinear logarithmic correlation between ASPECTS-NWU and stroke-onset time, which was in accordance with the study by Brooks et al.^{13,28} This nonlinear correlation may be a strength of NWU versus the real “time clock,” considering its quantitative nature. We performed a stratified analysis of the association between ASPECTS-NWU and prognosis according to the stroke-onset time. A higher ASPECTS-NWU was more consistently observed in patients with a poor prognosis than those with a good prognosis, regardless of the time window. Therefore, NWU provides an individualized estimate of the ischemic

pathophysiology, the real tissue clock, which directly relates to the functional outcomes after treatment.

Several studies have emphasized the potential to expand the indicators of AIS treatment for patients in the extended window using the baseline ASPECTS on NCCT.^{8,10,29} Patients with an unfavorable prognosis usually have lower baseline ASPECTS (<6).³⁰ In our study, not surprisingly, a lower ASPECTS was associated with an unfavorable prognosis. However, when NWU was added to the multivariable logistic regression analyses, ASPECTS was not an independent predictor of functional outcome. ASPECTS can only quantify the spatial extension and volume of ischemic lesions, whereas NWU additionally provides an imaging dimension for characterizing ischemic lesion pathophysiology and identifying the dynamic evolution of individual ischemic edema. Therefore, NWU may be more suitable for stratifying patient outcomes. The results from a subgroup analysis for patients with a low ASPECTS ($n = 68$) further supported this point of view. Patients with low ASPECTS (≤ 5) are generally considered unsuitable for endovascular therapy.³ However, favorable outcomes were achieved in 18 (34.6%) of the 52 patients who had successful revascularization in our study. Lower ASPECTS-NWU was the only independent imaging predictor of a favorable outcome at 90 days. Several recent studies have reported a benefit of MT in carefully selected patients with low ASPECTS.^{31,32} In accordance with the previous studies, our findings suggest that this subset of patients should not be entirely excluded from endovascular treatment. In our study, a simple NCCT-based paradigm may allow the selection of patients with a large infarct core.

There were several limitations to this study. First, despite its promise in quantifying the evolution and severity of brain edema, challenges still existed in the measurements of NWU values. The ASPECTS-based approach in our study may obviate the need for CTP but may rely on the presence of early ischemic changes.

Careful verification of all affected ASPECTS regions by experienced doctors is necessary. Moreover, the affected ASPECTS regions might only be ischemic for part of the total defined region, which may consequently lead to an underestimation of the true NWU. Therefore, the median ASPECTS-NWU in our study (6.83%) was lower than the previously reported NWU measure based on CTP. An accurate means of automatically extracting infarct regions and measuring NWU on the basis of NCCT is warranted and would be of benefit for standardizing NWU measurement in large-cohort studies and clinical trials of stroke. Second, because we enrolled patients who received only standard medical treatment without MT, vessel recanalization of these patients could only be assessed by follow-up CTA or MRA. However, most (73.2%) of our patients underwent MT, and vessel recanalization was assessed according to the mTICI grade on DSA. Finally, this was a retrospective, single-center study; therefore, the results may not be generalized to all patients with stroke. In addition, the number of patients with a low ASPECTS was relatively small. Further prospective studies are warranted to investigate the generalizability of our results and the utility of NWU for the selection of patients for treatment, especially those with a large ischemic core at admission.

CONCLUSIONS

The simplified ASPECTS-NWU could provide pathophysiologic information about individual ischemic lesions and could be correlated with the 90-day neurologic outcomes, regardless of the stroke-onset time, in patients with AIS and LVO. A lower ASPECTS-NWU may independently predict favorable neurologic outcomes at 90 days, even in the subgroup of patients with low ASPECTS (≤ 5). Integrating ASPECTS-NWU with the clinical models could improve the efficiency of outcome stratification.

Disclosure forms provided by the authors are available with the full text and PDF of this article at www.ajnr.org.

REFERENCES

- Albers GW, Marks MP, Kemp S, et al; DEFUSE 3 Investigators. **Thrombectomy for stroke at 6 to 16 hours with selection by perfusion imaging.** *N Engl J Med* 2018;378:708–18 CrossRef Medline
- Nogueira RG, Jadhav AP, Haussen DC, et al; DAWN Trial Investigators. **Thrombectomy 6 to 24 hours after stroke with a mismatch between deficit and infarct.** *N Engl J Med* 2018;378:11–21 CrossRef Medline
- Powers WJ, Rabinstein AA, Ackerson T, et al; American Heart Association Stroke Council. **2018 Guidelines for the Early Management of Patients with Acute Ischemic Stroke: A Guideline for Healthcare Professionals From the American Heart Association/American Stroke Association.** *Stroke* 2018;49:e46–110 CrossRef Medline
- Heit JJ, Wintermark M. **Perfusion computed tomography for the evaluation of acute ischemic stroke: strengths and pitfalls.** *Stroke* 2016;47:1153–58 CrossRef Medline
- Vagal A, Wintermark M, Nael K, et al. **Automated CT perfusion imaging for acute ischemic stroke: Pearls and pitfalls for real-world use.** *Neurology* 2019;93:888–98 CrossRef Medline
- Martins N, Aires A, Mendez B, et al. **Ghost infarct core and admission computed tomography perfusion: redefining the role of neuroimaging in acute ischemic stroke.** *Interv Neurol* 2018;7:513–21 CrossRef Medline
- Rotem SH, Mor S, Chen B, et al. **Infarct core reliability by CT perfusion is a time-dependent phenomenon.** *J Neuroimaging* 2020;30:240–45 CrossRef Medline
- Nguyen TN, Abdalkader M, Nagel S, et al. **Noncontrast computed tomography vs computed tomography perfusion or magnetic resonance imaging selection in late presentation of stroke with large-vessel occlusion.** *JAMA Neurol* 2022;79:22–31 CrossRef Medline
- Nogueira RG, Haussen DC, Liebeskind D; et al; Trevo Registry and DAWN Trial Investigators. **Stroke imaging selection modality and endovascular therapy outcomes in the early and extended time windows.** *Stroke* 2021;52:491–97 CrossRef Medline
- Bousslama M, Haussen DC, Rodrigues G, et al. **Novel selection paradigms for endovascular stroke treatment in the extended time window.** *J Neurol Neurosurg Psychiatry* 2021;92:1152–57 CrossRef Medline
- Siegler JE, Messe SR, Sucharew H, et al. **Noncontrast CT versus perfusion-based core estimation in large vessel occlusion: the blood pressure after endovascular stroke therapy study.** *J Neuroimaging* 2020;30:219–26 CrossRef Medline
- Nawabi J, Flottmann F, Kemmling A, et al. **Elevated early lesion water uptake in acute stroke predicts poor outcome despite successful recanalization: when “tissue clock” and “time clock” are desynchronized.** *Int J Stroke* 2021;16:863–72 CrossRef Medline
- Broocks G, Flottmann F, Scheibel A, et al. **Quantitative lesion water uptake in acute stroke computed tomography is a predictor of malignant infarction.** *Stroke* 2018;49:1906–12 CrossRef Medline
- Shi J, Wu H, Dong Z, et al. **Automated quantitative lesion water uptake in acute stroke is a predictor of malignant cerebral edema.** *Eur Radiol* 2022;32:2771–80 CrossRef Medline
- Nawabi J, Knip H, Schon G, et al. **Hemorrhage after endovascular recanalization in acute stroke: lesion extent, collaterals and degree of ischemic water uptake mediate tissue vulnerability.** *Front Neurol* 2019;10:569 CrossRef Medline
- Broocks G, Hanning U, Flottmann F, et al. **Clinical benefit of thrombectomy in stroke patients with low ASPECTS is mediated by oedema reduction.** *Brain* 2019;142:1399–407 CrossRef Medline
- Maegerlein C, Fischer J, Monch S, et al. **Automated calculation of the alberta stroke program early CT score: feasibility and reliability.** *Radiology* 2019;291:141–48 CrossRef Medline
- Cheng X, Wu H, Shi J, et al. **ASPECTS-based net water uptake as an imaging biomarker for lesion age in acute ischemic stroke.** *J Neurol* 2021;268:4744–51 CrossRef Medline
- Goyal M, Ospel JM, Menon B, et al. **Challenging the ischemic core concept in acute ischemic stroke imaging.** *Stroke* 2020;51:3147–55 CrossRef Medline
- Boned S, Padroni M, Rubiera M, et al. **Admission CT perfusion may overestimate initial infarct core: the ghost infarct core concept.** *J Neurointerv Surg* 2017;9:66–69 CrossRef Medline
- Broocks G, Flottmann F, Ernst M, et al. **Computed tomography-based imaging of voxel-wise lesion water uptake in ischemic brain: relationship between density and direct volumetry.** *Invest Radiol* 2018;53:207–13 CrossRef Medline
- Cheng X, Shi J, Wu H, et al. **Review of net water uptake in the management of acute ischemic stroke.** *Eur Radiol* 2022;32:5517–24 CrossRef Medline
- Nawabi J, Flottmann F, Hanning U, et al. **Futile recanalization with poor clinical outcome is associated with increased edema volume after ischemic stroke.** *Invest Radiol* 2019;54:282–87 CrossRef Medline
- Broocks G, Hanning U, Faizy TD, et al. **Ischemic lesion growth in acute stroke: Water uptake quantification distinguishes between edema and tissue infarct.** *J Cereb Blood Flow Metab* 2020;40:823–32 CrossRef Medline
- Broocks G, Kemmling A, Teßarek S, et al. **Quantitative lesion water uptake as stroke imaging biomarker: a tool for treatment selection in the extended time window?** *Stroke* 2022;53:201–09 CrossRef Medline
- Minnerup J, Broocks G, Kalkoffen J, et al. **Computed tomography-based quantification of lesion water uptake identifies patients**

- within 4.5 hours of stroke onset: a multicenter observational study.** *Ann Neurol* 2016;80:924–34 CrossRef Medline
27. Broocks G, Leischner H, Hanning U, et al. **Lesion age imaging in acute stroke: water uptake in CT versus DWI-FLAIR mismatch.** *Ann Neurol* 2020;88:1144–52 CrossRef Medline
 28. Broocks G, Elsayed S, Kniep H, et al. **Early prediction of malignant cerebellar edema in posterior circulation stroke using quantitative lesion water uptake.** *Neurosurgery* 2021;88:531–37 CrossRef Medline
 29. Nagel S, Herweh C, Pfaff JA, et al. **Simplified selection criteria for patients with longer or unknown time to treatment predict good outcome after mechanical thrombectomy.** *J Neurointerv Surg* 2019;11:559–62 CrossRef Medline
 30. Goyal M, Menon BK, van Zwam WH, et al; HERMES Collaborators. **Endovascular thrombectomy after large-vessel ischaemic stroke: a meta-analysis of individual patient data from five randomised trials.** *Lancet* 2016;387:1723–31 CrossRef Medline
 31. Broocks G, Kniep H, Schramm P, et al. **Patients with low Alberta Stroke Program Early CT Score (ASPECTS) but good collaterals benefit from endovascular recanalization.** *J Neurointerv Surg* 2020;12:747–52 CrossRef Medline
 32. Deb-Chatterji M, Pinnschmidt H, Flottmann F, et al; GSR-ET Investigators. **Predictors of independent outcome of thrombectomy in stroke patients with large baseline infarcts in clinical practice: a multi-center analysis.** *J Neurointerv Surg* 2020;12:1064–68 CrossRef Medline

Topological Structural Brain Connectivity Alterations in Aspartylglucosaminuria: A Case-Control Study

U. Roine, A.M. Tokola, T. Autti, and T. Roine



ABSTRACT

BACKGROUND AND PURPOSE: We investigated global and local properties of the structural brain connectivity networks in aspartylglucosaminuria, an autosomal recessive and progressive neurodegenerative lysosomal storage disease. Brain connectivity in aspartylglucosaminuria has not been investigated before, but previous structural MR imaging studies have shown brain atrophy, delayed myelination, and decreased thalamic and increased periventricular WM T2 signal intensity.

MATERIALS AND METHODS: We acquired diffusion MR imaging and T1-weighted data from 12 patients with aspartylglucosaminuria (mean age, 23 [SD, 8] years; 5 men), and 30 healthy controls (mean age, 25 [SD, 10] years; 13 men). We performed whole-brain constrained spherical deconvolution tractography, which enables the reconstruction of neural tracts through regions with complex fiber configurations, and used graph-theoretical analysis to investigate the structural brain connectivity networks.

RESULTS: The integration of the networks was decreased, as demonstrated by a decreased normalized global efficiency and an increased normalized characteristic path length. In addition, the average strength of the networks was decreased. In the local analyses, we found decreased strength in 11 nodes, including, for example, the right thalamus, right putamen, and, bilaterally, several occipital and temporal regions.

CONCLUSIONS: We found global and local structural connectivity alterations in aspartylglucosaminuria. Biomarkers related to the treatment efficacy are needed, and brain network properties may provide the means for long term follow-up.

ABBREVIATION: AGU = aspartylglucosaminuria

Aspartylglucosaminuria (AGU) is a rare, progressive, neurodegenerative lysosomal storage disease. It is inherited in a recessive manner and is caused by a mutation in the aspartylglucosaminidase (AGA) gene located in 4q34.3.¹ Due to the isolated population, it has developed in Finland, where the estimated incidence of AGU is 1:18,000 and there are about 160–200

patients with AGU in the country.² It has been estimated that 200–300 patients with AGU exist worldwide.² More than 30 AGA variants have been identified in patients with AGU, but in Finland, 98% of patients have the AGU_{FIN} major variant.³ The mutations in the AGA gene result in deficient activity of a lysosomal hydrolase enzyme called aspartylglucosaminidase, which is responsible for breaking a N-glycosidic bond between carbohydrates and proteins, and this leads to excessive accumulation of uncleaved aspartylglucosamine and other glycoasparagines in tissues.^{1,2} With time, AGU affects the whole body, including the CNS, in a progressive manner.

The first neurologic signs are often developmental delays, such as clumsy walking and delayed speech, noticed around 12–15 months of age, and progressive intellectual impairment finally leads to severe intellectual disability.⁴ Autistic features, behavioral disturbances, epilepsy, and disrupted sleep patterns may be present.⁴ Motor skills also deteriorate with time, and skeletal and connective tissue abnormalities may be present.⁴ Typical facial features include macroglossia, thick lips, low and wide nasal bridge, short nose, puffy eyelids, and broad face.⁴ After early macrocephaly, the head size reduces, though the

Received March 23, 2022; accepted after revision November 16.

From the Department of Radiology (U.R., A.M.T., T.A., T.R.), HUS Medical Imaging Center, and Department of Pediatric Neurology (U.R.), Children's Hospital, University of Helsinki and Helsinki University Hospital, Helsinki, Finland; Department of Neuroscience and Biomedical Engineering (T.R.), Aalto University School of Science, Espoo, Finland; and Turku Brain and Mind Center (T.R.), University of Turku, Turku, Finland.

T. Autti and T. Roine contributed equally to this work.

U.R. received funding from the Finnish Medical Foundation and the Arvo and Lea Ylppö Foundation. A.M.T. received funding from the Rinnekoti Research Foundation, the Finnish Brain Foundation, and the Arvo and Lea Ylppö Foundation. T.R. received funding from the Finnish Cultural Foundation.

Please address correspondence to Timo Roine, MD, HUS Medical Imaging Center, Radiology, University of Helsinki and Helsinki University Hospital, PL 22 (Haartmaninkatu 4), FI-00014 Helsingin Yliopisto, Finland; e-mail: timo.roine@iki.fi; @TimoRoine

Indicates article with online supplemental data.

<http://dx.doi.org/10.3174/ajnr.A7745>

skull may be thickened.⁵ The disease leads to a premature death, typically before 45 years of age.⁶

The AGU diagnosis is made on the basis of genetic testing, though biochemical tests of accumulated aspartylglucosamine in urine can be useful for screening purposes.⁴ No curative therapies currently exist, but several preclinical studies aiming at enzyme replacement or gene therapy have been published,⁷⁻¹⁰ and in 2018, a 4-year clinical trial was initiated with a pharmacologic chaperone called betaine.¹¹ It facilitates the correct folding of aspartylglucosaminidase mutants, because most AGA variants cause misfolding of the protein.⁴ The benefit of hematopoietic stem cell transplantation is unclear.⁴

With the emerging new treatments, new methods to evaluate the response are needed. Biochemical tests, such as aspartylglucosaminidase enzyme activity, could potentially be used as surrogate biomarkers.⁴ MR imaging-based measures, including structural brain connectivity, could provide a means for evaluating the progression of the disease.

Conventional MR imaging studies in AGU have shown brain atrophy, delayed myelination, decreased thalamic T2 signal intensity, and increased T2 signal intensity in the periventricular WM.¹²⁻¹⁶ In addition, on the basis of a visual analysis, poor differentiation between white and gray matter, thinning of the corpus callosum, cerebellar atrophy, and mild ventricular dilation have been reported.¹⁴ Representative figures of the abnormalities in conventional MR imaging have been published by Tokola et al.¹⁴ Diffusion MR imaging has been used to study a 10-year-old boy with AGU, and decreased fractional anisotropy was found in the corpus callosum and thalamocortical pulvinar tracts compared with his healthy twin brother.¹⁷

Possible alterations in structural brain connectivity have not been investigated in AGU. Diffusion MR imaging followed by whole-brain tractography and graph-theoretical methods can be used to reliably study the whole-brain connectivity in health and disease.¹⁸⁻²¹ The association of structural brain connectivity with the response to medication has also been studied, for example, in bipolar disorder and schizophrenia.^{22,23} The aim of the current study was to recognize possible global or local abnormalities in the structural brain connectivity networks in patients with AGU compared with healthy controls. On the basis of the findings in another lysosomal storage disease,²⁴ juvenile neuronal ceroid lipofuscinosis, we expected to find globally decreased integration of the structural brain connectivity networks in AGU. In addition, we expected to find several local alterations in the connectivity based on the wide spectrum of the symptoms.

MATERIALS AND METHODS

In summary, we performed whole-brain tractography on the basis of diffusion MR imaging data to reconstruct the WM tracts in the brain and segmented the GM of the brain into 164 anatomic regions. Then, we reconstructed structural brain connectivity networks by assigning each end of the reconstructed fiber tracts to corresponding segmented anatomic regions and used graph-theoretical methods to investigate the global and local properties in the structural brain connectivity networks of patients with AGU and healthy controls.

Participants

Twelve patients with AGU, mean age, 23 years 11 months (SD, 8 years 3 months) (range, 9–35 years; 5 males) and 30 healthy age- and sex-matched controls, mean age, 25 years 5 months (SD, 9 years 11 months) (range, 9–46 years; 13 males), participated in this study. Due to the rarity of the disease, we were not able to recruit more patients. Two-way *t* tests with a significance threshold $\alpha < .05$ were used to determine sufficient age- and sex-matching of the two groups. All patients were diagnosed using a urine test showing elevated levels of aspartylglucosamine and a blood test showing deficiency in the AGA enzyme. The control subjects were healthy volunteers recruited from the Helsinki and Uusimaa region who had no neurologic, psychiatric, or other major diagnoses or medications. All participants and/or their parents gave informed consent before the study, which was approved by the local ethics committee of the Hospital District of Helsinki and Uusimaa (ethics permission, 247/E7/2007).

MR Imaging Acquisition

The MR imaging data were acquired with an Achieva 3T machine (Phillips Healthcare) at the Helsinki University Hospital, Finland, from 2007 to 2012. Sedation was not used during the scanning due to ethical reasons. T1 3D axial series were acquired with $1 \times 1 \times 1$ mm resolution (TR = 68.15 ms, TE = 3.75 ms, matrix size = 256×256 mm, flip angle = 8°). Two radiologists visually evaluated the conventional sequences, and the findings have been reported previously.¹⁴ For the single-shot axial diffusion-weighted data, 32 gradient orientations, a diffusion-weighting = 1000 s/mm^2 , TR = 10,809 ms, TE = 59.5 ms, FOV = 224×224 mm, and an isotropic 2-mm voxel size was used. One image was acquired with no diffusion-weighting.

Reconstruction of the Structural Brain Connectivity Networks

First, the data were corrected for motion²⁵ and eddy current-induced distortions in ExploreDTI (<https://www.exploredti.com/>).²⁶ Because no reverse phase-encoding data were available, echo-planar imaging distortions were corrected via nonlinear registration with cubic b-splines to the T1-weighted data.²⁷ Then, we performed constrained spherical deconvolution based whole-brain streamline tractography, which enables the reconstruction of neural tracts through regions with complex WM configurations, such as crossing fibers.^{28,29} Next, we segmented 164 cortical and subcortical GM areas from the T1-weighted images using FreeSurfer (<http://surfer.nmr.mgh.harvard.edu>).^{30,31} The validity of the segmentations was visually confirmed for all subjects. Finally, we reconstructed structural brain connectivity networks, connectomes, by assigning the reconstructed streamline tracts to the GM areas on the basis of their end points.^{18,19} These GM areas became the nodes of the network, and the edges between the nodes were weighted by the number of the reconstructed tracts between each pair of areas, resulting in a 164×164 connectivity matrix. The reconstruction of structural brain connectivity networks is presented in Fig 1.

Graph-Theoretical Analyses

Graph-theoretical analyses were performed with the Brain Connectivity Toolbox in Matlab (MathWorks).³² We investigated

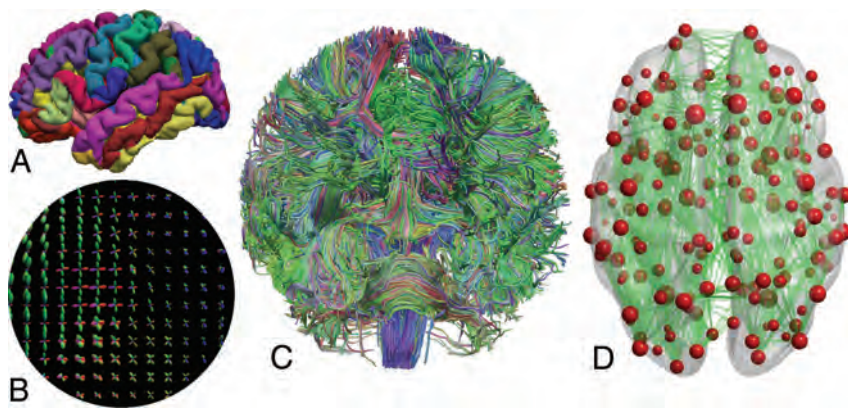


FIG 1. Reconstruction of structural brain connectivity networks. **A**, Cortical and subcortical GM was parcellated into 164 regions based on the T1-weighted images. **B**, Constrained spherical deconvolution was used to estimate complex fiber orientation distributions from diffusion MR imaging data. **C**, Whole-brain probabilistic streamline tractography was performed to reconstruct (**D**) structural brain connectivity networks, in which nodes represent GM regions and the edges between the nodes represent the WM connectivity (number of streamlines) between the regions. The size of the nodes corresponds to the strength of the node, and the opacity of the edges is scaled according to the number of streamlines. The fiber orientation distributions and whole-brain tractography are colored according to the directions in the brain: red (left-right), blue (superior-inferior), and green (anterior-posterior).

7 global (betweenness centrality, normalized clustering coefficient, normalized global efficiency, normalized characteristic path length, small-worldness, degree, and strength) and 3 local (betweenness centrality, efficiency, and strength) properties of the structural connectome.¹⁹ These properties were compared between the patients with AGU and the control subjects. In addition, the correlations of the global properties with age were also investigated both in patients with AGU and controls.

Statistical Analyses

Statistical analyses were performed in SPSS Statistics, Version 27 (IBM). Age and sex were used as covariates in all analyses except for the correlation analyses between the global network properties and age. There were no missing data. The Bonferroni correction was used to correct for the family-wise error rate using $n = 7$ for the global analyses and $n = 164$ for the local node-level analyses. Due to the small sample size, the assumptions of normality and homogeneity of variances for the F tests were rigorously checked for each variable, and whenever the assumptions were not met, a nonparametric Mann-Whitney U test (2-sided, corrected for ties) was used instead.³³ However, because the covariates cannot be taken into account in the nonparametric test, we chose to report only the findings that were significant using both approaches.

Scientific Visualizations

BrainNet Viewer (<https://www.nitrc.org/projects/bnv/>),³⁴ MRtrix3 (<https://www.mrtrix.org/>),³⁵ seaborn (<https://seaborn.pydata.org/>),³⁶ and Matplotlib (<https://matplotlib.org/>)³⁷ were used to produce the scientific visualizations.

RESULTS

We investigated both global and local properties of the structural connectome in patients with AGU compared with control subjects. Of the global properties, small-worldness ($F = 11.6$, $P = .0006$),

strength ($F = 15.9$, $P = .0003$), degree ($F = 8.4$, $P = .006$), and normalized global efficiency ($F = 15.5$, $P = .0003$) were significantly decreased, and characteristic path length was significantly increased ($F = 35.9$, $P = .0000006$) in AGU after Bonferroni correction for multiple comparisons, as demonstrated in Fig 2. The results, except for node degree, also remained significant without using age and sex as covariates. However, when taking into account the assumptions of the F tests, normality and homoscedasticity, the differences in small-worldness and degree were not statistically significant in the nonparametric Mann-Whitney U tests.

We also investigated the correlation between the global properties and age in both the patients and controls. As shown in Fig 3, the normalized clustering coefficient and average strength decreased with age in both patients with

AGU and control subjects while being lower at all ages in AGU. Moreover, in characteristic path length, global efficiency, small-worldness, and degree, the differences between the 2 groups were smaller in the younger subjects and increased with age.

In the local node-level analyses, we found decreased strength in 12 nodes using F tests and age and sex as covariates. In 11 of these nodes, the strength was also significantly decreased using a nonparametric Mann-Whitney U test performed without using age and sex as covariates whenever the assumptions of the F test were not met. These regions included the right thalamus, right putamen, and several nodes in the occipital and temporal regions in both hemispheres, shown in Fig 4 and the Online Supplemental Data. Local efficiency or betweenness centrality were not affected. The results were corrected for multiple comparisons using a Bonferroni-corrected significance threshold of $P < .05/164 = .0003$. The complete node-level results are presented in the Online Supplemental Data.

DISCUSSION

The purpose of our study was to investigate whether there are global or local abnormalities in the structural brain connectivity networks in patients with AGU. First, we performed whole-brain tractography to reconstruct the WM tracts in the brain, then we segmented the GM into 164 anatomic areas, and finally, we reconstructed structural brain networks, which we analyzed by using graph-theoretical tools. We found both global and local topological alterations in the brain connectivity in patients with AGU compared with the control group. In addition, we observed an altered age relationship in patients with AGU.

To investigate the integration of the networks, we calculated normalized global efficiency³⁸ and normalized characteristic path length,³⁹ which both showed decreased integration in patients with AGU. Characteristic path length is primarily affected by longer paths; global efficiency, by shorter paths. Thus, our results

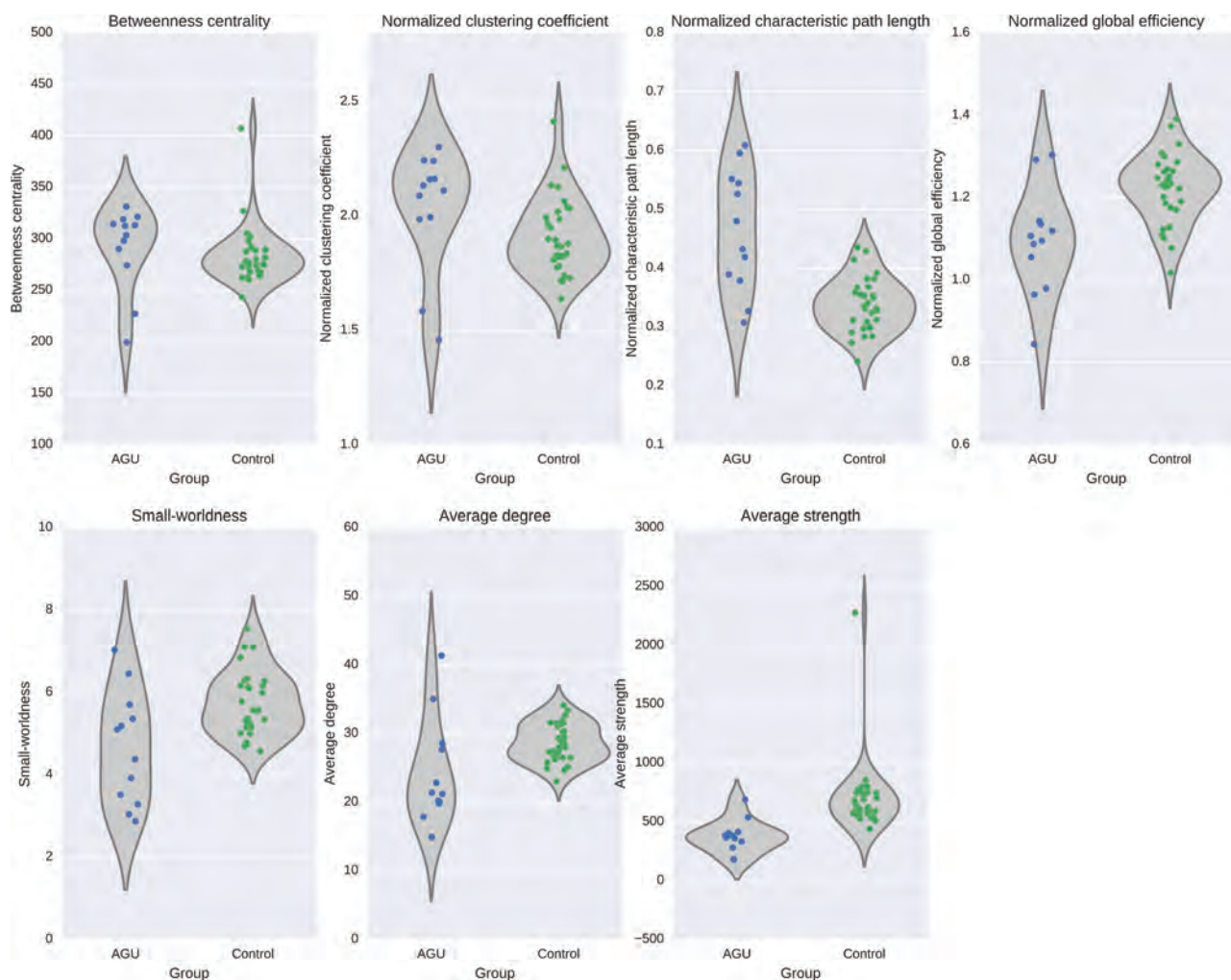


FIG 2. Global graph theoretical properties of the structural brain connectivity networks in patients with AGU and control subjects. The violin plots show the full distribution of the data via kernel density plots.

suggest that alterations in both shorter and longer paths are present in patients with AGU compared with control subjects.

We investigated the segregation of the brain networks using the normalized clustering coefficient,⁴⁰ which measures the fraction of triangles formed by neighboring nodes compared with all possible triangles between them. However, no differences were found in the normalized clustering coefficient between patients with AGU and control subjects. Finally, the average strength was decreased in the brain networks of patients with AGU, suggesting overall decreased global connectivity in AGU.

The development and organization of brain circuitry require coordination of a complex set of neurodevelopmental events, which may be disturbed in AGU. We know that myelination is delayed and deficient in AGU, the volume of WM is decreased in school-aged children even in visual evaluation, and general atrophy is slowly progressive during the following years.^{15,41,42} Vacuolation of neurons and neuronal loss have been reported in neuropathologic studies among patients with AGU with advanced disease.¹⁵ The delayed and deficient myelination and neuronal loss may disturb synaptogenesis as well as pruning, resulting in impaired integration of networks. Furthermore,

accumulation of iron in the thalamic nuclei in AGU, which has been shown with susceptibility-weighted imaging in school-aged patients,^{43,44} may disturb the connectivity of various thalamic circuits. The relationship between iron concentration and structural connectivity has not been thoroughly investigated, but in one study, significant correlations between the iron levels of the subthalamic nuclei and the number of WM tracts terminating in different GM areas were shown in patients with Parkinson disease.⁴⁵ In another study, higher cortical iron concentration was associated with lower (task-based) functional connectivity within a frontoparietal working memory network and with poorer working memory performance.⁴⁶

In the local analyses, we found decreased strength in 12 GM areas, of which 11 were also significant when a nonparametric Mann-Whitney *U* test was used whenever the assumptions of the *F* tests were not met. These included the right thalamus and putamen, which have previously been shown to have a decreased T2-weighted signal intensity in AGU.¹⁴ In addition, the strengths of the left thalamus ($P = .003$) and left putamen ($P = .002$) were decreased but did not endure correction for multiple comparisons (Online Supplemental Data). We also found decreased

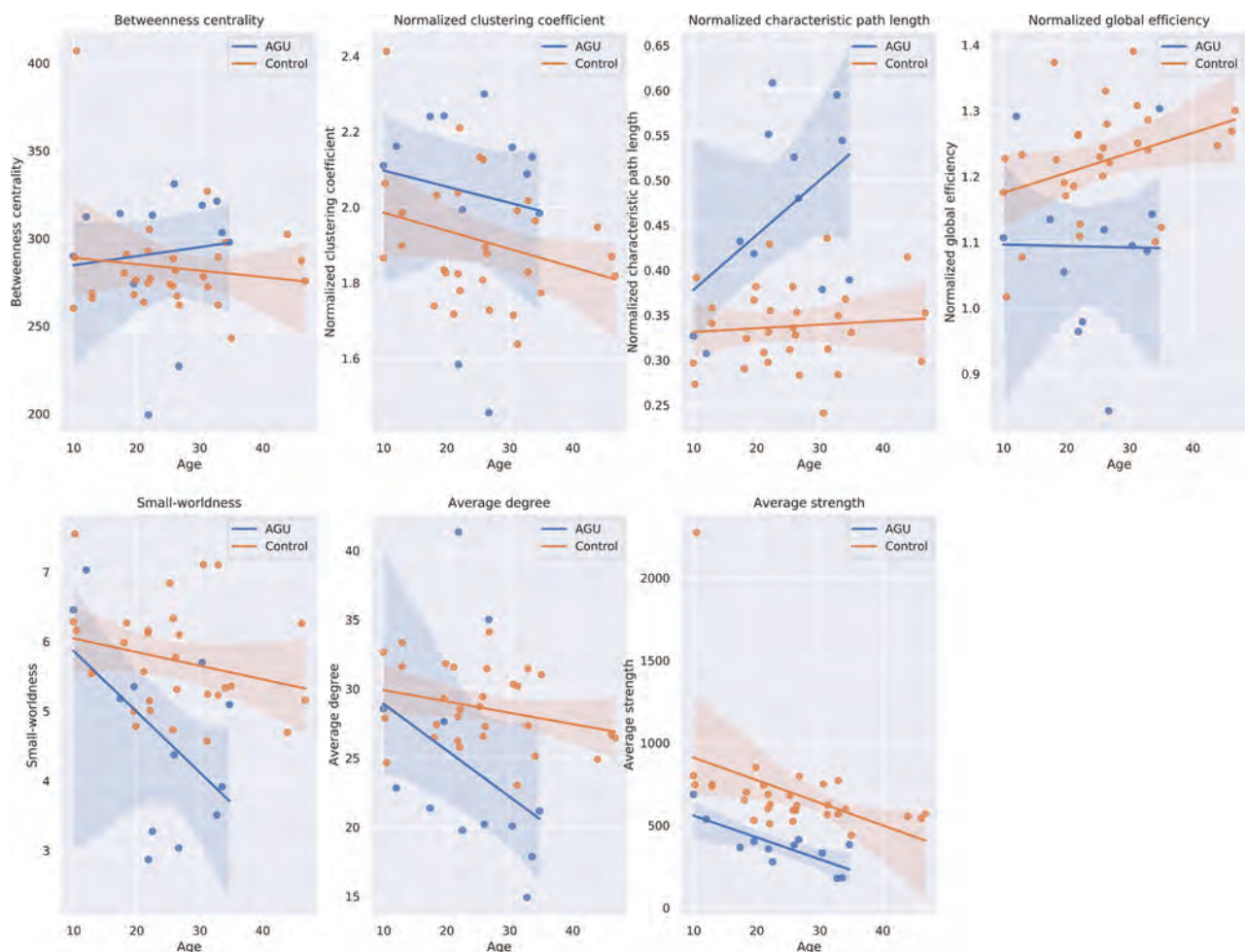


FIG 3. Correlation of the global network properties with age in patients with AGU and control subjects. The *shaded area* shows the 95% confidence interval for the regression lines.

strength bilaterally in the middle temporal gyri, responsible for recognition of known faces and accessing word meaning while reading,⁴⁷ and in the left planum temporale, a highly lateralized structure overlapping with the Wernicke area and involved in early auditory processing including language and music.^{48–50} Its symmetric development has been related to dyslexia⁵¹ and stuttering.⁵² The decrease in the strength of the left planum temporale found in this study may indicate increased symmetry in AGU.

We have also recently investigated the WM abnormalities in another lysosomal storage disease, juvenile neuronal ceroid lipofuscinosis (lysosomal/endosomal transmembrane protein, batteinn [CLN3]). In the microstructural analyses, we found globally decreased anisotropy and increased diffusivity in patients with CLN3 compared with controls.⁵³ Locally, we found decreased anisotropy and increased diffusivity in the corona radiata and posterior thalamic radiation. We also found significant global and local network alterations that correlated with the disease severity in CLN3, including significantly decreased integration and degree of the structural brain networks.²⁴ Consistent findings in these lysosomal storage diseases may indicate that integration of the structural brain networks is decreased in lysosomal storage diseases in general. Moreover, the local

network properties of the left planum temporale were affected in both AGU and CLN3.

Limitations of this study include the small sample size and suboptimal acquisition parameters (low b-value and number of gradient orientations).⁵⁴ However, AGU is a rare disease, and larger sample sizes are difficult to collect. Unfortunately, we do not have sufficient clinical data for these patients available; therefore, although it would have increased the clinical importance of our findings, we could not perform any correlation analyses between the brain connectivity metrics and clinical variables. Although we carefully verified the success of the segmentations for each subject, we did not account for conventional MR imaging findings or WM hyperintensities in the statistical analyses.

In the future, we would recommend using higher diffusion-weighting with multiple b-values to be able to investigate more specific properties of the WM tracts such as fiber density.⁵⁵ Furthermore, the relationship among the properties of the structural brain connectivity networks, iron accumulation, and clinical variables such as disease severity should be investigated. Finally, biomarkers for treatment efficacy are needed, and structural connectivity network analysis may provide means for long-term follow-up.

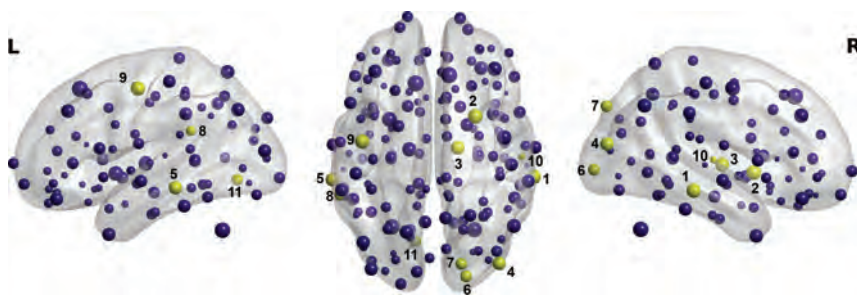


FIG 4. Local alterations in the strength of the structural brain connectivity networks in AGU compared with control subjects. Decreased strength of the structural brain connectivity networks in AGU compared with control subjects was found in 11 nodes (Online Supplemental Data), shown in yellow: 1) right middle temporal gyrus, 2) right putamen, 3) right thalamus, 4) right middle occipital gyrus, 5) left middle temporal gyrus, 6) right occipital pole, 7) right superior occipital gyrus, 8) left planum temporale, 9) left precentral gyrus, 10) right transverse temporal gyrus, and 11) left lingual gyrus. These results endured the Bonferroni correction for multiple comparisons. The size of the nodes corresponds to their strength. The complete results are presented in the Online Supplemental Data.

CONCLUSIONS

We investigated the graph-theoretical properties of the structural brain connectivity networks in AGU and found highly significant global topological alterations such as decreased integration of the networks in AGU. In addition, we found decreased strength in 11 regions, including the right thalamus and putamen, previously also found to be affected in conventional MR imaging studies of AGU. Our results may also be helpful in planning studies concerning other neurodegenerative diseases.



Disclosure forms provided by the authors are available with the full text and PDF of this article at www.ajnr.org.

REFERENCES

- Saarela J, von SC, Peltonen L, et al. A novel aspartylglucosaminuria mutation affects translocation of aspartylglucosaminidase. *Hum Mutat* 2004;24:350–51 CrossRef Medline
- Arvio M, Mononen I. Aspartylglucosaminuria: a review. *Orphanet J Rare Dis* 2016;11:162 CrossRef Medline
- Syvänen AC, Ikonen E, Manninen T, et al. Convenient and quantitative determination of the frequency of a mutant allele using solid-phase minisequencing: application to aspartylglucosaminuria in Finland. *Genomics* 1992;12:590–95 CrossRef Medline
- Goodspeed K, Feng C, Laine M, et al. Aspartylglucosaminuria: clinical presentation and potential therapies. *J Child Neurol* 2021;36:403–14 CrossRef Medline
- Arvio M, Arvio P, Hurmerinta K, et al. Reduction in head size in patients with aspartylglucosaminuria. *Acta Neurol Scand* 2005;112:335–37 CrossRef Medline
- Arvio P, Arvio M. Progressive nature of aspartylglucosaminuria. *Acta Paediatr* 2007;91:255–57 CrossRef Medline
- Dunder U, Valtonen P, Kelo E, et al. Early initiation of enzyme replacement therapy improves metabolic correction in the brain tissue of aspartylglucosaminuria mice. *J Inher Metab Dis* 2010;33:611–17 CrossRef Medline
- Kelo E, Dunder U, Mononen I. Massive accumulation of Man2GlcNAc2-Asn in nonneuronal tissues of glycosylasparaginase-deficient mice and its removal by enzyme replacement therapy. *Glycobiology* 2005;15:79–85 CrossRef Medline
- Peltola M, Kytälä A, Heinonen O, et al. Adenovirus-mediated gene transfer results in decreased lysosomal storage in brain and total correction in liver of aspartylglucosaminuria (AGU) mouse. *Gene Ther* 1998;5:1314–21 CrossRef Medline
- Virta S, Rapola J, Jalanko A, et al. Use of nonviral promoters in adenovirus-mediated gene therapy: reduction of lysosomal storage in the aspartylglucosaminuria mouse. *J Gene Med* 2006;8:699–706 CrossRef Medline
- Banning A, Gülec C, Rouvinen J, et al. Identification of small molecule compounds for pharmacological chaperone therapy of aspartylglucosaminuria. *Sci Rep* 2016;6:37583 CrossRef Medline
- Autti T, Joensuu R, Åberg L. Decreased T2 signal in the thalami may be a sign of lysosomal storage disease. *Neuroradiology* 2007;49:571–78 CrossRef Medline
- Autti T, Lönnqvist T, Joensuu R. Bilateral pulvinar signal intensity decrease on T2-weighted images in patients with aspartylglucosaminuria. *Acta Radiol* 2008;49:687–92 CrossRef Medline
- Tokola A, Åberg L, Autti T. Brain MRI findings in aspartylglucosaminuria. *J Neuroradiol* 2015;42:345–57 CrossRef Medline
- Autti T, Raininko R, Haltia M, et al. Aspartylglucosaminuria: radiologic course of the disease with histopathologic correlation. *J Child Neurol* 1997;12:369–75 CrossRef Medline
- Goodspeed K, Horton D, Lowden A, et al. A cross-sectional natural history study of aspartylglucosaminuria. *JIMD Rep* 2022;63:425–33 CrossRef Medline
- Tokola A, Brandstack N, Hakkarainen A, et al. White matter microstructure and subcortical gray matter structure volumes in aspartylglucosaminuria; a 5-year follow-up brain MRI study of an adolescent with aspartylglucosaminuria and his healthy twin brother. *JIMD Rep* 2017;35:105–15 CrossRef Medline
- Hagmann P, Cammoun L, Gigandet X, et al. Mapping the structural core of human cerebral cortex. *PLoS Biol* 2008;6:e159–93 CrossRef Medline
- Bullmore E, Sporns O. Complex brain networks: graph theoretical analysis of structural and functional systems. *Nat Rev Neurosci* 2009;10:186–98 CrossRef Medline
- Griffa A, Baumann PS, Thiran JP, et al. Structural connectomics in brain diseases. *Neuroimage* 2013;80:515–26 CrossRef Medline
- Roine T, Jeurissen B, Perrone D, et al. Reproducibility and intercorrelation of graph theoretical measures in structural brain connectivity networks. *Med Image Anal* 2019;52:56–67 CrossRef Medline
- Lei D, Li W, Tallman MJ, et al. Changes in the brain structural connectome after a prospective randomized clinical trial of lithium and quetiapine treatment in youth with bipolar disorder. *Neuropsychopharmacology* 2021;46:1315–23 CrossRef Medline
- Hu M, Zong X, Zheng J, et al. Risperidone-induced topological alterations of anatomical brain network in first-episode drug-naïve schizophrenia patients: a longitudinal diffusion tensor imaging study. *Psychol Med* 2016;46:2549–60 CrossRef Medline
- Roine T, Roine U, Tokola A, et al. Topological alterations of the structural brain connectivity network in children with juvenile neuronal ceroid lipofuscinosis. *AJNR Am J Neuroradiol* 2019;40:2146–53 CrossRef Medline
- Leemans A, Jones DK. The B-matrix must be rotated when correcting for subject motion in DTI data. *Magn Reson Med* 2009;61:1336–49 CrossRef Medline
- Leemans A, Jeurissen B, Sijbers J, et al. ExploreDTI: a graphical toolbox for processing, analyzing, and visualizing diffusion MR data. January 2009. In: *Proceedings of the 17th Annual Meeting of the International Society for Magnetic Resonance in Medicine*, 2009;3537
- Irfanoglu MO, Walker L, Sarlls J, et al. Effects of image distortions originating from susceptibility variations and concomitant fields

- on diffusion MRI tractography results. *Neuroimage* 2012;61:275–88 CrossRef Medline
28. Jeurissen B, Leemans A, Jones DK, et al. Probabilistic fiber tracking using the residual bootstrap with constrained spherical deconvolution. *Hum Brain Mapp* 2011;32:461–79 CrossRef Medline
 29. Tournier JD, Calamante F, Connelly A. Robust determination of the fibre orientation distribution in diffusion MRI: non-negativity constrained super-resolved spherical deconvolution. *Neuroimage* 2007;35:1459–72 CrossRef Medline
 30. Destrieux C, Fischl B, Dale A, et al. Automatic parcellation of human cortical gyri and sulci using standard anatomical nomenclature. *Neuroimage* 2010;53:1–15 CrossRef Medline
 31. Fischl B. FreeSurfer. *Neuroimage* 2012;62:774–81 CrossRef Medline
 32. Rubinov M, Sporns O. Complex network measures of brain connectivity: uses and interpretations. *Neuroimage* 2010;52:1059–69 CrossRef Medline
 33. Mann HB, Whitney DR. On a test of whether one of two random variables is stochastically larger than the other. *Ann Math Stat* 1947;18:50–60 CrossRef
 34. Xia M, Wang J, He Y. BrainNet Viewer: a network visualization tool for human brain connectomics. *PLoS One* 2013;8:e68910 CrossRef Medline
 35. Tournier JD, Smith R, Raffelt D, et al. MRtrix3: a fast, flexible and open software framework for medical image processing and visualisation. *Neuroimage* 2019;202:116137 CrossRef Medline
 36. Waskom M. Seaborn: statistical data visualization. *J Open Source Softw.* 2021;6:3021 CrossRef
 37. Hunter JD. Matplotlib: a 2D graphics environment. *Comput Sci Eng* 2007;9:90–95 CrossRef
 38. Latora V, Marchiori M. Efficient behavior of small-world networks. *Phys Rev Lett* 2001;87:198701 CrossRef Medline
 39. Watts DJ, Strogatz SH. Collective dynamics of “small-world” networks. *Nature* 1998;393:440–42 CrossRef Medline
 40. Saramäki J, Kivelä M, Onnela JP, et al. Generalizations of the clustering coefficient to weighted complex networks. *Phys Rev E Stat Nonlin Soft Matter Phys.* 2007;75(2 Pt 2):027105 CrossRef Medline
 41. Arstila A, Palo J, Haltia M, et al. Aspartylglucosaminuria I: fine structural studies on liver, kidney and brain. *Acta Neuropathol* 1972;20:207–16 CrossRef Medline
 42. Haltia M, Palo J, Autio S. Aspartylglycosaminuria: a generalized storage disease. *Acta Neuropathol* 1975;31:243–55 CrossRef Medline
 43. Tokola A, Laine M, Tikkanen R, et al. Susceptibility-weighted imaging findings in aspartylglucosaminuria. *AJNR Am J Neuroradiol* 2019;40:1850–54 CrossRef Medline
 44. Sairanen V, Tokola A, Tikkanen R, et al. Statistical permutation test reveals progressive and region-specific iron accumulation in the thalami of children with aspartylglucosaminuria. *Brain Sci* 2020;10:677 CrossRef Medline
 45. Dimov A, Patel W, Yao Y, et al. Iron concentration linked to structural connectivity in the subthalamic nucleus: implications for deep brain stimulation. *J Neurosurg* 2019 Jan 18. [Epub head of print] CrossRef Medline
 46. Zachariou V, Bauer CE, Seago ER, et al. Cortical iron disrupts functional connectivity networks supporting working memory performance in older adults. *Neuroimage* 2020;223:117309 CrossRef Medline
 47. Acheson DJ, Hagoort P. Stimulating the brain’s language network: syntactic ambiguity resolution after TMS to the inferior frontal gyrus and middle temporal gyrus. *J Cogn Neurosci* 2013;25:1664–77 CrossRef
 48. Binder JR, Frost JA, Hammeke TA, et al. Function of the left planum temporale in auditory and linguistic processing. *Brain* 1996;119:1239–47 CrossRef Medline
 49. Keenan JP, Thangaraj V, Halpern AR, et al. Absolute pitch and planum temporale. *Neuroimage* 2001;14:1402–08 CrossRef Medline
 50. Dorsaint-Pierre R, Penhune VB, Watkins KE, et al. Asymmetries of the planum temporale and Heschl’s gyrus: relationship to language lateralization. *Brain* 2006;129:1164–76 CrossRef Medline
 51. Larsen JP, Høien T, Lundberg I, et al. MRI evaluation of the size and symmetry of the planum temporale in adolescents with developmental dyslexia. *Brain Lang* 1990;39:289–301 CrossRef Medline
 52. Foundas AL, Bollich AM, Feldman J, et al. Aberrant auditory processing and atypical planum temporale in developmental stuttering. *Neurology* 2004;63:1640–46 CrossRef Medline
 53. Roine U, Roine T, Hakkarainen A, et al. Global and widespread local white matter abnormalities in juvenile neuronal ceroid lipofuscinosis. *AJNR Am J Neuroradiol* 2018;39:1349–54 CrossRef Medline
 54. Tournier JD, Calamante F, Connelly A. Determination of the appropriate b value and number of gradient directions for high-angular-resolution diffusion-weighted imaging. *NMR Biomed* 2013;26:1775–86 CrossRef Medline
 55. Raffelt D, Tournier JD, Rose S, et al. Apparent fibre density: a novel measure for the analysis of diffusion-weighted magnetic resonance images. *Neuroimage* 2012;59:3976–94 CrossRef Medline

Viz.ai Implementation of Stroke Augmented Intelligence and Communications Platform to Improve Indicators and Outcomes for a Comprehensive Stroke Center and Network

M.E. Figurelle, D.M. Meyer, E.S. Perrinez,  D. Paulson, J.S. Pannell, D.R. Santiago-Dieppa, A.A. Khalessi,  D.S. Bolar,  J. Bykowski, and  B.C. Meyer



ABSTRACT

BACKGROUND AND PURPOSE: Comprehensive stroke centers continually strive to narrow neurointerventional time metrics. Although process improvements have been put in place to streamline workflows, complex pathways, disparate imaging locations, and fragmented communications all highlight the need for continued improvement.

MATERIALS AND METHODS: This Quality Improvement Initiative (VISION) was implemented to assess our transition to the Viz.ai platform for immediate image review and centralized communication and their effect on key performance indicators in our comprehensive stroke center. We compared periods before and following deployment. Sequential patients having undergone stroke thrombectomy were included. Both direct arriving large-vessel occlusion and Brain Emergency Management Initiative telemedicine transfer large-vessel occlusion cases were assessed as were subgroups of OnHours and OffHours. Text messaging thread counts were compared between time periods to assess communications. Mann-Whitney *U* and Student *t* tests were used.

RESULTS: Eighty-two neurointerventional cases were analyzed pre vs. post time periods: (DALVO-OnHours 7 versus 7, DALVO-OffHours 10 versus 5, BEMI-OnHours 13 versus 6, BEMI-OffHours 17 versus 17). DALVO-OffHours had a 39% door-to-groin reduction (157 versus 95 minutes, $P = .009$). DALVO-All showed a 32% reduction (127 versus 86 minutes, $P = .006$). BEMI-All improved 33% (42 versus 28 minutes, $P = .036$). Text messaging thread counts improved 30% (39 versus 27, $P = .04$).

CONCLUSIONS: There was an immediate improvement following Viz.ai implementation for both direct arriving and telemedicine transfer thrombectomy cases. In the greatest opportunity subset (direct arriving large-vessel occlusion-OffHours: direct arriving cases requiring team mobilization off-hours), we noted a 39% improvement. With Viz.ai, we noted that immediate access to images and streamlined communications improved door-to-groin time metrics for thrombectomy. These results have implications for future care processes and can be a model for centers striving to optimize workflow and improve thrombectomy timeliness.

ABBREVIATIONS: BEMI = Brain Emergency Management Initiative telemedicine transfer LVO; DALVO = direct arriving LVO; HIPAA = Health Insurance Portability and Accountability Act; LVO = large-vessel occlusion

For acute stroke, rtPA is the only approved pharmacologic treatment.¹ For nonpharmacologic interventions, neurointerventional radiology procedures have become standard of care for patients with anterior circulation strokes within a 6-hour time window.^{2,3} Thrombectomy, in appropriately selected patients, is also effective in the extended 6- to 24-hour window.³⁻⁵ Thrombectomy is the most effective procedure for reducing functional disability for patients with large-vessel occlusion (LVO).⁶ Treating facilities such as comprehensive stroke centers assess key time metrics to

continually improve quality of care. These metrics include goals of door-to-needle times within 60 minutes in 85% and within 30 minutes in 50% of patients with acute ischemic stroke treated with IV thrombolytics, as well as door-to-device times within 90 minutes (for direct arriving) and within 60 minutes (for transfer) patients.⁷ Numerous process-improvement workflows have been put in place to help attain these goals for tPA and thrombectomy.⁸⁻¹⁰ Centers strive to improve door-to-groin and door-to-recanalization times because rapid triage and fast reperfusion times are important predictors of outcome.¹¹ Numerous strategies, including improved processes, transfer enhancements, and direct admission to the angiogram suite, have shown improvements in patients with LVO.¹²⁻¹⁸ At our comprehensive stroke center, time metrics were not ideal, so continued improvement pathways were needed.

Stroke telemedicine (telestroke) networks are in place to help evaluate patients and transfer those that require a step up in care

Received August 11, 2022; accepted after revision October 17.

From the University of California, San Diego, San Diego, California.

Please address correspondence to Brett C. Meyer, MD, Department of Neurosciences, UC San Diego Health, 3rd Medical Offices North, Suite 3, 200 West Arbor Dr, San Diego, CA 92103-8466; e-mail: bcmeyer@health.ucsd.edu

 Indicates article with online supplemental data.

<http://dx.doi.org/10.3174/ajnr.A7716>

to thrombectomy-capable centers. Although telestroke improves access and the correctness of decision-making,¹⁹ transfers still fare worse than patients who directly arrive to thrombectomy-capable centers due to the added transfer time.²⁰ Although much of this additional time is obligatory given the distance from thrombectomy centers, decreasing transfer time is also a critical goal. Our center has put in place the Brain Emergency Management Initiative (BEMI) transfer pathway for patients evaluated initially at participating telestroke centers that require transfer for possible thrombectomy. This process has enabled a rapid transfer for possible embolectomy by decreasing operational redundancy, and functions well in our telehealth paradigm.¹⁷ Although patients arrive quickly because of BEMI, communications between hyperacute teams still remain complex. Nontransfer, direct arriving LVO (DALVO) cases can increase the communication burden because the time window between patient arrival and intervention is compressed (these cases do not allow the additional time buffer of telestroke, which allows mobilization of angiography teams while a patient is being transferred).

Weaknesses often found in stroke-care pathways are poor communication and poor cooperation among health professionals and facilities.²¹ In acute stroke, communication processes can be complex because numerous teams require timely communication and rapid mobilization for patients with both BEMI and DALVO. Communication pathways place a strong onus on the coordinating provider to ensure that all parties are aware of patient status, destination, and timing. All this would take place during the decision-making process regarding whether the patient was a candidate for transfer (for BEMI cases) or a candidate for neurointervention based on advanced imaging techniques that our comprehensive stroke center has had in place since the initial embolectomy trials in both the standard and extended time windows (for patients with both BEMI and DALVO).^{4,5,22}

In our center, complex pathways, disparate imaging locations, and fragmented communications all highlighted a need for continued improvement in our hyperacute stroke-care pathway. We sought a solution that allowed the following: 1) immediate/mobile access to advanced imaging, 2) advanced CT perfusion mapping to help guide quick interventional decision-making, and 3) a Health Insurance Portability and Accountability Act (HIPAA)-compliant communications platform allowing a coordinated, single-location, secure, text-messaging thread for all care team members to access and be aware of patient status, decision information, and patient destination/location. Our aim was to determine whether we could improve neurointerventional time metrics.

MATERIALS AND METHODS

The Viz neuroimaging platform (Viz.ai; <http://viz.ai>) was implemented to optimize assessment and synchronize workflow for patients with acute stroke, with additional focus on those patients who may be potential candidates for neurointervention. Using artificial intelligence, this system uses machine learning techniques for automated neuroimaging processing and interpretation. Additional features include real-time, HIPAA-compliant, dynamic viewing of high-fidelity images on mobile devices, group communication messaging, and an artificial intelligence algorithm that automatically identifies suspected LVO strokes on CTA. We transitioned to the

use of Viz.ai on January 18, 2021, for clinical care, we maintained research licenses for use of RAPID (iSchemaView).

In an institutional review board–approved Quality Initiative project, we implemented the Viz.ai Implementation of Stroke augmented Intelligence and communications platform to improve Indicators and Outcomes for a comprehensive stroke center and Network (VISIION) pathway for hyperacute stroke assessments for cases of both BEMI and DALVO. This assessed an improvement in times in our comprehensive stroke center. The advanced imaging platform, very similar to our prior experience with RAPID, allowed our hyperacute stroke teams access to images on a secure mobile platform to assess LVO. On-screen tools allowed image rotation in 3D space to better assess vessel morphology as well as review advanced imaging such as CT perfusion maps for cases thought to be potential candidates for neurointervention in the extended window. Providers downloaded the HIPAA-compliant Viz.ai medical tool and used HIPAA-compliant user credentials for access. This secure access allowed review of patient images from our hub facilities (and indirectly from our spoke sites because we already had virtual private network access to these images). The secure text-messaging thread (Fig 1, right) allowed all credentialed participants to access a single point of communication for awareness of patient status, medical issues, and next steps. More than 250 team members were given access, including the stroke team, neurointerventional team, neuroradiology, neurocritical care, charge nurse, transfer center, and house supervisor. Since deployment, additional service areas have been offered access (eg, CT team, angiography team, anesthesia team, and registration team). Providers are able to toggle the setting to “on-call” so as to be aware of cases only when on-shift. It is estimated that only 15–25 providers were actively toggled to on-call during any shift. When a stroke code is called (from either internal or external sites in our network), the stroke provider evaluates the patient and accesses the Viz.ai images on a hand-held device (desktop access was not yet enabled at time of the pilot). The neurointerventional team is contacted using the secure app, and care determinations such as appropriateness for rtPA and thrombectomy are made, including decisions to transfer patients for intervention.

In this initiative, we compared thrombectomy cases from a pre-Viz.ai period (June 10, 2020, to January 17, 2021) with a post-deployment period (January 18, 2021, to June 17, 2021) to assess improved time metrics. Sequential acute stroke cases, requiring embolectomy, were included in this analysis. Cases were further stratified into BEMI (OnHours and OffHours) and DALVO (OnHours and OffHours) on the basis of whether the angiography team was in-house or required activation and mobilization to the hospital (Fig 2). OnHours included weekdays, while OffHours included nights, weekends, and holidays. Comparisons were made for the overall group, for the DALVO and BEMI subgroups, and for the OnHours and OffHours subgroups, comparing the pre- to postimplementation periods. Time outcomes assessed for this initiative included door-to-CT, team activation-to-groin, door-to-groin, door-to-device, and door-to-recanalization. For transfer cases, additional time outcomes were assessed, including spoke code-to-transfer decision, transfer decision-to-hub door, and spoke door-to-groin. To assess whether a

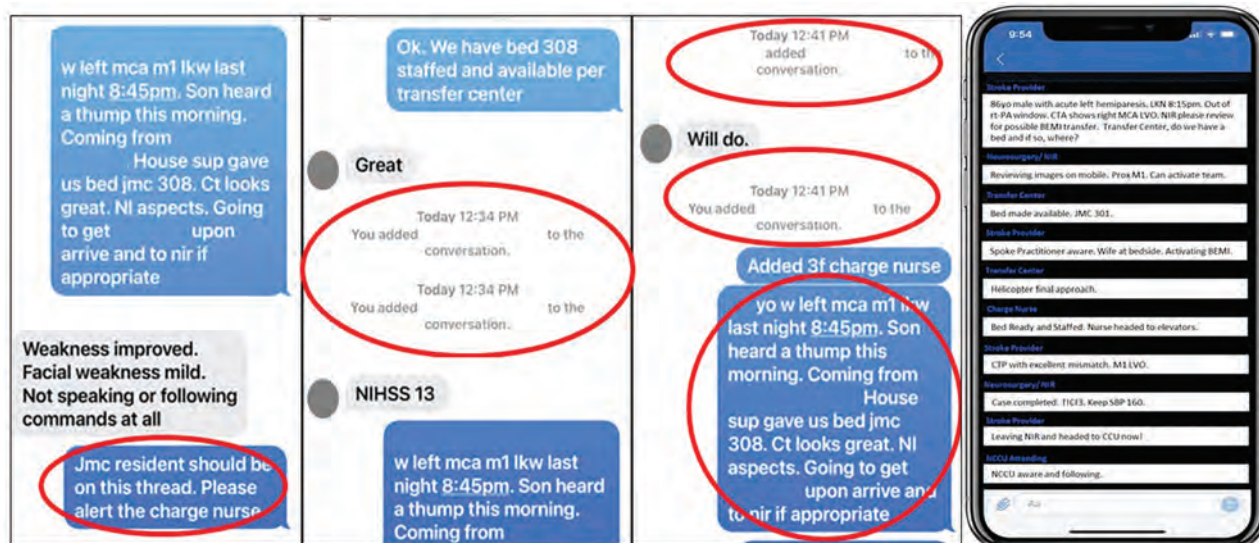


FIG 1. Team messaging. An encrypted message pre-Viz.ai implementation shows fragmented communication, addition of parties who then have limited data and the need for redundant explanations (left), and a post-Viz.ai implementation example of a secure text-messaging thread with all relevant parties able to view and contribute to a centralized text-messaging thread (right).

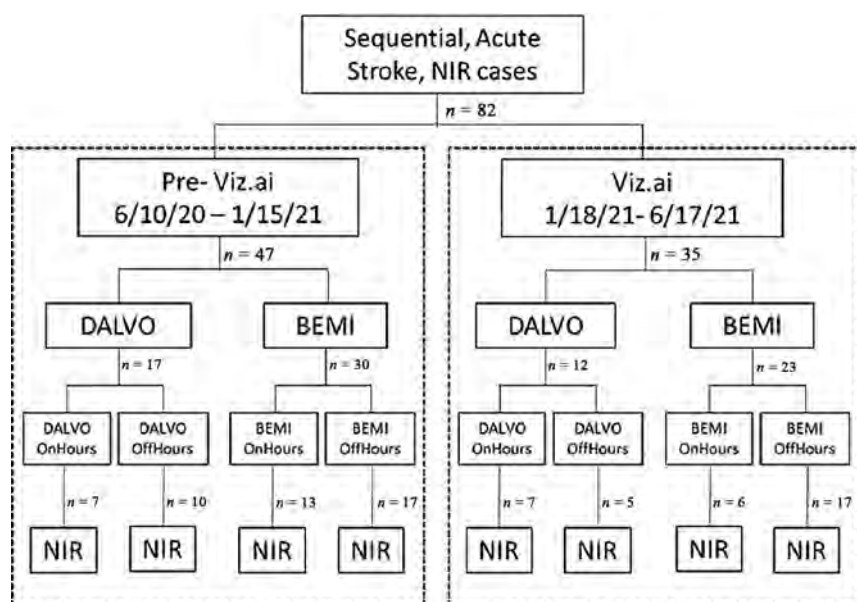


FIG 2. Pre-Viz.ai and postimplementation Viz.ai time periods and case numbers. This nonrandomized, pre-/postassessment design compared pre-implementation cases with postimplementation cases, stratified by DALVO and BEMI subgroups, numbers in each subgroup, and OnHours or OffHours are listed. NIR indicates neurointervention cases.

quantitative signal could be noted for communication optimization, we assessed text-messaging thread count totals, comparing the first 3 months of the pilot with the second 3 months of the pilot (as well as compared with the last 3 months of our current use of the platform) to assess whether the improved process could be reflected in the number of text messages sent by providers across time. Text-messaging thread counts were defined as the number of specific text entries on a text-message thread for an individual case. The Mann-Whitney *U* test was used for non-normally distributed data. The Student *t* test was used for mean comparisons of text-

messaging thread counts. Viz.ai had no influence on the direction of results or publication.

RESULTS

A total of 82 patients having undergone embolectomy were assessed overall, pre-Viz.ai-versus-post-Viz.ai implementation (47 pre-Viz.ai, 35 post-Viz.ai) (Online Supplemental Data). This pilot assessment included a comparison of 29 DALVO patients (17 versus 12) and 53 BEMI patients (30 versus 23). There were 14 DALVO OnHours cases (7 versus 7), 15 DALVO OffHours cases (10 versus 5), 19 BEMI OnHours cases (13 versus 6), and 34 BEMI OffHours cases (17 versus 17).

For door-to-groin comparisons, DALVO-OffHours had a significant 39% reduction (157 versus 95 minutes, $P = .009$). DALVO-All showed a significant 32% reduction (127 versus 86 minutes, $P = .006$). BEMI-All had a significant 33% reduction in median door-to-groin times (42 versus 28 minutes, $P = .036$). DALVO-OnHours improved 19% (97 versus 79 minutes, $P = .201$). BEMI-OnHours improved 18% (37 versus 31 minutes, $P = .337$). BEMI-OffHours improved 38% (45 versus 28 minutes, $P = .077$). Overall, there was a 22% reduction (50 versus 39 minutes, $P = .066$) in door-to-groin times after Viz.ai implementation.

We also analyzed other time metric outcomes. For door-to-CT, DALVO-OffHours had a significant 92.2% reduction (25.5 versus 2 minutes, $P = .01$), and DALVO-All improved 73.2% (20.5 versus 5.5 minutes, $P = .002$). For hub door-to-device, DALVO-All

improved 30.3% (160.0 versus 111.5 minutes, $P = .035$), and BEMI-All improved 18.6% (59 versus 48 minutes, $P = .039$). For hub door-to-recanalization, DALVO-All improved 25.9% (162 versus 120 minutes, $P = .02$) and BEMI-All improved 17.1% (70 versus 58 minutes, $P = .042$). The remaining results are noted in the Online Supplemental Data. As an additional measure of outcomes, we added the percentage of thrombectomy cases meeting specific targets. Using 90 minutes (for DALVO) and 60 minutes (for BEMI) as targets for the door-to-groin or door-to-device, we noted significance for door-to-groin DALVO-OffHours (0% versus 40%, $P = .049$), DALVO-ALL (17.65% versus 66.67%, $P = .0091$), and Overall (63.83% versus 85.71%, $P = .028$) favoring the implementation, but we only noted significance for similarly timed door-to-device targets for the BEMI-OffHours group (43.75% versus 80%, $P = .044$).

As a quantifiable measure of whether the new communication strategy was improved, we analyzed the text-messaging thread count totals for all patients who underwent embolectomy in the post-go-live Viz.ai period (Online Supplemental Data). Comparing the text-messaging thread counts from the first 3 months of the pilot with the second 3 months of the pilot, we noted no difference, but comparing the first 3 months of the pilot with the most recent 3 months when we used the communications platform, we noted a statistically significant 30% improvement in text-messaging thread counts per case (38.6 versus 27.2, $P = .04$). No differences were noted for DALVO or BEMI subgroup comparisons.

DISCUSSION

Our comprehensive stroke center is well-versed in providing time-sensitive decision-making and striving toward optimal treatment time windows for both rtPA and thrombectomy. Published protocols have shown that process/time improvements can correlate with LVO recanalization or good outcome.¹²⁻¹⁶ We sought a solution that allowed access to advanced CT perfusion mapping and immediate/mobile access to a HIPAA-compliant communications platform for coordination between all care team members to improve our time metrics further. Because there are no definitive data noting whether one algorithm/perfusion map technique is superior to another, assessing for which platform had a more optimal algorithm/perfusion map technique did not guide a change to the Viz.ai platform.²³ Determining differences between perfusion maps and additional imaging tools was beyond the scope of this project. Our aims were solely focused on improving access to imaging and improving communication strategies to afford improved time metrics for thrombectomy cases.

Our DALVO and BEMI pathways begin with the stroke provider evaluating the patient (either in person or via telestroke) for thrombectomy consideration. Images are sent to our advanced imaging tool where CTs and CTAs are reviewed. For the patients with LVO in the 6- to 24-hour window, the perfusion algorithm provides mismatch data for review. Before this pilot, if the patient was a potential thrombectomy candidate, the stroke provider would contact numerous providers via pager, Secure Chat message, cell phone, or encrypted text message. For each team, the stroke provider needed to investigate who was on call and determine that provider's preferred contact method. The first contact

would usually be the neurointerventional provider on-call (to discuss whether the patient was a potential thrombectomy candidate), followed by the Neurocritical Care Unit attending physician and fellow, transfer center, house supervisor, nursing, neuroradiology, stroke team members, and registration teams. At each point, details of the case were discussed, resulting in redundancy and persons not all having the same, most up-to-date information. Most of the time, discussions occurred via telephone contact or alphanumeric texting on pagers forwarded to cell-phones. Sometimes text message threads were used (encryption was encouraged to protect health information), depending on individual processes. As noted in Fig 1, left, numerous providers were added at different points in the conversation, and information required repetition throughout the course of the discussion. Because providers may have been communicating via phone, pager, or messaging systems, it was not uncommon for individuals to be left out, it was frequent to not be certain who was the right on-call person, and it was inevitable that some individuals had different information from others as a result of using various noncentralized systems.

On January 18, 2021, our program began using the Via.ai tool. The advanced imaging viewer allowed hand-held smartphone device access to the CT, CTA, and CTP perfusion maps and the ability to review and rotate images using a 3D tool. The embedded communication tool also allowed more coordinated and centralized review regarding treatment decisions, transfer needs, patient status, management, and destination concerns.

Our pilot results noted a robust improvement in door-to-groin, door-to-device, and door-to-recanalization times for many of the groups assessed. Historically, our largest concern was for the DALVO cases because the time from the first interaction until the patient reaches the angiosuite is far more compressed. The telemedicine BEMI cases afford more lead time for angiography teams to arrive at the hub center before the patient arrives. Expectations were that if a large difference was noted, it would be most easily found in DALVO cases at off-hours when the angiography team was not in house and mobilization was required to arrive at the hub. Our results showed a 39% reduction in door-to-groin times for these DALVO OffHours cases. Our interpretation is that the rapid imaging access by relevant teams and coordinated communications among all resulted in quicker decision-to-treat and decision-to-activate the angiography team. Prior analyses reported that there is often significant delay in thrombectomy related to in-hospital time delays, with the greatest delays occurring during the imaging "picture-suite" time windows, which is improved by more parallel processing.²⁴ Our results showed similar door-to-groin time improvements.

In many respects, telemedicine transfers benefit from prehospital notification. Prehospital notification of stroke reduces in-hospital delay because it allows earlier activation of the stroke, imaging, and potentially angiography teams.^{25,26} As is also noted in our results, this reduction should result in decreased door-to-groin times for BEMI compared with DALVO cases. We did not expect to find significant pre- versus post time differences within the transfer population itself. In our analysis, BEMI telemedicine transfer cases also showed a significant 33% door-to-groin time improvement. Given the small subgroup sizes and smaller effect

size seen, we did not show differences in BEMI subgroup analyses based on OnHours or OffHours, and the absolute minutes saved were noted to be less than in DALVO cases (13.5 compared with 41 minutes). This finding was to be expected because the teams had ample opportunity to mobilize ahead of time, resulting in quicker door-to-groin times in BEMI than in DALVO. Overall, a 33% difference in door-to-groin times was still noted in these BEMI transfer cases, resulting in a significant time improvement for these transfers. Door-to-device and door-to-recanalization times showed similar results, lending support to our findings not being due to chance.

Experientially, our teams noted a substantial improvement in communications during this pilot. Stroke providers did not need to access on-call schedules or look up phone numbers to relay time-sensitive information to different services. Just as important, providers did not lose time re-explaining, re-paging, or re-texting information. We were unable to find fewer text-message thread counts comparing the first half of the implementation period with the second half of the implementation period. Reasons may include a small sample size ($n = 35$) with some comparison groups being as small as 2 samples or because no difference exists. We were unable to compare prepilot text-message thread counts because no standard communication pathways then existed. Providers may have used various systems to communicate. Although it is assumed that absolute numbers of messages transmitted would have been higher in the pre-implementation period, we could only compare early-to-late deployment periods. The final reason may be related to the quality of data transmitted. The ease of communication (with simplified access to all parties) may have been countered by a lower threshold to simply send more messages but of shorter length each. Assessing character counts was beyond the scope of this pilot.

When we assessed a longer experience with the communications platform, that comparison showed 30% fewer text messages being sent per case. This finding is a quantitative surrogate for significantly improved communications. Although this shows improved communications because data were not adjusted for many potentially confounding variables (patients in different time windows, rtPA versus no rtPA, patients who could consent versus requiring surrogate contact and so forth), we think that a longer experience with the platform would help balance any potential variability. However, the noted 30% improvement in text-message thread counts is both clinically and statistically significant. Providers qualitatively report that the ability to access and use a single, secure platform in which all parties on-call can view a real-time, accurate, and longitudinal message string detailing critical patient-related information has improved the provider experience. Because this was a Quality Improvement project, specific provider surveys assessing satisfaction were not instituted. Adjusting for the above variables was beyond the scope of this Quality Improvement project.

This article has some limitations owing to its Quality Improvement design, small sample, and limited scope. Because this project focused only on thrombectomy time metrics, additional research questions could not be included and questions regarding functional outcome metrics could not be addressed. Similarly, the nonrandomized, real-world, pre/post design makes

it difficult to prove that the significantly improved time metrics were not the result of other interventions deployed clinically, though we had not implemented any new stroke regimen focused on thrombectomy improvement during this time period. No neurointerventional-specific changes were implemented during this time period, and the small pilot period during which other interventions could have been added make this less likely though not impossible. Concern that improvement was due to more rapid transfers due to our BEMI transfer protocol is unlikely because our BEMI protocol has been unchanged for 6 years.¹⁷

Because this project was limited to data already being collected, we were unable to assess provider satisfaction via survey (for qualitative or quantitative improvement in communication) or assess discharge disposition or 90-day outcome (to assess whether the significant time improvement translated to functional outcome). Given the inability to separate our critical variables that resulted in this real-world time improvement, we are unable to determine whether the immediate/mobile access to advanced imaging CT perfusion maps, the advanced ability to rotate images in 3D space for better/quicker image review by stroke or neurointerventional provider, or the streamlined communications portal individually accounted for our time improvement. In all likelihood, it was a combination of the 3, resulting in quicker decision-making because of more streamlined access to advanced imaging and more streamlined communications.

Before our transition to Viz.ai, we used the clinical version of RAPID (not the research version) with an automatic push of results to e-mail on desktop or phone (and some providers had automatic push to a smartphone app as well), but it did not yet have a centralized communication pathway or messaging other than via e-mail notification. Other publications have shown a similar impact of RapidAI (<https://www.rapidai.com/>) on treatment times in patients with LVO.²⁷ Thus, we cannot determine whether the benefits found were due to the communication platform, the particular method of image viewing, the advanced imaging algorithms, or a combination of the above. The absence of and then implementation of an integrated communications platform may have itself contributed some to our improved communications and improved time metrics. The use of text message count as a surrogate for streamlined communication may not reflect improved communication because more messaging may reflect either better or worse communication depending on the context and content. These software platforms also include numerous alerts making “alert fatigue” a possible concern. Providers can disable or limit the alerts at their discretion. Additional service groups are being added to the platform even a year after deployment, and total user count increasing not decreasing supports the stability and sustainability of the use of the product at our centers. Finally, whether there is sustainability with time or whether this improvement period was only during the initial postimplementation period will be important to investigate.

CONCLUSIONS

Overall, the Viz.ai platform has been shown to benefit both DALVO and BEMI patients at our comprehensive stroke center for door-to-groin, door-to-device, and door-to-recanalization

for many of the groups assessed. In the greatest opportunity subset (DALVO-OffHours: direct-arriving patients requiring team mobilization off-hours), we noted a 39% improvement in door-to-groin times. For telemedicine transfer patients, we also noted a 32.5% improvement in the BEMI-All transfer group times. These improved times are likely due to immediate/mobile access to advanced imaging, the advanced CT perfusion mapping to help guide quick neurointerventional decision-making, and a HIPAA-compliant communications platform allowing a coordinated, single-location, secure text-messaging thread for all care team members to access and be aware of patient status, decision information, and patient destination/location. These results support the assertion that quicker decision-making results in more rapid team activation and improved neurointerventional time metrics. Quality Improvement initiatives aimed at improving all time windows from symptom recognition to recanalization should continue to be encouraged.^{12–16} These results could be a model for other centers that may not already have a robust system in place for DALVO and BEMI cases. Further analysis in a larger data set and assessing sustainability is ongoing.

Ethics Approval

This project was approved by the University of California San Diego institutional review board as a Quality Improvement Initiative.

ACKNOWLEDGMENTS

The authors acknowledge Ms Stephanie Rubenstein for her assistance. We would also like to thank the University of California, San Diego Health Enterprise, and the Department of Radiology for supporting operational initiatives designed to improve access to advanced imaging tools to improve patient care.

Disclosure forms provided by the authors are available with the full text and PDF of this article at www.ajnr.org.

REFERENCES

1. The National Institute of Neurological Disorders and Stroke rt-PA Stroke Study Group. **Tissue plasminogen activator for acute ischemic stroke.** *N Engl J Med* 1995;333:1581–87 CrossRef Medline
2. Fransen PS, Beumer D, Berkhemer OA, et al; MR CLEAN Investigators. **MR CLEAN, a multicenter randomized clinical trial of endovascular treatment for acute ischemic stroke in the Netherlands: study protocol for a randomized controlled trial.** *Trials* 2014;15:343 CrossRef Medline
3. Powers WJ, Rabinstein AA, Ackerson T, et al; American Heart Association Stroke Council. **2018 Guidelines for the Early Management of Patients with Acute Ischemic Stroke: A Guideline for Healthcare Professionals from the American Heart Association/American Stroke Association.** *Stroke* 2018;49:e46–110 CrossRef Medline
4. Albers GW, Marks MP, Kemp S, et al; DEFUSE 3 Investigators. **Thrombectomy for stroke at 6 to 16 hours with selection by perfusion imaging.** *N Engl J Med* 2018;378:708–18 CrossRef Medline
5. Nogueira RG, Jadhav AP, Haussen DC, et al; DAWN Trial Investigators. **Thrombectomy 6 to 24 hours after stroke with a**

- mismatch between deficit and infarct.** *N Engl J Med* 2018;378:11–21 CrossRef Medline
6. Saver JL, Goyal M, van der Lugt A, et al; HERMES Collaborators. **Time to treatment with endovascular thrombectomy and outcomes from ischemic stroke: a meta-analysis.** *JAMA* 2016;316:1279–88 CrossRef Medline
7. Target: **Stroke Phase III. Introducing Target: Stroke Phase III.** <https://www.heart.org/en/professional/quality-improvement/target-stroke/introducing-target-stroke-phase-iii>. Accessed October 6, 2022
8. Grotta JC. **tPA for stroke: important progress in achieving faster treatment.** *JAMA* 2014;311:1615–17 CrossRef Medline
9. Fonarow GC, Zhao X, Smith EE, et al. **Door-to-needle times for tissue plasminogen activator administration and clinical outcomes in acute ischemic stroke before and after a quality improvement initiative.** *JAMA* 2014;311:1632–40 CrossRef Medline
10. Lopez-Rivera V, Salazar-Marioni S, Abdelkhalq R, et al. **Integrated stroke system model expands availability of endovascular therapy while maintaining quality outcomes.** *Stroke* 2021;52:1022–29 CrossRef Medline
11. Goyal M, Menon BK, van Zwam WH, et al; HERMES Collaborators. **Endovascular thrombectomy after large-vessel ischaemic stroke: a meta-analysis of individual patient data from five randomised trials.** *Lancet* 2016;387:1723–31 CrossRef Medline
12. Kim SC, Lee CY, Kim CH, et al. **The effectiveness of systemic and endovascular intra-arterial thrombectomy protocol for decreasing door-to-recanalization time duration.** *J Cerebrovasc Endovasc Neurosurg* 2022;24:24–35 CrossRef Medline
13. Aghaebrahim A, Streib C, Rangaraju S, et al. **Streamlining door to recanalization processes in endovascular stroke therapy.** *J Neurointerv Surg* 2017;9:340–45 CrossRef Medline
14. Frei D, McGraw C, McCarthy K, et al. **A standardized neurointerventional thrombectomy protocol leads to faster recanalization times.** *J Neurointerv Surg* 2017;9:1035–40 CrossRef Medline
15. Panezai S, Meghpara S, Kulhari A, et al. **Institution of Code Neurointervention and its impact on reaction and treatment times.** *J Vasc Interv Neurol* 2020;11:1–5
16. Jahan R, Saver JL, Schwamm LH, et al. **Association between time to treatment with endovascular reperfusion therapy and outcomes in patients with acute ischemic stroke treated in clinical practice.** *JAMA* 2019;322:252–63 CrossRef Medline
17. Modir R, Meyer D, Hamidy M, et al. **Brain emergency management initiative for optimizing Hub-Helicopter Emergency Medical Systems-Spoke Transfer Networks.** *Air Med J* 2020;39:103–06 CrossRef Medline
18. Mendez B, Requena M, Aires A, et al. **Direct transfer to angio-suite to reduce workflow times and increase favorable clinical outcome.** *Stroke* 2018;49:2723–27 CrossRef Medline
19. Meyer BC, Raman R, Hemmen T, et al. **Efficacy of site-independent telemedicine in the STroke DOC trial: a randomised, blinded, prospective study.** *Lancet Neurol* 2008;7:787–95 CrossRef Medline
20. Goyal M, Jadhav AP, Bonafe A, et al; SWIFT PRIME Investigators. **Analysis of workflow and time to treatment and the effects on outcome in endovascular treatment of acute ischemic stroke: results from the SWIFT PRIME randomized controlled trial.** *Radiology* 2016;279:888–97 CrossRef Medline
21. Gache K, Leleu H, Nitenberg G, et al. **Main barriers to effective implementation of stroke care pathways in France: a qualitative study.** *BMC Health Serv Res* 2014;14:95 CrossRef Medline
22. Kidwell CS, Jahan R, Gornbein J, et al; MR RESCUE Investigators. **A trial of imaging selection and endovascular treatment for ischemic stroke.** *N Engl J Med* 2013;368:914–23 CrossRef Medline
23. Murray NM, Unberath M, Hager GD, et al. **Artificial intelligence to diagnose ischemic stroke and identify large vessel occlusions: a systematic review.** *J Neurointerv Surg* 2020;12:156–64 CrossRef Medline

24. Mehta BP, Leslie-Mazwi TM, Chandra RV, et al. **Reducing door-to-puncture times for intra-arterial stroke therapy: a pilot quality improvement project.** *J Am Heart Assoc* 2014;3:e000963 CrossRef Medline
25. Lin CB, Peterson ED, Smith EE, et al. **Emergency medical service hospital prenotification is associated with improved evaluation and treatment of acute ischemic stroke.** *Circ Cardiovasc Qual Outcomes* 2012;5:514–22 CrossRef Medline
26. Patel MD, Rose KM, O'Brien EC, et al. **Prehospital notification by emergency medical services reduces delays in stroke evaluation: findings from the North Carolina stroke care collaborative.** *Stroke* 2011;42:2263–68 CrossRef Medline
27. Al-Kawaz M, Primiani C, Urrutia V, et al. **Impact of RapidAI mobile application on treatment times in patients with large vessel occlusion.** *J Neurointerv Surg* 2022;14:233–36 CrossRef Medline

Association between Infarct Location and Hemorrhagic Transformation of Acute Ischemic Stroke following Successful Recanalization after Mechanical Thrombectomy

H. Ni, G.-D. Lu, Y. Hang, Z.-Y. Jia, Y.-Z. Cao, H.-B. Shi, S. Liu, and L.-B. Zhao



ABSTRACT

BACKGROUND AND PURPOSE: The association between infarct location and hemorrhagic transformation of acute ischemic stroke after mechanical thrombectomy is not understood. We aimed to evaluate the association between CTP-based ischemic core variables at admission and hemorrhagic transformation after a successful thrombectomy.

MATERIALS AND METHODS: We retrospectively analyzed patients who underwent endovascular thrombectomy for acute anterior circulation large-vessel occlusion between October 2019 and June 2021. We enrolled 146 patients with visible ischemic core on pre-treatment CTP who had successful reperfusion. The ischemic core infarct territories were classified into the cortical and subcortical areas and then qualitatively and quantitatively analyzed by CTP. Logistic regression and receiver operating characteristic curve analyses were performed to determine the association between ischemic core variables and hemorrhagic transformation.

RESULTS: Of the 146 patients analyzed, 72 (49.3%) had hemorrhagic transformation and 23 (15.8%) had symptomatic intracerebral hemorrhage. Multivariate analysis showed that subcortical infarcts were independently associated with hemorrhagic transformation (OR, 8.06; 95% CI, 2.31–28.10; $P = .001$) and subcortical infarct volume was independently linked to symptomatic intracerebral hemorrhage (OR, 1.05; 95% CI, 1.01–1.09; $P = .039$). The receiver operating characteristic curve indicated that subcortical infarcts can predict hemorrhagic transformation accurately (area under the curve = 0.755; 95% CI, 0.68–0.82; $P < .001$) and subcortical infarct volume can predict symptomatic intracerebral hemorrhage (area under the curve = 0.694; 95% CI, 0.61–0.77; $P = .002$).

CONCLUSIONS: Subcortical infarcts seen on CTP at admission are associated with hemorrhagic transformation in patients after successful thrombectomy, and subcortical infarct volume may influence the risk of symptomatic intracerebral hemorrhage.

ABBREVIATIONS: HI = hemorrhagic infarction; HT = hemorrhagic transformation; ICC = intraclass correlation coefficient; IQR = interquartile range; PH = parenchymal hematoma; ROC = receiver operating characteristic; sICH = symptomatic intracerebral hemorrhage

Mechanical thrombectomy is a standard approach used in patients with acute ischemic stroke caused by anterior circulation large-vessel occlusion.¹ Hemorrhagic transformation (HT) and symptomatic intracerebral hemorrhage (sICH) after thrombectomy may decrease or eliminate the benefits of reperfusion, resulting in poor functional outcomes for patients with acute ischemic stroke.^{2–5} The main mechanism of HT after thrombectomy is thought to be acute reperfusion injuries to the disrupted BBB.^{6,7} Data from the Contact Aspiration versus Stent Retriever for

Successful Revascularization (ASTER) randomized trial showed that there was no significant lesion growth following successful recanalization with mechanical thrombectomy.⁸ Additionally, previous research reported that pretreatment BBB leakage within infarcted brain tissue before reperfusion was associated with HT.⁷ However, the evidence for the association between ischemic infarct location and size at admission and hemorrhagic events after thrombectomy is inconclusive.^{9–13} A common limitation of previous studies was that they used the ASPECTS for grading the ischemic core, which does not provide detailed information on the location and volume of the ischemic core.


Our study sought to investigate the association between the pre-treatment infarct core location and HT in patients with acute ischemic stroke after a successful thrombectomy. We classified infarcts into those in the cortical and subcortical areas, and we used CTP to qualitatively and quantitatively analyze core infarcts at admission. We hypothesized that the location and size of an infarct at admission are associated with HT after successful thrombectomy.

Received September 15, 2022; accepted after revision November 16.

From the Department of Interventional Radiology, The First Affiliated Hospital of Nanjing Medical University, Nanjing, China.

H. Ni and G.-D. Lu contributed equally to this work.

Please address correspondence to Lin-Bo Zhao, MD, PhD, Department of Interventional Radiology, The First Affiliated Hospital with Nanjing Medical University, 300 Guangzhou Rd, Gulou District, Nanjing, Jiangsu Province 210029, China; e-mail: linbozhao@163.com

 Indicates article with online supplemental data.

<http://dx.doi.org/10.3174/ajnr.A7742>

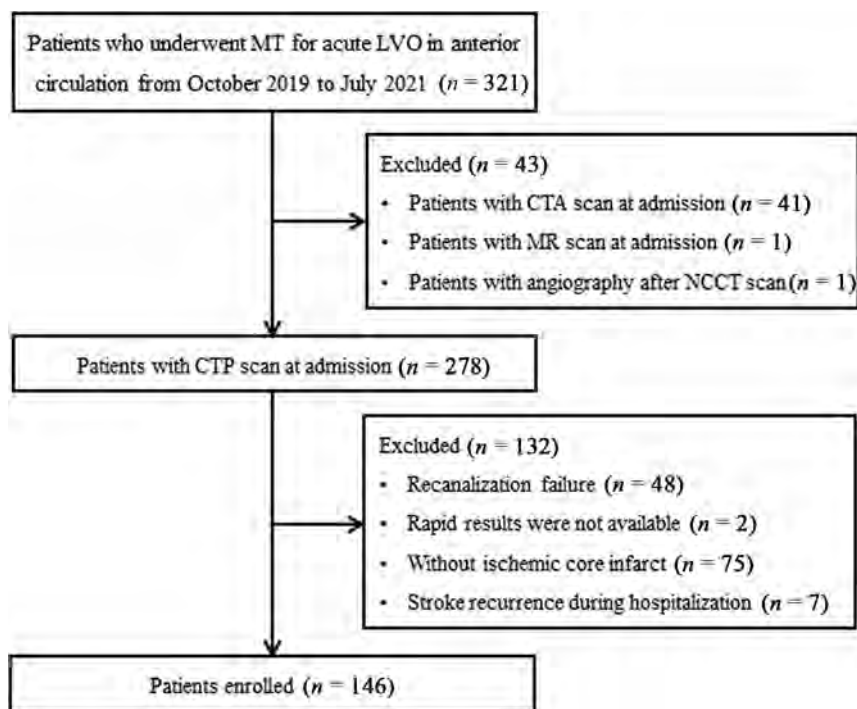


FIG 1. Patient-selection flow chart. MT indicates mechanical thrombectomy; LVO, large-vessel occlusion.

MATERIALS AND METHODS

Population Selection

Between October 2019 and June 2021, we retrospectively reviewed consecutive patients who underwent mechanical thrombectomy for acute anterior circulation large-vessel occlusions using our stroke database. The selection criteria were as follows: 1) 18 years or age or older; 2) an initial NIHSS score of ≥ 6 ; 3) a prestroke mRS score of 0 or 1; 4) last-known-well time of < 24 hours; 5) occlusion of the ICA and/or MCA M1 or M2; 6) successful recanalization after thrombectomy; and 7) ischemic core volume evaluated by CTP at admission ($\text{CBF} < 30\%$) > 0 mL.¹⁴ The exclusion criteria were as follows: 1) occlusion of posterior circulation; 2) mechanical thrombectomy not performed or failed recanalization; 3) CTP not performed due to renal failure, contrast medium allergy, or other reasons; 4) nondiagnostic quality of CTP or ischemic core volume of 0 mL; and 5) stroke recurrence during hospitalization. Because our study is a retrospective study, the requirement for informed consent from patients was waived. The study was approved by our institutional review board. Figure 1 shows the flow chart for patient selection.

Clinical Evaluation

We collected and reviewed demographic and clinical information including age, sex, medical history (hypertension, diabetes mellitus, myocardial infarction, hyperlipidemia, atrial fibrillation, history of ischemic stroke, smoking, coagulation index, baseline NIHSS score, baseline ASPECTS, treatment with IV alteplase before thrombectomy, and blood pressure at admission), imaging data, procedural details, workflow, and clinical outcomes at 90 days. The NIHSS score was used to evaluate stroke severity. A CT scan was obtained within the first 24 hours after the procedure

and repeated after 5–7 days to discriminate HT from contrast staining, which disappears on a follow-up CT.¹⁵ HT subtypes (HI 1, HI 2, PH 1, and PH 2) were classified according to the European Cooperative Acute Stroke Study II (ECASS II) criteria.¹⁶ sICH was defined as hemorrhage seen on CT that was accompanied by deterioration in a patient's neurologic status and an increase in the NIHSS score (≥ 4 points).¹⁶ Clinical outcomes were assessed with the mRS score; a good outcome was defined as an mRS score of 0–2 at 90 days after treatment. The mRS scores at 3 months were obtained from the clinic records or through telephone interviews.

Image Analysis

Multimodal CT-based images, including noncontrast CT, CTP, and postprocessed series, are routinely obtained in patients with suspected acute ischemic stroke at our institution. The automated ASPECTS with a standardized 10-point scale was obtained from noncontrast CT. We processed perfusion images with the commercial software RAPID (iSchemaView) and automatically obtained the colored parametric CTP maps. The volumes of the ischemic core infarcts ($\text{CBF} < 30\%$) were obtained from the CTP maps. All CTP images were visually inspected, and qualitative assessments of the core infarcts were performed. Ischemic core infarct patterns were classified as follows: 1) involving the subcortical area (regardless of whether the cortical area was involved); and 2) involving the cortical area only. The subcortical infarct areas include the caudate, lentiform nucleus, internal capsule, and insular ribbon. The quantitative assessment of the cortical and subcortical core infarcts was performed by manually segmenting parametric CTP maps using the open-source software ITK-SNAP (<http://www.itksnap.org>). The collateral status from DSA was determined using the American Society of Interventional and Therapeutic Neuroradiology/Society of Interventional Radiology guidelines. A simplified dichotomized judgment was used to improve interobserver agreement: good collaterals (grade 3–4) and poor collaterals (grades 0–2).¹⁷ The imaging data were assessed by 2 experienced neuroradiologists who were blinded to the clinical treatment and outcomes. A third neuroradiologist helped them reach a consensus if there were any discrepancies between the 2 neuroradiologists. The results of 3 representative cases are shown in the Online Supplemental Data.

Intra-Arterial Therapy

According to current guidelines, within 4.5 hours of stroke onset, patients are eligible for IV recombinant tPA before endovascular therapy. Endovascular thrombectomy was performed with the patient under local anesthesia or conscious sedation. A stent retriever was recommended as a first-line thrombectomy device,

but other devices were also permitted. The modified TICI score was used to assess the recanalization grade. Successful reperfusion was defined as a modified TICI score of 2b or 3. Rescue therapies performed after failed mechanical thrombectomy included permanent stent placement, balloon angioplasty, and use of a glycoprotein IIb/IIIa antagonist. Patients who had successful recanalization received standard care in the stroke unit, and the systolic blood pressure was controlled (<180 mm Hg) for the first 24 hours after mechanical thrombectomy.

Statistical Analysis

Continuous variables were described as means (SD) or medians (interquartile range [IQR]), and categorical variables, as frequencies (percentage). The Shapiro-Wilk test and histograms were used to assess the normality of distribution. The Student *t* test and the Mann-Whitney *U* test were performed to analyze continuous data. The Fisher exact test was used for the analyses of categorical data. Significant clinical factors ($P < .1$) identified using univariate analyses were included in the multivariate logistic regression model to determine ORs and CIs. The receiver operating characteristic (ROC) curve analyses were applied to identify the effectiveness of significant variables for predicting HT and sICH after successful endovascular therapy. The Cohen κ was used to assess the interrater reproducibility for ischemic core location and collateral status evaluation. The intraclass correlation coefficient (ICC) was performed to evaluate the interreader agreement for the ischemic core volume segment. Results of the Cohen κ coefficient and the ICC were interpreted as follows: κ /ICC < 0.4 was considered poor reproducibility; $0.4 < \kappa$ /ICC ≤ 0.75 was considered fair-to-good; and $0.75 < \kappa$ /ICC ≤ 1.00 was considered excellent. The SPSS 26.0 (IBM) and MedCalc for Windows (Version 11.0; MedCalc Software) software packages were used for analysis. A *P* value < .05 was considered statistically significant.

RESULTS

Of the 321 patients with acute ischemic stroke reviewed during the study period, 146 patients met the inclusion criteria and were enrolled in the study. The mean age of patients was 71 (SD, 11.7) years, and 49.3% were women. The median baseline NIHSS score was 17 (IQR, 12–21), the median baseline ASPECTS was 7 (IQR, 5–8), and the median American Society of Interventional and Therapeutic Neuroradiology/Society of Interventional Radiology grade was 2 (IQR, 1–3). The number of patients who had occlusions in the ICA, MCA, and ICA plus MCA was 47 (32.2%), 87 (59.6%), and 12 (8.2%), respectively. The causes of the stroke were cardioembolism (83, 56.8% of patients), large-artery atherosclerosis (38, 26.0% of patients), and undetermined (25, 17.1% of patients). Of the 146 enrolled patients who had a CTP at admission, 97 of them (66.4%) had symptom onset that was <6 hours. IV tPA was administered in 45 patients (30.8%) before mechanical thrombectomy.

The assessment of infarct location and volume and collateral status showed excellent interrater agreement ($\kappa = 0.908$ and 0.826 , respectively). The interreader reproducibility for the ischemic core volume segment was also excellent (ICC = 0.819). The CTP images of 92 patients (63.0%) showed a subcortical infarct. The median ischemic core volume determined by CTP maps was

19 mL (IQR, 9–44 mL), and the median infarct core volumes of the cortical and subcortical areas were 12 mL (IQR, 0–32 mL) and 7 mL (IQR, 0–14 mL), respectively. HT was identified in 72/146 patients (49.3%) after successful thrombectomy, and sICH was diagnosed in 23/146 patients (15.8%). In patients with HT, 5.5% (8/146) had HI 1, 13.7% (20/146) had HI 2, 15.1% (22/146) had PH 1, and 15.1% (22/146) had PH 2. The distribution of ischemic core infarct territories in patients with dichotomized HT and non-hemorrhagic transformation subtypes is shown in Fig 2. Patients with any HT subtype had a relatively high proportion of subcortical infarcts (75.0% in HI 1, 85.0% in HI 2, 95.5% in PH 1, and 90.9% in PH 2). This proportion was relatively low in patients with the nonhemorrhagic transformation subtype (37.8%). Functional independence at 3 months was achieved in 72 (49.3%) patients.

The Online Supplemental Data show a comparison of characteristics between patients with and without hemorrhagic complications. Diabetes mellitus was more common in patients with HT than in those without HT (29.2% versus 10.8%, $P < .01$). Compared with patients without HT, patients with HT had a higher median NIHSS score (19 versus 16, $P = .03$), a lower median ASPECTS (6 versus 7, $P < .01$), worse collateral circulation (76.4% versus 36.5%, $P < .01$), and more passes of the retriever of ≥ 3 (34.7% versus 17.6%, $P = .02$). HT was more frequently observed in patients with subcortical infarcts (88.9% versus 37.8%, $P < .01$). Patients with HT had a larger median subcortical infarct volume compared with patients without HT (10 mL versus 0 mL, $P < .01$). In the multivariable regression analysis presented in the Online Supplemental Data, independent risk factors for HT were diabetes mellitus (OR, 4.54; 95% CI, 1.26–16.28; $P = .020$), core infarcts with subcortical involvement (OR, 8.06; 95% CI, 2.31–28.10; $P = .001$), poor collateral circulation (OR, 5.49; 95% CI, 2.15–14.01; $P < .001$), and >3 passes of a retriever (OR, 3.46; 95% CI 1.24–9.64; $P = .018$).

Patients with the sICH were older (76 versus 71 years of age, $P = .04$) and had a high prevalence of diabetes mellitus (39.1% versus 16.3%, $P = .01$), a higher baseline NIHSS score (21 versus 16, $P < .01$), a lower baseline ASPECTS (5 versus 7, $P < .01$), and worse collateral circulation (91.3% versus 49.6%, $P < .01$) than patients without sICH. Additionally, patients with sICH had more subcortical infarcts compared with those without sICH (87.0% versus 58.5%, $P = .01$). Subcortical infarct volume was higher in patients with sICH than in those without it (11 versus 6 mL, $P < .01$), whereas total core and cortical infarct volumes were not significantly associated with the occurrence of sICH (Online Supplemental Data). In the multivariable regression analysis, baseline ASPECTS (OR, 0.73; 95% CI, 0.57–0.93; $P = .010$), subcortical infarct volume (OR, 1.05; 95% CI, 1.01–1.09; $P = .039$), and collateral circulation (OR, 6.92; 95% CI, 1.47–32.73; $P = .015$) were significantly associated with sICH after successful thrombectomy (Online Supplemental Data).

The ROC curves that were used for predicting HT and sICH are shown in Fig 3. The sensitivity and specificity for predicting HT and subcortical infarct involvement were 88.9% and 62.6% (area under the curve = 0.755; 95% CI, 0.68–0.82; $P < .001$), respectively. The cutoff subcortical infarct volume used for the prediction of sICH was ≥ 22 mL, and sensitivity and specificity

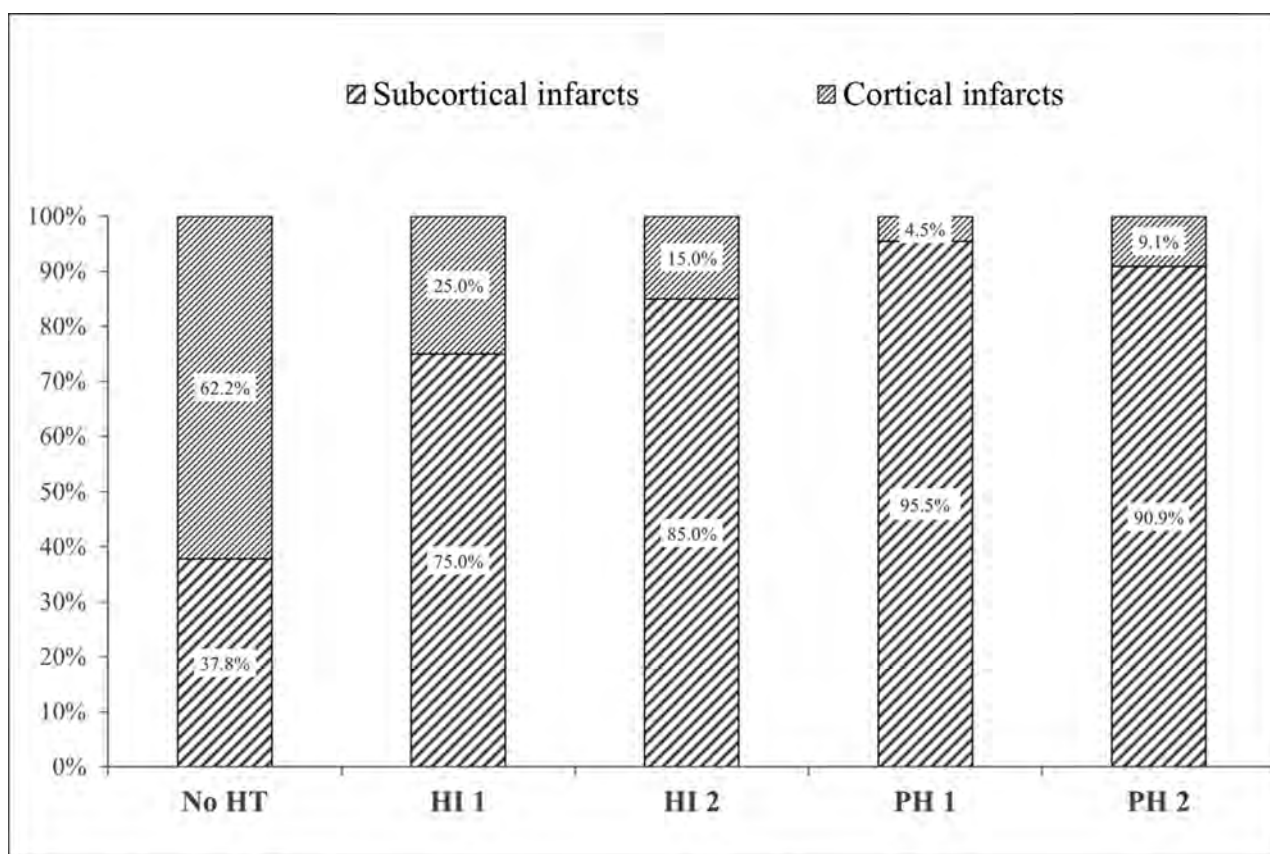


FIG 2. Distribution of ischemic core infarct patterns in patients with dichotomized HT and Non-HT subtypes.

were 34.8% and 96.8% (area under the curve = 0.694; 95% CI, 0.61–0.77; $P = .002$), respectively.

DISCUSSION

In this postthrombectomy patient cohort, we found that subcortical infarcts on admission CTP were associated with the occurrence of HT, and increased subcortical infarct core volume was associated with sICH. To the best of our knowledge, this study is the first to analyze the associations between CTP-based qualitative and quantitative core infarct variables and HT after successful thrombectomy.

The pathophysiologic mechanism of HT involves necrosis of cerebral infarct tissue, collateral circulation, BBB disruption, and infarct size.^{6,7,18–22} Previous reports have shown an association between pretreatment BBB disruption and HT in patients with acute ischemic stroke after mechanical thrombectomy.^{7,22} However, the association of BBB disruption, infarction extent, and ischemic core at admission with HT after thrombectomy is unclear. Most studies reported that the ischemic core graded by ASPECTS is linked to HT or sICH after endovascular thrombectomy.^{11–13} However, the multivariable regression analysis data from the Multicenter Randomized Clinical Trial of Endovascular Therapy for Acute Ischemic Stroke in the Netherlands (MR CLEAN) trial showed that the ASPECTS was not associated with HT or sICH.⁹ In this study, we quantified the pretreatment of ischemic core infarcts with CTP. We found that the total

ischemic core and cortical infarct volumes did not show a positive association with HT or sICH after a successful thrombectomy. In contrast, subcortical infarct occurrence and volume were associated with HT and sICH risk, respectively. These findings may represent an imaging marker predictive of HT and sICH after mechanical thrombectomy that could help manage patients with acute ischemic stroke.

Reperfusion injury, including activation of the endothelium, excess production of oxygen-free radicals, inflammatory responses, leukocyte recruitment, increase in cytokine production, and edema formation could aggravate BBB disruption and potentially cause HT.²³ Additionally, successful reperfusion after mechanical thrombectomy can cause acute hyperperfusion and hemodynamic changes to the infarct. The incidence of hyperperfusion after mechanical thrombectomy was relatively high in patients who achieved successful reperfusion.²⁴ Postischemic hyperperfusion on arterial spin-labeled perfusion MR imaging is associated with HT in patients who underwent reperfusion therapy.^{25,26} These hemodynamic changes, especially in the lenticulostriate artery territories, may influence the rate of HT after reperfusion.²⁷ Our findings support the hypothesis that subcortical infarcts, fed by perforating arteries, are associated with an increased incidence of HT.

Collateral circulation strongly influences the development of postrecanalization HT after acute large-vessel occlusion.⁹ The presence of unfavorable collaterals on angiography is one of the main reasons for HT after mechanical thrombectomy. Due to poor collateral flow, the hypoperfusion area may enhance the risk

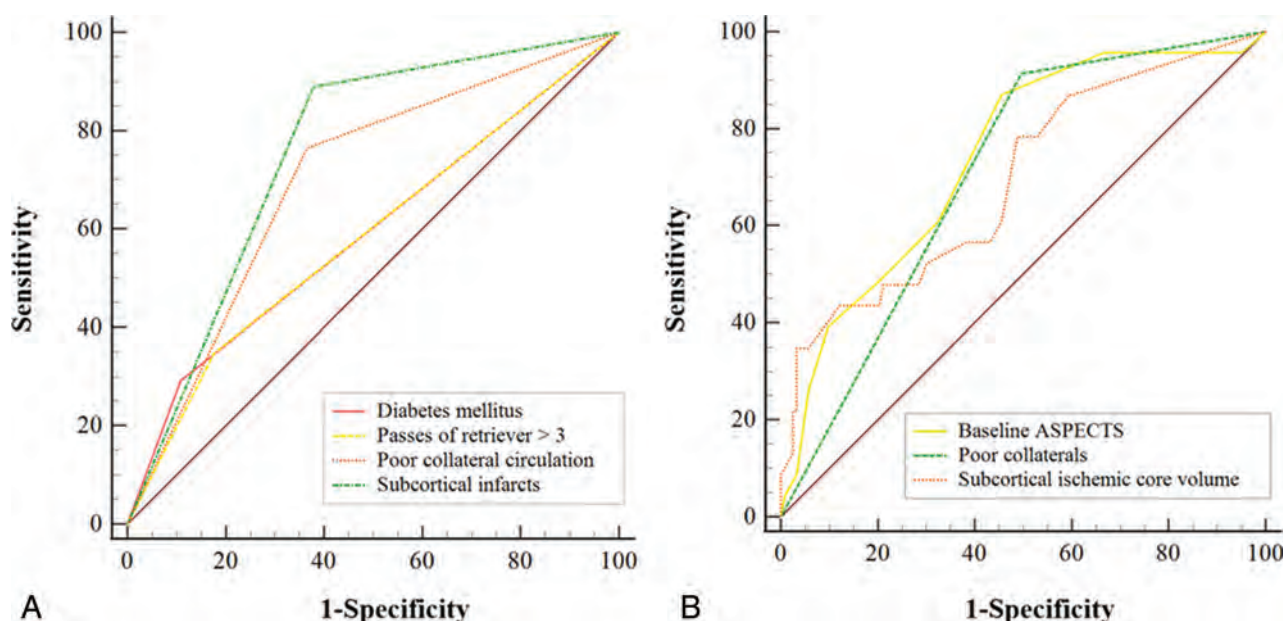


FIG 3. ROC analysis predicting HT (A) and sICH (B).

of HT after upstream recanalization. Arba et al⁷ found that pretreatment BBB disruption before reperfusion therapy was correlated with the extent of critically hypoperfused tissue. Subcortical tissue has poor leptomeningeal collaterals and more severe hypoperfusion compared with cortical tissue.¹⁸ BBB disruption and hemorrhagic conversion are more common in subcortical infarcts compared with cortical infarcts because of worse collateral anastomosis. Hence, our results show that subcortical infarction is associated with the occurrence of HT and increased subcortical core infarct volume is associated with sICH.

Several potential limitations should be mentioned in this study. First, it has the inherent limitations of its retrospective nature. Second, the boundaries between cortical and subcortical areas are sometimes difficult to distinguish accurately by manual infarct measurement. Artificial intelligence has enormous potential to achieve homogeneity in image interpretation in the future. Third, there may be certain differences between the core infarct volume obtained from CTP and the final true infarct size, though all patients underwent successful reperfusion. Fourth, the qualitative assessment by visual inspection could be feasible, but the quantitative infarct size assessment is not available immediately in clinical work.

CONCLUSIONS

This study shows that core infarct with subcortical involvement on CTP at admission is associated with an increased incidence of HT, and subcortical core infarct volume may influence the risk of sICH after a successful thrombectomy. The infarct location on CTP may be an imaging marker predictive of HT and sICH after mechanical thrombectomy that can help manage patients with acute stroke.

Disclosure forms provided by the authors are available with the full text and PDF of this article at www.ajnr.org.

REFERENCES

1. Powers WJ, Rabinstein AA, Ackerson T, et al; American Heart Association Stroke Council. **2018 Guidelines for the Early Management of Patients With Acute Ischemic Stroke: A Guideline for Healthcare Professionals From the American Heart Association/American Stroke Association.** *Stroke* 2018;49:e46–110 CrossRef Medline
2. Li W, Xing X, Wen C, et al. **Risk factors and functional outcome were associated with hemorrhagic transformation after mechanical thrombectomy for acute large vessel occlusion stroke.** *J Neurosurg Sci* 2020 Dec 15. [Epub ahead of print] CrossRef Medline
3. Lee YB, Yoon W, Lee YY, et al. **Predictors and impact of hemorrhagic transformations after endovascular thrombectomy in patients with acute large vessel occlusions.** *J Neurointerv Surg* 2019;11:469–73 CrossRef Medline
4. van Kranendonk KR, Treurniet KM, Boers AM, et al; MR CLEAN Investigators. **Hemorrhagic transformation is associated with poor functional outcome in patients with acute ischemic stroke due to a large vessel occlusion.** *J Neurointerv Surg* 2019;11:464–68 CrossRef Medline
5. Nogueira RG, Gupta R, Jovin TG, et al. **Predictors and clinical relevance of hemorrhagic transformation after endovascular therapy for anterior circulation large vessel occlusion strokes: a multicenter retrospective analysis of 1122 patients.** *J Neurointerv Surg* 2015;7:16–21 CrossRef Medline
6. Hong JM, Kim DS, Kim M. **Hemorrhagic transformation after ischemic stroke: mechanisms and management.** *Front Neurol* 2021;12:703258 CrossRef Medline
7. Arba F, Piccardi B, Palumbo V, et al. **Blood-brain barrier leakage and hemorrhagic transformation: the Reperfusion Injury in Ischemic Stroke (RISK) study.** *Eur J Neurol* 2021;28:3147–54 CrossRef Medline
8. Gauberti M, Lapergue B, Martinez de Lizarondo S, et al. **Ischemia-reperfusion injury after endovascular thrombectomy for ischemic stroke.** *Stroke* 2018;49:3071–74 CrossRef Medline
9. van Kranendonk KR, Treurniet KM, Boers AM, et al. MR CLEAN Investigators. **Clinical and imaging markers associated with hemorrhagic transformation in patients with acute ischemic stroke.** *Stroke* 2019;50:2037–43 CrossRef Medline
10. Brooks G, Hanning U, Flottmann F, et al. **Clinical benefit of thrombectomy in stroke patients with low ASPECTS is mediated by oedema reduction.** *Brain* 2019;142:1399–407 CrossRef Medline

11. Hao Y, Yang D, Wang H, et al; ACTUAL Investigators (Endovascular Treatment for Acute Anterior Circulation Ischemic Stroke Registry). **Predictors for symptomatic intracranial hemorrhage after endovascular treatment of acute ischemic stroke.** *Stroke* 2017;48:1203–09 CrossRef Medline
12. Nawabi J, Knierp H, Schon G, et al. **Hemorrhage after endovascular recanalization in acute stroke: lesion extent, collaterals and degree of ischemic water uptake mediate tissue vulnerability.** *Front Neurol* 2019;10:569 CrossRef Medline
13. Kaesmacher J, Kaesmacher M, Maegerlein C, et al. **Hemorrhagic transformations after thrombectomy: risk factors and clinical relevance.** *Cerebrovasc Dis* 2017;43:294–304 CrossRef Medline
14. Campbell BC, Christensen S, Levi CR, et al. **Cerebral blood flow is the optimal CT perfusion parameter for assessing infarct core.** *Stroke* 2011;42:3435–40 CrossRef Medline
15. Yoon W, Seo JJ, Kim JK, et al. **Contrast enhancement and contrast extravasation on computed tomography after intra-arterial thrombolysis in patients with acute ischemic stroke.** *Stroke* 2004;35:876–81 CrossRef Medline
16. Hacke W, Kaste M, Fieschi C, et al. **Randomised double-blind placebo-controlled trial of thrombolytic therapy with intravenous alteplase in acute ischaemic stroke (ECASS II): Second European-Australasian Acute Stroke Study Investigators.** *Lancet* 1998;352:1245–51 CrossRef Medline
17. Higashida RT, Furlan AJ, Roberts H, et al; Technology Assessment Committee of the Society of Interventional Radiology. **Trial design and reporting standards for intra-arterial cerebral thrombolysis for acute ischemic stroke.** *Stroke* 2003;34:e109–37 CrossRef Medline
18. Charbonnier G, Bonnet L, Biondi A, et al. **Intracranial bleeding after reperfusion therapy in acute ischemic stroke.** *Front Neurol* 2020;11:629920 CrossRef Medline
19. Arba F, Rinaldi C, Caimano D, et al. **Blood-brain barrier disruption and hemorrhagic transformation in acute ischemic stroke: systematic review and meta-analysis.** *Front Neurol* 2020;11:594613 CrossRef Medline
20. Sussman ES, Connolly ES Jr. **Hemorrhagic transformation: a review of the rate of hemorrhage in the major clinical trials of acute ischemic stroke.** *Front Neurol* 2013;4:69 CrossRef Medline
21. Bai J, Lyden PD. **Revisiting cerebral postischemic reperfusion injury: new insights in understanding reperfusion failure, hemorrhage, and edema.** *Int J Stroke* 2015;10:143–52 CrossRef Medline
22. Leigh R, Christensen S, Campbell BC, et al; DEFUSE 2 Investigators. **Pretreatment blood-brain barrier disruption and post-endovascular intracranial hemorrhage.** *Neurology* 2016;87:263–69 CrossRef Medline
23. Khatri R, McKinney AM, Swenson B, et al. **Blood-brain barrier, reperfusion injury, and hemorrhagic transformation in acute ischemic stroke.** *Neurology* 2012;79:S52–57 CrossRef Medline
24. Shimonaga K, Matsushige T, Hosogai M, et al. **Hyperperfusion after endovascular reperfusion therapy for acute ischemic stroke.** *J Stroke Cerebrovasc Dis* 2019;28:1212–18 CrossRef Medline
25. Okazaki S, Yamagami H, Yoshimoto T, et al. **Cerebral hyperperfusion on arterial spin labeling MRI after reperfusion therapy is related to hemorrhagic transformation.** *J Cereb Blood Flow Metab* 2017;37:3087–90 CrossRef Medline
26. Yu S, Liebeskind DS, Dua S, et al; UCLA Stroke Investigators. **Postischemic hyperperfusion on arterial spin labeled perfusion MRI is linked to hemorrhagic transformation in stroke.** *J Cereb Blood Flow Metab* 2015;35:630–37 CrossRef Medline
27. Haussen DC, Ferreira IM, Barreira C, et al. **Active reperfusion hemorrhage during thrombectomy: angiographic findings and real-time correlation with the CT “Spot Sign.”** *Interv Neurol* 2018;7:370–77 CrossRef Medline

WEB Treatment of Ruptured Intracranial Aneurysms: Long-Term Follow-up of a Single-Center Cohort of 100 Patients

 H. Kortman,  S.B.T. van Rooij,  U. Mutlu,  I. Boukrab,  W.J. van Rooij,  B. van der Pol, B. Burhani, and  J.P.P. Peluso



ABSTRACT

BACKGROUND AND PURPOSE: The Woven EndoBridge device (WEB) was introduced for the intrasaccular treatment of wide-neck aneurysms without the need for adjunctive devices. We used the WEB as a primary treatment for 100 ruptured aneurysms regardless of neck size or location. In this study, we present the long-term follow-up of 78 surviving patients.

MATERIALS AND METHODS: Between February 2015 and April 2017, one hundred ruptured aneurysms were treated with the WEB. For surviving patients, angiographic and clinical follow-up was scheduled at 3 months, and 3T MRA and clinical follow-up, at 6, 12, 36, and 60 months. Of 100 patients, 18 died during hospital admission, and in 4, the ruptured aneurysm was additionally treated. The remaining 78 patients had a mean follow-up of 51 months (median, 52 months; range, 5–84 months). There were 57 women and 21 men, with a mean age of 58.5 years (median, 59 years; range, 24–80 years). Of 78 aneurysms with long-term follow-up, 52 (66%) had a wide neck.

RESULTS: Of 78 ruptured aneurysms, 56 (72%) remained completely occluded and 17 (22%) had a stable small neck remnant. Five of 78 aneurysms (6%; 95% CI, 2.4%–14.5%) reopened during follow-up and were additionally treated. There were no rebleeds during follow-up.

CONCLUSIONS: Treatment of ruptured aneurysms with the WEB was safe and effective and has long-term results comparable with those of simple coiling of small-neck aneurysms. The WEB proved to be a valuable alternative to coils for both wide- and small-neck ruptured aneurysms without the need for stents, balloons, or antiplatelet therapy.

Endovascular treatment is recognized as the first therapeutic option for ruptured and unruptured intracranial aneurysms.¹ Endovascular treatment of wide-neck bifurcation aneurysms is challenging, and these aneurysms are associated with a higher rate of recanalization.² Bridging neck devices such as stents require dual-antiplatelet therapy and are associated with a higher rate of complications. With this anti-aggregation regimen, stent-assisted coiling in ruptured aneurysms has a higher inherent risk of early rebleed or hemorrhage in the postoperative period.^{3–5} Despite anti-aggregation, thromboembolic complications still occur.^{6,7}

Primarily for the endovascular treatment of wide-neck bifurcation aneurysms, the intrasaccular flow disruptor Woven

EndoBridge (WEB; MicroVention) has been developed, without the need for adjunctive devices. The first clinical results of the WEB device show good safety and efficacy.⁸ However, publications investigating WEB treatment for ruptured aneurysms are limited with short-term follow-up of up to 1 year on average.^{9,10} We published our first series of 100 ruptured aneurysms treated with the WEB device,¹¹ and in this publication, we will report the long-term follow-up.

MATERIALS AND METHODS

This observational study with prospectively collected data was compliant with our institutional privacy policy. The institutional review board gave exempt status for approval and informed consent. The study was performed in the Elisabeth Tweesteden Ziekenhuis in Tilburg, the Netherlands.

Population

This is the long-term follow-up of the previously published¹¹ cohort of 100 patients with ruptured aneurysms who were treated with the WEB between February 2015 and April 2017.

Received August 23, 2022; accepted after revision November 25.

From the Division of Neuroradiology (H.K., U.M., I.B.), Department of Radiology, and Department of Neurosurgery (B.v.d.P., B.B.), Elisabeth Tweesteden Ziekenhuis Hospital, Tilburg, the Netherlands; Department of Radiology (S.B.T.v.R.), Catharina Ziekenhuis, Eindhoven, the Netherlands; Department of Radiology (W.J.v.R.), Algemeen Ziekenhuis Turnhout, Turnhout, Belgium; and Division of Neuroradiology (J.P.P.), Department of Radiology, Universitair Ziekenhuis Leuven, Leuven, Belgium.

Please address correspondence to Hans Kortman, MD, Division of Neuroradiology, Department of Radiology, ETZ Elisabeth Hospital, PO Box 90151, 5000 LC Tilburg, the Netherlands; e-mail: h.kortman@etz.nl

<http://dx.doi.org/10.3174/ajnr.A7748>

WEB Device

The WEB is a self-expanding, retrievable, electrothermally detachable, nitinol braided device, which is placed in the aneurysm sac. The device existed in several iterations: initially, WEB dual-layer (WEB-DL), followed by a single layer in 2 shapes (barrel: WEB Single-Layer [SL], and spherical: WEB Single-Layer Sphere [SLS]), followed by a version that enhanced visualization (WEB-SL EV and WEB-SLS EV) by incorporating composite wire strands made from nitinol and platinum. The WEB-SL device is available in diameters ranging from 4 to 11 mm and heights ranging from 3 to 9 mm. The WEB-SLS has a spherical shape and is available in diameters ranging from 4 to 11 mm, each with a fixed height ranging between 2.6 and 9.6 mm. The WEBs with diameters of 4–7 mm can be delivered through a 0.021-inch internal diameter microcatheter; the WEBs with diameters of 8–9 mm, through a 0.027-inch microcatheter; and the WEBs with diameters of 10–11 mm, through a 0.033-inch microcatheter (VIA 21, 27, and 33; MicroVention). Last, a lower-profile range of WEBs compliant with a 0.017-inch microcatheter (VIA 17) has become available in clinical practice. Placed in the aneurysm, the WEB modifies the blood flow at the level of the neck and induces aneurysmal thrombosis. The WEB can be fully retrieved until final detachment by an electrothermal detachment system contained in a hand-held controller.

General Indications and Treatment

In our institution, the indication and technique of aneurysmal treatment are based on a multidisciplinary discussion for all admitted patients. However, the treatment of patients with ruptured aneurysms is primarily endovascular within 24 hours after admission. Because of previous poor results with stent-assisted coiling in ruptured aneurysms,⁷ from January 2015 onward, we tried to avoid using stents with inherent antiplatelet medication. Wide-neck aneurysms were treated with either the WEB device with coiling or surgical clipping. Immediate surgery was an option in good-grade patients with wide-neck anterior circulation aneurysms. In poor-grade patients with wide-neck aneurysms not suitable for endovascular treatment, the operation was generally postponed several days. The WEB device was initially developed for the treatment of wide-neck intracranial aneurysms as an alternative to balloon- or stent-assisted treatment. After our first encouraging experiences in unruptured wide-neck aneurysms, during the study period, we gradually expanded the indication to all aneurysms suitable for the WEB regardless of neck size, location, or rupture status.

With the patient under general anesthesia and using a femoral approach, a microcatheter was advanced into the aneurysm via a coaxial or triaxial approach. Hence, the aneurysm was occluded with coils or with a WEB. The WEB was slightly oversized according to the recommendations of the manufacturer. WEB sizes and shapes were recorded. WEB-DLs were not used. Apart from a single bolus of 5000 IU of heparin IV and continuous heparin in the pressure bags for flushing (1000 IU/L), no additional anticoagulation was used.

Data Collection and Follow-up

Patient demographics, treatment, and aneurysm characteristics were collected. Clinical grading during admission was according

to the Hunt and Hess scale, and clinical follow-up was classified in the mRS. For surviving patients, angiographic follow-up was scheduled at 3 months, and 3T MRA follow-up at 6, 12, 36, and 60 months. All imaging follow-up was accompanied by a clinical follow-up visit. Imaging data were interpreted by 2 experienced interventional neuroradiologists (H.K. and I.B.).

Statistical Analysis

Quantitative variables were expressed as means with descriptive statistics, and qualitative variables were expressed as frequencies or percentages with corresponding 95% confidence intervals.

RESULTS

Population

Between February 2015 and April 2017, two hundred forty-two patients with ruptured aneurysms were treated in our institution. Of these, 100 patients with ruptured aneurysms were selectively treated with the WEB. The results of this study are published elsewhere.¹¹ Seventeen patients (17%) died during hospitalization as a consequence of SAH. One patient (1%) died after a thromboembolic complication during WEB placement; and, we additionally treated 4 aneurysms (4%): In 1 patient with a 13-mm ruptured pericallosal artery aneurysm, a WEB was placed to protect the dome only. This aneurysm was later additionally clipped. In 1 patient, the WEB was undersized, but this feature was only noticed after detachment. Follow-up angiography after 1 week showed an aneurysm remnant that was then occluded with coils. In 2 patients, coils were placed in the aneurysm daughter sac through a jailed second microcatheter before a detachment of the WEB in the main dome of the aneurysm. The remaining 78 patients are the subjects of this study.

There were 21 men and 57 women, with a mean age of 58.5 years (median, 59 years; range, 24–80 years). The clinical condition at the time of treatment was Hunt and Hess 1–2 in 48 patients, 3 in 24 patients, and 4–5 in 6 patients. The timing of treatment after SAH was 0–1 day in 68 patients, 2–4 days in 5 patients, and >4 days in 5 patients. The aneurysm location was the anterior communicating artery in 35 patients, the posterior communicating artery in 15 patients, the middle cerebral artery in 15 patients, the pericallosal artery in 4 patients, the basilar tip in 4 patients, the superior cerebellar artery in 3 patients, the carotid tip in 1 patient, and the ophthalmic artery in 1 patient. The mean aneurysm size was 5.4 mm (median, 5 mm; range, 3–12 mm). Of 78 aneurysms, 52 (66%) had a wide neck, defined as ≥ 4 mm or a dome-to-neck ratio of ≤ 1.5 . Four patients had 1 additional unruptured aneurysm treated in the same session, 1 with WEB and 3 with coils. One patient had 3 additional unruptured aneurysms treated with the WEB in the same session.

Follow-up

The mean follow-up of 78 patients was 51 months (median, 52 months; range, 5–84 months). Sixty-four patients (82%) had all imaging and clinical visits. The mean follow-up in this subgroup was 56 months (median, 54 months; range, 41–84 months). Fourteen patients (18%) discontinued follow-up; 9 opted out of scheduled follow-up visits. Three patients ended up depending on long-term care after SAH, and the family opted out of follow-up

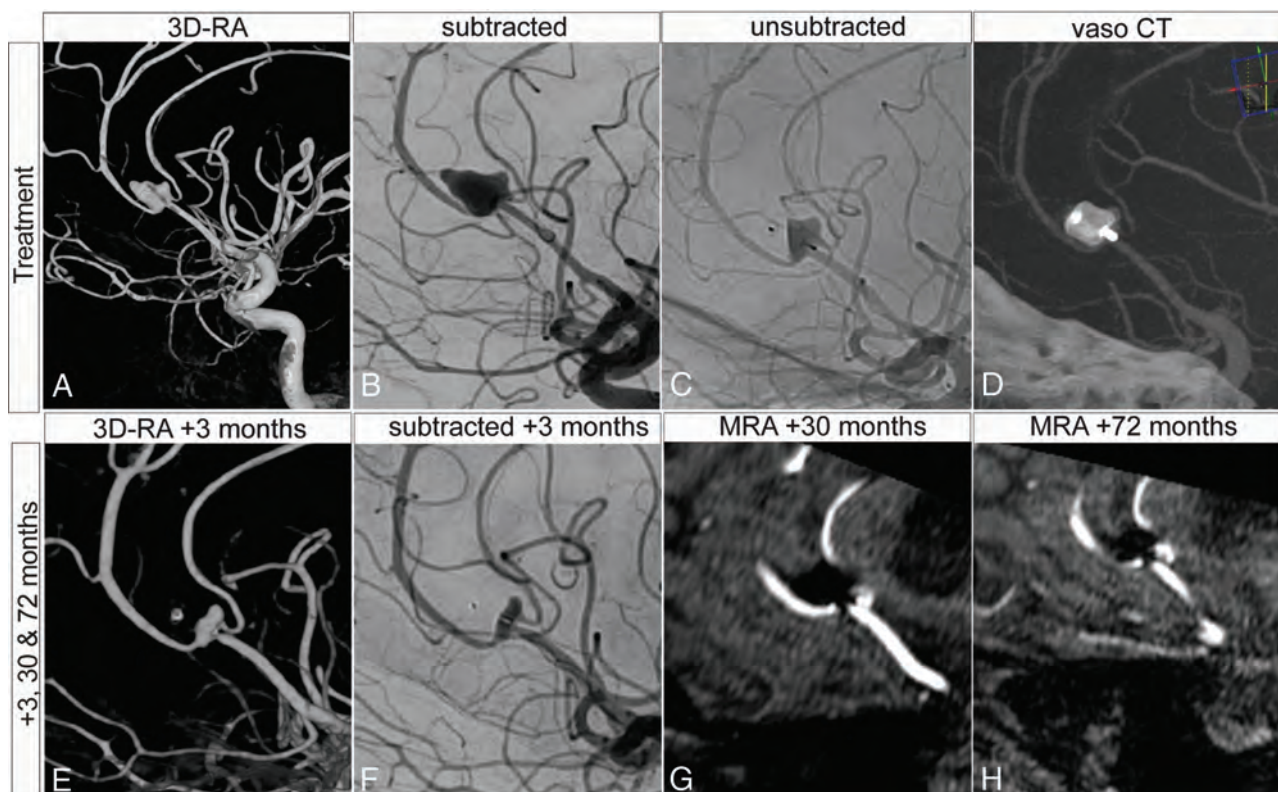


FIG 1. A 58-year-old woman presenting with an SAH, Hunt and Hess grade 3, from a pericallosal aneurysm. The patient had 2 additional aneurysms (not shown). A–D, Treatment of the aneurysm with a WEB-SL 6 × 4. A small neck remnant was accepted to keep the pericallosal artery patent. E–H, Long-term follow-up with DSA and MRA up to 72 months demonstrates stable aneurysm occlusion and patency of the pericallosal artery. VasoCT (Phillips Healthcare).

after discharge. Finally, 2 patients (2.6%) were lost to follow-up and could not be contacted. The last imaging and clinical visits were at 5 and 6 months after treatment, respectively. The average follow-up in this subgroup was 17 months (mode, 18; range, 5–34 months).

Morbidity and Mortality

Of 78 patients, 71 (91%) had mRS 0–2, and 7 (9%) had mRS 3–5 at discharge from our hospital.¹¹

At last follow-up, 73 (94%) patients had mRS 0–2, and 5 (6%) had mRS 3–5. Two patients went from mRS 3–5 to mRS 0–2. There were no rebleeds from the ruptured aneurysm or thromboembolic events, either clinically or on MR imaging during long-term follow-up.

Aneurysm Occlusion and Retreatment

Of 78 ruptured aneurysms, 56 (72%) remained completely occluded (illustrative case, Fig 1), and 17 (22%) had a small neck remnant that was accepted at 3-month angiographic follow-up and remained stable with time on MRA. Five patients (6%) had a reopening of the aneurysm requiring additional treatment. One patient with a reopening of the aneurysm had additional treatment with pCONus (phenox) and coiling. This did not stop aneurysm growth, and the patient was retreated for a third time with an LVIS stent (MicroVention) and coiling. This third procedure was complicated by a small thalamus infarct. One patient underwent aneurysm clipping, and 3 patients received

an additional WEB (illustrative case, Fig 2), of which 1 had to be treated with coiling for the third time (Table).

DISCUSSION

This long-term follow-up study demonstrates that primary treatment of ruptured intracranial aneurysms with the WEB device is both safe and effective, with no rebleeds during follow-up. Of 100 patients initially treated with the WEB device in our series, 18 died in the first 3 months of follow-up.¹¹ After almost 5 years of follow-up, no additional deaths or deterioration in mRS scores was identified. Two patients increased their clinical condition to mRS 0–2 with time. This change brought the overall mortality rate after long-term follow-up in our series of 100 patients with ruptured aneurysm to 18% (95% CI). This is more than the percentage quoted in the 5-year long-term follow-up International Subarachnoid Aneurysm Trial (ISAT),¹² in which 1073 patients underwent coil embolization for ruptured aneurysms, and the overall mortality rate after 5 years was 11% (95% CI). However, 23% of our study patients were admitted in severe clinical conditions (Hunt and Hess grades 4–5) compared with 12% in ISAT. In addition, our study included wide-neck aneurysms that were not suitable for coiling and were excluded from ISAT.

Prevention of rebleeding is the primary goal in the treatment of ruptured aneurysms. In our long-term follow-up, there were no rebleeds and 6% required retreatment after 3 months. This outcome is slightly better compared with ISAT, in which the rate

of rebleeding was 1.9% in the first 30 days¹³ and late retreatment (>3 months after the first treatment) was 9%.

As mentioned in our previously published series, 66% had a wide neck, and treatment complications occurred in 9%. These percentages are relatively low compared with those in stent-assisted coiling, which is another commonly used technique for the treatment of wide-neck bifurcation aneurysms. Two recently published meta-analyses examining the efficacy of stent-assisted

coiling in the treatment of ruptured wide-neck bifurcation aneurysms demonstrated total complication rates of around 20%.^{6,14} In the meta-analysis by Bsat et al,⁶ the thromboembolic complication rate was 9.1%, which is comparable with that in our cohort. However, the rates of postinterventional rebleeding and hemorrhagic complications were 2.5% and 8.7%, respectively, in stent-assisted coiling compared with 0% in our series. This result is likely due to the dual-antiplatelet therapy necessary for stent-

assisted coiling. When using the WEB device, we have not used anti-aggregation therapy in any of our patients with ruptured aneurysms. This result demonstrates the safety profile of the WEB device when treating ruptured wide-neck bifurcation aneurysms without antiplatelet therapy.

In our series, 72% of aneurysms were angiographically completely occluded, and 22% had a small neck remnant. This neck remnant is a frequently observed phenomenon after WEB implantation in the aneurysm sack also called “WEB Shape Modification.”¹⁵ WEB Shape Modification describes a decrease in the device height due to the deepening of the central recess of the device, probably due to compression. These neck remnants generally do not require retreatment because they are expected to be stable.^{15,16} Nevertheless, there are currently no supporting long-term data, and the clinical significance of neck remnants remains a matter of debate. Critics argue that neck remnants due to WEB compression should not be neglected because neck remnants carry an inherent risk of rerupture, as demonstrated for coiling.¹⁷ However, our series demonstrates that WEB Shape Modification after treatment of ruptured aneurysms does not lead to aneurysm growth or rerupture during long-term follow-up.

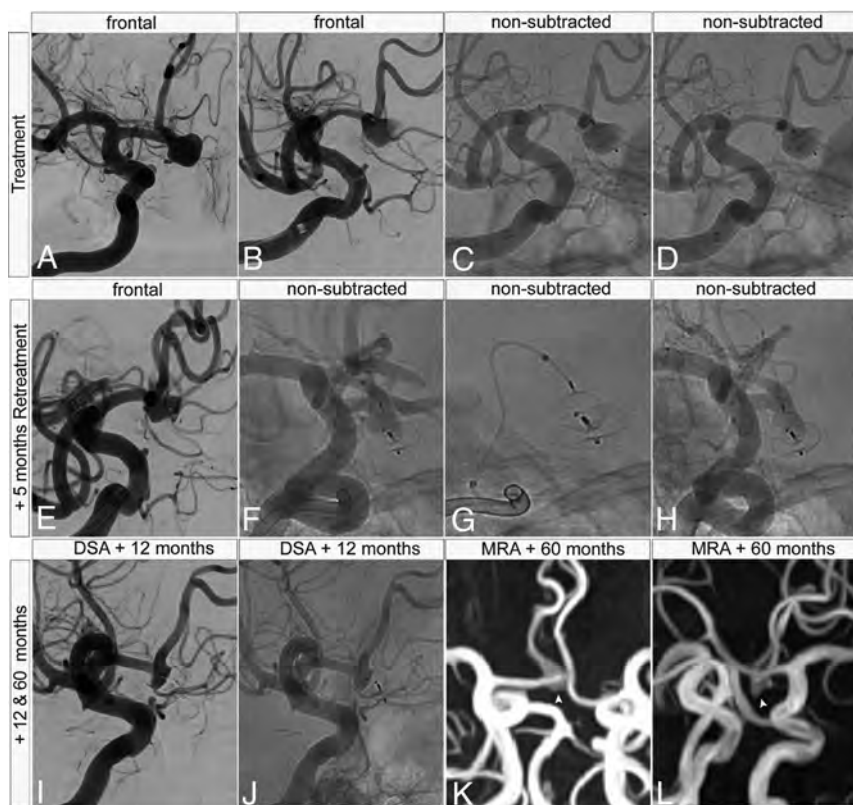


FIG 2. A 52-year-old woman presenting with SAH, Hunt and Hess grade 3, from an 8-mm anterior communicating artery aneurysm. A–D, WEB-SL 9 × 3 placement in the aneurysm. After detachment, there was unintended impaction of the proximal portion of the WEB (D), indicating potential undersizing and resulting in a small neck remnant that was accepted in the acute phase of the SAH. E–H, Follow-up angiography demonstrates WEB impaction and a growing 5-mm neck remnant, which was retreated with a WEB-SL 6 × 3 mm. I–L, A 12-month DSA and 48-month MRA demonstrate a small neck remnant that remains stable on long-term follow-up (white arrowheads).

Five patients with a ruptured aneurysm requiring retreatment

Decade of Life	Aneurysm Location	Hunt and Hess	WEB	Timing and Method of Retreatment	Timing and Method of Second Retreatment	Last Follow-up
7th	Basilar tip	4–5	SLS 8	+10 Months WEB-SL 8 × 3	—	+54 Months MRA
3rd	PcomA ^a	1–2	SLS 4	+4 Months WEB-SL 3, 5 × 2 ^b	+10 Months Coiling	+52 Months MRA
6th	AcomA	3	SL 9 × 4	+5 Months WEB-SL 6 × 3 ^b	—	+60 months MRA
6th	Superior cerebellar	3	SLS 11	+20 Months pCONus and coiling	+33 months LVIS stent and coiling	+58 Months MRA
6th	PcomA ^a	1–2	SL 7 × 4	+19 Months Clipping	—	+19 Months Preclip DSA

Note:—AcomA indicates anterior communicating artery; —, N/A; PcomA, posterior communicating artery; Preclip, right before aneurysm clipping.

^a Fetal origin.

^b WEB 17 system.

Limitations

Limitations of this study include the single-center and uncontrolled design; therefore, there is a possibility of selection bias. Another limitation is the self-reporting of angiographic results and the limited number of patients.

CONCLUSIONS

WEB treatment of ruptured intracranial aneurysms is feasible, effective, and safe and has good long-term follow-up results. The stable aneurysm occlusion rate is high, and the retreatment rate with the WEB is low during the long term. The WEB provides a valuable alternative to coils and seems to be a better alternative to stent-assisted coiling.

Disclosure forms provided by the authors are available with the full text and PDF of this article at www.ajnr.org.

REFERENCES

1. Cognard C, Pierot L, Anxionnat R, et al; Clarity Study Group. **Results of embolization used as the first treatment choice in a consecutive nonselected population of ruptured aneurysms: clinical results of the Clarity GDC study.** *Neurosurgery* 2011;69:837–41; discussion 842 CrossRef Medline
2. Pierot L, Cognard C, Anxionnat R, et al; CLARITY Investigators. **Endovascular treatment of ruptured intracranial aneurysms: factors affecting midterm quality anatomic results—analysis in a prospective, multicenter series of patients (CLARITY).** *AJNR Am J Neuroradiol* 2012;33:1475–80 CrossRef Medline
3. Chalouhi N, Jabbour P, Singhal S, et al. **Stent-assisted coiling of intracranial aneurysms: predictors of complications, recanalization, and outcome in 508 cases.** *Stroke* 2013;44:1348–53 CrossRef Medline
4. Pötin M, Blanc R, Spelle L, et al. **Stent-assisted coiling of intracranial aneurysms: clinical and angiographic results in 216 consecutive aneurysms.** *Stroke* 2010;41:1110–15 CrossRef Medline
5. Chung J, Lim YC, Suh SH, et al. **Stent-assisted coil embolization of ruptured wide-necked aneurysms in the acute period: Incidence of and risk factors for periprocedural complications: clinical article.** *J Neurosurg* 2014;121:4–11 CrossRef Medline
6. Bsat S, Bsat A, Tamim H, et al. **Safety of stent-assisted coiling for the treatment of wide-necked ruptured aneurysm: a systematic literature review and meta-analysis of prevalence.** *Interv Neuroradiol* 2020;26:547–56 CrossRef Medline
7. Bechan RS, Sprengers ME, Majoie CB, et al. **Stent-assisted coil embolization of intracranial aneurysms: complications in acutely ruptured versus unruptured aneurysms.** *AJNR Am J Neuroradiol* 2016;37:502–07 CrossRef Medline
8. Asnafi S, Rouchaud A, Pierot L, et al. **Efficacy and safety of the Woven EndoBridge (WEB) device for the treatment of intracranial aneurysms: a systematic review and meta-analysis.** *AJNR Am J Neuroradiol* 2016;37:2287–92 CrossRef Medline
9. Essibayi MA, Lanzino G, Brinjikji W. **Safety and efficacy of the Woven EndoBridge device for treatment of ruptured intracranial aneurysms: a systematic review and meta-analysis.** *AJNR Am J Neuroradiol* 2021;42:1627–32 CrossRef Medline
10. Monteiro A, Lazar AL, Waqas M, et al. **Treatment of ruptured intracranial aneurysms with the Woven EndoBridge device: a systematic review.** *J Neurointerv Surg* 2021;14:366–70 CrossRef Medline
11. Van Rooij SB, Van Rooij WJ, Peluso JP, et al. **WEB treatment of ruptured intracranial aneurysms: a single-center cohort of 100 patients.** *AJNR Am J Neuroradiol* 2017;38:2282–87 CrossRef Medline
12. Molyneux AJ, Kerr RS, Birks J, et al. **Risk of recurrent subarachnoid haemorrhage, death, or dependence and standardised mortality ratios after clipping or coiling of an intracranial aneurysm in the International Subarachnoid Aneurysm Trial (ISAT): long-term follow-up.** *Lancet Neurol* 2009;8:427–33 CrossRef Medline
13. Molyneux A, Kerr R, Stratton I, et al; International Subarachnoid Aneurysm Trial (ISAT) Collaborative Group. **International Subarachnoid Aneurysm Trial (ISAT) of neurosurgical clipping versus endovascular coiling in 2143 patients with ruptured intracranial aneurysms: a randomized trial.** *J Stroke Cerebrovasc Dis* 2002;11:304–14 CrossRef Medline
14. Zhang X, Zuo Q, Tang H, et al. **Stent assisted coiling versus non-stent assisted coiling for the management of ruptured intracranial aneurysms: a meta-analysis and systematic review.** *J Neurointerv Surg* 2019;11:489–96 CrossRef Medline
15. Rosskopf J, Braun M, Dreyhaupt J, et al. **Shape modification is common in Woven EndoBridge-treated intracranial aneurysms: a longitudinal quantitative analysis study.** *AJNR Am J Neuroradiol* 2020;41:1652–56 CrossRef Medline
16. Janot K, Herbreteau D, Amélot A, et al. **Quantitative evaluation of WEB shape modification: a five-year follow-up study.** *J Neuroradiol* 2019;47:193–96 CrossRef Medline
17. Johnston SC, Dowd CF, Higashida RT, et al; CARAT Investigators. **Predictors of rehemorrhage after treatment of ruptured intracranial aneurysms: the Cerebral Aneurysm Rerupture After Treatment (CARAT) study.** *Stroke* 2008;39:120–25 CrossRef Medline

Association of Left Vertebral Artery Hypoplasia with Posterior Circulation Stroke and the Functional Outcome of Patients with Atrial Fibrillation–Related Cardioembolic Stroke

J.-H. Bae, J.-C. Ryu, S.H. Ha, B.J. Kim, D.-W. Kang, S.U. Kwon, J.-S. Kim, and J.Y. Chang



ABSTRACT

BACKGROUND AND PURPOSE: A cardiogenic embolus could reach the posterior circulation through the right vertebral artery because of a relatively larger diameter in cases of left vertebral artery hypoplasia. Hence, we investigated whether left vertebral artery hypoplasia is associated with cardiac embolisms with atrial fibrillation in the posterior circulation and its functional outcomes.

MATERIALS AND METHODS: In this monocentric retrospective study, patients with acute cardioembolic stroke with atrial fibrillation were enrolled and underwent CT or neck MRA, which visualized the aortic arch and subclavian arteries. The laterality and size of vertebral artery hypoplasia were recorded. Posterior circulation stroke, basilar artery occlusion, and the functional outcomes after 3 months were investigated.

RESULTS: This study included 407 patients; the patients with left vertebral artery hypoplasia experienced a higher rate of posterior circulation stroke (19 versus 73; 42.2% versus 20.2%; $P = .001$) and basilar artery occlusion (5 versus 10; 11.1% versus 2.8%; $P = .005$) than the patients without left vertebral artery hypoplasia. Multivariate analysis revealed that left vertebral artery hypoplasia showed an association with lower odds of achieving a good functional outcome 3 months after the stroke (OR = 0.4; 95% CI, 0.2–0.9; $P = .027$).

CONCLUSIONS: Patients with cardioembolic stroke and left vertebral artery hypoplasia had posterior circulation stroke, basilar artery occlusion, and poor functional outcomes after 3 months.

ABBREVIATIONS: PICA = posterior inferior cerebellar artery infarction; VA = vertebral artery; VAH = vertebral artery hypoplasia

Anatomic variations in the posterior circulation are common, particularly in the vertebral arteries (VAs).¹ Congenital vertebral artery hypoplasia (VAH) is present in 1.9%–26.5% of the population. It is associated with posterior circulation ischemic stroke due to stenosis in the hypoplastic segment and the resultant ipsilateral cerebellar hypoperfusion.^{2–5} It is uncertain whether VAH influences cardioembolic stroke in the posterior circulation.

Although conflicting results exist, previous studies have reported that cardiogenic cerebral embolisms have a right-sided

propensity in acute stroke.^{6,7} This is because the innominate artery, which supplies the right VA and right common carotid artery, has the largest caliber and travels superior and parallel to the direction of the ascending aorta.^{6,7}

Patients with left VAH have a right VA with a relatively larger diameter. On the basis of this evidence, we assumed that cardiogenic emboli might reach the right VA more often than the left VA. We hypothesized that the patients with cardiogenic stroke with left VAH may have posterior circulation stroke, basilar artery occlusion, and less functional independence after 3 months.

Received April 20, 2022; accepted after revision November 11.

From the Department of Neurology (J.-H.B., J.-C.R., S.H.H., B.J.K., D.-W.K., S.U.K., J.Y.C.), Asan Medical Center, University of Ulsan, College of Medicine, Seoul, Korea; and Department of Neurology (J.-S.K.), Gangneung Asan Hospital, Gangneung, Korea.

This research was supported by a grant from the Korea Health Technology R&D Project through the Korea Health Industry Development Institute, funded by the Ministry of Health and Welfare, Republic of Korea [grant No. HI18C2383].

Please address correspondence Jun Young Chang, MD, PhD, Department of Neurology, Asan Medical Center, University of Ulsan, College of Medicine, 88 Olympic-ro 43-gil, Songpa-gu, Seoul, Korea, 138-736; e-mail: noyerpapa@gmail.com

Indicates open access to non-subscribers at www.ajnr.org

Indicates article with online supplemental data.

<http://dx.doi.org/10.3174/ajnr.A7738>

MATERIALS AND METHODS

We assessed all patients with stroke admitted to the Stroke Center at single tertiary referral hospital, Seoul, South Korea, between January 1, 2017, and August 31, 2020. The patients were screened for an acute symptomatic stroke due to cardiac embolism with atrial fibrillation. Patients with >50% stenosis in a symptomatic vessel were excluded. We selected patients with ischemic stroke who underwent MR imaging and MRA during admission, when the ischemic lesions were assessed by DWI. Demographics, risk

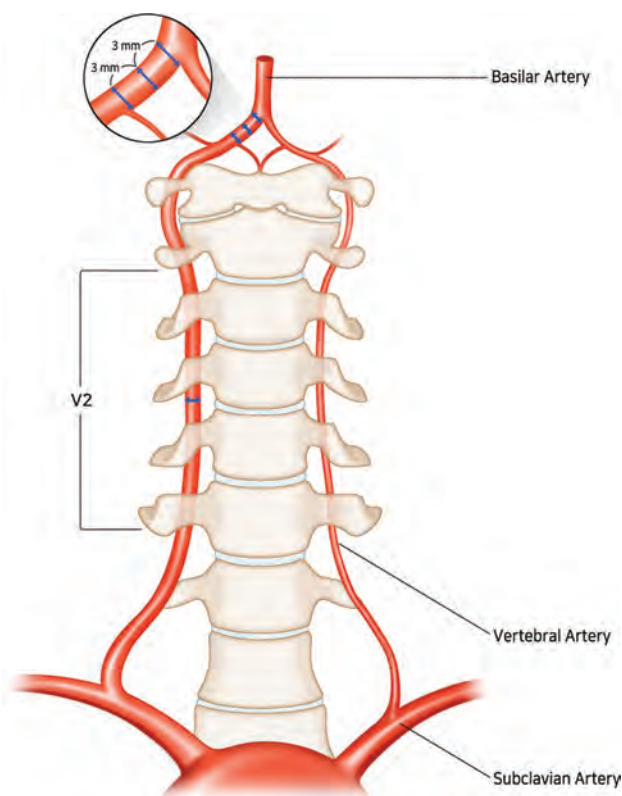


FIG 1. Measuring the diameter of the VA. The diameter of each VA was calculated as the average of the measurements made at 3 consecutive points, spaced 3 mm apart, starting from the vertebrobasilar junction.

factors, NIHSS score on admission, and 3-month mRS were collected. The ethics committee of Asan Medical Center approved this study, and the need for informed consent was waived because of the retrospective nature of the study.

Brain Imaging Analysis

All MRAs included intracranial and neck vessels. We assessed VAH in all patients. The diameter of each VA was calculated as the average of the measurements made at 3 consecutive points, spaced 3 mm apart, starting from the vertebrobasilar junction (both VAs and the basilar artery). We examined the midportion of the intervertebral segment (V2), which is less susceptible to atherosclerotic changes or artifacts in patients with distal VA stenosis (Fig 1).^{3,8} VAH was defined as a VA with a diameter of ≤ 2 mm, and the contralateral larger VA was defined as the dominant VA. Symmetric VA was defined as both vertebral arteries having a diameter of > 2 mm.²⁻⁴ Patients were classified as having either a posterior circulation stroke or an anterior circulation stroke. To demonstrate a cardiac embolus passing through the dominant VA, we measured the frequency and laterality of VAH in the patients with cardioembolic stroke and contralateral posterior inferior cerebellar artery infarction (PICA).

Outcome Variables

In accordance with the widely used mRS grades, we defined mRS 0–2 as good functional outcome (functional independence) and mRS 3–6 as poor functional outcome. mRS 0–3 was used to

define independent walking.⁹ We evaluated the relationship between mRS 0–2 at 3 months after the stroke and left VAH as the primary outcome, and mRS 0–3 (independent walking) at 3 months after the stroke and left VAH as the secondary outcome.⁹

Statistical Analysis

Differences between the groups (ie, patients with left VAH versus others, right PICA versus left PICA, and good functional outcome versus poor functional outcome) were analyzed using the Student *t* test, χ^2 test, and Mann-Whitney *U* test, whichever was appropriate, for continuous and categorical variables. We performed a multiple regression analysis to determine which variables were independent predictors of achieving mRS 0–2 and mRS 0–3 at 3 months after the stroke. Categorical variables were entered into a univariate logistic regression model, including demographic variables (ie, age, sex, and risk factors for stroke), anatomic variables (laterality of VAH), basilar artery occlusion, and the location of the stroke lesion (posterior or anterior circulation). Results are given as ORs as estimates of the relative risk with 95% CI. Analysis was performed using SPSS, Version 26.0 (IBM), and $P < .05$ was considered statistically significant.

RESULTS

Between January 2017 and August 2020, adult patients with acute ischemic stroke were enrolled. Brain MR imaging and 3-month mRS data were available for 2366 patients. Of these, 621 patients had cardioembolic strokes (Online Supplemental Data). Among them, 407 patients were diagnosed with atrial fibrillation before or during hospitalization. The mean age was 73.3 (SD, 10.5) years, and 196 (48.2%) were women. In total, 144 (35.4%) patients with VAH and 263 (64.6%) patients without VAH were enrolled. Left VAH was detected in 45 (11.1%) patients (Table 1).

Left VAH, Posterior Circulation Cardioembolic Stroke, and Basilar Artery Occlusion

Compared with patients without left VAH in the univariate analysis, patients with left VAH were more often women (62.2% versus 46.4%, $P = .045$), had posterior circulation strokes more frequently (42.2% versus 20.2%, $P = .001$), exhibited more basilar artery occlusion (11.1% versus 2.8%, $P = .005$), and were less likely to achieve mRS 0–3 (independent walking) at 3 months after the stroke (55.6% versus 70.7%, $P = .038$) (Table 1 and Fig 2). Patients with right VAH showed no difference in posterior circulation stroke, basilar artery occlusion, and reaching mRS 0–2 (good functional outcome) and mRS 0–3 (independent walking) 3 months after the stroke compared with the patients without right VAH in the univariate analysis (Online Supplemental Data). To demonstrate that cardiac emboli passed through the dominant right VA (contralateral to the left VAH), we performed a subgroup analysis of 49 patients with posterior circulation infarction involving the unilateral PICA territory. Compared with the left PICA group, the right PICA group was associated with left VAH and a larger right VA (6 versus 1; 28.6% versus 3.6%; $P = .013$). The right PICA group showed no association with right VAH compared with the left PICA group (Table 2).

Table 1: Characteristics of patients with cardioembolic stroke with atrial fibrillation with left VA hypoplasia and others^a

	Total (n = 407)	Left VAH (n = 45)	Others (n = 362)	P Value
Age (yr)	73.3 (SD, 10.5)	74.9 (SD, 10.1)	73.1 (SD, 10.5)	.276
Female sex	196 (48.2)	25 (62.2)	160 (46.4)	.045
Hypertension	279 (68.6)	35 (77.8)	244 (67.4)	.157
Diabetes mellitus	113 (27.8)	15 (33.3)	98 (27.1)	.376
Hyperlipidemia	129 (31.7)	11 (24.4)	118 (32.6)	.268
Ischemic heart disease	80 (19.7)	6 (13.3)	74 (20.4)	.258
History of stroke	107 (26.3)	9 (20.0)	98 (27.1)	.309
Current smoker	110 (27.0)	11 (24.4)	99 (27.3)	.679
Initial NIHSS	6.0 (2.0–13.0)	6.0 (2.5–11.5)	6.0 (2.0–13.0)	.886
Lesion location				
Anterior circulation	293 (72.0)	23 (51.1)	270 (74.6)	.001
Posterior circulation	92 (22.6)	19 (42.2)	73 (20.2)	.001
Both	22 (5.4)	3 (6.7)	19 (5.2)	.692
BAO	15 (3.7)	5 (11.1)	10 (2.8)	.005
3-Month mRS	2.0 (0.3–4.0)	3.0 (1.0–5.0)	2.0 (0.0–4.0)	.067
3-Month mRS 0–2	234 (57.5)	20 (44.4)	214 (59.1)	.060
3-Months mRS 0–3	281 (69.0)	25 (55.6)	256 (70.7)	.038

Note:—BAO indicates basilar artery occlusion.

^aResults are presented as number and percentage, mean, or median (25th–75th percentile).



FIG 2. Basilar artery occlusion in a patient with left VAH (A) showing right posterior inferior cerebellar artery infarction due to cardioembolism (B), whose 3-month mRS was 4. Follow-up MRA shows a recanalized basilar artery (C).

Left VAH and Poor Functional Outcome

Comparisons between the mRS 0–2 (good functional outcome) group and the mRS 3–6 (poor functional outcome) group are summarized in Table 3. Compared with the poor functional outcome group, patients with good functional outcome were younger (mean age, 70.8 [SD, 9.8] versus 76.7 [SD, 10.5] years, $P < .001$); were less often women (41.5% versus 57.2%, $P = .002$); had less hypertension (64.5% versus 74.0%, $P = .042$) and diabetes mellitus (22.8% versus 35.8%, $P = .002$) and a previous stroke history

(19.2% versus 35.8%, $P < .001$); were current smokers (32.1% versus 20.2%, $P = .008$); had a lower initial NIHSS score (3.0 [interquartile range, 1.0–7.0] versus 13.0 [interquartile range, 6.0–17.0], $P < .001$); and had less basilar artery occlusion (1.7% versus 6.4%, $P = .014$). The 3-month mRS 0–2 (good functional outcome) showed a trend toward an inverse association with left VAH compared with patients with 3-month mRS 3–6 (poor functional outcome) in univariate analysis (8.5% versus 14.5%, $P = .060$). Compared with patients with 3-month mRS 4–6, patients with 3-month mRS 0–3 (independent walking) showed a reverse association with left VAH in the univariate analysis (8.9% versus 15.9%, $P = .038$) (Online Supplemental Data).

In the multivariable analysis (including the presence of left VAH, sex, age, hypertension, diabetes mellitus, current smoking, previous stroke history, and initial NIHSS), the presence of left VAH showed an association with lower odds of achieving mRS 0–2 (good functional outcome) 3 months after the stroke (OR = 0.4; 95% CI, 0.2–0.9; $P = .027$). The presence of left VAH showed less attainment of mRS 0–3 (independent walking) at 3 months after the stroke (OR = 0.4; 95% CI, 0.2–0.8; $P = .016$).

DISCUSSION

We found that left VAH is associated with posterior circulation stroke, basilar artery occlusion, and poor functional outcome after 3 months in patients with cardioembolic stroke with atrial fibrillation. Previous studies reported that posterior circulation strokes represented about 20% of all ischemic strokes.¹⁰ In our study, 42.2% of the patients with left VAH had a posterior circulation stroke.

Recent studies have emphasized the clinical importance of VAH on stroke and reported that patients with VAH are at a high risk of posterior circulation stroke.^{1,2} Previous studies reported that VAH is associated with ipsilateral atherosclerotic stenosis in the VA and posterior circulation stroke.^{3,5} Thierfelder et al⁴ reported that VAH could lead to relative hypoperfusion in the ipsilateral PICA. Bilateral VAH may have a unique pattern in the infarction territory that involves multiple vascular territories, and it is mostly bilateral.¹¹

Perren et al¹ reported that more than one-half of posterior circulation strokes in patients with VAH were presumably embolic. Although there are conflicting results, previous studies have disclosed that cardiogenic embolisms have a right-sided propensity in acute stroke. Our study explained the mechanism for posterior circulation stroke in patients with left VAH, in whom the cardiac emboli pass through the dominant right VA.

Several mechanisms may explain our results. The right VA (a branch of the right subclavian artery) has the largest caliber and travels superior and parallel to the direction of the ascending

Table 2: Characteristics of patients with cardioembolic stroke with PICA territory infarction contralateral to VAH^a

VAH	Right PICA Territory Infarction (n = 21)	Left PICA Territory Infarction (n = 28)	P Value
Left	6 (28.6)	1 (3.6)	.013
Right	5 (23.8)	9 (32.1)	.523
Symmetric	10 (47.6)	18 (64.3)	.243

^a Results are presented as number and percentage.

Table 3: Characteristics of patients with atrial fibrillation–related cardioembolic stroke with good functional outcome (mRS 0–2) versus poor functional outcome (mRS 3–6)^a

	3-Month mRS 0–2 (n = 234)	3-Month mRS 3–6 (n = 173)	P Value
Age (yr)	70.8 (SD, 9.8)	76.7 (SD, 10.5)	<.001
Female sex	92 (41.5)	93 (57.2)	.002
Hypertension	151 (64.5)	128 (74.0)	.042
Diabetes mellitus	51 (22.8)	62 (35.8)	.002
Hyperlipidemia	79 (33.8)	50 (28.9)	.298
Ischemic heart disease	49 (20.9)	31 (17.9)	.448
History of stroke	45 (19.2)	62 (35.8)	<.001
Current smoker	75 (32.1)	35 (20.2)	.008
Initial NIHSS	3.0 (1.0–7.0)	13.0 (6.0–17.0)	<.001
VAH			
Right	59 (25.2)	40 (23.1)	.627
Left	20 (8.5)	25 (14.5)	.060
Symmetric	155 (66.2)	108 (62.4)	.427
Lesion location			
Anterior circulation	164 (70.1)	129 (74.6)	.260
Posterior circulation	59 (25.2)	33 (19.1)	.108
Both	11 (4.7)	11 (6.4)	.465
BAO	4 (1.7)	11 (6.4)	.014

Note:—BAO indicates basilar artery occlusion.

^a Results presented as number and percentage, mean, or median (25th–75th percentile).

aorta; therefore, we could assume that a cardiogenic embolus will reach the right VA orifice more often than the contralateral left VA orifice.^{6,7} Because the diameter of the right VA is relatively larger in patients with left VAH, the cardiogenic emboli can reach the posterior circulation through the right VA more often than in the patients with symmetric VA or right VAH. This theory may be supported by our analysis that the right PICA is associated with left VAH (6 versus 1; 28.6% versus 3.6%; $P = .013$) compared with the left PICA group. We presumed that patients with left VAH have a dominant right VA with a larger diameter, occasionally wider than 4 mm and similar to that of the basilar artery.^{1,2} A cardiogenic embolus large enough to occlude the basilar artery might have a higher chance of passing through the dominant right VA.

Posterior circulation stroke is a marker of poor functional outcome in patients with acute ischemic stroke.¹² Basilar artery occlusion is known to be associated with poor functional outcome and high mortality.^{13,14} A higher percentage of posterior circulation strokes and basilar artery occlusion might explain the poor 3-month functional outcomes in the patients with left VAH.

There are limitations to our study. The possibility that a posterior circulation infarction might be due to atherosclerosis or dissection of the VA was not excluded.¹⁰ However, patients with vertebrobasilar artery stenosis of $>50\%$ were excluded in our cohort; therefore, the possibility of stroke due to atherosclerosis or dissection is not high. Second, there are patients with variations in the anatomy of the vertebrobasilar artery, such as the

absence of the PICA, PICA duplication, and fenestration, which were not evaluated in this study.¹⁵ Third, our study cohort does not represent the general population because we conducted a retrospective analysis at a single-center with a relatively small number of patients. Therefore, prospective studies with larger numbers of patients are necessary to determine the causative relationship between left VAH and posterior circulation stroke. Fourth, with such a small sample size, it is difficult to consider clinically significant the result that patients with right PICA showed a higher rate of left VAH than patients with left PICA. Although statistically significant, type II error may have affected the results.

CONCLUSIONS

Left VAH is associated with posterior circulation stroke, basilar artery occlusion, and poor 3-month functional outcomes in patients with cardioembolic stroke

Disclosure forms provided by the authors are available with the full text and PDF of this article at www.ajnr.org.

REFERENCES

1. Perren F, Poggia D, Landis T, et al. **Vertebral artery hypoplasia: a predisposing factor for posterior circulation stroke?** *Neurology* 2007;68:65–67 CrossRef Medline
2. Kulyk C, Voltan C, Simonetto M, et al. **Vertebral artery hypoplasia: an innocent lamb or a disguise?** *J Neurol* 2018;265:2346–52 CrossRef Medline
3. Park JH, Kim JM, Roh JK. **Hypoplastic vertebral artery: frequency and associations with ischaemic stroke territory.** *J Neurol Neurosurg Psychiatry* 2007;78:954–58 CrossRef Medline
4. Thierfelder KM, Baumann AB, Sommer WH, et al. **Vertebral artery hypoplasia: frequency and effect on cerebellar blood flow characteristics.** *Stroke* 2014;45:1363–68 CrossRef Medline
5. Dinc Y, Ozpar R, Emir B, et al. **Vertebral artery hypoplasia as an independent risk factor of posterior circulation atherosclerosis and ischemic stroke.** *Medicine (Baltimore)* 2021;100:e27280 CrossRef Medline
6. Kim HJ, Song JM, Kwon SU, et al. **Right-left propensity and lesion patterns between cardiogenic and aortogenic cerebral embolisms.** *Stroke* 2011;42:2323–25 CrossRef Medline
7. Park KY, Kim YB, Chung PW, et al. **Right-side propensity of cardiogenic emboli in acute ischemic stroke with atrial fibrillation.** *Scand Cardiovasc J* 2014;48:335–38 CrossRef Medline
8. Hong JM, Chung CS, Bang OY, et al. **Vertebral artery dominance contributes to basilar artery curvature and peri-vertebrobasilar junctional infarcts.** *J Neurol Neurosurg Psychiatry* 2009;80:1087–89 CrossRef Medline
9. Banks JL, Marotta CA. **Outcomes validity and reliability of the modified Rankin scale: implications for stroke clinical trials.** *Stroke* 2007;38:1091–96 CrossRef Medline
10. Markus HS, van der Worp HB, Rothwell PM. **Posterior circulation ischaemic stroke and transient ischaemic attack: diagnosis,**

- investigation, and secondary prevention. *Lancet Neurol* 2013;12:989–98 CrossRef Medline
11. Hsu CF, Chen KW, Su CH, et al. **Bilateral vertebral artery hypoplasia and fetal-type variants of the posterior cerebral artery in acute ischemic stroke.** *Front Neurol* 2021;12:582149 CrossRef Medline
 12. Sommer P, Posekany A, Serles W, et al; Austrian Stroke Unit Registry Collaborators. **Is functional outcome different in posterior and anterior circulation stroke?** *Stroke* 2018;49:2728–32 CrossRef Medline
 13. Mattle HP, Arnold M, Lindsberg PJ, et al. **Basilar artery occlusion.** *Lancet Neurol* 2011;10:1002–14 CrossRef Medline
 14. Langezaal LC, van der Hoeven E, Mont’Alverne FJ; et al; BASICS Study Group. **Endovascular therapy for stroke due to basilar-artery occlusion.** *N Engl J Med* 2021;384:1910–20 CrossRef Medline
 15. Pekcevik Y, Pekcevik R. **Variations of the cerebellar arteries at CT angiography.** *Surg Radiol Anat* 2014;36:455–61 CrossRef Medline

Retrospective Analysis of the Association of a Small Vestibular Aqueduct with Cochleovestibular Symptoms in a Large, Single-Center Cohort Undergoing CT

K. Bouhadjer, L.V. Romo, M.J. Brennan, B.M. Kozak, E. Hattingen, A.F. Juliano, H.D. Curtin, and K.L. Reinshagen

ABSTRACT

BACKGROUND AND PURPOSE: Temporal bones in some patients with Ménière disease have demonstrated small vestibular aqueducts; however, the prevalence and clinical importance of small vestibular aqueducts remain unclear in patients without Ménière disease. This study correlates the presence of a small vestibular aqueduct with cochleovestibular symptoms.

MATERIALS AND METHODS: Consecutive temporal bone CTs in adults from January to December 2020 were reviewed. The midpoint vestibular aqueduct size in the 45°-oblique Pöschl view was measured by 2 reviewers independently in 684 patients (1346 ears). Retrospective chart review for the clinical diagnosis of Ménière disease, the presence of cochleovestibular symptoms, and indications for CT was performed.

RESULTS: Fifty-two of 684 patients (7.6% of patients, 62/1346 ears) had small vestibular aqueducts. Twelve patients (15/1346 ears) had Ménière disease. Five of 12 patients with Ménière disease (5 ears) had a small vestibular aqueduct. There was a significant correlation between a small vestibular aqueduct and Ménière disease ($P < .001$). There was no statistical difference between the small vestibular aqueduct cohort and the cohort with normal vestibular aqueducts (0.3–0.7 mm) regarding tinnitus ($P = .06$), hearing loss ($P = .88$), vertigo ($P = .26$), dizziness ($P = .83$), and aural fullness ($P = .61$).

CONCLUSIONS: While patients with Ménière disease were proportionately more likely to have a small vestibular aqueduct than patients without Ménière disease, the small vestibular aqueduct was more frequently seen in patients without Ménière disease and had no correlation with hearing loss, vertigo, dizziness, or aural fullness. We suggest that the finding of a small vestibular aqueduct on CT could be reported by radiologists as a possible finding in Ménière disease, but it remains of uncertain, and potentially unlikely, clinical importance in the absence of symptoms of Ménière disease.

ABBREVIATIONS: VA = vestibular aqueduct; MD = Ménière disease

The vestibular aqueduct (VA) is a small, bony channel in the posterior petrous temporal bone, which encloses the endolymphatic duct and a portion of the endolymphatic sac. Dysfunctions of the endolymphatic sac and duct are intimately related to the surrounding VA.¹ Based on normative data, the midpoint VA size in the 45° oblique Pöschl plane ranges from 0.3 to 0.7 mm.² Enlarged vestibular aqueducts may be seen in the setting of underlying cochlear malformations, and subtle changes in size can be associated with impairment of hearing and balance.^{3–5} An enlarged

VA has been associated with sensorineural hearing loss, though the exact pathogenesis is thought to be multifactorial and is not fully understood.^{3,6–10} The clinical importance of a small VA, however, remains unclear. Temporal bones in some patients with Ménière disease (MD), a disorder of the inner ear, characterized by episodes of vertigo, fluctuating hearing loss, tinnitus, and aural fullness, have demonstrated thin or narrow VAs.^{11–19} The clinical diagnosis of MD is dichotomized into definite or probable MD. Definite MD requires the following: 1) ≥ 2 episodes of vertigo lasting 20 minutes to 12 hours; 2) low- to medium-frequency sensorineural hearing loss in the affected ear on at least 1 occasion before, during, or after one of the episodes of vertigo; 3) fluctuating aural symptoms (hearing, tinnitus, or fullness) in the affected ear; and 4) exclusion of other known causes. The clinical diagnosis of probable MD requires the following: 1) ≥ 2 episodes of vertigo or dizziness lasting 20 minutes to 24 hours; 2) fluctuating aural symptoms in the affected ear; and 3) exclusion of other known causes.²⁰ The

Received July 19, 2022; accepted after revision November 4.

From the Department of Radiology (K.B., L.V.R., M.J.B., A.F.J., H.D.C., K.L.R.), Massachusetts Eye and Ear, Boston, Massachusetts; Neuroradiology Division (B.M.K.), Massachusetts General Hospital, Boston, Massachusetts; and Institut für Neuroradiologie (E.H.), Universitätsmedizin der Goethe Universität Frankfurt, Frankfurt am Main, Germany.

Please address correspondence to Katherine L. Reinshagen, MD, Department of Radiology, 243 Charles St, Massachusetts Eye and Ear, Boston, MA 02114; e-mail: katherine_reinshagen@meei.harvard.edu; @klreinshagen

<https://dx.doi.org/10.3174/ajnr.A7734>

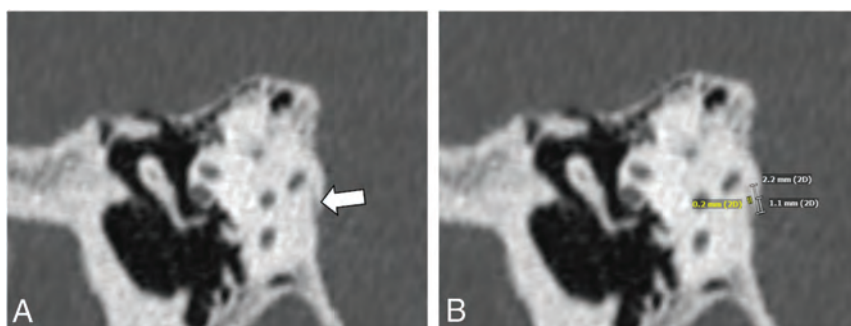


FIGURE Representative Pöschl reformatted multidetector CT image of a 59-year-old patient shows a small VA (A, white arrow) with measurement (0.2 mm) at the midpoint (B).

Table 1: Indications for CT in the 52 patients with small VAs

Indication	No. of Patients
Cochlear implant follow-up or preop planning	10
Cholesteatoma	8
Hearing loss	6
Superior semicircular canal dehiscence	5
Tinnitus	3
Dizziness	3
Infection	3
Patulous eustachian tube	2
Otosclerosis	2
Aural fullness	2
Otorrhea	2
Ossicular anomaly	1
Osteoradionecrosis	1
Tympanic membrane perforation	1
Disequilibrium	1
Vestibular schwannoma	1
Ménière disease	1

Note:—Preop indicates preoperative.

pathogenesis of MD is still unclear but elevated endolymphatic pressure and endolymphatic hydrops are commonly accepted as important associations.

The purpose of this study was to explore the prevalence of small VAs found on temporal bone CTs and the correlation of small VAs with cochleovestibular symptoms and the presence of MD.

MATERIALS AND METHODS

Subjects

This retrospective study received approval (institutional review board No. 2020P003465) from the Massachusetts General Brigham Institutional Review Board. Inclusion criteria were patients 18–95 years of age who underwent dedicated multidetector CT or cone-beam CT of the temporal bone from January 2020 to December 2020 at Massachusetts Eye and Ear. Seven hundred seventy-three CT scans were reviewed. Forty CTs were excluded because these patients underwent >1 CT in the 1-year period of study and only 1 study was included for each patient. Forty-nine CTs were excluded due to motion artifacts preventing accurate measurement of the VA. Six hundred eighty-four patients (1346 ears) were included in the study. Twenty-two patients underwent single-sided conebeam CT of the temporal bones accounting for the discrepancy between

ears and patients. We reviewed the patients' medical records for a clinical diagnosis of definite or probable MD, the presence of dizziness or vertigo, aural fullness, tinnitus, hearing loss, and the indication for the performed CT scan.

Imaging Acquisition

Multidetector CT (Discovery CT750 HD; GE Healthcare) of the temporal bone was performed with 120 kV (peak), 240 mA, FOV = 100 × 100 mm, matrix = 512 × 512, 0.6-mm section thickness with 0.3-mm overlap.

Conebeam CT (3D Accuitomo; J Morita) of the temporal bone was performed with a 90-kV(peak), 8-mA, high-resolution mode with an exposure time of 30.8 seconds, FOV = 64 × 64 mm, matrix = 512 × 512, 0.5-mm section thickness.

Reader Assessment

Two observers retrospectively assessed the midpoint VA size in the 45° oblique Pöschl plane view (Figure). On the basis of Juliano et al,² VA sizes <0.3 mm were reviewed by consensus and considered borderline small-to-small VAs.

Statistical Analysis

Statistical analysis was performed using the R statistical and computing software, Version 4.0.4 (<https://www.r-project.org>). The Fisher exact test was used to assess the association between the presence of a small VA and clinical symptomatology. *P* values < .05 were considered statistically significant.

RESULTS

In this study, 684 patients (mean age, 53 years; range, 18–95 years; 315 men [46%], 369 women [54%]) were included. Fifty-two patients (7.6% of patients; 62 ears, 4.6% of ears) had VAs ranging from nonvisible to borderline small (10 bilateral, 42 unilateral). Twelve ears had nonvisible VAs, whereas 50 ears had visible VAs of <0.3 mm. Enlarged VAs were observed in 39 patients (range, 0.8–3.2 mm; 14 bilateral, 25 unilateral). A VA within the expected normal range of 0.3–0.7 mm was observed in 593 patients (1168 ears).

Of these 52 patients with nonvisible-to-borderline small VAs, 33 patients (63.5%) had hearing loss: sensorineural (13 patients), conductive (7 patients), or mixed hearing loss (6 patients). Seven patients had hearing loss that was unspecified by type in the medical record. Five patients had a history of cholesteatoma. Vestibular symptoms in the 52 patients with nonvisible-to-borderline small VAs were reported as follows: dizziness (6 patients, 11.5%) and vertigo (6 patients, 11.5%). Both dizziness and vertigo were reported in 3 patients. Nine patients reported tinnitus (17%). The indication for CT of the 52 patients with nonvisible-to-borderline small VAs is listed in Table 1.

The distribution of cochleovestibular symptoms by VA size is listed in Table 2. The distribution of the type of hearing loss by VA size is listed in Table 3. Twelve patients (15 of 1346 ears)

Table 2: Distribution of patients with cochleovestibular symptoms by VA size

VA Size	Total (No.)	MD (No.)	Tinnitus (No.)	Dizziness (No.)	Vertigo (No.)	Aural Fullness (No.)
<0.3 mm	52	5	9	6	6	0
0.3 mm ≤ x ≤ 0.7 mm	593	7	182	79	41	13
>0.7 mm	39	0	14	2	2	1

Table 3: Distribution of patients by hearing loss type and VA size

VA Size	Total Patients (No.)	HL (No.)	SNHL (No.)	CHL (No.)	MHL (No.)	UHL (No.)
<0.3 mm	52	33	13	7	6	7
0.3 mm ≤ x ≤ 0.7 mm	593	364	132	100	54	78
>0.7 mm	39	27	12	6	1	8

Note:—HL indicates hearing loss; SNHL, sensorineural hearing loss; CHL, conductive hearing loss; MHL, mixed hearing loss; UHL, unspecified hearing loss.

Table 4: Comparison of VA size and presence of MD by number of ears

VA Size	Total No. Ears	MD
<0.3 mm	62	5
0.3 mm ≤ x ≤ 0.7 mm	1231	10
>0.7 mm	53	0

were affected by MD with 5 ears having a small VA (Table 4). Although small VAs can be seen in ears without MD, there was a statistically significant correlation between small or nonvisible VAs and MD (5 of 62 ears with a small VA had MD compared with 10 of 1231 ears with a normal-sized VA having MD; Fisher exact test, $P < .001$). No patients with MD had an enlarged VA. There was no statistical difference between patients with small VAs and patients with normal-sized VAs with regard to a reported history of tinnitus ($P = .06$), vertigo ($P = .26$), dizziness ($P = .83$), aural fullness ($P = .61$), the presence of hearing loss ($P = .88$), or a specific type of hearing loss (conductive hearing loss, $P = .69$; sensorineural hearing loss, $P = .61$; mixed hearing loss, $P = .62$; and unspecified hearing loss, $P > .99$).

DISCUSSION

An enlarged VA is well-described in the literature and is seen in genetic syndromes like Pendred syndrome and in cochlear anomalies such as incomplete partition type II. Enlarged VAs have been correlated with adverse hearing outcomes, and recent studies have shown that VA size correlates negatively with hearing outcomes (pure tone average, speech reception threshold, and word-recognition score).^{6,21} Because of its clinical implications, the finding of an enlarged VA is typically reported by radiologists. In contrast, a small or nonvisible VA has not been reported regularly in our practice because the clinical importance of small VAs in patients without MD remains unclear.

The etiology of the small or hypoplastic VA is incompletely understood. It has been hypothesized that a small VA may be due to congenital hypoplasia of the VA and endolymphatic sac.^{22,23} While the correlation of a small VA and MD has been the focus of many studies, our study attempted to understand the finding of a small VA in a broader clinical context and ultimately understand whether this finding is important to the encountering radiologist. As expected, our data confirm the significant correlation between small VAs and MD in a large cohort of 684 patients as seen in smaller prior studies.^{16,18,19,24,25} A small VA can lead to endolymphatic hydrops, which is strongly associated with MD.

However, in our cohort, 10 of 15 ears (67%) affected by MD had normal-sized VAs, suggesting that the development of MD is likely multifactorial. Most ears (57 of 62, 92%) in our cohort with small VAs did not have MD at the time of imaging. In addition, no significant difference was found regarding the presence of cochleovestibular symptoms such as vertigo ($P = .26$), dizziness ($P = .83$), aural fullness ($P = .61$), and tinnitus (0.06) between patients with normal-sized VAs and those with small VAs. Therefore, although the finding of a small or nonvisible VA should prompt consideration of MD when encountered by the radiologist, in the absence of symptoms of MD, a small VA is more commonly seen in patients without MD and has no correlation with other cochleovestibular symptoms in our cohort.

Limitations

Our results have some limitations. Due to the retrospective cross-sectional study design, the major limitation of this study is that CT scans were acquired at a single time point in the patient's clinical course; therefore, our data can only provide the prevalence of MD or other cochleovestibular symptoms in our patients at the time of CT. This limitation is particularly noteworthy because a hallmark of MD is its fluctuating and progressive nature and MD attacks possibly being spread out by periods of remission lasting months to years. Thus, the diagnosis of MD may require longer-term follow-up.^{26,27} Future studies assessing longitudinal data in the medical record during a lengthy period would be imperative to understand whether the presence of a small VA places a person at risk of developing MD or other cochleovestibular symptoms.

In addition, the measurements of VAs made in this study reflect the size of the midpoint and do not analyze the morphology or other VA-related information such as angular trajectory as introduced by Bächinger et al.²⁸ Most interesting, angular trajectory measurements of the VA have recently been shown to be predictive of progression of unilateral MD to bilateral MD, though their prediction of disease from asymptomatic patients to MD has not yet been established.²⁹ Measurement of the angular trajectory of the VA is more labor-intensive and is challenging in the setting of nonvisible VAs. We chose to use measurements in the Pöschl plane view because they can be made easily with high interrater reliability.² Future studies using the angular trajectory in patients without MD and assessing their progression to MD could be a valuable addition to the literature.

Finally, although this study has a large sample size, all patients had conditions that required care at a tertiary care center and

temporal bone CTs. Thus, the data are subject to selection bias, which may affect our conclusions and limit our ability to extract the true prevalence of a small VA in the general population. In our cohort, the overall prevalence of small VAs was higher than expected in the general population, possibly due to selection bias. On the basis of normative data from Juliano et al,² we should have expected 3% of the study population to have small VAs; however, in our cohort, 7.6% of patients (4.6% of ears) had small VAs. Future studies could consider assessing the prevalence of a small VA in nontemporal bone CTs, though precise measurements of the VA are often challenging in nondedicated temporal bone studies due to its inherent shape and small size.

CONCLUSIONS

In our large cohort of consecutive patients undergoing temporal bone imaging, small or nonvisible VAs were seen in up to 7.6% of our patients (52 of 684 patients) or 4.6% of ears (62 of 1346 ears). While patients with MD were proportionately more likely to have a small VA than patients without MD, the small VA was more frequently seen in patients without MD and had no correlation with hearing loss, vertigo, dizziness, or aural fullness. We suggest that small or nonvisible VAs on CT scans should be considered by radiologists as a possible finding in MD, though this finding at a single time point remains of uncertain, and potentially unlikely, clinical importance in the absence of MD or MD symptoms.

Disclosure forms provided by the authors are available with the full text and PDF of this article at www.ajnr.org.

REFERENCES

- Kodama A, Sando I. Postnatal development of the vestibular aqueduct and endolymphatic sac. *Ann Otol Rhinol Laryngol Suppl* 1982;96:3–12 CrossRef Medline
- Juliano AF, Ting EY, Mingkwansook V, et al. Vestibular aqueduct measurements in the 45° oblique (Pöschl) plane. *AJNR Am J Neuroradiol* 2016;37:1331–37 CrossRef Medline
- Irving RM, Jackler RK. Large vestibular aqueduct syndrome. *Current Opinion in Otolaryngology & Head and Neck Surgery* 1997;5:267–71
- Reinshagen KL, Curtin HD, Quesnel AM, et al. Measurement for detection of incomplete partition type II anomalies on MR imaging. *AJNR Am J Neuroradiol* 2017;38:2003–07 CrossRef Medline
- Bouhadjer K, Tissiera K, Farris CW, et al. Retrospective review of mid-point vestibular aqueduct size in the 45° oblique (Pöschl) plane and correlation with hearing loss in patients with enlarged vestibular aqueduct. *AJNR Am J Neuroradiol* 2021;42:2215–21 CrossRef Medline
- Pryor SP, Madeo AC, Reynolds JC, et al. SLC26A4/PDS genotype-phenotype correlation in hearing loss with enlargement of the vestibular aqueduct (EVA): evidence that Pendred syndrome and non-syndromic EVA are distinct clinical and genetic entities. *J Med Genet* 2005;42:159–65 CrossRef Medline
- Madden C, Halsted M, Meinzen-Derr J, et al. The influence of mutations in the SLC26A4 gene on the temporal bone in a population with enlarged vestibular aqueduct. *Arch Otolaryngol Head Neck Surg* 2007;133:162–68 CrossRef Medline
- Birkenhäger R, Zimmer AJ, Maier W, et al. Evidence of a novel gene for the LAV-syndrome [in German]. *Laryngorhinootologie* 2007;86:102–06 CrossRef Medline
- Zhao FF, Lan L, Wang DY, et al. Correlation analysis of genotypes, auditory function, and vestibular size in Chinese children with enlarged vestibular aqueduct syndrome. *Acta Otolaryngol* 2013;133:1242–49 CrossRef Medline
- Merchant SN, Rosowski JJ. Conductive hearing loss caused by third-window lesions of the inner ear. *Otol Neurotol* 2008;29:282–89 CrossRef Medline
- Rizvi SS, Smith LE. Idiopathic endolymphatic hydrops and the vestibular aqueduct. *Ann Otol Rhinol Laryngol* 1981;90:77–79 CrossRef Medline
- Sando I, Ikeda M. The vestibular aqueduct in patients with Meniere's disease: a temporal bone histopathological investigation. *Acta Otolaryngol* 1984;97:558–70 CrossRef Medline
- Stahle J, Wilbrand HF, Rask-Andersen H. Temporal bone characteristics in Meniere's disease. *Ann N Y Acad Sci* 1981;374:794–807 CrossRef Medline
- Stahle J, Wilbrand H. The vestibular aqueduct in patients with Meniere's disease: a tomographic and clinical investigation. *Acta Otolaryngol* 1974;78:36–48 CrossRef Medline
- Masutani H, Takahashi H, Sando I, et al. Vestibular aqueduct in Meniere's disease and non-Meniere's disease with endolymphatic hydrops: a computer aided volumetric study. *Auris Nasus Larynx* 1991;18:351–57 CrossRef Medline
- Kodama A, Sando I. Dimensional anatomy of the vestibular aqueduct and the endolymphatic sac (rugose portion) in human temporal bones: statistical analysis of 79 bones. *Ann Otol Rhinol Laryngol Suppl* 1982;96:13–20 Medline
- Clemis JD, Valvassori GE. Recent radiographic and clinical observations on the vestibular aqueduct: (a preliminary report). *Otolaryngol Clin North Am* 1968;1:339–52 CrossRef
- Grosser D, Willenborg K, Dellani P, et al. Vestibular aqueduct size correlates with the degree of cochlear hydrops in patients with and without Meniere's disease. *Otol Neurotol* 2021;42:e1532–36 CrossRef Medline
- Miyashita T, Toyama Y, Inamoto R, et al. Evaluation of the vestibular aqueduct in Ménière's disease using multiplanar reconstruction images of CT. *Auris Nasus Larynx* 2012;39:567–71 CrossRef Medline
- Lopez-Escamez JA, Carey J, Chung WH, et al; Korean Balance Society. Diagnostic criteria for Meniere's disease. *J Vestib Res* 2015;25:1–7 CrossRef Medline
- Ascha MS, Manzoor N, Gupta A, et al. Vestibular aqueduct mid-point width and hearing loss in patients with an enlarged vestibular aqueduct. *JAMA Otolaryngol Head Neck Surg* 2017;143:601–08 CrossRef Medline
- Egami T, Sando I, Black FO. Hypoplasia of the vestibular aqueduct and endolymphatic sac in endolymphatic hydrops. *Otolaryngology* 1978;86:ORL327–39 CrossRef Medline
- Hebbar GK, Rask-Andersen H, Linthicum FH. Three-dimensional analysis of 61 human endolymphatic ducts and sacs in ears with and without Meniere's disease. *Ann Otol Rhinol Laryngol* 1991;100:219–25 CrossRef Medline
- Krombach GA, van den Boom M, Di Martino E, et al. Computed tomography of the inner ear: size of anatomical structures in the normal temporal bone and in the temporal bone of patients with Meniere's disease. *Eur Radiol* 2005;15:1505–13 CrossRef Medline
- Maiolo V, Savastio G, Modugno GC, et al. Relationship between multidetector CT imaging of the vestibular aqueduct and inner ear pathologies. *Neuroradiol J* 2013;26:683–92 CrossRef Medline
- Basura GJ, Adams ME, Monfared A, et al. Clinical practice guideline: Ménière's disease. *Otolaryngol Head Neck Surg* 2020;162:S1–55 [PMC]CrossRef Medline
- Watanabe Y, Mizukoshi K, Shojaku H, et al. Epidemiological and clinical characteristics of Meniere's disease in Japan. *Acta Otolaryngol Suppl* 1995;519:206–10 CrossRef Medline
- Bächinger D, Luu NN, Kempfle JS, et al. Vestibular aqueduct morphology correlates with endolymphatic sac pathologies in Meniere's disease: a correlative histology and computed tomography study. *Otol Neurotol* 2019;40:e548–55 CrossRef Medline
- Bächinger D, Schuknecht B, Długaczky J, et al. Radiological configuration of the vestibular aqueduct predicts bilateral progression in Meniere's disease. *Front Neurol* 2021;12:674170 CrossRef Medline

Dynamic Contrast-Enhanced MRI Parameters and Normalized ADC Values Could Aid Differentiation of Skull Base Osteomyelitis from Nasopharyngeal Cancer

A. Baba, R. Kurokawa, M. Kurokawa, Y. Ota, and A. Srinivasan



ABSTRACT

BACKGROUND AND PURPOSE: The skull base osteomyelitis sometimes can be difficult to distinguish from nasopharyngeal cancer. This study aimed to investigate the differences between skull base osteomyelitis and nasopharyngeal cancer using dynamic contrast-enhanced MR imaging and normalized ADC values.

MATERIALS AND METHODS: This study included 8 and 12 patients with skull base osteomyelitis and nasopharyngeal cancer, respectively, who underwent dynamic contrast-enhanced MR imaging and DWI before primary treatment. Quantitative dynamic contrast-enhanced MR imaging parameters and ADC values of the ROIs were analyzed. Normalized ADC parameters were calculated by dividing the ROIs of the lesion by that of the spinal cord.

RESULTS: The rate transfer constant between extravascular extracellular space and blood plasma per minute (Kep) was significantly lower in patients with skull base osteomyelitis than in those with nasopharyngeal cancer (median, 0.43 versus 0.57; $P = .04$). The optimal cutoff value of Kep was 0.48 (area under the curve, 0.78; 95% CI, 0.55–1). The normalized mean ADC was significantly higher in patients with skull base osteomyelitis than in those with nasopharyngeal cancer (median, 1.90 versus 0.87; $P < .001$). The cutoff value of normalized mean ADC was 1.55 (area under the curve, 0.96; 95% CI, 0.87–1). The area under the curve of the combination of dynamic contrast-enhanced MR imaging parameters (Kep and extravascular extracellular space volume per unit tissue volume) was 0.89 (95% CI, 0.73–1), and the area under the curve of the combination of dynamic contrast-enhanced MR imaging parameters and normalized mean ADC value was 0.98 (95% CI, 0.93–1).

CONCLUSIONS: Quantitative dynamic contrast-enhanced MR imaging parameters and normalized ADC values may be useful in differentiating skull base osteomyelitis and nasopharyngeal cancer. The combination of dynamic contrast-enhanced MR imaging parameters and normalized ADC values outperformed each measure in isolation.

ABBREVIATIONS: AUC = area under the curve; DCE = dynamic contrast-enhanced; EES = extravascular extracellular space; K^{trans} = volume transfer constant between extravascular extracellular space and blood plasma per minute; Kep = rate transfer constant between EES and blood plasma per minute; $nADC_{mean}$ = normalized mean ADC; NPC = nasopharyngeal cancer; Ve = EES volume per unit tissue volume; Vp = plasma volume; SBO = skull base osteomyelitis

Skull base osteomyelitis (SBO) is a rare and potentially life-threatening infection of the skull base.¹ SBO is typically caused by an inadequately treated ear or paranasal infection in patients with diabetes, older age, or immune suppression.^{1–3} Mucosal pathology and biopsy culture are important approaches for the diagnosis of SBO, and diagnostic imaging has a complementary value when necessary to exclude the malignant potential.^{1,4,5} However,

SBO sometimes can be difficult to distinguish from malignancies clinically and radiologically, especially nasopharyngeal cancer (NPC). Radiologically, SBO may show masslike, asymmetric soft-tissue involvement, and NPC may show skull base involvement, making the diagnosis challenging. To date, there have been no reliable studies to differentiate SBO and NPC on MR imaging morphologic findings, and no imaging characteristics have been established to clearly distinguish these 2 diseases.⁶ There is only a report of the utility of ADC values in DWI in quantitatively differentiating SBO from malignancy,⁷ and the clinical utility and significance of this diagnostic method are noteworthy.

Dynamic contrast-enhanced MR imaging (DCE-MR imaging) is a contrast-enhanced perfusion imaging technique, and several quantitative parameters can be obtained on the basis of this technique. DCE-MR imaging has been used to differentiate neoplastic and non-neoplastic lesions,^{8,9} though the evidence for DCE-MR

Received August 11, 2022; accepted after revision November 15.

From the Division of Neuroradiology (A.B., R.K., M.K., Y.O., A.S.), Department of Radiology, University of Michigan, Ann Arbor, Michigan; and Department of Radiology (A.B.), The Jikei University School of Medicine, Tokyo, Japan.

Please address correspondence to Akira Baba, MD, PhD, Division of Neuroradiology, Department of Radiology, University of Michigan, 1500 E. Medical Center Dr, Ann Arbor, MI 48109; e-mail: akirababa0120@gmail.com

Indicates article with online supplemental data.

<http://dx.doi.org/10.3174/ajnr.A7740>

imaging in differentiating SBO from NPC has not been reported. This study aimed to evaluate the diagnostic performance for differentiating SBO and NPC using ADC and DCE-MR imaging parameters.

MATERIALS AND METHODS

We obtained our institutional review board exemption for this retrospective study from University of Michigan, and patient consent was waived. Data were acquired in compliance with all applicable Health Insurance Portability and Accountability Act regulations. All procedures followed were in accordance with the Helsinki Declaration of 1975, as revised in 2008. Data were deidentified before any analysis.

Patients

Consecutive patients diagnosed with SBO and NPC who underwent both pretreatment DCE-MR imaging and pretreatment DWI between December 2015 and February 2022 were included. All included patients were imaged using Ingenia and Achieva systems (Philips Healthcare). Patients were considered to have SBO if they had a clinical history suggestive of osteomyelitis, with pathologically proved inflammatory changes or culture-proved causative bacteria and improvement with subsequent treatment. As for SBO, we excluded 8 patients who had been previously treated with surgery or radiation therapy for tumors proximal to the skull base so that we could avoid encountering any overlap in imaging features between SBO and posttreatment changes in the same patient that would make the analysis difficult. All NPC cases were pathologically confirmed.

MR Imaging Acquisition

MR imaging examinations were performed using 1.5T ($n = 10$) and 3T ($n = 10$) MR imaging systems (Ingenia, Achieva; Philips Healthcare). DWI was performed with b-values of 0 and 1000 s/mm^2 and the following parameters: TR range, 3500–11,000 ms; TE range, 70–92 ms; number of excitations, 1–2; section thickness/gap, 4–6/0–1 mm; FOV, 225–255 \times 235–255 mm; matrix, 140–200 \times 130–200; and 3 diffusion directions. DCE-MR imaging was performed via 3D T1-weighted fast-field echo. Parameters for 3D T1-weighted fast-field echo were as follows: TR, 4.4–4.8 ms; TE, 2 ms; flip angles, 30°; section thickness/gap, 5/–2.5 mm; FOV, 240 \times 240 mm; matrix, 240 \times 240; number of excitations, 1; number of slices per dynamic scan, 48; temporal resolution, 8.8 seconds; total acquisition time, 4 minutes 24 seconds. An intravenous bolus of 20 mL of gadobenate dimeglumine contrast (MultiHance; Bracco Diagnostics) was administered through a peripheral arm vein using a power injector with a flow rate of 5.0 mL/s, followed by a 20-mL saline flush.

Data Analysis

The demographic characteristics, including age, sex, the presence of ear or paranasal sinus lesions, a history of diabetes mellitus, cranial nerve symptoms, pathology, causative culture bacteria, treatment method, and clinical course, of patients with SBO and the characteristics, including age, sex, pathology, and T classification, of patients with NPC were reviewed from the electronic medical records.

ADC Analysis

ADC maps were constructed by a monoexponential fitting model using OleaSphere (Version 3.0; Olea Medical). Two board-certified radiologists with 9 and 13 years of experience outlined 3 separate ROIs on the ADC maps, predominantly including the low-signal region while excluding cystic or necrotic regions from ROIs with consensus. Another ROI for ADC was placed as a reference in the spinal cord,¹⁰ which was seen in the same section imaging. ROI sizes ranged from 7 to 18 mm.² For each ROI, the normalized mean ADC ($\text{nADC}_{\text{mean}}$) was calculated by dividing the mean ADC by the reference mean ADC of the spinal cord. The $\text{nADC}_{\text{mean}}$ of 3 ROIs was averaged.

DCE Analysis

Quantitative DCE-MR imaging analysis was performed using OleaSphere (Version 3.0) on the basis of the extended Tofts model, by which pixel-based parameter maps are calculated from time-intensity curves. An arterial input function was calculated automatically using cluster analysis techniques, and deconvolution of the arterial input function was performed with a time-insensitive block-circulant singular-value decomposition.¹¹ The 2 board-certified radiologists with 9 and 13 years of experience outlined 3 separate ROIs in the lesions on permeability maps, predominantly including the enhancing components while excluding cystic or necrotic regions from the ROIs with consensus. The calculated quantitative vascular permeability parameters were as follows; extravascular extracellular space (EES), volume per unit tissue volume (V_e), fractional plasma volume (V_p), volume transfer constant between EES and blood plasma per minute (K^{trans}), and rate transfer constant between EES and blood plasma per minute (Kep).

Statistical Analyses

Shapiro-Wilk tests were performed to confirm the normality of distribution in each numeric parameter. The Mann-Whitney U test was used to compare DCE-MR imaging quantitative parameters (V_p , V_e , K^{trans} , Kep) and $\text{nADC}_{\text{mean}}$ between SBO and NPC. Two-sided P values $< .05$ were considered statistically significant. For parameters with 2-sided P values $< .20$, the optimal cutoff values in the receiver operating characteristics analysis were determined as values to maximize the Youden index (sensitivity + specificity – 1).¹² Diagnostic performances were calculated on the basis of the cutoff values. The area under the receiver operating characteristic curve of the combination parameters was calculated. All statistical analyses were performed using R statistical and computing software, Version 3.6.1 (<http://www.r-project.org/>).

RESULTS

Patients

In this study, 20 patients were included, 8 and 12 of whom had SBO and NPC, respectively. Patients' demographic and clinical data are summarized in Online Supplemental Data and Table 1.

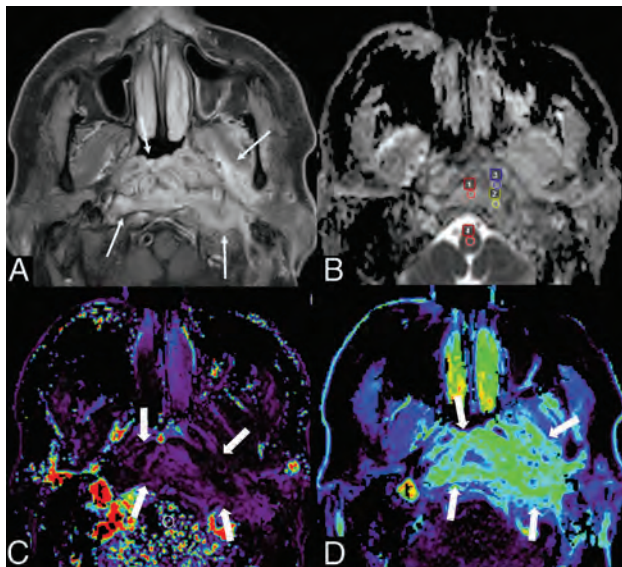
Half of the patients with SBO had ear lesions, followed by sinus lesions. All patients with SBO had diabetes mellitus. Many patients with SBO presented with cranial nerve symptoms, with cranial nerve XII symptoms being the most common. Cultured causative bacteria of SBO were *Pseudomonas aeruginosa*, *Staphylococcus aureus*, and culture-negative.

Table 1: Demographic and clinical information of nasopharyngeal cancer

Clinical Information	
Demographic	
Sex	Male = 8, female = 4
Median age (range) (yr)	52.5 (36–69)
Clinical	
Pathology	
Squamous cell carcinoma	12/12 (100.0%)
T classification	
T1	2/12 (16.7%)
T2	5/12 (41.7%)
T3	2/12 (16.7%)
T4	3/12 (25.0%)

Table 2: DCE-MR imaging and ADC parameters^a

DCE Parameters	SBO	Nasopharyngeal Cancer	P Value
Ve	0.48 (0.36–0.55)	0.38 (0.14–0.63)	.15
Vp	0.14 (0.04–2.36)	0.12 (0.05–0.26)	.99
K^{trans} (min^{-1})	0.20 (0.15–0.39)	0.28 (0.06–1.42)	.51
Kep (min^{-1})	0.43 (0.31–0.48)	0.57 (0.31–3.70)	.04 ^b
ADC value	1.48 (1.14–1.84)	0.69 (0.55–1.39)	<.001 ^b
Reference ADC	0.79 (0.54–0.94)	0.81 (0.73–0.90)	.39
nADC _{mean}	1.90 (0.61–2.48)	0.87 (0.61–1.90)	<.001 ^b

^a Data are median and range.^b Statistically significant.**FIG 1.** A case of SBO in a 68-year-old man. Postcontrast fat-suppressed T1-weighted image (A) shows ill-defined enhancement in the nasopharynx, prevertebral space, left parapharyngeal space, and left masticator space (arrows). The ADC map (B) shows 3 ROIs (Nos. 1–3, small circles) within high-signal lesion and 1 ROI (No. 4, small circle) for reference in the spinal cord, with an nADC_{mean} of 1.86. DCE-MR imaging (C, Kep map; D, Ve map) shows the lesion (thick arrows) with a Kep of 0.42 minute⁻¹ and Ve of 0.54.**DCE-MR Imaging and ADC Parameters**

The results of DCE-MR imaging and ADC analyses are summarized in Table 2. A pulsed input pattern was observed in the arterial input function curves in all patients. Kep was significantly lower in patients with SBO than in those with NPC ($P = .04$). The optimal

cutoff value of Kep was 0.48 (area under the curve [AUC], 0.78; 95% CI, 0.55–1), and that of Ve was 0.43 (AUC, 0.70; 95% CI, 0.45–0.95). The nADC_{mean} was significantly higher in patients with SBO than in those with NPC ($P < .001$). The optimal cutoff value of the nADC_{mean} was 1.55 (AUC, 0.96; 95% CI, 0.87–1). Representative MR images of SBO and NPC are demonstrated in Figs 1 and 2. The AUC of the combination of DCE-MR imaging parameters (Kep and Ve) was 0.89 (95% CI, 0.73–1), and the AUC of the combination of DCE-MR imaging parameters and the nADC_{mean} was 0.98 (95% CI, 0.93–1). The decision tree in differentiating SBO and NPC is shown in Fig 3.

DISCUSSION

This study evaluated the characteristics and differences in the quantitative parameters from DCE-MR imaging and normalized ADC values in DWI between SBO and NPC. Kep and nADC_{mean} showed significant differences between SBO and NPC. The combined Kep and Ve and the nADC_{mean} had a remarkably high AUC of 0.98 for differentiating SBO and NPC.

SBO is typically associated with an improperly treated ear or paranasal sinus infections in older patients with diabetes or those who are immunocompromised.^{1–3} Previous studies have reported a high incidence of ear and paranasal sinus complications,^{2,13} and in the present study, ear (50%) and paranasal sinus (25%) lesions were identified. Approximately half of the patients had histories of diabetes,^{1,2,13} and all patients in the current study had diabetes. Cranial nerve symptoms were observed in 57%–83% of patients^{1,2} and were noted in many patients in the present study (75%). *P. aeruginosa* and *S aureus* have been reported as the major causative pathogens,^{1,2,13} and the results were similar in the present study.

Mucosal pathology and biopsy culture are important clinical approaches in the diagnosis of SBO. However, when pathology results are false-negative or inconclusive, when cultures are negative, or when disease persists despite appropriate antibiotic therapy, it is clinically important to rule out malignant possibilities, including nasopharyngeal cancer.^{1,4,5} Additionally, diagnostic imaging with MR imaging has clinical value in providing complementary assistance for ruling these out.^{1,4,5}

SBO is associated with cranial nerve symptoms such as dysphagia and facial paralysis, which can clinically mimic a malignant tumor of the skull base.⁶ Therefore, the biopsy and culture described above are essential to differentiate SBO from malignant lesions,¹⁴ and more alarming, there are culture-negative SBO cases.^{15–17} These clinical challenges often delay the diagnosis of SBO.^{2,18} In addition, radiological imaging plays an important role in establishing a diagnosis, estimating disease extent, and monitoring the treatment response of SBO,¹⁹ which can sometimes clinically mimic malignancy by presenting masslike and asymmetric soft-tissue infiltrates, making the diagnosis difficult.^{2,3,6,14,15,20} Therefore, identifying quantitative imaging indicators to diagnose SBO radiologically is important.

DWI is a noninvasive MR imaging sequence used to visualize changes in the motion of water molecules and is a surrogate marker of cell density. The ADC value, a parameter calculated from DWI, has been useful in distinguishing benign from malignant head and neck tumors and in distinguishing recurrence

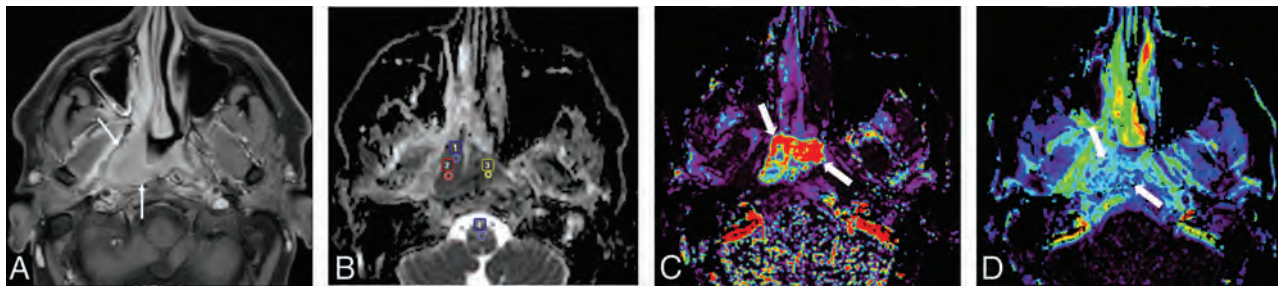


FIG 2. A case of nasopharyngeal cancer in a 37-year-old man. A mass lesion with enhancement (arrows) mainly on the right side of the nasopharynx is observed on the postcontrast fat-suppressed T1-weighted image (A). An ADC map (B) shows 3 ROIs (Nos. 1–3, small circles) within a low-signal lesion and 1 ROI (No. 4, small circle) for reference in the spinal cord, with an $nADC_{mean}$ of 0.86. DCE-MR imaging (C, Kep map; D, Ve map) shows the lesion (thick arrows) with a Kep of 3.14 minute^{-1} and a Ve of 0.36.

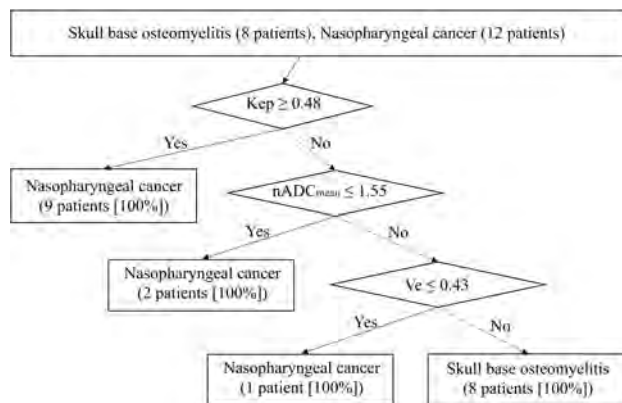


FIG 3. The decision tree model incorporating DCE parameters (Kep and Ve) and the $nADC_{mean}$.

from posttreatment changes of head and neck cancers.^{21,22} Ozgen et al⁷ reported the utility of ADC values in differentiating SBO from skull base malignancies. The study showed that SBO had significantly higher ADC values compared with skull base malignancies (mean ADC value, 1.26 versus 0.75 [NPC], 0.59 [malignant lymphoma], and 0.99 [metastasis] $\times 10^{-3} \text{ mm}^2$) and a cutoff value of $1.08 \times 10^{-3} \text{ mm}^2$ with a sensitivity of 0.89, specificity of 0.86, and accuracy of 0.86.⁷

Because absolute ADC values can vary from scanner to scanner on the basis of the model and Tesla strength, we attempted to reduce this variability by normalizing the lesion ADC value with an internal standard, in this case the spinal cord ADC. In the present study, SBO showed significantly higher normalized ADC values than NPC, with a sensitivity of 0.92, specificity of 1.00, and AUC of 0.96 when the cutoff value was set at 1.55, indicating high diagnostic performance. As in the previous report, normalized ADC is also useful for diagnosing both. Normalization of ADC is considered valuable for correcting for age and intermodel differences.^{12,23} In addition, there has been no study investigating the use of normalized ADC values in DWI in differentiating SBO from NPC.

DCE-MR imaging has been used to differentiate neoplastic and non-neoplastic pathologies using its quantitative and semi-quantitative parameters.^{8,9} However, the diagnostic role of DCE-MR imaging in differentiating SBO and malignancies is unknown. In the present study, the combined AUC of Kep and Ve was 0.89.

Furthermore, the combination of DCE-MR imaging parameters and the $nADC_{mean}$ showed a remarkably high AUC value of 0.98. DCE-MR imaging parameters and $nADC_{mean}$ are quantitative information that can be obtained during a single MR imaging procedure, and the combined evaluation of these parameters and their clinical application might be beneficial to patients.

The present study has some limitations. This was a single-center, retrospective study with a small number of patients. Future studies with a larger number of patients are warranted.

CONCLUSIONS

The combination of quantitative DCE-MR imaging parameters and normalized ADC values showed high diagnostic performance and may be useful in differentiating SBO and NPC. The combination of DCE-MR imaging parameters and normalized ADC values outperformed each measure in isolation.

Disclosure forms provided by the authors are available with the full text and PDF of this article at www.ajnr.org.

REFERENCES

- Johnson AK, Batra PS. Central skull base osteomyelitis: an emerging clinical entity. *Laryngoscope* 2014;124:1083–87 CrossRef Medline
- Álvarez Jáñez F, Barriga LQ, Iñigo TR, et al. Diagnosis of skull base osteomyelitis. *Radiographics* 2021;41:156–74 CrossRef Medline
- Chang PC, Fischbein NJ, Holliday RA. Central skull base osteomyelitis in patients without otitis externa: imaging findings. *AJNR Am J Neuroradiol* 2003;24:1310–16 Medline
- Khan M, Quadri S, Kazmi A, et al. A comprehensive review of skull base osteomyelitis: diagnostic and therapeutic challenges among various presentations. *Asian J Neurosurg* 2018;13:959–70 CrossRef Medline
- Auinger AB, Dahm V, Stanisz I, et al. The challenging diagnosis and follow-up of skull base osteomyelitis in clinical practice. *Eur Arch Otorhinolaryngol* 2021;278:4681–88 CrossRef Medline
- van Kroonenburgh AM, van der Meer WL, Bothof RJ, et al. Advanced imaging techniques in skull base osteomyelitis due to malignant otitis externa. *Curr Radiol Rep* 2018;6:3 CrossRef Medline
- Ozgen B, Oguz KK, Cila A. Diffusion MR imaging features of skull base osteomyelitis compared with skull base malignancy. *AJNR Am J Neuroradiol* 2011;32:179–84 CrossRef Medline
- Morabito R, Alafaci C, Pergolizzi S, et al. DCE and DSC perfusion MRI diagnostic accuracy in the follow-up of primary and metastatic intra-axial brain tumors treated by radiosurgery with CyberKnife. *Radiat Oncol* 2019;14:65 CrossRef Medline
- Albano D, Bruno F, Agostini A, et al; the Young SIRM Working Group. Dynamic contrast-enhanced (DCE) imaging: state of the art

- and applications in whole-body imaging. *Jpn J Radiol* 2022;40:341–66 CrossRef Medline
10. Koontz NA, Wiggins RH. **Differentiation of benign and malignant head and neck lesions with diffusion tensor imaging and DWI.** *AJR Am J Roentgenol* 2017;208:1110–15 CrossRef Medline
 11. Mouridsen K, Christensen S, Gyldensted L, et al. **Automatic selection of arterial input function using cluster analysis.** *Magn Reson Med* 2006;55:524–31 CrossRef Medline
 12. Kurokawa R, Kurokawa M, Baba A, et al. **Dynamic susceptibility contrast-MRI parameters, ADC values, and the T2-FLAIR mismatch sign are useful to differentiate between H3-mutant and H3-wild-type high-grade midline glioma.** *Eur Radiol* 2022;32:3672–82 CrossRef Medline
 13. Prasad SC, Prasad KC, Kumar A, et al. **Osteomyelitis of the temporal bone: terminology, diagnosis, and management.** *J Neurol Surg B Skull Base* 2014;75:324–31 CrossRef Medline
 14. Singhal A, Sotoudeh H, Chapman PR. **Skull base osteomyelitis imaging.** *Curr Opin Otolaryngol Head Neck Surg* 2021;29:333–41 CrossRef Medline
 15. See A, Tan TY, Gan EC. **Atypical culture-negative skull base osteomyelitis masquerading as advanced nasopharyngeal carcinoma.** *Am J Otolaryngol* 2016;37:236–39 CrossRef Medline
 16. Sokołowski J, Lachowska M, Karchier E, et al. **Skull base osteomyelitis: factors implicating clinical outcome.** *Acta Neurol Belg* 2019;119:431–37 CrossRef Medline
 17. Spielmann PM, Yu R, Neeff M. **Skull base osteomyelitis: current microbiology and management.** *J Laryngol Otol* 2013;127(127 Suppl 1):8–12 CrossRef Medline
 18. Mahdyoun P, Pulcini C, Gahide I, et al. **Necrotizing otitis externa: a systematic review.** *Otol Neurotol* 2013;34:620–29 CrossRef Medline
 19. Vaidyanathan S, Lingam RK. **Imaging of acute and chronic skull base infection.** *Neuroimaging Clin N Am* 2021;31:571–98 CrossRef Medline
 20. Ganheva AD, Kuthubutheen J. **A diagnostic dilemma of central skull base osteomyelitis mimicking neoplasia in a diabetic patient.** *BMJ Case Rep* 2013;2013:bcr2012007183 CrossRef
 21. Surov A, Meyer HJ, Wienke A. **Apparent diffusion coefficient for distinguishing between malignant and benign lesions in the head and neck region: a systematic review and meta-analysis.** *Front Oncol* 2019;9:1362 CrossRef Medline
 22. Baba A, Kurokawa R, Kurokawa M, et al. **ADC for differentiation between posttreatment changes and recurrence in head and neck cancer: a systematic review and meta-analysis.** *AJNR Am J Neuroradiol* 2022;43:442–47 CrossRef Medline
 23. Ding X, Xu H, Zhou J, et al. **Reproducibility of normalized apparent diffusion coefficient measurements on 3.0-T diffusion-weighted imaging of normal pancreas in a healthy population.** *Medicine (Baltimore)* 2019;98:e15104 CrossRef Medline

Subtle Malformation of the Cochlear Apex and Genetic Abnormalities: Beyond the “Thorny” Cochlea

F. D’Arco, A. Biswas, E. Clement, K. Rajput, and A.F. Juliano

ABSTRACT

SUMMARY: With the routine use of high-resolution heavily T2-weighted sequences to evaluate patients with hearing deficits, new, subtle phenotypes of cochlear malformations are being discovered and an increasing number of genotype-phenotype correlations are being found through a reverse phenotype approach, which can help guide geneticists. In this brief report, we present subtle malformations of the apical turn of the cochlea related to 3 genetic mutations, emphasizing the importance of a careful assessment of the cochlear apex.

ABBREVIATIONS: BOR = branchio-oto-renal syndrome; DEGCAGS = DEvelopmental delay with Gastrointestinal, Cardiovascular, Genitourinary, and Skeletal abnormalities; IAC = internal auditory canal; SNHL = sensorineural hearing loss

With the use of high-resolution sequences in MR imaging assessment of patients with congenital sensorineural hearing loss (SNHL), newer phenotypes of cochlear malformations have been described, including several types of cochlear hypoplasias.^{1,2} There is increasing recognition that specific radiologic appearances of the cochlea and temporal bone may be associated with specific syndromes or genetic mutations.^{3–6} Thus, an imaging phenotype can suggest an underlying genotype, contributing to clinical and genetic work-up of the patient.

The normal cochlea has an apical turn that is smooth in contour and evenly tubular throughout its length. The apex (following the basal and middle turns) typically spans 180°–270° around the center point, resulting in a cochlea with 2.5–2.75 turns total.⁷

Here, we describe subtle malformations of the apical aspect of the cochlea in 5 patients with 3 different genetic abnormalities and cochleovestibular symptoms; these apical malformations were chosen among the authors by consensus. The patients were selected from the Great Ormond Street Hospital database of dysplastic cochleae. We retrospectively reviewed the database for all cases that involved an anomaly in the apical

turn, yielding these 5 cases. All these cases had genetic diagnoses available. We describe possible genetic mechanisms that may cause apical turn anomalies, and emphasize the importance of not overlooking such subtle cochlear abnormalities.

CASE SERIES

TKFC-Related Disorder

A 7-year-old patient known to have a biallelic mutation in the *TKFC* gene (Mendelian Inheritance in Man, 618805), with congenital cataracts, microphthalmia, and developmental delay, underwent MR imaging of the brain and inner ear/internal auditory canal (IAC) for balance difficulties and hypersensitivity to loud and sudden noises without hearing loss.

MR imaging of the brain demonstrated bilateral cataracts and cerebellar atrophy. A high-resolution 3D heavily T2-weighted sequence of the IAC revealed symmetric subtle cochlear abnormality characterized by a peculiar appearance of the upper part of the cochlea with an extra half-turn beyond the apical turn, resulting in >3 turns total (Fig 1A).⁷ The apical turn and the extra half-turn were not pointed but were smooth and flat like a normal apical turn. The cochlear height, measured in accordance with described methods in the literature (Fig 1B), was 6 mm (above the normal range of 4.3–5.4 mm).^{8,9} The cochleovestibular nerves were present and normal in course and caliber. The other inner ear structures were normal as well, including preserved internal partitioning of both cochleae.

Presumed DEGCAGS Syndrome (*ZNF699* Gene)

A 7-month-old boy with a homozygous variant of unknown significance in the *ZNF699* gene (presumed diagnosis of DEvelopmental

Received August 11, 2022; accepted after revision November 15.

From the Departments of Radiology (F.D., A.B.), Clinical Genetics (E.C.), and Audiological Medicine (K.R.), Great Ormond Street Hospital for Children, National Health Service Foundation Trust, London, UK; and Department of Radiology (A.F.J.), Massachusetts Eye and Ear, Harvard Medical School, Boston, Massachusetts.

Please address correspondence to Amy F. Juliano, MD, Department of Radiology, Massachusetts Eye and Ear, 243 Charles St, Boston, MA 02114; e-mail: amy_juliano@meei.harvard.edu; @amyfjuliano

<http://dx.doi.org/10.3174/ajnr.A7746>



FIG 1. A, High-resolution 3D heavily T2-weighted MR images of the inner ear and IAC in a patient with a *TKFC*-related disorder. There is an extra turn (arrows) at the apical portion of the cochlea beyond the usual apical turn and an overall greater cochlear height. The cochlear nerves are present, the modiolus is normal in appearance, and there is normal internal partitioning. Contrast this appearance with that of the normal cochlear apical turn seen in Fig 3B, without an extra turn beyond it. B, Coronal CT image through the cochlea shows the method to measure cochlear height as defined by Shim et al.⁸ The maximal height of the cochlea is measured along an axis perpendicular to the oval window (white line).

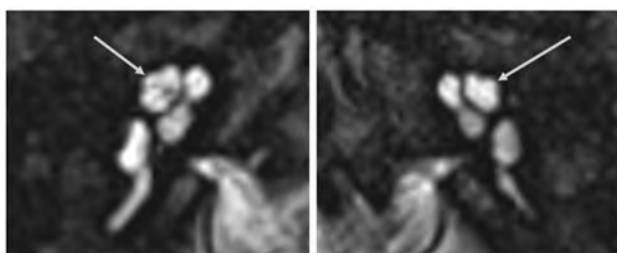


FIG 2. High-resolution 3D heavily T2-weighted MR images of the inner ear and IAC in a patient with a *ZNF699* gene mutation. The uppermost turn of the cochlear apex following the middle turn has a short and stumpy shape (arrows).

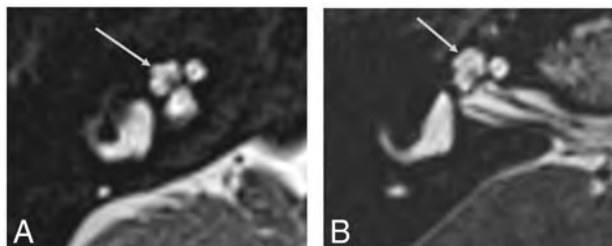


FIG 3. High-resolution 3D heavily T2-weighted MR image of a typical *SIX1*-BOR protuberant "thorny" tip of the cochlea (arrow in A) in comparison with a healthy control in whom the apical turn is uniform and relatively flat and tubular (arrow in B).

delay with Gastrointestinal, Cardiovascular, Genitourinary, and Skeletal abnormalities [DEGCAGS] syndrome [Mendelian Inheritance in Man, 619488]) presented with bilateral profound SNHL. He also had developmental delay, atrial septal defect, dysmorphic features, and congenital clavicle deformity.

MR imaging of the IAC was performed to investigate the hearing loss. It demonstrated bilateral abnormality of the apical turn of the cochlea, very similar to the "thorny" cochlea described by Pao et al,¹⁰ in relation to *SIX1* mutation in branchio-oto-renal syndrome (BOR). The cochlear apex was irregular, with a short, stumplike shape (Fig 2). There was mild hypoplasia of the cochlear nerve on the left, but otherwise the inner ear structures were normal bilaterally. The cochlear height was 5.8 and 5.7 mm on the right and left, respectively.

SIX1-Related BOR

Searching our institutional archive for genetic malformations, we found, among patients with a genetic diagnosis of BOR syndrome, 3 patients with confirmed *SIX1* mutation. Five of these 6 cochleae showed a characteristic "thorny" apical turn, with a small, pointed protuberant appearance (Fig 3). These patients presented with SNHL and other clinical abnormalities expected in BOR due to a *SIX1* genetic mutation (ie, otic and branchial defects consistently seen, renal defects variably seen, and less prevalent than among individuals with BOR related to an *EYA1* genetic muta-

tion).¹¹ Two of them were previously included in the study by Pao et al.¹⁰

DISCUSSION

All patients included in this case series presented with labyrinthine symptoms (4 with SNHL and 1 with balance difficulties and sound hypersensitivity) and very subtle malformations of the cochlear apical turn, which were overlooked by the reporting radiologists in 3 of the 5 cases.

The genetics of inner ear development are not completely understood, but we know that, at some point during embryologic development, genes polarize toward the cochlear (ventral) or vestibulocanalicular (dorsal) components of the otic capsule.¹² It is also clear, from radiologic studies of cochleae fitting the description of the so-called cochlear hypoplasia type 4 anomaly, that the basal turn of the cochlea may be relatively preserved while the middle and apical turns are more affected.¹³ Indeed, this is the case in the "unwound" cochlea in patients with BOR^{14,15} and in the extreme hypoplastic cochlea in patients with Walker-Warburg syndrome.⁴

In patients with BOR, both *EYA1* and *SIX1* are expressed in the ventral (cochlear) part of the developing otic vesicle, but the expression of *SIX1* is dependent on that of *EYA1*, and its expression is more prominent in the cochlear apex in murine models.^{10,16} This accounts for the different phenotypes seen among patients with BOR with mutations in the *EYA1* versus the *SIX1* gene, with only the apex being malformed in those with *SIX1* mutations.

Although the role of the *TKFC* gene in ear development has not been reported, patients with this mutation may have progressive low-frequency hearing impairment.¹⁷ This specific type of hearing loss may be explained by morphologic abnormalities in the cochlear apex, which allows hearing of low pitches. In fact, the role of the shape of the apical cochlea has been correlated, in a comparative study among different species, with low-frequency hearing limits.¹⁸ Our case of *TKFC*-related disorder represents an example of clinicoradiologic correlation that can shed light on previously unknown functions of specific genes in ear development, including rare genetic mutations that lead to multisystemic abnormalities.

DEGCAGS syndrome is due to an autosomal recessive mutation in the *ZNF699* gene and is characterized by neurodevelopmental

delay, abnormal facial features, growth delay, syndactyly/polydactyly, and anemia/pancytopenia.¹⁹ This gene encodes for a nuclear zinc-finger protein with a possible function in nucleic acid binding.²⁰ Little is known about the role of this gene, but patients described with this syndrome have SNHL as a constant symptom.¹⁹ It is, therefore, likely that the cause of the SNHL is related to a specific role of this gene in the development of the apical part of the cochlea. Again, the reverse phenotyping approach in this case can help define as yet suboptimally understood gene functions.

CONCLUSIONS

Subtle abnormalities of the inner ears, particularly those involving the apical part of the cochlea, can be easily overlooked, even with the use of optimal 3D high-resolution heavily-T2-weighted sequences on a 3T MR imaging scanner. We described 5 patients with 3 genetic abnormalities, all characterized by labyrinthine symptoms and malformation of the apical aspect of the cochlea and otherwise normal inner ear anatomy. These findings correlate with clinical symptoms of hearing impairment and shed light on the role of rare genetic abnormalities in inner ear development. A diligent search for these at-times subtle findings must be conducted, especially in cases of MR imaging of the IAC with seemingly negative findings in symptomatic patients.

This report adds to the growing evidence of genotype-phenotype correlation between syndromic and/or congenital deafness and anomaly of the cochlear apex in children.

Disclosure forms provided by the authors are available with the full text and PDF of this article at www.ajnr.org.

REFERENCES

1. Sennaroglu L. Histopathology of inner ear malformations: do we have enough evidence to explain pathophysiology? *Cochlear Implants Int* 2016;17:3–20 CrossRef Medline
2. Quirk B, Youssef A, Ganau M, et al. Radiological diagnosis of the inner ear malformations in children with sensorineural hearing loss. *BJR Open* 2019;1:20180050 CrossRef Medline
3. Siddiqui A, D'Amico A, Colafati GS, et al. Hypothalamic malformations in patients with X-linked deafness and incomplete partition type 3. *Neuroradiology* 2019;61:949–52 CrossRef Medline
4. Talenti G, Robson C, Severino MS, et al. Characteristic cochlear hypoplasia in patients with Walker-Warburg syndrome: a radiologic study of the inner ear in α -dystroglycan-related muscular disorders. *AJNR Am J Neuroradiol* 2021;42:167–72 CrossRef Medline
5. D'Arco F, Sanverdi E, O'Brien WT, et al. The link between inner ear malformations and the rest of the body: what we know so far about genetic, imaging and histology. *Neuroradiology* 2020;62:539–44 CrossRef Medline
6. D'Arco F, Youssef A, Ioannidou E, et al. Temporal bone and intracranial abnormalities in syndromic causes of hearing loss: an updated guide. *Eur J Radiol* 2020;123:108803 CrossRef Medline
7. Biedron S, Westhofen M, Ilgner J. On the number of turns in human cochleae. *Otol Neurotol* 2009;30:414–17 CrossRef Medline
8. Shim HJ, Shin JE, Chung JW, et al. Inner ear anomalies in cochlear implantees: importance of radiologic measurements in the classification. *Otol Neurotol* 2006;27:831–37 CrossRef Medline
9. D'Arco F, Talenti G, Lakshmanan R, et al. Do measurements of inner ear structures help in the diagnosis of inner ear malformations? A review of literature. *Otol Neurotol* 2017;38:e384–92 CrossRef Medline
10. Pao J, D'Arco F, Clement E, et al. Re-examining the cochlea in branchio-oto-renal syndrome: genotype-phenotype correlation. *AJNR Am J Neuroradiol* 2022;43:309–14 CrossRef Medline
11. Ruf RG, Xu PX, Silvius D, et al. SIX1 mutations cause branchio-oto-renal syndrome by disruption of EYA1-SIX1-DNA complexes. *Proc Natl Acad Sci U S A* 2004;101:8090–95 CrossRef Medline
12. Chatterjee S, Kraus P, Lufkin T. A symphony of inner ear developmental control genes. *BMC Genet* 2010;11:68 CrossRef Medline
13. Talenti G, Manara R, Brotto D, et al. High-resolution 3 T magnetic resonance findings in cochlear hypoplasias and incomplete partition anomalies: a pictorial essay. *Br J Radiol* 2018;91:20180120 CrossRef Medline
14. Hsu A, Desai N, Paldino MJ. The unwound cochlea: a specific imaging marker of branchio-oto-renal syndrome. *AJNR Am J Neuroradiol* 2018;39:2345–49 CrossRef Medline
15. Robson CD. Congenital hearing impairment. *Pediatr Radiol* 2006;36:309–24 CrossRef Medline
16. Zheng W, Huang L, Wei ZB, et al. The role of Six1 in mammalian auditory system development. *Development* 2003;130:3989–4000 CrossRef Medline
17. Wortmann SB, Meunier B, Mestek-Boukhibar L, et al. Bi-allelic variants in TKFC encoding trikinase/FMN cyclase are associated with cataracts and multisystem disease. *Am J Hum Genet* 2020;106:256–63 CrossRef Medline
18. Manoussaki D, Chadwick RS, Ketten DR, et al. The influence of cochlear shape on low-frequency hearing. *Proc Natl Acad Sci U S A* 2008;105:6162–66 CrossRef Medline
19. Bertoli-Avella AM, Kandaswamy KK, Khan S, et al. Combining exome/genome sequencing with data repository analysis reveals novel gene-disease associations for a wide range of genetic disorders. *Genet Med* 2021;23:1551–68 CrossRef Medline
20. Scholz H, Franz M, Heberlein U. The hangover gene defines a stress pathway required for ethanol tolerance development. *Nature* 2005;436:845–47 CrossRef Medline

Development of Gestational Age–Based Fetal Brain and Intracranial Volume Reference Norms Using Deep Learning

C.B.N. Tran, P. Nedelec, D.A. Weiss, J.D. Rudie, L. Kini, L.P. Sugrue, O.A. Glenn, C.P. Hess, and A.M. Rauschecker



ABSTRACT

BACKGROUND AND PURPOSE: Fetal brain MR imaging interpretations are subjective and require subspecialty expertise. We aimed to develop a deep learning algorithm for automatically measuring intracranial and brain volumes of fetal brain MRIs across gestational ages.

MATERIALS AND METHODS: This retrospective study included 246 patients with singleton pregnancies at 19–38 weeks gestation. A 3D U-Net was trained to segment the intracranial contents of 2D fetal brain MRIs in the axial, coronal, and sagittal planes. An additional 3D U-Net was trained to segment the brain from the output of the first model. Models were tested on MRIs of 10 patients (28 planes) via Dice coefficients and volume comparison with manual reference segmentations. Trained U-Nets were applied to 200 additional MRIs to develop normative reference intracranial and brain volumes across gestational ages and then to 9 pathologic fetal brains.

RESULTS: Fetal intracranial and brain compartments were automatically segmented in a mean of 6.8 (SD, 1.2) seconds with median Dices score of 0.95 and 0.90, respectively (interquartile ranges, 0.91–0.96/0.89–0.91) on the test set. Correlation with manual volume measurements was high (Pearson $r = 0.996$, $P < .001$). Normative samples of intracranial and brain volumes across gestational ages were developed. Eight of 9 pathologic fetal intracranial volumes were automatically predicted to be >2 SDs from this age-specific reference mean. There were no effects of fetal sex, maternal diabetes, or maternal age on intracranial or brain volumes across gestational ages.

CONCLUSIONS: Deep learning techniques can quickly and accurately quantify intracranial and brain volumes on clinical fetal brain MRIs and identify abnormal volumes on the basis of a normative reference standard.

ABBREVIATIONS: GA = gestational age; IQR = interquartile range; SS-FSE = single-shot fast spin-echo

In vivo fetal imaging, modalities such as ultrasonography and MR imaging, plays a central role in the assessment of fetal health and development during pregnancy. Fetal ultrasonography¹ and MR imaging have complementary strengths, with MR imaging

less limited by factors such as oligohydramnios, challenging fetal presentation, or acoustic shadowing from the ossifying calvaria.² MR imaging can also provide superior anatomic detail, which is an important consideration when assessing potential abnormalities of some fetal structures, especially in the fetal brain.³ Thus, fetal brain MR imaging is performed in pregnant patients as early as 18 weeks of gestational age (GA), often after an anomaly is suspected on sonography, to provide further clarification for clinical management.⁴ Fetal brain MR imaging is rapidly growing as a standard imaging technique for informing management decisions.

However, interpretation of fetal brain MR imaging remains a substantial challenge. Radiologic evaluation of fetal MR imaging is largely subjective and requires a high level of subspecialty expertise for consistent and accurate interpretation. Quantitative analysis is generally limited to 1D biometric measurements such as cerebral biparietal diameter or the transverse diameter of the

Received June 21, 2022; accepted after revision November 4.

From the Department of Radiology & Biomedical Imaging, University of California, San Francisco, San Francisco, California.

C.B.N. Tran and P. Nedelec contributed equally to this manuscript (co-first authors).

The project described was supported by the Radiological Society of North America's Research & Education Foundation, through a Carestream Health/Radiological Society of North America Research Scholar Grant (A.M.R.).

The content is solely the responsibility of the authors and does not necessarily represent the official views of the Radiological Society of North America's Research & Education Foundation.

Please address correspondence to Andreas M. Rauschecker, MD, PhD, Department of Radiology & Biomedical Imaging, University of California, San Francisco, 513 Parnassus Ave, Room S-261, Box 0628, San Francisco, CA 94143-0628; e-mail: andreas.rauschecker@ucsf.edu; @DrDreMDPhD

Indicates open access to non-subscribers at www.ajnr.org

<http://dx.doi.org/10.3174/ajnr.A7747>

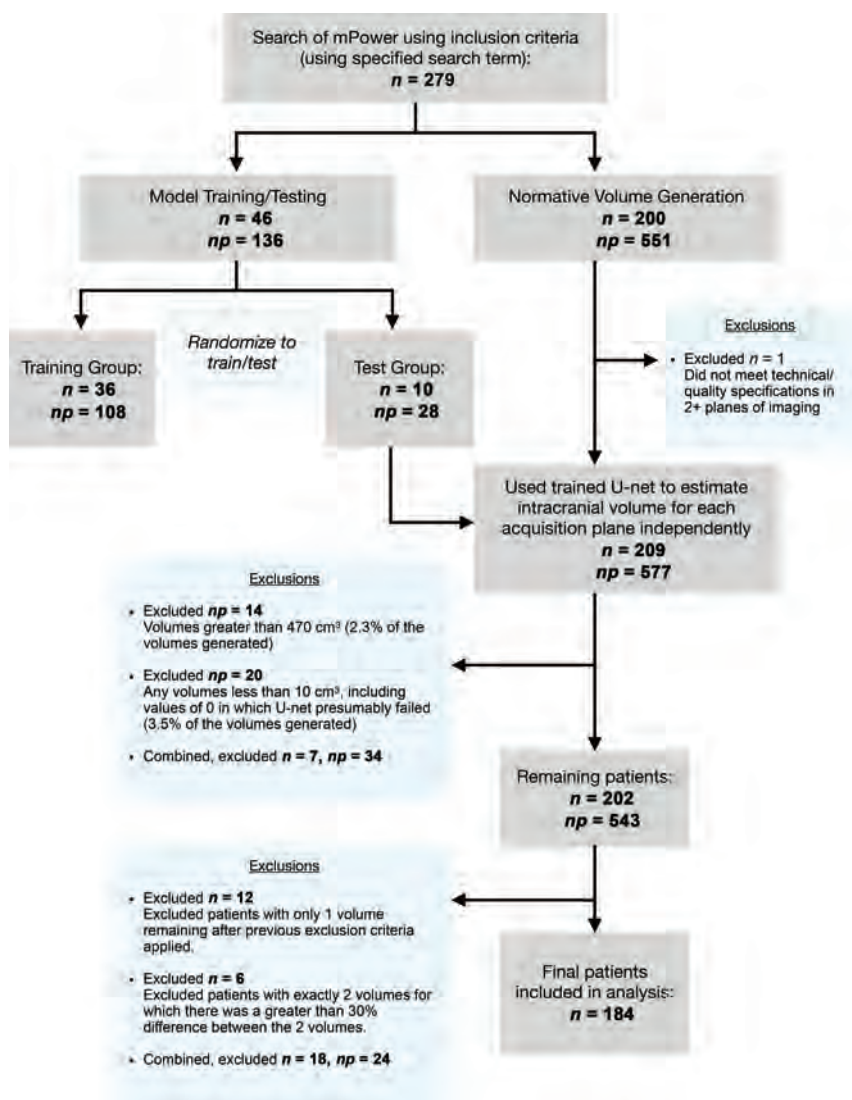


FIG 1. Flow chart shows study subject selection per exclusion criteria, from initial patient search to training set and test set randomization and development of a normative volume data set. *n* indicates the number of patients; *np*, number of planes of imaging.

atria of the lateral ventricles.^{5,6} Such manual measurements are performed as single linear measurements of 3D structures and are inherently subjective and prone to error.

While methods exist for quantitative evaluation of fetal MR imaging,^{7,8} including a normative atlas of the fetal brain,⁹ these methods typically use atlas-based segmentation techniques. Such techniques are well-suited for research questions but have limited clinical utility due to long processing times (hours) and frequent failure of segmentation in clinical cases that involve anatomic abnormalities.

Conversely, automated deep learning-based segmentation methods have the potential to consistently and objectively evaluate individual fetal intracranial and brain volumes in seconds. In particular, the U-Net architecture has proved highly effective for other biomedical segmentation tasks.^{10,11} Obtaining quantitative estimates of intracranial/brain volume and deviations from normative data via automated deep learning methods

would represent a major advancement in objective clinical and large-scale research assessments of fetal MR imaging.

We sought to develop a deep learning-based method for automated fetal brain MR imaging segmentation and volume quantification from single-shot fast spin-echo (SS-FSE) T2-weighted MRIs. Given the clinical relevance of fetal intracranial and brain volumes, analogous to routine 2D thecal and cerebral biparietal diameter measurements, our proof-of-concept study was specifically aimed at developing a method for fast and accurate measurement of these 3D volumes. Our ultimate goal was to apply the method to a large clinical population of fetal brain MRIs with normal findings to develop a normative reference for intracranial and brain volumes across a wide range of GAs.

MATERIALS AND METHODS

Definitions

Intracranial volume is defined as total volume within the cranium, including the brain, meninges, and CSF within the subarachnoid spaces and ventricles. Brain volume is defined as the combined volume of the brain parenchyma and ventricles. These 3D volume measurements are analogous to 2D thecal and cerebral biparietal/fronto-occipital diameters, which are currently used in clinical practice.

Patient and Data Selection

This retrospective study was approved by the institutional review board of the University of California, San Francisco, with a waiver of informed consent based on minimal risk. Included were a total of 246 study patients (ages, 16–45 years; median age, 33) who underwent fetal MRIs (SS-FSE T2WI) between 1999 and 2021.

Patients were identified by searching radiology reports in the institutional radiology archives (mPower; Nuance Communications). Inclusion criteria were patients with singleton pregnancies who underwent fetal brain MR imaging at our institution. Patients with abnormalities on their fetal MR imaging radiology report were excluded. Of the remaining patients, 46 patients were randomly sampled to constitute the training ($n = 36$) and test ($n = 10$) data sets (Fig 1, left column). The 10 patients included in the test sample were selected to include a representative range of GAs. The remaining 36 cases were assigned to the training sample, and their GAs were confirmed to also be representative of a wide range of GAs typical of the patients that undergo fetal MR imaging. For each patient, 1 optimal (non-motion-degraded) 3D

volume was manually chosen for each of the 3 planes of acquisition (axial, coronal, and sagittal).

An additional 9 patients' fetal MRIs were acquired using the search terms "microcephaly" and "macrocephaly" in the radiology report, to estimate fetal intracranial volume in cases of pathology in which intracranial volume was subjectively abnormal, as assessed by the pediatric neuroradiologist at the time of clinical interpretation.

Finally, an additional 200 patients' fetal brain MRIs were obtained through consecutive selection from the initial search, and these formed the data set for measuring normal intracranial volume (Fig 1, right column). This set of patients was selected to include only patients with normal intracranial and brain volumes for GA. However, to be representative of the clinical population, we allowed inclusion of patients with mild extracranial (eg, neck or spine) abnormalities ($n = 19$) and variations/mild abnormalities of intracranial structures (eg, mildly prominent subarachnoid or posterior fossa CSF spaces) ($n = 12$) but with normal biparietal measurements.

Additional Data from Chart Review

The GA of all fetuses at the time of MR imaging was obtained via chart review. In addition, maternal age at the time of MR imaging, the presence of maternal diabetes, and fetal sex were obtained via chart review when available, noting that not all auxiliary information was present for each patient.

MR Imaging Parameters and Ground Truth Segmentations

Ground truth intracranial and brain volume segmentations were based on manual segmentations performed by a medical student or radiology resident (C.B.N.T.) using ITK-SNAP (www.itksnap.org) and verified by a neuroradiologist (A.M.R., with 3 years' postresidency experience including with fetal brain MR imaging). Manual segmentations were independently performed in each plane of acquisition (axial, coronal, sagittal).

Imaging data were acquired using SS-FSE T2WI in a range of imaging parameters typical of clinical fetal brain MR imaging studies (TE range = 58–102 ms, median = 94 ms; TR range = 1–8 seconds, median = 4 seconds; in-plane resolution = 0.8–0.95 mm, median = 0.94 mm; section thickness = 2–4 mm, median = 3 mm).

Image Preprocessing

Images, while obtained using 2D acquisition protocols, were treated as 3D volumes by concatenating slices into a volumetric image. The advantage of treating images as 3D volumes is that information in slices adjacent to any particular 2D section may be informative for segmentation. These volumes were normalized by the mean signal intensity to zero mean and unit standard deviations (SDs). Individual acquisitions were resampled to a 1-mm^3 3D isotropic volume via linear interpolation. During training, elastic transformations¹² were applied to the images for data augmentation. These included small random rotations, translations, scaling, and free-form deformations. To fit within graphic memory constraints, the full-resolution augmented imaging volume was divided into $96 \times 96 \times 96$ mm cubes (3D patches) as the network input. During training, the cubes were randomly sampled across

the full-image volumes. The fetal intracranial contents may constitute only a relatively small portion of the entire MR image, which also includes portions of the mother's anatomy and other fetal anatomy. Therefore, to prevent sample imbalance, we sampled the same number of patches that included fetal intracranial voxels as those that excluded fetal intracranial voxels during training. A total of 60 patches were extracted from each training imaging volume ($n = 36 \times 3 = 108$), with 3 random augmentations per volume, resulting in 180 patches per volume or a total of 19,440 training patches. During testing, the MR imaging volume was densely sampled with the cubes using a step size of 32 mm in each direction, resulting in a 64-mm overlap between cubes. The overlapped segmentation predictions were averaged.

Convolutional Neural Network Model Architecture (U-Net) and Training

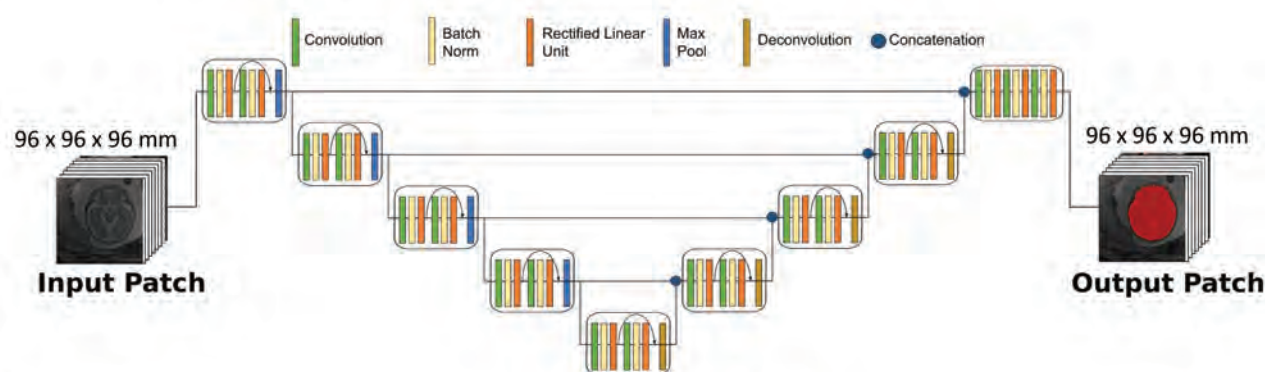
We used a 3D U-Net convolutional neural network architecture for segmentation of fetal brain MRIs. The same architecture was used unmodified from one previously developed to perform automated FLAIR lesion and intracranial metastases segmentations on MR imaging of the adult brain.^{10,11} Our focus was on expanding the clinical application of this architecture by training it to perform intracranial and brain volume segmentations of fetal brain MR imaging. Thus, 2 sequential models were trained, the first for intracranial segmentation and a second for segmenting the brain from the intracranial volume identified by the first model. For the intracranial model, training was performed in 3 acquisition planes (axial, coronal, sagittal) when available across the 36 patients in the training set, treating each acquisition as an independent training sample, for 108 total training volumes. For the brain model, training was performed on a subset of 31 randomly chosen volumes using the same data augmentation parameters and a 6-fold cross-validation to create an ensemble model from a small training data set. For both models, we used a kernel size of $3 \times 3 \times 3$, a dilation factor of 2 across all convolutional layers, and a batch size of twenty-four 3D patches. Cross-entropy loss and an Adam optimizer with a learning rate of 5×10^{-4} were used. The models were trained for 30 and 270 epochs, respectively. Hyperparameter optimization was not performed. Thresholding of the probability maps was set to 0.7 to decrease the false-positive rate relative to a threshold of 0.5. The network was implemented using TensorFlow 2 (www.tensorflow.org). Implementation was on a DGX-2 AI server, Version 4.5.0 (GNU/Linux 4.15.0–128-generic x86_64; NVIDIA).

Convolutional Neural Network Model Testing

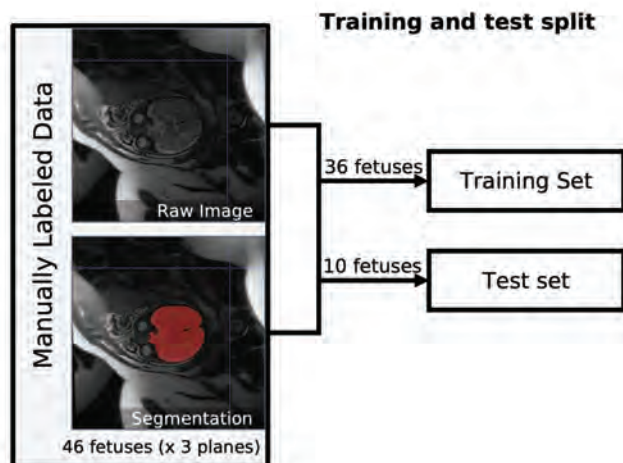
Testing was conducted on 10 independent test patients, each with 2–3 acquisition planes, for a total of 28 test samples. During testing, the outputs of both models were postprocessed by taking the largest contiguous cluster of voxels and discarding the remaining predicted voxels to eliminate small false-positives outside the fetal intracranial contents. For the brain model, inner holes were also filled (`scipy.ndimage.binary_fill_holes`; SciPy 1.8.1; scipy.org).

The pretrained U-Nets were ultimately applied to a large set of fetal brain MRIs with clinically normal findings, as assessed by the radiology report, to develop a normative reference for intracranial and brain volume across GAs (Fig 2).

A U-Net architecture



B



C Pipeline

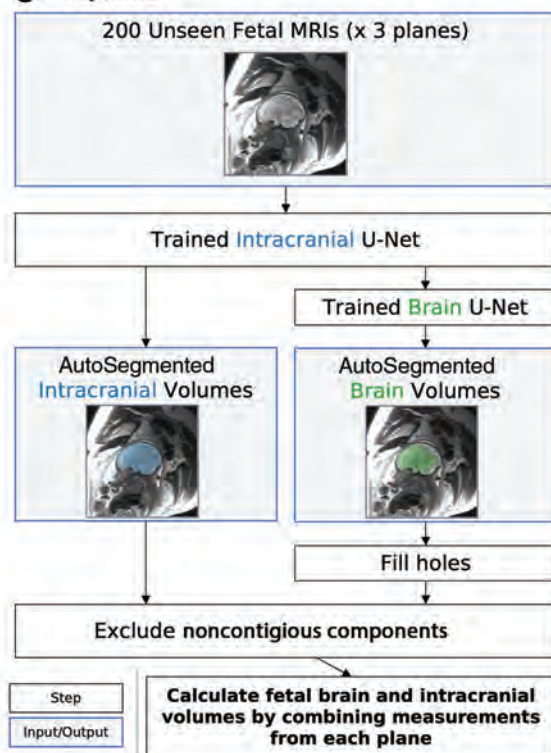


FIG 2. Method for training and testing the U-Nets. A, Schematic of 3D U-Net architecture used for training with sample input and output patch is shown. B, Manually segmented images were split into training ($n = 36$ patients) and test ($n = 10$ patients) sets. C, After confirmation of adequate segmentation performance on the test set, the trained U-Nets were applied to an additional 200 fetal brain MRIs for calculating normal fetal intracranial and brain volumes across GAs.

Normative Volume Generation

For the additional set of 200 fetal MRIs with normal findings without manual segmentation, a single high-quality image volume for each acquisition plane was chosen manually, as above. This process is very fast, taking approximately 3 seconds per volume. The volumes generated by the U-Net for the 10 patients in the test group were also included in the normative sample. For the brain model, an ensemble model was built by averaging all probability prediction maps of all 6 folds and then thresholding them at 0.7 to create the binary segmentation. Exclusion criteria (Fig 1) were applied separately to patients and acquisitions,

including patient MRIs that did not meet technical/quality specifications in at least 2 planes of imaging (eg, highly motion-degraded images or early termination of the examination) and generated volumes for each plane of imaging that were not biologically plausible ($<10 \text{ cm}^3$ or >2 SDs of the entire distribution of volumes). Patients were then excluded from the normative sample if only a single generated volume remained or if exactly 2 volumes remained but there was a large ($>30\%$) discrepancy between the calculated volumes, thereby limiting confidence in the estimate. This process resulted in a final total of 184 patients in the normative reference group.

Volume Calculations

Predictions of intracranial and brain volumes were calculated from predicted segmentations independently for each imaging plane. To arrive at a single intracranial and brain volume estimate for each fetus, we combined these 3 data points for each patient applied independently to intracranial and brain volumes as follows: After applying the exclusion criteria, notably excluding biologically implausible statistical outlier volumes defined as $<10 \text{ cm}^3$ or $>470 \text{ cm}^3$ of intracranial volume or 373 cm^3 of brain volume (>2 SDs of entire underlying distribution), the median of the remaining 2–3 data points was used to estimate the total volume for each fetus. If only a single data point remained after exclusion criteria were applied, then this patient was excluded from the set of normative volumes (Fig 1).

Code Sharing

All code used for training and testing the model in this article has been made available at <https://github.com/rauschecker-sugrue-labs/fetal-brain-segmentation>. Code includes image preprocessing, model training, and model inference, including combining individual measurements from varying planes of acquisition into a final volume estimate.

Statistical Analysis

Segmentation Assessment. Performance of the intracranial U-Net was evaluated on the 28 test samples via comparison with manual segmentations. Performance of the brain U-Net was evaluated for each of the 6 folds (5–6 volumes each) on the data unseen by that fold. Dice scores were calculated for each test sample, comparing segmentations predicted by U-Net with the human reference standard. Mean and median Dice scores were assessed for each acquisition plane to assess the quality of automated segmentation by the acquisition plane. A Pearson correlation test was used to determine whether there was an association between GA and the Dice score.

Volumetry Assessment and Statistical Analysis. Total fetal intracranial and brain volumes calculated from processed U-Net outputs on their respective test samples were compared with those calculated from manual segmentations on the same test samples. A Pearson correlation test was used to determine the association between the volumes calculated from both methods. The root median square percentage error of those volumes was calculated, and 95% limits of agreement for each comparison were calculated. In addition, we performed a repeated measures ANOVA to assess whether any consistent pattern of differences in the volume calculations existed, depending on the acquisition plane chosen.

To investigate the effects of acquired demographic variables (fetal sex, maternal diabetes, and maternal age, binarized as \geq or <35 years), we computed linear regressions for each demographic variable and for each category. To determine whether any significant differences existed between categories within a demographic variable, a bootstrapping technique was used. Specifically, the differences in the slopes and intercepts of best fit lines for 50,000 random permutations of these categories were computed, and a z

score and 2-tailed P value of the original data from this analysis are reported.

Stata/MP (Version 16; <https://www.stata.com/features/overview/statamp/>), Excel (Version 16.37; Microsoft), custom Matlab (R2019a; MathWorks) scripts, and custom Python (Version 3.8) scripts were used for these analyses. P values $< .05$ were considered statistically significant.

RESULTS

Patient Demographics

Training Set. GAs of the 36 fetuses comprising the training set ranged from 20.6 to 36.9 weeks (median, 24.6 weeks). Maternal age ranged from 19 to 40 years (median, 33 years). Nine (25%) fetuses were female, 19 (53%) were male, and 8 (22%) were of unknown sex. Four (11%) fetuses had a mother with a known history of diabetes.

Test Set. GAs of the 10 fetuses comprising the test set ranged from 20.7 to 36.1 weeks (median, 27.4 weeks). Maternal age ranged from 16 to 38 years (median, 33.5 years). Three (30%) fetuses were female, 5 (50%) were male, and 2 (20%) were of unknown sex. One (10%) fetus had a mother with a known history of diabetes.

Normative Values Set. GAs of the 184 fetuses comprising the final normative values set ranged from 19.9 to 37.7 weeks (median, 24.6 weeks). Maternal age ranged from 16 to 45 years (median, 33 years). Forty-eight (26%) subjects were female, 67 (36%) were male (including one XXY fetus), and 69 (37%) were of unknown sex. Twenty-four (13%) fetuses had a mother with a known history of diabetes.

Segmentation and Volumetry Performance on the Test Set. The convolutional neural networks resulted in highly accurate segmentations of fetal brains across a wide range of GAs (Fig 3). On test samples, overlap between segmentations predicted by the U-Nets and by human reference standards were near-perfect for both intracranial and brain segmentations. For intracranial segmentations, the median Dice score was 0.95 (interquartile range [IQR], 0.94–0.96) in the axial plane, 0.94 (IQR, 0.91–0.96) in the coronal plane, and 0.94 (IQR, 0.90–0.96) in the sagittal plane; and for brain, 0.90 (IQR, 0.89–0.90) in the axial plane, 0.89 (IQR, 0.88–0.90) in the coronal plane, and 0.90 (IQR, 0.90–0.91) in the sagittal plane (Fig 3B). A Pearson correlation test revealed a statistically significant positive association of $r = 0.49$ between GA and the Dice score ($P = .006$) for intracranial segmentations. A repeated measures ANOVA demonstrated that there was no consistent pattern of differences in the volume calculations, depending on the acquisition plane chosen ($P = .56$). There was no consistent bias of volumes generated by the automated-versus-manual intracranial segmentations (Fig 3C).

The automated method generated total intracranial volumes highly correlated with manual measurements (Pearson $r = 0.996$, $P < .001$). The volumes generated had low error, with a root median squared percentage error of 3.3% (Fig 3D). As expected, GA and estimated intracranial volume were correlated (Spearman $\rho = 0.92$, $P < .001$).

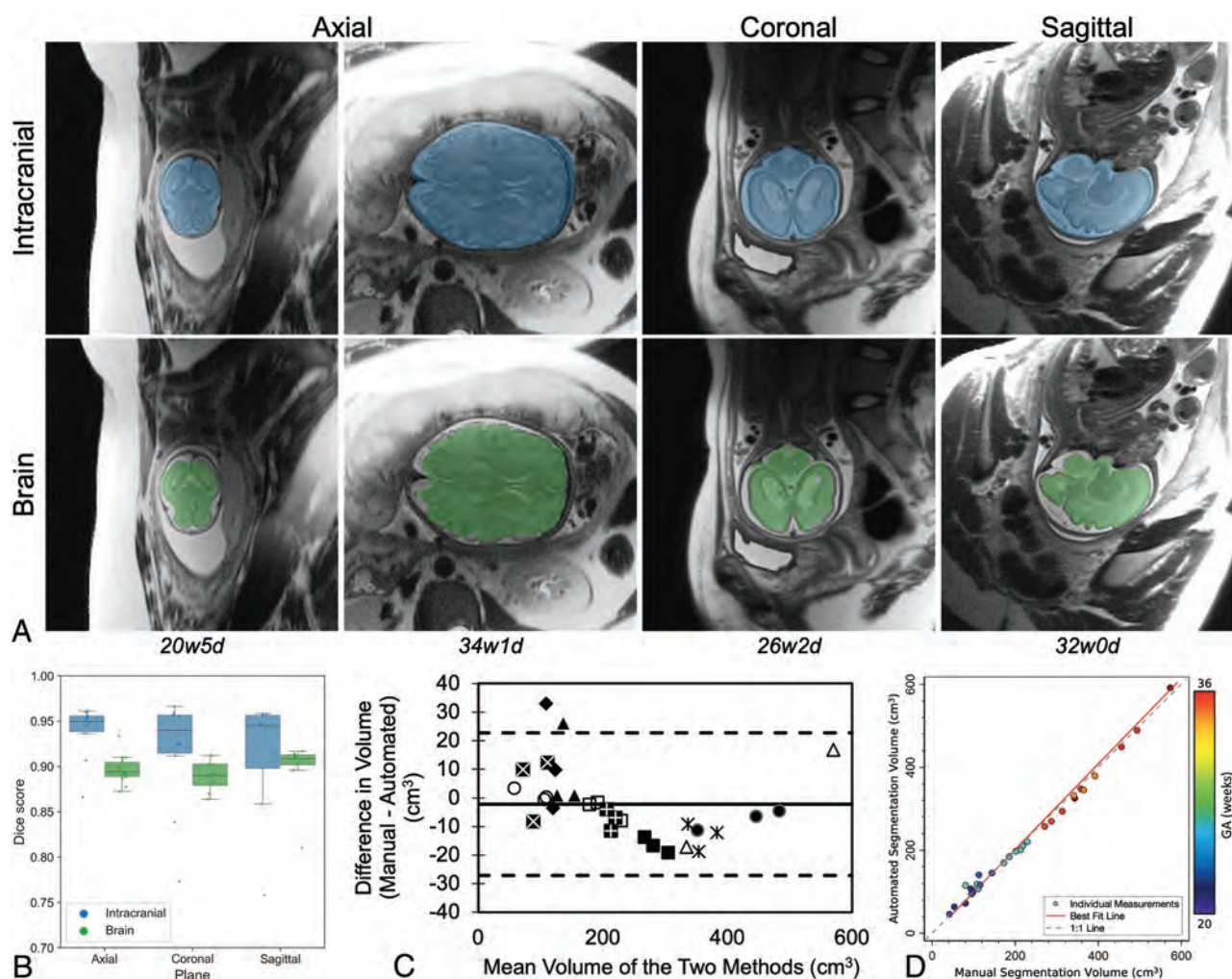


FIG 3. Performance of the U-Net for automated segmentation of intracranial (blue) and brain (green) volumes on the test set. *A*, Representative examples of the segmentation overlay on a section of the original brain MR imaging in various acquisition planes across multiple gestational ages (w = weeks, d = days). *B*, Individual Dice scores and boxplots compare the automated with the ground truth manual segmentation within axial, coronal, and sagittal dimensions, distinguishing scores for intracranial and brain segmentations. *C*, Bland-Altman plot demonstrates no linear trend in the difference between manual and automatically calculated intracranial volumes across the range of volumes tested. Each type of marker corresponds to axial, sagittal, and coronal measurements on an individual fetal brain. *D*, Scatterplot demonstrates strong agreement between manual and automated intracranial segmentation volumes, color-coded by GA. The best fit line and the 1:1 identity line are shown, nearly overlapping.

Timing of the U-Net

For an individual fetal brain MRI using our hardware, the U-Net produced an intracranial segmentation and associated mean volume in 6.8 (SD, 1.2) seconds on average. By comparison, an experienced human manually segmenting these volumes requires approximately 15 minutes for an accurate segmentation in an individual acquisition plane.

Normative Intracranial and Brain Volumes across GAs

To determine normal intracranial and brain volumes across a large population of fetal brain MRIs, we applied the trained 3D U-Nets to 209 clinically normal fetal brain MRIs ($n = 184$ after the exclusions described in Materials and Methods). As described in further detail in Materials and Methods, the models were applied in individual planes of acquisition (axial, sagittal, and coronal), which were then combined into 1 estimate of intracranial volume per fetus.

As expected, intracranial and brain volumes increased with GA, as did the variability of volumes (Fig 4 and Table). For example, the mean intracranial volume at 22–24 weeks was 103 (SD, 14) cm^3 ($n = 60$), while the mean intracranial volume at 32–34 weeks was 319 (SD, 48) cm^3 ($n = 17$).

To demonstrate the utility of this normative sample of automated fetal brain MR imaging volume measurements, we applied the trained intracranial U-Net to 9 pathologic brain MRIs (Fig 5A). Eight of the 9 volume calculations fell outside 2 SDs below or above the normative sample volumes (for GA), and the ninth volume was nearly 2 SDs above the average. We further investigated the relationship between GA and intracranial volume as a function of several demographic variables, such as fetal sex (Fig 5B), maternal age (Fig 5C), and the presence of maternal diabetes (Fig 5D). There were no appreciable effects of these demographic variables on the relationship between GA and intracranial volume in our data set, as shown by analyzing

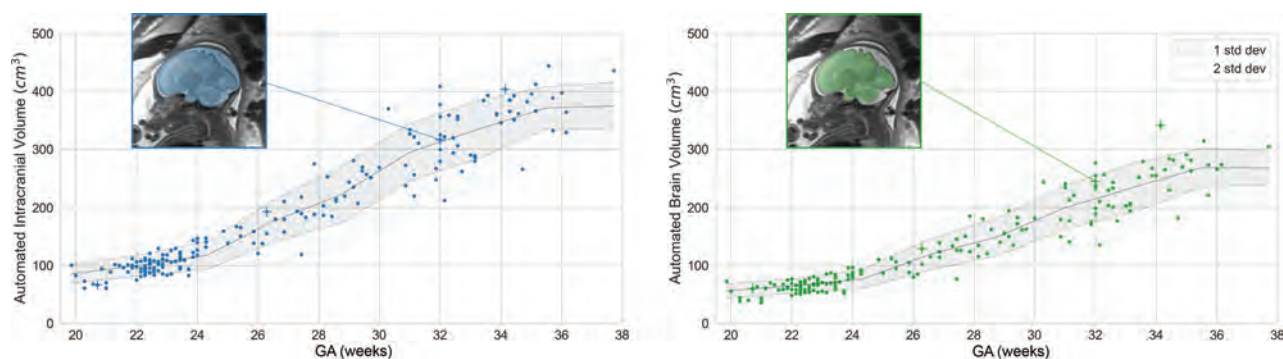


FIG 4. Intracranial (blue) and brain (green) volumes as a function of GA across 184 fetal MRIs with normal findings. Individual points represent automated measurements of volume in individual fetal brain MRIs. The *center line* represents a moving average across these points, ± 1 (dark shading) or ± 2 (light shading) SDs. One fetal brain is shown as an example in the insets. Images shown in Figure 3A are denoted by a +.

Intracranial ($n=184$) and brain ($n=178$) volumes (5th, 50th, and 95th percentiles) as a function of GA across a set MRIs of fetuses with clinically normal brains, grouped by 2-week intervals

GA (Weeks)	Intracranial Volume			Brain Volume		
	5th	50th	95th	5th	50th	95th
19.5–21.5	60.4	71.2	100.8	37.1	49.7	70.8
21.5–23.5	82.8	99.8	122.2	53.1	65.5	80.5
23.5–25.5	91.8	139.5	166.0	54.7	86.9	110.6
25.5–27.5	120.2	169.1	213.5	78.8	114.6	141.2
27.5–29.5	184.4	217.0	276.0	119.4	150.4	187.5
29.5–31.5	229.1	269.9	350.1	145.2	180.2	241.7
31.5–33.5	248.9	306.0	383.4	172.0	206.8	255.8
33.5–35.5	321.4	366.3	406.3	213.2	268.1	307.9

the differences in best fit lines among categories (P values for slope and intercept respectively: maternal age, .16, .15; fetal sex, .80, .81; and maternal diabetes, .45, .37).

DISCUSSION

We demonstrate that a 3D U-Net produced accurate automated segmentations and volumetric measurements of fetal intracranial and brain volumes on clinical 2D MRIs acquired in 3 planes. The U-Net functions across a wide range of GAs (19–38 weeks). Automated estimates of intracranial and brain volume closely approximated calculations of intracranial volume based on manual segmentations (Fig 3). This method has the potential to provide accurate volumetric data that can be incorporated into assessments of fetal neurologic development in a clinical population.

After validating the accuracy of volumetric measurements, the automated deep learning-based method was applied to 184 fetal brain MRIs with normal findings to develop a reference standard of normal intracranial and brain volumes across GAs (Fig 4). By comparing individuals' automated volumes with this reference standard, we were able to correctly identify most pathologic (microcephalic and macrocephalic) brain volumes in a few seconds, demonstrating the potential clinical utility of this approach.

Our method was trained on and applied to a population of fetal brain MRIs with clinically normal findings, as assessed by the absence of reported abnormalities on a pediatric neuroradiologist's report. The variability of resulting measurements may be higher for this clinical population than for a population of completely

normal pregnancies recruited for a specific research study, in which mothers with comorbidities might be excluded. Prior studies have deployed atlas-based methods for fetal brain segmentation.^{13–15} Although methods such as those of Jarvis et al,¹⁶ provide grossly similar total intracranial volume measurements, small differences in normative values were noted, and further research will need to identify whether such differences may be due to measurement techniques, patient sampling differences, or other factors. The advantage of applying our method in a heterogeneous clinical population is that normative values are needed for this population of clinically normal fetuses, to which the clinical tool would ultimately be applied.

The results of the automated segmentation of fetal brain MRIs using our 3D U-Net are comparable with those of prior studies using 2D U-Nets to segment the fetal brain.^{7,17} For example, Li et al⁷ demonstrated similarly high Dice scores with a 2D U-Net after training on 212 fetal brains (23–38 weeks of age) for the purpose of building an atlas of 35 fetal brains in the Chinese population. However, this study did not provide normative values across the population. Our results are also in line with a recent report using a 3D U-Net for multicompartiment fetal brain segmentation, demonstrating improved results compared with atlas-based techniques.¹⁸ However, this new method requires a slice-to-volume reconstruction before the application of the U-Net, which can be difficult to implement robustly, requiring additional technical expertise. In contrast, our method functions on 2D images directly, combining multiple measurements in different planes of acquisition, simplifying the method's use. We make this method and all related code publicly available and easy to use so that larger normative data sets may be easily built across institutions.

The automated deep learning method developed here lends itself well to both clinical and research use. For clinical use, the speed of processing of the method allows near real-time quantitative volumetric data to be obtained. From a research perspective, the method can be used at the population level to examine associations between various genetic or environmental exposures and fetal brain development. For example, by using automated volume calculations from our normative population, we demonstrate that in our data, there are no significant effects of maternal diabetes,¹⁹ fetal sex,²⁰ or maternal age²¹ on the relationship between GA and total intracranial volume. The lack of an effect of fetal sex on brain

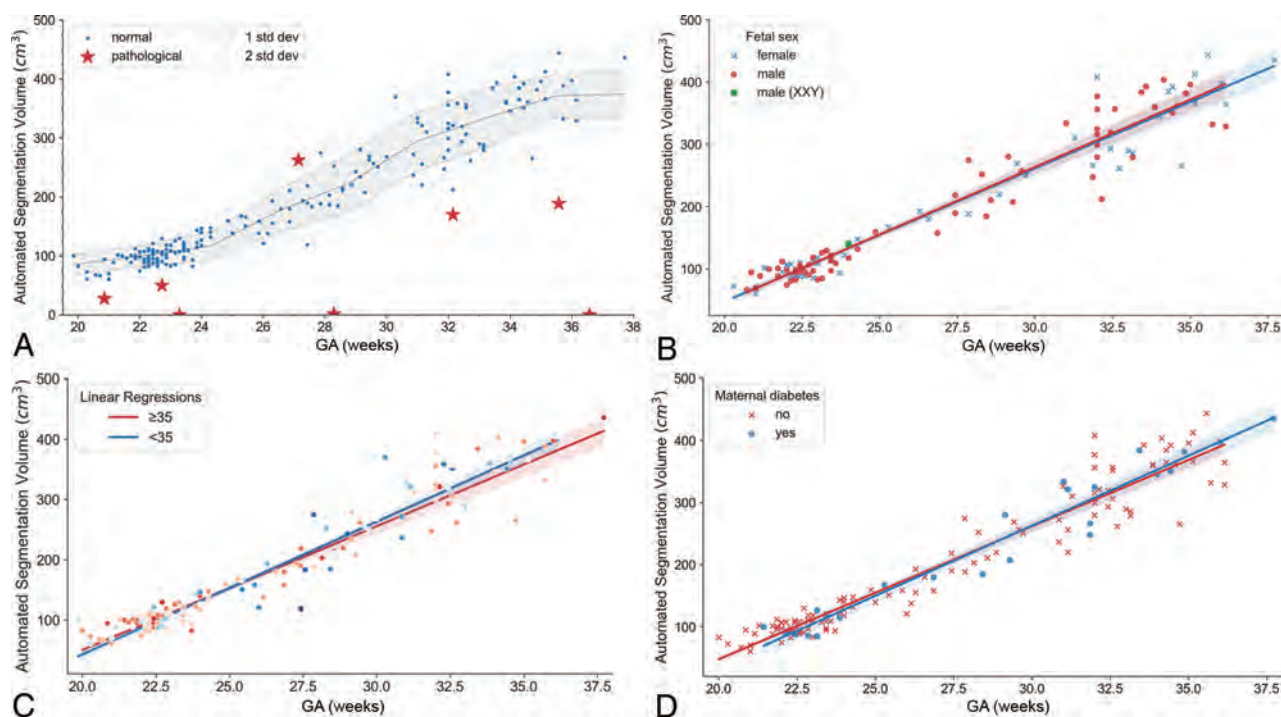


FIG 5. A, Intracranial volumes as a function of GA, as shown in Fig 4, with estimates of intracranial volume on pathologic brains added (red markers). Pathologic brain volumes fall outside the range of normal values from the normative data set. B, Intracranial volumes as a function of GA color-coded by fetal sex. C, Intracranial volumes as a function of GA color-coded by maternal age. D, Intracranial volumes as a function of GA color-coded by maternal diabetes status. B–D, The solid lines are linear regression models, with the shaded areas representing 95% confidence intervals.

volume may seem surprising, given recent²² and prior²⁰ results demonstrating sexual dimorphisms in brain volume subregions, including total brain volume. However, associational studies, including our own, have relatively small sample sizes (less than thousands of samples), which can result in seemingly conflicting results,²³ lending urgency to the need for simple tools that can quantify aspects of fetal brain MR imaging across multiple institutions to create large normative data sets. Larger samples may reveal, for example, that these sexual differences emerge only later in gestation,²⁰ which smaller samples cannot adequately resolve.

There are several limitations to this study. The study was only applied to images from a single institution; inference of fetal intracranial volumes at other institutions would require further algorithmic evaluation and possibly additional training.²⁴ The algorithm was trained on only a small number of studies, and while this training combined with efficient use of data resulted in impressive performance, it is likely that more accurate and more extensive normative data could be created by increasing the training data set size. A larger data set would also give the opportunity to create a validation split that could be used to perform hyperparameter optimization and thus additionally improve the performance of the model. Furthermore, the algorithm trained here only produces 2 quantitative values, namely intracranial and brain volumes. Future work will use similar methods to produce additional quantitative measurements, such as volumes of brain substructures (eg, cerebellum, pons, corpus callosum) or measures of whole-brain morphology (eg, sulcation), toward a more complete quantitative fetal brain evaluation. Finally, the current process of applying the U-Net to

each plane of acquisition individually was developed to provide a trade-off between accurate segmentations and manual intervention. While 9 acquisitions (3 in each plane) are obtained for each fetal MR imaging at our institution, our method currently requires manual selection of the best acquisition for each plane of imaging to avoid inclusion of acquisitions with motion or other artifacts, mirroring routine clinical practice. Methods could be incorporated to automatically disregard acquisitions with excessive artifacts or motion and to include additional available acquisitions for more robust volume measurements.

CONCLUSIONS

Automated deep learning methods can achieve accurate segmentations of fetal brain MR imaging and provide accurate quantitative estimates of fetal intracranial and brain volumes across a wide range of GAs. This method, which is made available to the research community, allows the largely automated creation of normative references for clinical and research applications.

Disclosure forms provided by the authors are available with the full text and PDF of this article at www.ajnr.org.

REFERENCES

- Reddy UM, Filly RA, Copel JA; Pregnancy and Perinatology Branch, Eunice Kennedy Shriver National Institute of Child Health and Human Development, Department of Health and Human Services, NIH. Prenatal imaging: ultrasonography and magnetic resonance imaging. *Obstet Gynecol* 2008;112:145–57 CrossRef Medline

2. Glenn OA, Barkovich AJ. **Magnetic resonance imaging of the fetal brain and spine: an increasingly important tool in prenatal diagnosis, Part 1.** *AJNR Am J Neuroradiol* 2006;27:1604–11 Medline
3. Girard NJ, Chaumoitre K. **The brain in the belly: what and how of fetal neuroimaging?** *J Magn Reson Imaging* 2012;36:788–804 CrossRef Medline
4. Glenn OA, Barkovich AJ. **Magnetic resonance imaging of the fetal brain and spine: an increasingly important tool in prenatal diagnosis: Part 2.** *AJNR Am J Neuroradiol* 2006;27:1807–14 Medline
5. Parazzini C, Righini A, Rustico M, et al. **Prenatal magnetic resonance imaging: brain normal linear biometric values below 24 gestational weeks.** *Neuroradiol* 2008;50:877–83 CrossRef Medline
6. Conte G, Milani S, Palumbo G, et al. **Prenatal brain MR imaging: reference linear biometric centiles between 20 and 24 gestational weeks.** *AJNR Am J Neuroradiol* 2018;39:963–67 CrossRef Medline
7. Li H, Yan G, Luo W, et al. **Mapping fetal brain development based on automated segmentation and 4D brain atlas.** *Brain Struct Funct* 2021;226:1961–72 CrossRef Medline
8. Andescavage NN, Plessis AD, McCarter R, et al. **Complex trajectories of brain development in the healthy human fetus.** *Cereb Cortex (Cortex)* 2017;27:5274–83 CrossRef Medline
9. Gholipour A, Rollins CK, Velasco-Annis C, et al. **A normative spatiotemporal MRI atlas of the fetal brain for automatic segmentation and analysis of early brain growth.** *Sci Rep* 2017;7:476 CrossRef Medline
10. Duong MT, Rudie JD, Wang J, et al. **Convolutional neural network for automated FLAIR lesion segmentation on clinical brain MR imaging.** *AJNR Am J Neuroradiol* 2019;40:1282–90 CrossRef Medline
11. Rudie JD, Weiss DA, Colby JB, et al. **Three-dimensional U-Net convolutional neural network for detection and segmentation of intracranial metastases.** *Radiology Artif Intell* 2021;3:e200204 CrossRef Medline
12. Platt JC, Simard PY, Steinkraus D. **Best practices for convolutional neural networks.** 2003. <https://www.researchgate.net/publication/2880624>. Accessed August 20, 2021
13. Habas PA, Kim K, Rousseau F, et al. **Atlas-based segmentation of developing tissues in the human brain with quantitative validation in young fetuses.** *Hum Brain Mapp* 2010;31:1348–58 CrossRef Medline
14. Serag A, Aljabar P, Ball G, et al. **Construction of a consistent high-definition spatio-temporal atlas of the developing brain using adaptive kernel regression.** *Neuroimage* 2012;59:2255–65 CrossRef Medline
15. Gholipour A, Estroff JA, Barnewolt CE, et al. **Fetal brain volumetry through MRI volumetric reconstruction and segmentation.** *Int J Comput Assist Radiol Surg* 2011;6:329–39 CrossRef Medline
16. Jarvis DA, Finney CR, Griffiths PD. **Normative volume measurements of the fetal intra-cranial compartments using 3D volume in utero MR imaging.** *Eur Radiol* 2019;29:3488–95 CrossRef Medline
17. Khalili N, Lessmann N, Turk E, et al. **Automatic brain tissue segmentation in fetal MRI using convolutional neural networks.** *Magn Reson Imaging* 2019;64:77–89 CrossRef Medline
18. Zhao L, Asis-Cruz JD, Feng X, et al. **Automated 3D fetal brain segmentation using an optimized deep learning approach.** *AJNR Am J Neuroradiol* 2022;43:448–54 CrossRef Medline
19. Denison FC, Macnaught G, Semple SI, et al. **Brain development in fetuses of mothers with diabetes: a case-control MR imaging study.** *AJNR Am J Neuroradiol* 2017;38:1037–44 CrossRef Medline
20. Studholme C, Kroenke CD, Dighe M. **Motion corrected MRI differentiates male and female human brain growth trajectories from mid-gestation.** *Nat Commun* 2020;11:3038 CrossRef Medline
21. Knickmeyer RC, Xia K, Lu Z, et al. **Impact of demographic and obstetric factors on infant brain volumes: a population neuroscience study.** *Cereb Cortex* 2017;27:5616–25 CrossRef Medline
22. Machado-Rivas F, Gandhi J, Choi JJ, et al. **Normal growth, sexual dimorphism, and lateral asymmetries at fetal brain MRI.** *Radiology* 2022;303:162–70 CrossRef Medline
23. Marek S, Tervo-Clemmens B, Calabro FJ, et al. **Reproducible brain-wide association studies require thousands of individuals.** *Nature* 2022;603:654–60 CrossRef Medline
24. Rauschecker AM, Nedelec P, Sugrue LP, et al. **Interinstitutional portability of a deep learning brain MRI lesion segmentation algorithm.** *Radiol Artif Intell* 2022;4:e200152 CrossRef Medline

Dilated Optic Nerve Sheath in Mucopolysaccharidosis I: Common and Not Necessarily High Intracranial Pressure

 S. Huang,  T. Lund,  P. Orchard,  A. Gupta, and  D. Nascene

ABSTRACT

SUMMARY: Hydrocephalus is one of the earliest manifestations of mucopolysaccharidosis I-Hurler syndrome, and delayed treatment of hydrocephalus can lead to neurocognitive delay or even death. Optic nerve sheath diameter has been established as a noninvasive measurement to detect elevated intracranial pressure. This study aimed to establish correlations between optic nerve sheath diameter and opening pressure. Forty-nine MR images and opening pressures in patients with mucopolysaccharidosis I-Hurler syndrome were retrospectively reviewed from 2008 to 2020. The optic nerve sheath diameter was measured 3 mm posterior to the posterior margin of the globe (retrobulbar) and 10 mm anterior to the optic foramen (midpoint segment), and the average was taken between the 2 eyes. Opening pressure was measured with the patient in the lateral decubitus position with controlled end-tidal CO₂ on the same day as the MR imaging. The average retrobulbar optic nerve sheath diameter was 5.33 mm, higher than the previously reported measurement in healthy controls, in patients with idiopathic intracranial hypertension, and there was a positive correlation between age and the optic nerve sheath diameter measured at the retrobulbar or midpoint segment (retrobulbar segment, $R^2 = 0.27$, $P < .01$; midpoint segment, $R^2 = 0.20$, $P < .01$). However, there was no correlation between retrobulbar or midpoint segment optic nerve sheath diameter and opening pressure (retrobulbar segment, $R^2 = 0.02$, $P = .17$; midpoint segment, $R^2 = 0.03$, $P < .12$). This study shows a higher average optic nerve sheath diameter in patients with mucopolysaccharidosis I-Hurler syndrome than in healthy controls regardless of the location of the measurement. However, the degree of optic nerve sheath dilation does not correlate with opening pressure, suggesting that increased optic nerve sheath diameter is an ocular manifestation of mucopolysaccharidosis I-Hurler syndrome itself rather than a marker of elevated intracranial pressure.

ABBREVIATIONS: GAG = glycosaminoglycan; ICP = intracranial pressure; IIH = idiopathic intracranial hypertension; MPSIH = mucopolysaccharidosis type I-Hurler syndrome; ONSD = optic nerve sheath diameter; OP = opening pressure

Mucopolysaccharidosis type I-Hurler syndrome (MPSIH) is a progressive disorder caused by a deficiency of alpha-L-iduronidase, critical in glycosaminoglycan (GAG) metabolism. Hydrocephalus is one of the earliest manifestations of MPSIH, and its pathophysiology is theorized to be due to deposits of GAG and/or skull abnormalities.¹ One study reported that 30.6% of patients developed hydrocephalus before hematopoietic stem cell transplantation and 16.5% of patients required shunt placement.² However, patients with MPSIH may also have profound brain atrophy resulting in ventriculomegaly, thus making the diagnosis of hydrocephalus challenging.¹

Optic nerve sheath diameter (ONSD) has been established as a reliable predictor for patients suspected of having idiopathic intracranial hypertension (IIH). The subarachnoid space surrounding the optic nerve expands in response to elevated intracranial pressure (ICP), due to its connection to the CSF. It has been established that patients with IIH have higher ONSDs than healthy controls.³⁻⁵ One case series demonstrated elevated ONSD in patients with MPSIH compared with a healthy pediatric cohort, but it was unclear whether this finding was due to elevated ICP or ocular manifestations of MPSIH.⁶

In this study, the average ONSD and the opening pressure (OP) were examined and analyzed to see whether the ONSD could predict elevated ICP in patients with MPSIH.

MATERIALS AND METHODS

All patients with MPSIH who were treated with stem cell transplantation between the 2008 and 2020 at the University of Minnesota were retrospectively reviewed. Patients who had

Received September 23, 2022; accepted after revision December 5.

From the Department of Neurosurgery (S.H.), Division of Pediatric Blood and Marrow Transplant (T.L., P.O., A.G.), and Department of Radiology (D.N.), University of Minnesota, Minneapolis, Minnesota.

Please address correspondence to Shiwei Huang, MD, Department of Neurosurgery, University of Minnesota, 420 Delaware St SE MMC 96, Room D429, Mayo Building, Minneapolis, MN 55455; e-mail: huan2256@umn.edu

<http://dx.doi.org/10.3174/ajnr.A7755>

concomitant brain MR imaging studies under sedation and lumbar punctures with OP measurements during the pretransplant evaluation were identified. Patients with ventriculoperitoneal shunts and those without documented OPs were excluded. The ONSD was measured perpendicular to the optic nerve on axial T2-weighted images (either 1-mm reconstructed images when 3D T2-weighted images were obtained or 3 mm when 2D T2-weighted turbo spin-echo images were obtained) in 2 locations, approximately 3 mm posterior to the optic disc (retrobulbar segment) and approximately 10 mm anterior to the orbital apex (midpoint segment) (Fig 1). Measurements from both eyes were obtained, and the average of each patient was considered in the analysis. Although the institutional imaging protocol has changed and occasionally images were obtained outside our institution, the measurements could be easily and reliably obtained in all cases. The consensus review was achieved between a neurosurgery resident and a neuroradiologist attending. OP was obtained with the patient under sedation via lumbar puncture in the lateral decubitus position with 25–40 mm Hg of end-tidal CO₂. The results were reported as mean and 95% confidence interval. The ONSD was plotted versus age,

and the OP was plotted versus ONSD. Correlation coefficients were reported.

RESULTS

Sixty-six patients were reviewed retrospectively, and 6 patients with shunts were excluded from the analysis. Sixteen patients who never had documented OP were excluded. A total of 44 measurements of the OP were recorded with an average of 22.3 cm H₂O (95% CI, 0.1–24.5 cm H₂O). Forty-four MR imaging brain scans were examined for the ONSD: The retrobulbar segment average was 5.33 mm (95% CI, 5.07–5.58 mm), and the midpoint segment average was 4.68 mm (95% CI, 4.46–4.90 mm; $P < .01$). The average ONSD was further stratified into 3 age groups, 0–1 year ($n = 16$), 1–2 years ($n = 22$), and >2 years ($n = 6$) as shown in the Table. There was an increase in the average ONSD measured both at the retrobulbar and midpoint segments from 0–1 to 1–2 years: 4.67–5.75 mm ($P < .01$) and 4.09–5.06 mm ($P < .01$) (Table). There was a statistically significant correlation between age and the ONSD at the retrobulbar segment ($R^2 = 0.27$, $P < .01$) and midpoint ($R^2 = 0.20$, $P < .01$)

(Fig 2). However, while there was a trend toward increased ICP with increased ONSD at the retrobulbar segment ($R^2 = 0.02$, $P = .17$) and midpoint ($R^2 = 0.03$, $P = .12$), this did not reach statistical significance (Fig 3).

DISCUSSION

MPSIH is a severe lysosomal storage disease, and one of the earliest manifestations is hydrocephalus. Delayed recognition and treatment can lead to neurocognitive developmental delay or even mortality.^{7,8} Moreover, it has been previously shown that the average

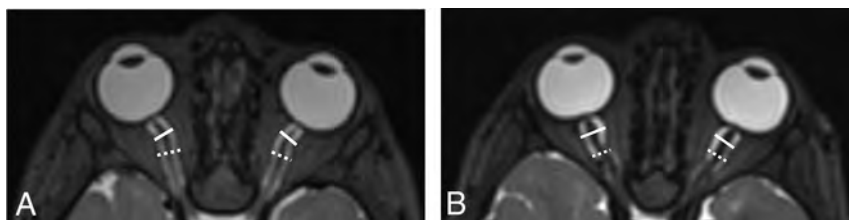


FIG 1. A, Axial T2-weighted MR image of the brain shows *white solid lines* indicating the retrobulbar ONSD and *white dashed lines* indicating the midpoint of the ONSD. This patient's OP was elevated at 31 cm H₂O, while the average ONSD was 5.8 mm at the retrobulbar area and 5.4 mm at the midpoint. B, Axial T2-weighted MR image of the brain shows *white solid lines* indicating the retrobulbar ONSD and *white dashed lines* indicating the midpoint ONSD. The courses of the optic nerves in this patient are more tortuous than those in the patient shown in A. This patient's OP was normal at 17 cm H₂O, while the average ONSD was 8.3 mm at the retrobulbar area and 6.5 mm at the midpoint.

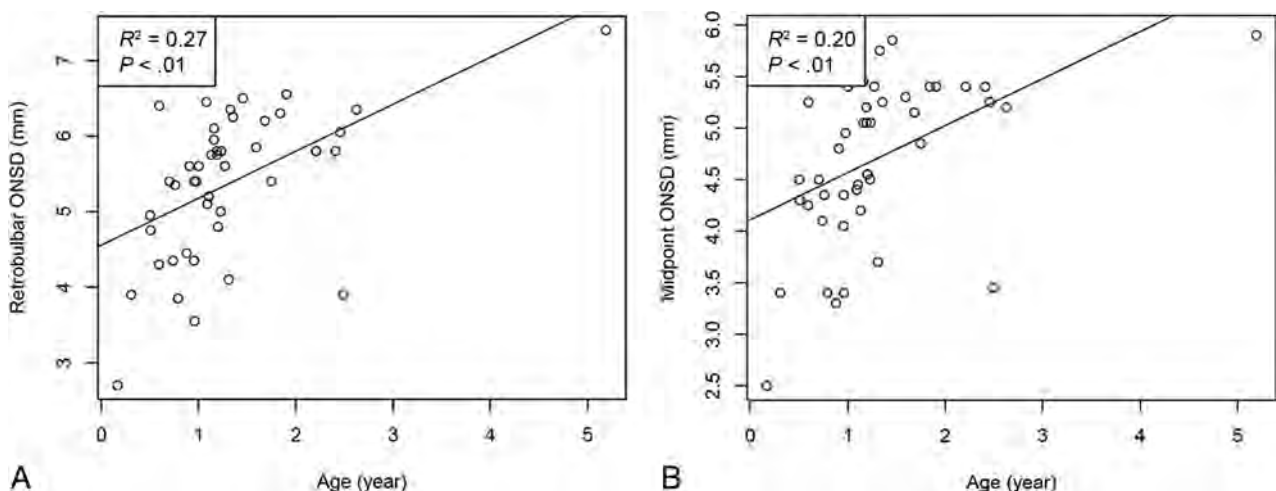


FIG 2. A, Scatterplot between retrobulbar ONSD and age shows a positive correlation ($R^2 = 0.27$, $P < .01$). B, Scatterplot between the midpoint ONSD and age shows a positive correlation ($R^2 = 0.20$, $P < .01$).

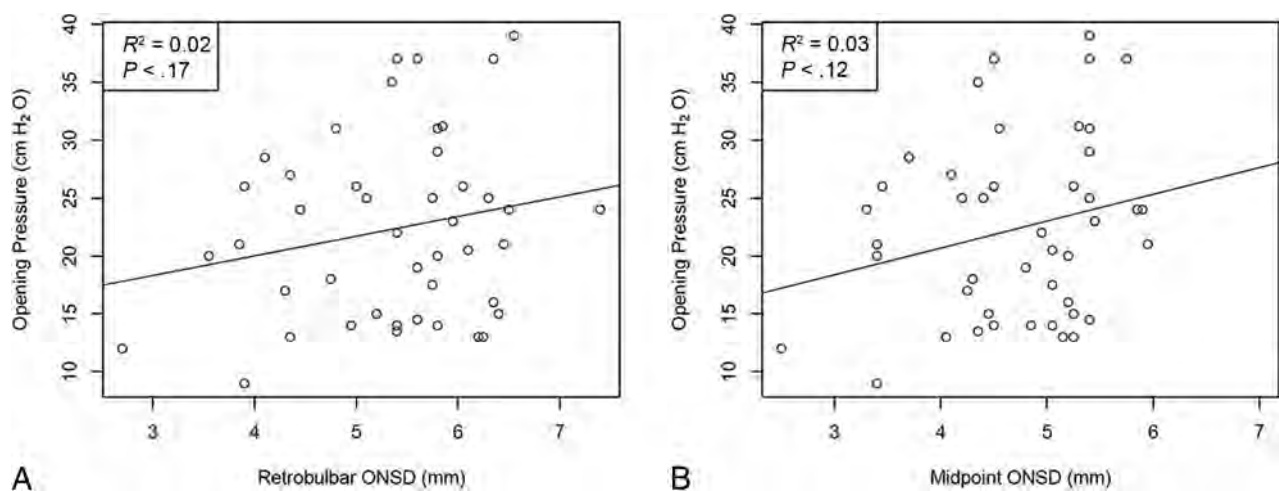


FIG 3. A, Scatterplot between the retrobulbar ONSD and OP does not show a correlation ($R^2 = 0.02$, $P = .17$). B, Scatterplot between the retrobulbar ONSD and OP does not show a correlation ($R^2 = 0.03$, $P = .12$).

Number of ONSDs, average ONSD, and 95% CI stratified by age

Age Group (yr)	No.	Average Retrobulbar ONSD (mm)	95% CI (mm)	Average Midpoint ONSD (mm)	95% CI (mm)
0–1	16	4.67	4.23–5.11	4.09	3.75–4.43
1–2	22	5.75	5.49–5.99	5.06	4.83–5.29
>2	6	5.88	5.05–6.72	5.10	4.48–5.82

OP is elevated in the MPSIH cohort compared with the healthy pediatric population.⁹ ONSD has been recognized as a useful, noninvasive measurement to detect elevated intracranial pressure. The subarachnoid space between the optic nerve sheath and the optic nerve widens as the intracranial pressure increases due to its connection to the intracranial CSF. Multiple studies have examined its utility in patients with suspected IIH and have established the average values in pediatric populations and the pediatric IIH populations.^{3–5,10}

However, there is controversy regarding the best location along the optic nerve for the ONSD assessment, and the technique and measurements often vary from study to study. While most studies report retrobulbar measurements, some authors strongly advocate midpoint measurements. One reason is that histologic studies have shown that the dura close to the globe is more capacious and the dura close to the optic foramen becomes tighter. Eye movement can alter the shape and diameter of the loose dura that is close to the globe. Another reason is that the retrobulbar dura can also be affected by the ocular pathology itself and lead to an increase in the ONSD.¹¹ With greater retrobulbar ONSD in this study, it confirmed the previous finding that retrobulbar ONSDs are larger than midpoint ONSDs due to the larger subarachnoid space in the immediate retrobulbar region than in the midpoint segment posterior to the globe (Table).

Janthanimi and Dumrongpisutikul¹² reported a retrobulbar ONSD of 4.81 mm for 0–1 year, 5.0 mm for 1–2 years, 4.9 mm for 2–3 years, and 5.2 mm for 3–4 years in healthy patients. Shofty et al¹³ measured the midpoint ONSD in healthy children and children with IIH, stratified by age groups. They reported that among children younger than 3 years of age, an average of 3.1 mm was

measured in the healthy cohort compared with 4.35 mm in the IIH cohort. Unfortunately, there are no reported reference measurements in the literature in patients with MPSIH. There are prior case series reporting optic nerve edema in more than one-half of the cohort, with 1 study reporting an average retrobulbar ONSD of 5.25–6.71 mm, markedly more elevated than in a healthy population, and another study of 66 patients with the diagnosis of mucopolysaccharidosis I, II, and VI, comparable with the mean ONSD of 5.33 mm in our study.^{6,14,15}

Contrary to the prevalence of increased ONSD, 1 study reported 30.6% of patients developing hydrocephalus before treatment, with only 16.5% eventually requiring shunt placement.² Therefore, it was unclear whether the mechanism of the increase in ONSD is intracranial hypertension or GAG deposits in the subarachnoid space or a combination of both.⁶

In this study, we examined pediatric patients who did not have shunts and reported average retrobulbar ONSDs of 5.33 mm, which is higher than the previously reported mean in healthy cohorts and patients with IIH.¹³ When the measurements were further broken down by age group, the ONSD in our cohort was larger than that in the study of Janthanimi and Dumrongpisutikul¹² in every patient age group except in the 0- to 1-year group (Table). These findings re-demonstrate the previous finding that the ONSD in patients with MPSIH is larger than that in healthy cohorts. The increase in the ONSD with age also illustrates a similar pattern observed in healthy cohorts, but it is unclear whether the relationship between ONSD and age is a manifestation of normal physiological change or further deposits of GAG (Fig 2).¹³ Most interesting, in our study, a sharp increase in the ONSD was observed from 0–1 year to 1–2

years; perhaps it can be partially explained by a rapid increase in the size of the optic nerve itself in the first 2 years of life.¹⁶

The normal range of OP in the pediatric population has been a subject of debate in the literature. Initially, the proposed normal upper limit of OP in healthy children was <20 cm H₂O, and it was not until 1994 when Ellis¹⁷ performed serial lumbar punctures with the patient in the lateral decubitus position in patients with leukemia and found a mean OP of 19 cm H₂O and a normal range of 10–28 cm H₂O. Recent studies have reported a mean OP of 19.6 cm H₂O, with a range of 11.5–28 cm H₂O, which further suggested that the normal upper limit of OP should be 28 cm H₂O.^{18,19} In fact, intracranial pressure of >28 cm H₂O is one of the diagnostic criteria for IIT; the estimated incidence of pediatric ITH is 0.6–0.7 cases per 100,000 children.^{20,21} The average OP in our patient cohort was elevated at 22.3 cm H₂O compared with the normal mean of <20 cm H₂O in a healthy population.^{17–19} Although there is no established normal OP in the MPSIH population, the OP in this study is comparable with the results in a previous study in which a mean of 24 cm H₂O was reported.⁹ Contrary to the population without MPSIH, there was no statistically significant correlation found between the increased ONSD and increased OP measurements. As illustrated in Fig 1, patients with large ONSDs may, paradoxically, have low OP and vice versa. These findings challenged the notion that the increase in ONSD in patients with MPSIH is purely driven by elevated intracranial pressure (Fig 3). It is possible that GAG deposition and/or inflammatory changes play a role in this finding. Therefore, while elevated ICP is common in MPSIH, increased ONSD does not appear to be an accurate predictor of elevated intracranial pressure.

CONCLUSIONS

ONSD has been established as a noninvasive tool to suggest elevated intracranial pressure, but its adoption in patients with MPSIH is questionable. This study demonstrates higher ONSDs in patients with MPSIH than in healthy controls, but it does not accurately predict increased ICP.

Disclosure forms provided by the authors are available with the full text and PDF of this article at www.ajnr.org.

REFERENCES

1. Alden TD, Amartino H, Dalla Corte A, et al. **Surgical management of neurological manifestations of mucopolysaccharidosis disorders.** *Mol Genet Metab* 2017;122:41–48 CrossRef Medline
2. Aldenhoven M, Wynn RF, Orchard PJ, et al. **Long-term outcome of Hurler syndrome patients after hematopoietic cell transplantation: an international multicenter study.** *Blood* 2015;125:2164–72 CrossRef Medline
3. Kishk NA, Ebraheim AM, Ashour AS, et al. **Optic nerve sonographic examination to predict raised intracranial pressure in idiopathic intracranial hypertension: the cut-off points.** *Neuroradiol J* 2018;31:490–95 CrossRef Medline
4. Munawar K, Khan MT, Hussain SW, et al. **Optic nerve sheath diameter correlation with elevated intracranial pressure determined via ultrasound.** *Cureus* 2019;11:e4145 CrossRef Medline
5. Kapoor KG, Katz SE, Grzybowski DM, et al. **Cerebrospinal fluid outflow: an evolving perspective.** *Brain Res Bull* 2008;77:327–34 CrossRef Medline
6. Schumacher RG, Brzezinska R, Schulze-Frenking G, et al. **Sonographic ocular findings in patients with mucopolysaccharidoses I, II and VI.** *Pediatr Radiol* 2008;38:543–50 CrossRef Medline
7. Muenzer J, Wraith JE, Clarke LA; International Consensus Panel on Management and Treatment of Mucopolysaccharidosis I. **Mucopolysaccharidosis I: management and treatment guidelines.** *Pediatrics* 2009;123:19–29 CrossRef Medline
8. Kubaski F, de Oliveira Poswar F, Michelin-Tirelli K, et al. **Mucopolysaccharidosis type I.** *Diagnostics* 2020;10:161 CrossRef Medline
9. Raymond GV, Pasquali M, Polgreen LE, et al. **Elevated cerebral spinal fluid biomarkers in children with mucopolysaccharidosis I-H.** *Sci Rep* 2016;6:38305 CrossRef Medline
10. Lochner P, Czosnyka M, Naldi A, et al. **Optic nerve sheath diameter: present and future perspectives for neurologists and critical care physicians.** *Neurol Sci* 2019;40:2447–57 CrossRef Medline
11. Vaiman M, Abuita R, Bekerman I. **Optic nerve sheath diameters in healthy adults measured by computer tomography.** *Int J Ophthalmol* 2015;8:1240–44 CrossRef Medline
12. Janthanani P, Dumrongpisutikul N. **Pediatric optic nerve and optic nerve sheath diameter on magnetic resonance imaging.** *Pediatr Radiol* 2019;49:1071–77 CrossRef Medline
13. Shofty B, Ben-Sira L, Constantini S, et al. **Optic nerve sheath diameter on MR imaging: establishment of norms and comparison of pediatric patients with idiopathic intracranial hypertension with healthy controls.** *AJNR Am J Neuroradiol* 2012;33:366–69 CrossRef Medline
14. Gratton SM, Neerukonda T. **Mucopolysaccharidosis type 1 and bilateral optic disc edema.** *Neuroophthalmology* 2019;43:394–96 CrossRef Medline
15. Summers CG, Ashworth JL. **Ocular manifestations as key features for diagnosing mucopolysaccharidoses.** *Rheumatology (Oxford)* 2011;50:v34–40 CrossRef Medline
16. Al-Haddad CE, Sebaaly MG, Tutunji RN, et al. **Optic nerve measurement on MRI in the pediatric population: normative values and correlations.** *AJNR Am J Neuroradiol* 2018;39:369–74 CrossRef Medline
17. Ellis R. **Lumbar cerebrospinal fluid opening pressure measured in a flexed lateral decubitus position in children.** *Pediatrics* 1994;93:622–23 CrossRef Medline
18. Avery RA. **Reference range of cerebrospinal fluid opening pressure in children: historical overview and current data.** *Neuropediatrics* 2014;45:206–11 CrossRef Medline
19. Avery RA, Shah SS, Licht DJ, et al. **Reference range for cerebrospinal fluid opening pressure in children.** *N Engl J Med* 2010;363:891–93 CrossRef Medline
20. Bursztyn LL, Sharan S, Walsh L, et al. **Has rising pediatric obesity increased the incidence of idiopathic intracranial hypertension in children?** *Can J Ophthalmol* 2014;49:87–91 CrossRef Medline
21. Matthews YY, Dean F, Lim MJ, et al. **Pseudotumor cerebri syndrome in childhood: incidence, clinical profile and risk factors in a national prospective population-based cohort study.** *Arch Dis Child* 2017;102:715–21 CrossRef Medline

Enhancing Annular Fissures and High-Intensity Zones: Pain, Internal Derangement, and Anesthetic Response at Provocation Lumbar Discography

W.S. Bartynski, V. Agarwal, H. Trang, A.I. Bandos, W.E. Rothfus, J. Tsay, W.T. Delfyett, and B. Nastasi

ABSTRACT

BACKGROUND AND PURPOSE: A high-intensity zone identified on preprocedural MR imaging is known to correlate with pain at provocation lumbar discography. The correlation between enhancing annular fissures and pain at provocation lumbar discography has not been comprehensively evaluated. The purpose of this study was to assess the pain response and imaging features at enhancing annular fissure nonoperated disc levels identified on preprocedural MR imaging with comparison with the high-intensity zone and nonenhancing disc levels in patients referred for provocation lumbar discography.

MATERIALS AND METHODS: One-hundred nonoperated discs in 44 patients were retrospectively evaluated for an enhancing annular fissure on sagittal postcontrast T1-weighted pre-discogram MR imaging. Enhancing annular fissure discs were graded on the sagittal T2-weighted sequence (Grade 4: like CSF to Grade 1: negative/barely visible) for high-intensity-zone conspicuity. High-intensity-zone detection was performed independently. In the primary assessment, enhancing annular fissure and high-intensity zones were associated with pain response at provocation lumbar discography. Additional analysis included intradiscal anesthetic response and postdiscogram CT appearance.

RESULTS: Thirty-nine discs demonstrated an enhancing annular fissure, with 23/39 demonstrating a high-intensity zone. The presence of a high-intensity zone predicted severe pain (concordant + nonconcordant; $P = .005$, sensitivity of 40%, specificity of 94%) and concordant pain ($P = .007$, sensitivity of 39%, specificity of 86%) at provocation lumbar discography. Enhancing annular fissures without a detected high-intensity zone were more frequently observed among severely painful (50%) and concordant (36%) discs than among discs negative for pain (9%; $P = .01$). This finding resulted in a substantially greater overall sensitivity of enhancing annular fissures for severe ($P < .001$, 64%) and concordant pain ($P = .008$, 61%), significantly improving the overall predictive ability of a high-intensity zone alone. A high-intensity zone went undetected in 9/11 Grade 1 disc levels with concordant pain present in 7/9.

CONCLUSIONS: Consideration of enhancing annular fissures on preprocedural MR imaging substantially improves the prediction of severe/concordant pain in provocation lumbar discography.

ABBREVIATIONS: DEG = Dallas discogram disc degeneration feature; EAF = enhancing annular fissure; FSU = functional spinal unit; HIZ = high-intensity zone; LBP = low back pain; PLD = provocation lumbar discography; RDef = Dallas discogram radial annular defect/tear feature; VAS = visual analog scale

A high-intensity zone (HIZ) is a well-recognized observation associated with disc degeneration, typically identified along the posterior annular margin on lumbar T2-weighted MR imaging.¹⁻³ HIZs can be seen in both symptomatic and asymptomatic patients.¹⁻⁷ The HIZ most frequently associated with a peripheral

concentric annular fissure and/or a full-thickness radial annular tear has been shown to correlate with axial low back pain (LBP) reproduced at provocation lumbar discography (PLD) with reported sensitivities ranging from 25% to 97% and specificities ranging from 83% to 95% for concordant pain.^{4-6,8-10} The primary purpose of discography is to identify concordant discs or disc levels in patients with chronic LBP for appropriate treatment targeting (ie, fusion or direct disc-focused treatments).

Enhancement into an annular fissure/tear has been seen in symptomatic lumbar discs to include globoid or linear enhancement into the posterior annular margin and/or adjacent annular substance and appears to correlate with local in-growth of granulation tissue.¹¹⁻¹³ Enhancement has also been recognized in peripheral annular fissures of asymptomatic patients.² Most studies

Received July 5, 2022; accepted after revision November 22.

From the Department of Radiology (W.S.B., V.A., H.T., W.E.R., J.T., W.T.D., B.N.), Division of Neuroradiology, University of Pittsburgh, Presbyterian University Hospital, Pittsburgh, Pennsylvania; Department of Radiology (H.T.), St. Clair Hospital, Pittsburgh, Pennsylvania; Department of Biostatistics (A.I.B.), Graduate School of Public Health, University of Pittsburgh, Pittsburgh, Pennsylvania; Department of Radiology (J.T.), Cleveland Clinic, Cleveland, Ohio; and Brighton Radiology Associates, PC (B.N.), Monaca, Pennsylvania.

Please address correspondence to: Walter S. Bartynski, MD, 3920 Gift Blvd, Johns Island, SC 2945; e-mail: walter.bartynski@gmail.com

<http://dx.doi.org/10.3174/ajnr.A7749>

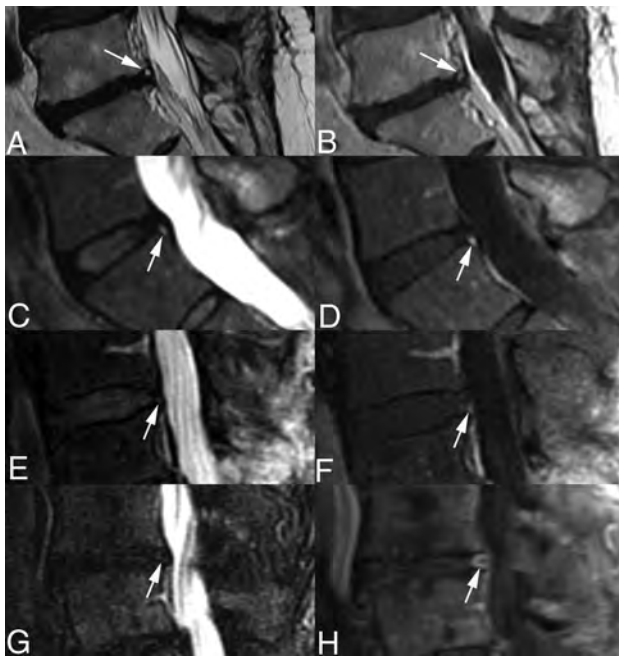


FIG 1. T2-weighted sequence grading of annular fissures detected on postcontrast T1-weighted imaging. *A*, Grade 4 annular fissure: annular fissure signal has high signal intensity (*arrow*) with signal that is greater than that of adjacent spinal fluid, consistent with an HIZ. *B*, Enhancement in the Grade 4 annular fissure (*arrow*). *C*, Grade 3 annular fissure: annular fissure signal has high signal intensity (*arrow*) with signal that is less than that of the adjacent spinal fluid, consistent with an HIZ. *D*, Enhancement in the Grade 3 annular fissure (*arrow*). *E*, Grade 2 annular fissure: annular fissure signal is focally abnormal but with mixed intermediate-to-low signal intensity (*arrow*) appearing close to the signal of the degenerative disc without a definite HIZ. *F*, Enhancement in the Grade 2 annular fissure (*arrow*). *G*, Grade 1 annular fissure: annular fissure signal is abnormal and has low signal intensity (*arrow*), appearing similar to the signal of other portions of the severely degenerative disc. *H*, Enhancement in the Grade 1 annular fissure (*arrow*).

correlating discography with peripheral annular fissures/tears have focused on the standard T2-weighted imaging findings recognized along the posterior or posterior-lateral margin of the disc.^{1-6,8-10} To our knowledge, no study has comprehensively assessed the imaging/discography correlation of enhancing annular fissures (EAFs).

The purpose of this study was the following:

- 1) To evaluate the incidence of EAFs and HIZs found on preprocedural enhanced MR imaging at nonoperated lumbar levels in a cohort of patients referred for PLD.
- 2) To compare the pain response between EAF disc levels, HIZ discs levels, and nonenhancing disc levels encountered at PLD.
- 3) To explore features of internal derangement and the intradiscal anesthetic response in EAF discs.

The primary outcome of the study is the pain response (concordant, nonconcordant, negative), which is compared for discs presenting with EAF, HIZ, or nonenhancement. Our hypothesis was that identifying discs positive for EAF will substantially improve the prediction of painful disc levels at PLD, in particular concordant painful disc levels.

MATERIALS AND METHODS

During a 5-year period, 494 consecutive patients underwent PLD at our institution, of whom 64 were identified as having preprocedural MR imaging studies with both unenhanced and enhanced sequences, typically because of chronic LBP along with a prior spine operation. Patients were referred for provocation discography by spine-focused orthopedic surgeons or neurosurgeons and were being evaluated to identify clinically positive concordant disc levels that would be appropriate for surgery, typically fusion.

Seventeen of 64 patients had prior interbody fusion; 3 patients lacked sagittal postcontrast T1-weighted MR imaging and these 20 patients were, therefore, excluded. University of Pittsburgh institutional review board approval was obtained for this retrospective study.

Imaging Evaluations

Identifying EAFs. The MR imaging studies in the remaining 44 patients with chronic LBP (obtained 0–43 months before PLD; average, 5.1 months) were retrospectively assessed for the following: 1) the presence or absence of an EAF on the sagittal enhanced T1-weighted sequence, and/or 2) an HIZ on the sagittal T2-weighted imaging sequence, by 3 experienced neuroradiologists by consensus (consensus group 1). Readers had no knowledge of which discs were studied at discography or whether a disc was symptomatic at discography.

MR imaging accompanied 10 patients from an outside institution (Signa 1.5T, GE Healthcare; Magnetom 1.5T, Siemens; Infinion 1.5T, Phillips Healthcare) with 34 scans obtained at our institution (Signa, 1.5T; GE Healthcare). All studies had sagittal T1 spin-echo or turbo spin-echo (typically TR = 400–600, TE = minimum, matrix = 256 × 192 to 512 × 512, section = 3–5 mm); sagittal T2, typically FSE/TSE T2 with fat saturation (TR = 2300–4350 ms, TE = 80–100 ms, matrix = 256 × 192 to 512 × 512, section = 3–5 mm); and sagittal T1 postcontrast spin-echo or turbo spin-echo (typically TR = 400–600, TE = minimum, matrix = 256 × 192 to 512 × 512, section = 3–5 mm) with axial T2 and T1 available. Sagittal STIR was available in 5 patients.

An annular fissure was considered present when enhancement was seen to penetrate the posterior or posterior-lateral annular margin in a rounded-globoid and/or linear pattern, in particular the posterior annular margin, on the sagittal postcontrast T1-weighted sequence (EAF) or when a typical HIZ was seen along the annular margin on the sagittal T2-weighted sequence. In 26 patients, an EAF and/or a typical peripheral annular fissure was identified at ≥1 lumbar disc. In 18 patients, no EAF was identified on postcontrast T1-weighted imaging and no HIZ was identified on the sagittal T2 sequence.

Preprocedural MR imaging was compared with the reports and imaging features from the corresponding PLD. Previously operated disc levels (having prior discectomy) were excluded from the analysis.

Grading HIZs. Many EAFs identifiable on the sagittal postcontrast T1-weighted sequence were considered difficult to identify as HIZs on the sagittal T2-weighted sequence. Therefore, EAF discs were further consensus-graded by consensus group 1 (Grade 4 to

Grade 1) for visualization and signal characteristics on the sagittal T2 (Fig 1).

Blinded HIZ Detection. Two different neuroradiologists (consensus group 2) assessed the sagittal T2-weighted sequences independently for the presence/absence of an HIZ in all 26 patients with EAFs at all lumbar disc levels. Interpreters had no knowledge of the intent of the analysis, including disc levels of interest. Differences were resolved by consensus.

Disc Degeneration Grading on MR Imaging. Studied discs were graded for the degree of disc degeneration on preprocedural MR imaging (Pfirschmann Grades: I–V) by 2 experienced neuroradiologists by consensus.¹⁴

Lumbar Discography Technique

After informed consent, 2 experienced neuroradiologists performed discography in a standard fashion.^{15,16} The patient's LBP history was clarified and recorded using the 0–10 Visual Analog Scale (VAS; 0 = no pain, 10 = worst pain imaginable) including the most severe LBP experienced and immediate preprocedural LBP levels. Limited IV conscious sedation (fentanyl, 0.05 mg; midazolam [Versed], 1 mg) was given just before the procedure, but the level of consciousness was never affected.

The lumbar region was cleansed and draped, and with C-arm fluoroscopy (OEC 9800; GE Healthcare), a local anesthetic was applied and the center of the disc was accessed using a double-needle technique (20-ga guiding needle, 25-ga 15-cm to 20-cm curved Chiba needle). L3–4 to L5–S1 were typically studied in all patients, and all needles were placed concordantly. The anticipated normal/control disc level, L3–4, was usually studied first with more superior levels added if L3–4 was painful on injection.

Discs were studied with a moderate-to-rapid hand injection (iohexol, Omnipaque; GE Healthcare, 240 mg of iodine/mL, 0.25–0.30 mL/s) consistent with the prior hand-injection rate estimates of Derby et al.¹⁷ Contrast was delivered using a 3-mL syringe and a 0.6-mL Pediatric Connector (Non-DEHP IV Catheter Extension Set; Baxter Interlink System) under direct fluoroscopic visualization, with anterior-posterior and lateral spot films obtained during and/or following the injections.

In normal nonpainful discs, minimal injection resistance is usually encountered until a firm end point is reached when no additional contrast can be injected (typical injection volume, 1.5 mL; range, 1–2.5 mL).¹⁸ In degenerative or painful disc levels, the injection volume was dependent on the following: 1) reaching a firm injection end point, 2) encountering a positive clearly established LBP response, or 3) exaggerated disc capacity, typically encountered in severely degenerative or leaking discs (typical injection volume, approximately 2 mL; range, 0.3–4.5 mL).¹⁸

Patients were kept unaware of whether a level was being provoked or which level was being studied. The response to the injection was observed by the operator, and with a positive pain response, the features of the pain were clarified, the VAS level of pain was established, and these items were recorded in a manner similar to the technique of Walsh et al.^{15,16}

Consistent with prior lumbar discography studies,^{4–6} the provoked pain response to disc injection is usually identified by the

patient as being either concordant (ie, typical of their familiar pain) or nonconcordant (ie, not their familiar pain). Concordant and many nonconcordant painful discs are commonly described by the patient as “severe,” reporting a VAS pain level ≥ 7 . If a severely painful disc was encountered (usually VAS ≥ 7), preservative-free lidocaine (2% strength, 1–1.5 mL of lidocaine HCl, Xylocaine-MPF; Fresenius Kabi USA) was injected into the disc in an attempt to reduce the patient's provoked pain and allow response clarity in subsequently studied lumbar levels. At some severely painful disc levels, a typical contrast injection end point was reached, leading to volume limitation preventing the anesthetic injection.

During disc testing, the patient's immediate response to the injection, the perception of provoked pain (concordant or nonconcordant), and injection end point response (if present) were the primary focus of the discographer. Syringe-disc pressures were not recorded during injection.

Postdiscogram CT. Immediately following discography, all patients underwent postdiscogram CT (Lightspeed, GE Healthcare) performed using bone/soft-tissue algorithms with either direct axial 3-mm-section acquisition or a spiral technique and 3-mm axial and sagittal reformatting with isotropic voxels. Disc internal derangement was graded by the Dallas discogram criteria, including degeneration (DEG; defined as annular fragmentation: Dallas Grade 1, <10%; Dallas Grade 2, < 50%; Dallas Grade 3, $\geq 50\%$) and radial annular defects/tears (RDef; defined as Dallas Grade 1, a radial tear projecting up to the inner annulus; Dallas Grade 2, radial tear to the outer annulus; and Dallas Grade 3, a radial tear beyond the outer annulus).^{4,5,19,20} Full-thickness Dallas Grade 3 RDef included annular gaps,¹⁹ a radial tear projecting into the peripheral annular tear (after Aprill and Bogduk,⁴ often labeled Grade 4), and a full-thickness radial tear with discographic contrast leakage (after Schellhas et al,⁵ often labeled Grade 5).

Statistical Analysis

The association of EAF and HIZ with categories of pain response was assessed using the generalized linear model for categorical data (PROC GENMOD, SAS Version 9.4; SAS Institute) accounting for a possible correlation in observations from the same patients and adjusting for possible confounders. The corresponding empirical standard errors were used to estimate the 95% confidence interval for proportions of discs (including sensitivity, specificity, and predictive values for severe provoked pain overall (concordant + nonconcordant and/or concordant pain). The overall predictive ability was illustrated using the receiver operating characteristic curves. Differences in the area under the receiver operating characteristic curves were assessed using the 95% confidence intervals based on using the nonparametric cluster bootstrap (with 10,000 resamples), with patients as sampling units.

In the secondary analyses, the overall association of the 3-category anesthetic response with the presence of leakage and EAF was tested in the context similar to that of the generalized linear model, accounting for possible correlation in observations from the same patients. The significant ($P = .05$ level) overall test was followed by comparisons among individual categories. In addition,

Table 1: Annular fissures identified and pain response at provocation discography

Peripheral Annular Morphology by MR Imaging	Discography-Provoked Pain Response			
	Severe Pain			Total
	Concordant Pain (% of Total)	Nonconcordant Pain (% of Total)	Negative for Pain	
EAFF	22/39 (56.4%)	10/39 (25.6%)	7/39 (18%)	39 (100%)
Focal high signal on T2WI only	0	0	1	1
No MR imaging evidence of annular fissure/tear	14/60 (23.3%)	4/60 (6.7%)	42/60 (70.0%)	60 (100%)
Total	36/100 (36%)	14/100 (14%)	50/100 (50%)	100 (100%)

Table 2: Thirty-nine discs positive for EAF—T2WI grade, HIZ detection, and unrecognized fissure/tear pain response

Annular Fissure/Tear CG-1 T2WI Grade	EAFs Identified on T1 Enhanced Sequence by CG-1	HIZs Identified on T2-Weighted Sequence by CG-2 (% EAFs)	Injection Pain Response of 16 Unrecognized Annular Fissures (HIZs) by CG-2 on T2WI		
			C	NC	N
4	8	7/8 (87.5%)		1	
3	12	10/12 (83.3%)	1		1
2	8	4/8 (50.0%)	1	2	1
1	11	2/11 (18.2%)	7	1	1
Total	39	23/39 (59.0%)	9	4	3

Note:—C indicates concordant levels; NC, nonconcordant levels; N, negative pain response; CG-1, consensus group 1; CG-2, consensus group 2.

evaluations of the radial defects and degenerative derangement were grouped into the abnormal morphology category.

RESULTS

Nineteen of 44 patients were men, and 25 were women, with an average age of 43.1 years (range, 19–64 years). Discography was performed in 100 nonoperated discs (L5–S1, 15; L4–5, 28; L3–4, 44; L2–3, 12; L1–2, 1). In 26/44 patients (59.1%), 39 EAFs were identified (single level, 14 patients; 2 levels, 11 patients; 3 levels, 1 patient). EAFs were located at the posterior annular margin in 37 discs and the posterior-lateral margin in 2 discs (L2–3, 3; L3–4, 12; L4–5, 19; L5–S1, 5) in the nonoperated discs that were studied by discography. In 2 of these patients, 3 additional nonoperated discs demonstrated an EAF but were not studied at discography; therefore, these discs were excluded.

In 1 patient positive for EAF, 1 disc demonstrated a small high signal zone on T2-weighted imaging only. Provocation response and postdiscogram CT findings were both negative, suggesting an intra-annular cyst. No HIZ or EAF was identified in 60 discs in 18 patients on the T2- or postcontrast T1-weighted sequence.

PLD Pain Observations

Provocation pain results are presented in Table 1. Severe pain overall was reported in 50/100 disc levels (50%) in 33 patients. Concordant pain was reported in 36/100 (36%) disc levels overall and in 36/50 (72%) disc levels with severe pain.

Peripheral Annular Fissure (EAF and HIZ) Identification. Comparisons of T2-weighted signal intensity grade in EAF discs (judged by consensus group 1) with traditional HIZ detection on the T2-weighted sequence (consensus group 2) are summarized in Table 2. An HIZ was identified by consensus group 2 in 23/39 discs (59%) with an EAF. The 23 discs positive for HIZ were identified only in discs with an EAF.

Grade 4 and 3 annular fissures/tears were commonly identified as an HIZ by consensus group 2 (87.5% and 83.3%, respectively). Lower signal intensity annular fissures/tears were less confidently recognized, with Grade 2 detected in 4/8 (50%) discs and Grade 1 detected in only 2/11 (18%) discs as an HIZ. In the Grade 1 group, 7/9 discs not perceived with an HIZ were at painful concordant levels (Table 2).

Presence of an EAF: Disc/Patient Characteristics and Pain Response.

Table 3 summarizes the rates of EAF identification for disc levels with different pain responses by levels of potentially relevant covariates. The frequency of EAF varied across the disc levels ($P = .002$), being most frequent at the L4–5 level (68%, 19/28). EAF was also more frequent in patients 41 years of age and older (50%, 29/58) than in patients of 40 years and younger (24%, 10/42; $P = .009$), but it was only fractionally more frequent in women (44%, 26/59) than in men (32%, 13/41); $P = .25$).

As shown in Table 3, overall, EAF was substantially more prevalent at disc levels with concordant pain (61%, 22/36) and nonconcordant pain (71%, 10/14) than at disc levels negative for pain (14%, 7/50; $P < .001$). This strong association of EAF with concordant and nonconcordant pain prevailed across the disc levels, sex, and patient age groups (adjusted $P < .001$). Nineteen of 26 patients (73%) with an EAF reported concordant pain at ≥ 1 disc level (single level, 17; two levels, 1; three levels, 1), with 5 of 26 patients (19%) reporting nonconcordant pain at ≥ 1 disc level, and 2 of 26 patients (8%) reporting no pain with the discogram injections.

For predicting disc levels with provoked severe pain overall, the presence of an EAF has a sensitivity of 64% (95% CI, 49%–77%), a specificity of 86% (95% CI, 72%–94%), and a positive predictive value of 82% (95% CI, 66%–92%) for a population with 50% of disc levels showing severe pain.

Similarly, for predicting disc levels with provoked concordant pain, the presence of an EAF has a sensitivity of 61% (95% CI,

Table 3: Proportions of discs with EAF for different pain responses by disc levels, sex, and patient age

Disc/Patient Characteristics	Discography Pain Response			
	Severe Pain		Negative for Pain (EAF %)	Overall (EAF %)
	Concordant Pain (EAF %)	Nonconcordant Pain (EAF %)		
Overall	22/36 (61%)	10/14 (71%)	7/50 (14%)	39/100 (39%)
Disc level				
L1–2 to L2–3 ^a	2/3 (67%)	0/1 (0%)	1/9 (11%)	3/13 (23%)
L3–4	4/11 (36%)	4/5 (80%)	4/28 (14%)	12/44 (27%)
L4–5	14/15 (93%)	3/3 (100%)	2/10 (20%)	19/28 (68%)
L5–S1	2/7 (29%)	3/5 (60%)	0/3 (0%)	5/15 (33%)
Sex				
Female	16/23 (70%)	5/7 (71%)	5/29 (17%)	26/59 (44%)
Male	6/13 (46%)	5/7 (71%)	2/21 (10%)	13/41 (32%)
Age				
Younger than 41 yr	16/24 (67%)	7/9 (78%)	6/25 (24%)	29/58 (50%)
41 yr or older	6/12 (50%)	3/5 (60%)	1/25 (4%)	10/42 (24%)

^a There was a single disc at L1–2 that did not have an EAF or pain on provocation.

Table 4: Response to provocative discography by imaging findings of HIZ and EAF (no discs identified with HIZ but without EAF)

Imaging Features	Discography Pain Response			
	Severe Pain (n = 50)		Negative for Pain (n = 50)	Total (n = 100)
	Concordant (n = 36)	Nonconcordant (n = 14)		
EAF+ HIZ+	14/36 (39%)	6/14 (43%)	3/50 (6%)	23/100
EAF+ HIZ–	8/36 (22%)	4/14 (29%)	4/50 (8%)	16/100
EAF– HIZ–	14/36 (39%)	4/14 (29%)	43/50 (86%)	61/100
Total	36 (100%)	14 (100%)	50 (100%)	100/100

42%–77%), a specificity of 73% (95% CI, 61%–83%), and a positive predictive value of 56% (95% CI, 41%–71%), for a population with 36% of disc levels showing concordant pain.

HIZ and EAF Pain Responses. With HIZs identified only in discs positive for EAF, combined consideration of EAF and HIZ distinguishes 3 categories of discs (Table 4): “EAF-positive, HIZ-positive,” “EAF-positive, HIZ-negative,” and “EAF-negative, HIZ-negative,” which are significantly associated with the pain response levels ($P < .001$).

HIZ Identification (EAF-Positive, HIZ-Positive Discs). An HIZ was recognized substantially more frequently at disc levels with concordant pain (39%, 14/36) and nonconcordant pain (43%, 6/14) than at disc levels negative for pain (6%, 3/50; $P = .003$; Table 4, row 1). The presence of an HIZ alone can be used for predicting concordant pain ($P = .007$), with a sensitivity of 39%, 14/36 (95% CI, 24%–56%); a specificity of 86%, 55/64 (95% CI, 75%–93%); and a positive predictive value of 61%, 14/23, (95% CI, 40%–78%) for a population with 36% of disc levels showing concordant pain (Fig 2A).

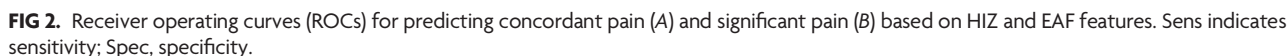
Similarly, for predicting severe pain overall, the presence of HIZ alone offers a sensitivity of 40%, 20/50 (95% CI, 27%–54%); a specificity of 94%, 47/50, (95% CI, 78%–99%); and a positive predictive value of 87%, 20/23 (95% CI, 59%–97%) for a population with 50% of disc levels showing severe pain (Fig 2B).

EAF without HIZ (EAF-Positive, HIZ-Negative Discs). Among 77 remaining discs without an HIZ (Table 4, rows 2 and 3), an EAF was also more frequent at disc levels with concordant pain (36%, 8/22) and nonconcordant pain (50%, 4/8) than at disc

levels negative for pain (9%, 4/47), with a statistically significant overall difference ($P = .010$). As a result, the identification of an EAF for disc levels without HIZ leads to an increase in the sensitivity of predicting both concordant painful disc levels (from 39% to 61%, $P = .008$) and severely painful disc levels overall (from 40% to 64%, $P < .001$), with relatively smaller sacrifice in specificity (resulting in an increase in the area under the receiver operating characteristic curves of 0.06; 95% CI, 0.0–0.12 and from 0.62 to 0.68 for predicting concordant pain, Fig 2A) and in an increase in the area under the receiver operating characteristic curves of 0.09; 95% CI, 0.04–0.14, and from 0.67 to 0.76 for severe pain (Fig 2B).

EAF Disc Internal Derangement Features

The presence of an annular fissure compared with the postdiscogram features of internal disc derangement is summarized in Table 5. The internal derangement categories are approximately equally represented among 100 discs studied, with 32%, 33%, and 35% of radial defects and degenerative and normal morphology, respectively. Abnormal morphology is strongly associated with severely painful discs (with a sensitivity of 88%, 44/50, and a specificity of 58%, 29/50, $P < .0001$) and is present in 92% (33/36; 95% CI, 77%–97%) of discs with significant concordant pain. (Abnormal morphology did not demonstrate a meaningful ability to differentiate concordant from nonconcordant painful discs.) Among 65 discs with abnormal morphology, EAF maintained a strong association with pain response, being present in 68% (40/44) of discs with significant pain, including in 67% (18/33) with concordant pain, while only in 33% (7/21) of discs negative for pain ($P = .013$).



Disc State	Discogram Pain Response												
	Severe Pain												
	Concordant			Discordant			Negative for Pain			Total			
	RDef	DEG	NI	RDef	DEG	NI	RDef	DEG	NI	RDef	DEG	NI	All
EAF	9	13	0	6	4 ^a	0	3	4	0	18	21	0	39
Focal high-signal T2 only	0	0	0	0	0	0	0	0	1	0	0	1	1
No annular fissure	6	5	3	2	1	1	7 ^b	7 ^{c,d}	28	15	13	32	60
Total	15	18	3	8	5	1	10	11	29	33	34	33	100

^d One Dallas Grade 1 disc; 1 Dallas Grade 2 disc.

The intradiscal anesthetic response of 40 severely painful disc levels is summarized in Table 7. Consistent with previous reports, the anesthetic response is significantly associated with the presence of contrast leakage ($P = .011$).^{16,19,21} The presence of leakage was

Table 6: EAF T2WI grade by CG-1 versus postdiscogram CT features of internal derangement—39 discs

Annular Fissure T2WI CG-1 Grade	Discogram Pain Response and Internal Derangement Features							
	Severe Pain						Total	
	Concordant Pain		Nonconcordant Pain		Negative for Pain			
	RDef	DEG	RDef	DEG	RDef	DEG	RDef	DEG
4	2	3	3	0	0	0	5	3
3	4	2	2	1	1	2	7	5
2	1	2	1	2	1	1	3	5
1	2	6	0	1 ^a	1	1	3	8
Total	9	13	6	4 ^a	3	4	18	21

Note:—DEG indicates degenerative change Dallas Grade 3 except for 1 disc; RDef, all radial defects (Dallas Grade 3); CG-1, consensus group 1.

^a Dallas Grade 1.

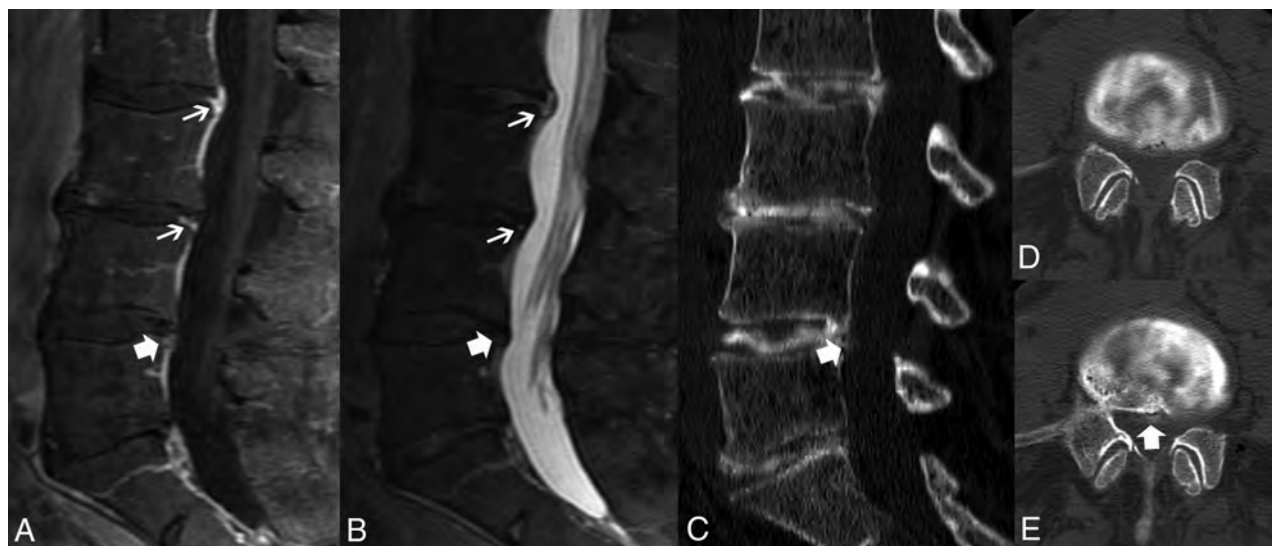


FIG 3. A 49-year-old woman with long-standing LBP and some bilateral leg radiation (most severe VAS = 10/10; immediate preprocedural VAS = 5/10) with prior discectomy at L5–S1. Concordant pain was provoked at L2–3, L3–4, and L4–5, with all 3 levels demonstrating partial provoked pain improvement with intradiscal lidocaine, and all 3 levels appearing contained on postdiscogram CT. **A**, Sagittal postcontrast T1-weighted image demonstrates posterior EAFs at L2–3, L3–4 (*thin arrows*), and L4–5 (*thick arrow*). **B**, Sagittal T2-weighted image. The L2–3 HIZ, considered Grade 4, and L3–4 HIZ, considered Grade 2 by consensus group 1, were identified as HIZs by consensus group 2 (*thin arrows*). The EAF at L4–5 considered a Grade 1 HIZ by consensus group 1 was not identified as an HIZ by consensus group 2 (*thick arrow*). **C**, Sagittal reconstructed CT image demonstrates the posterior annular margin at L4–5, consistent with the EAF (*thick arrow*). **D** and **E**, Axial postdiscogram CT images through the L4–5 disc demonstrates severe annular degeneration (Dallas Grade 3) with the posterior annular margin noted, consistent with the EAF (*thick arrow*).

most frequent among the discs with the total anesthetic improvement (82%, 14/17) and significantly less frequent for partial anesthetic improvement (29%, 2/7; $P = .038$) and no anesthetic improvement (31%, 5/16; $P = .011$). The anesthetic response was not associated with age, sex, disc level, or the presence of EAF. EAF was similarly represented in the discs with total, partial, and no improvement (65%, 11/17; 57%, 4/7; 81%, 13/16, respectively, $P = .36$).

Of the 40 severely painful discs that received intradiscal anesthetic, 31 were at concordant disc levels (total improvement, 12 [EAF: 8/12]; partial improvement, 7; no improvement, 12) and 9 were at nonconcordant disc levels (total improvement, 4 [EAF 3/4]; partial improvement, 0; no improvement, 5).

DISCUSSION

An HIZ (annular fissure/tear) identified on preprocedural MR imaging is known to correlate with provoked pain at discography.^{4,6} Our data demonstrate that enhancement in an annular

fissure/tear (an EAF) is more common than an HIZ alone and appears to represent a powerful indicator of a painful disc level in patients referred for PLD. The presence of an EAF appears predictive of severe pain overall as well as concordant pain provoked at discography, regardless of the disc level, sex, or age of the patients. In our series, all discs with an HIZ also demonstrated enhancement and were recognized as an EAF.

The primary purpose of discography is to identify concordant discs or disc levels in patients with chronic LBP for appropriate treatment planning. Concordant provoked pain was identified in 36 of 50 (72%) disc levels that responded with severe pain on injection. Overall, an EAF was significantly more sensitive than an HIZ in predicting disc levels with concordant pain (EAF 61% versus HIZ 39%, $P = .008$) and nonconcordant pain (EAF 64% versus HIZ 40%, $P < .001$), with relatively smaller sacrifice in specificity (due to enhancement present in negative disc levels). Concordant provoked pain was observed in 19 of 26 (73.1%) patients with an EAF (single disc level, 17; two disc levels, 1; three disc levels, 1).

Annular fissure enhancement likely correlates with in-growth of vascularized granulation tissue at an abnormal annular margin, probably reflecting complete or ongoing annular repair. In-growth of pain fibers has been documented into the deep annular and nuclear regions of severely degenerative discs and into the area of a RDef in animal models.^{22,23} Granulation tissue represented by the enhancing annular fissure/tear region can, therefore, carry nociceptive fibers, and this enhancing region could represent an important focal source of pain in many of these discs. Ross et al¹³ noted improved visualization of peripheral annular fissures after contrast enhancement. Stadnik et al,² evaluating asymptomatic patients (absent or without LBP for >6 months), observed that most annular fissures were more confidently identified after contrast enhancement with only 1 recognized on T2-weighted imaging only, paralleling our results.

Joint consideration of the presence of HIZ and/or EAF substantially improves the stand-alone ability of HIZ to predict concordant or severely painful disc levels (Fig 2). In particular,



FIG 4. A 29-year-old woman with complex LBP and leg pain (most severe VAS = 10/10; preprocedural VAS = 5/10) with prior L5–S1 discectomy. Concordant pain was provoked at L4–5 (VAS = 10/10). A, Sagittal T2-weighted sequence demonstrates a small annular fissure along the posterior annular margin (arrow), judged Grade 4 by consensus. B, Sagittal postcontrast T1-weighted sequence demonstrates enhancement in the annular fissure (arrow). C, Axial postdiscogram CT image demonstrates a full-thickness radial annular fissure (arrow) projecting into a small peripheral concentric annular fissure (arrowhead). D, Axial postdiscogram CT image demonstrates the posterior annular margin at the level of the peripheral concentric annular fissure (arrowhead), which corresponds to the HIZ identified on the T2-weighted sequence and EAF region demonstrated on the postcontrast T1-weighted sequence.

among discs without an HIZ, an EAF was substantially more frequently present at disc levels with concordant and nonconcordant pain than at disc levels negative for pain (36% and 50% versus 9%), leading to the significant increases in sensitivity, with only a small sacrifice in specificity. Thus, in addition to a significant stand-alone performance, EAF substantially improved the ability of HIZ to predict the pain response at PLD.

In our series, an HIZ was not identified on the T2-weighted sequence in 16 of 39 (41%) discs positive for EAF (Table 2). Progressive loss of annular fissure/tear signal has been noted when followed with serial imaging.²⁴ Presumably, the fluid-filled fissure/tear changes or the granulation tissue in the fissure/tear region matures and reduces in signal intensity and therefore conspicuity.

These poorly identified annular fissures and tears were highly important in our series. Nine of the 11 discs judged as Grade 1 HIZ were not recognized on the T2 sequence by consensus group 2, and 7 of these 9 disc levels were associated with concordant provoked pain (Table 2). Recognizing enhancement within these less conspicuous fissures/tears could result in important concordant levels being included at discography. Using the identification of an EAF in addition to an HIZ represents a powerful combination in predicting discs with concordant pain.

The intradiscal anesthetic response is considered the best correlate to true disc-origin provoked pain.^{25,26} This included evaluation of disc block, in which an anesthetic alone is injected into a putatively painful disc to assess baseline pain elimination. Consistent with prior reports, our data demonstrate that severely painful disc levels with complete pain relief typically had contrast leakage, while severely painful disc levels without pain improvement were usually contained (Table 6, $P < .01$).^{16,19,21} Complete provoked pain improvement suggests that the disc is the primary source of the pain.^{16,25,26} Partial pain reduction after intradiscal anesthetic suggests that the disc is a contributor but there is >1 pain source within the painful functional spinal unit (FSU). No pain improvement after intradiscal anesthetic suggests that other components of the FSU might be the primary contributors. An anesthetic response was seen at both concordant disc levels (total improvement, 12/31 discs; partial improvement, 7/31 discs) as well as nonconcordant disc levels (total improvement, 4/9 discs), strongly suggesting the true disc origin of all or a portion of the provoked pain.

Better specificity of true disc-origin LBP is becoming critical, in particular with evolving minimally invasive disc treatments such as biacuplasty, basivertebral nerve ablation, and intradiscal biologics. EAF identification might also improve correlation with more routine minimally invasive treatments such as epidural steroid administration.

Despite the presence of an EAF, presumably granulation tissue related to disc injury repair or local inflammation,^{11,12,27–29}

Table 7: Intradiscal lidocaine response—40 concordant and nonconcordant severely painful discs where anesthetic was injected

Disc State	Intradiscal Lidocaine-Provoked Pain Response			Total (n = 40)
	Total Improvement (n = 17)	Partial Improvement (n = 7)	No Improvement (n = 16)	
Leaking	14 (82%)	2 (29%)	5 (31%)	21 (53%)
Contained	3 (18%)	5 (71%)	11 (69%)	19 (48%)
Total	17 (100%)	7 (100%)	16 (100%)	40 (100%)

contrast leak is seen in many of these discs at discography. Annular repair of these severely internally deranged discs may be incomplete, with altered biomechanical function, variable disc strength, motion-related intermittent fiber dehiscence, and/or inflammatory disc by-product leakage leading to nociceptor irritation.²⁷ Contrast leakage is observed in both EAF and nonenhancing discs with similar intradiscal anesthetic responses. Why some discs develop enhancing granulation while others do not is unclear, though local inflammation might play a role.

An EAF was seen at 7 nonpainful disc levels, all demonstrating features of severe internal derangement, including 3 with RDefs and 4 with severe DEG. It is possible that these discs have successfully healed with in-growth of granulation tissue accounting for the enhancement features. Absence of pain on provocation in these discs might be related to the granulation tissue either lacking innervation or preventing irritant leakage.

An EAF was also identified at 10 nonconcordant severely painful discs, 9 of which demonstrated severe internal derangement on postdiscogram CT. These abnormal discs may also have healed with in-growth of granulation tissue. The nonconcordant pain might be coming from nociceptors in the disc-associated granulation tissue or pain provoked from other parts of the FSU, which were stimulated by disc injection but were not normally painful. With the high prevalence of disc degeneration in asymptomatic patients,^{3,30} it is not surprising that normally asymptomatic internally deranged discs are encountered in symptomatic patients at discography.

It is important to identify nonconcordant and nonpainful disc levels with an EAF because these would not be targets for disc-focused interventional treatments. Mechanisms have been proposed for the development of chronic LBP, including injury-activation of latent pain fibers,³¹ irritant alteration of spontaneous pain fiber firing,³² irritant-related neural phenotypic shift,³³ and central sensitization.^{34,35} A noninvasive imaging method separating chronically triggered nociceptors (ie, concordant pain) from quiescent pain fibers would be advantageous, in particular with reference to a visible putative target such as granulation tissue in discs positive for EAF.

Consistent with prior reports, our data support an HIZ remaining a strong predictor of concordant provoked pain ($P = .007$; sensitivity, 39%; specificity, 86%) on preprocedural MR imaging in patients with chronic LBP.^{4-6,8-10} An HIZ was also strongly predictive of disc levels with severe pain overall ($P = .005$; sensitivity, 40%) with high specificity (94%). All discs with an HIZ also demonstrated an EAF. An HIZ, therefore, appears highly specific for the concordant and nonconcordant pain provoked at discography.

A recent study evaluating FSU motion with disc injection demonstrates endplate elevation frequently with rocking, accentuating separation in the posterior annular region along with substantial facet motion.¹⁸ Disc injection biomechanically challenges the entire FSU in addition to inducing disc/endplate pressurization. In concordant disc levels, annular stretch in the region of the EAF (granulation tissue), disc irritant leakage, or even the posterior elements could be responsible for the provoked pain. In nonconcordant disc levels, similar areas of degeneration, disc leakage, or granulation tissue might be present but quiescent until

challenged either with disc injection or physical activity (mechanical irritation, injury-activation). An EAF (suggesting granulation tissue) was present in 3 of 4 nonconcordant significantly painful discs that demonstrated total pain improvement with intradiscal anesthetic. Further assessment might be important to better understand the exact sources of pain in the disc.

Limitations

Our study has several limitations. Discography remains a controversial procedure but is the only study with which we can challenge or physically examine the disc to assess pain provocation/concordance. While the observations encountered at PLD are routinely encountered at discography (concordant pain, nonconcordant pain, absent provoked pain), the criterion standard for disc origin or discogenic LBP is as yet not clearly defined. Comprehensive correlation between discography observations (including anesthetic response) and treatment results will likely improve our understanding of PLD as well as our understanding of true disc-origin LBP. Despite a large discography population, our sample size of patients with enhanced preprocedural imaging is small, because most patients have routine unenhanced imaging before the test. A larger patient population could reinforce the findings of this study. Discography is not yet a standardized procedure, with variable techniques practiced by different interventionalists. It is unknown whether our findings apply to all technique approaches, including slow injection with pressure monitoring as opposed to our more rapid hand-injection technique. While these observations appear to apply to a patient population with chronic severe LBP in which an operation is being considered, it is as yet unclear whether these observations would apply to the patient with short-duration LBP or less severe symptoms. More comprehensive MR imaging techniques could also be used to evaluate the presence of enhancing/nonenhancing annular fissures, supplementing these results.

CONCLUSIONS

An HIZ noted on preprocedural MR imaging remains an important predictor of a disc level with severe and/or concordant provoked pain in patients with chronic LBP referred for PLD.

EAFs were more frequently identified than HIZs on preprocedural MR imaging in our patients with chronic LBP referred for PLD. Independently, EAFs were strongly predictive of disc levels with severe and/or concordant provoked pain, demonstrating greater sensitivity than an HIZ and retaining high overall accuracy. EAFs identified at disc levels without a recognizable HIZ are also strongly associated with severe and/or concordant provoked pain, thereby substantially improving the stand-alone ability of the HIZ to predict severe and/or concordant pain. Annular fissures and tears appear more confidently identified after contrast administration, likely due to in-growth of granulation tissue and scar maturation.

Better identification of annular fissures could aid in planning levels studied at discography and further aid in preoperative planning when minimally invasive techniques like biacuplasty, basivertebral nerve ablation, and intradiscal biologics or surgery are considered for axial LBP.

Disclosure forms provided by the authors are available with the full text and PDF of this article at www.ajnr.org.

REFERENCES

- Weishaupt D, Zanetti M, Hodler J, et al. **MR imaging of the lumbar spine: prevalence of intervertebral disk extrusion and sequestration, nerve root compression, end plate abnormalities, and osteoarthritis of the facet joints in asymptomatic volunteers.** *Radiology* 1998;209:661–66 CrossRef Medline
- Stadnik TW, Lee RR, Coen HL, et al. **Annular tears and disk herniation: prevalence and contrast enhancement on MR images in the absence of low back pain or sciatica.** *Radiology* 1998;206:49–55 CrossRef Medline
- Jarvik JJ, Hollingworth W, Heagerty P, et al. **The Longitudinal Assessment of Imaging and Disability of the Back (LAIDBack) study: baseline data.** *Spine (Phila Pa 1976)* 2001;26:1158–66 CrossRef Medline
- Aprill C, Bogduk N. **High-intensity zone: a diagnostic sign of painful lumbar disc on magnetic resonance imaging.** *Br J Radiol* 1992;65:361–69 CrossRef Medline
- Schellhas KP, Pollei SR, Gundry CR, et al. **Lumbar disc high-intensity zone: correlation of magnetic resonance imaging and discography.** *Spine (Phila Pa 1976)* 1996;21:79–86 CrossRef Medline
- Saifuddin A, Braithwaite I, White J, et al. **The value of lumbar spine magnetic resonance imaging in the demonstration of annular tears.** *Spine (Phila Pa 1976)* 1998;23:453–57 CrossRef Medline
- Carragee EJ, Paragioudakis SJ, Khurana S. **2000 Volvo Award winner in clinical studies: lumbar high-intensity zone and discography in subjects without low back problems.** *Spine (Phila Pa 1976)* 2000;25:2987–92 CrossRef Medline
- Chen JY, Ding Y, Lv RY, et al. **Correlation between MR imaging and discography with provocative concordant pain in patients with low back pain.** *Clin J Pain* 2011;27:125–30 CrossRef Medline
- Fang C, Zhang W, Chen L, et al. **The correlation between the high-intensity zone on a T2-weighted MRI and positive outcomes of discography: a meta-analysis.** *J Orthop Surg Res* 2017;12:26 CrossRef Medline
- Chelala L, Trent G, Waldrop G, et al. **Positive predictive values of lumbar spine magnetic resonance imaging findings for provocative discography.** *J Comput Assist Tomogr* 2019;43:568–71 CrossRef Medline
- Peng B, Hou S, Wu W, et al. **The pathogenesis and clinical significance of a high-intensity zone (HIZ) of lumbar intervertebral disc on MR imaging in the patient with discogenic low back pain.** *Eur Spine J* 2006;15:583–87 CrossRef Medline
- Saifuddin A, Mitchell R, Taylor BA. **Extradural inflammation associated with annular tears: demonstration with gadolinium-enhanced lumbar spine MRI.** *Eur Spine J* 1999;8:34–39 CrossRef Medline
- Ross JS, Modic MT, Masaryk TJ. **Tears of the annulus fibrosus: assessment with Gd-DTPA-enhanced MR imaging.** *AJR Am J Roentgenol* 1990;154:159–62 CrossRef Medline
- Pfirrmann CW, Metzendorf A, Zanetti M, et al. **Magnetic resonance classification of lumbar intervertebral disc degeneration.** *Spine (Phila Pa 1976)* 2001;26:1873–78 CrossRef Medline
- Walsh TR, Weinstein JN, Spratt KF, et al. **Lumbar discography in normal subjects: a controlled, prospective study.** *J Bone Joint Surg Am* 1990;72:1081–88 CrossRef Medline
- Bartynski WS, Rothfus WE. **Pain improvement after intradiscal lidocaine administration in provocation lumbar diskography: association with diskographic contrast leakage.** *AJNR Am J Neuroradiol* 2007;28:1259–65 CrossRef Medline
- Derby R, Lee SH, Lee JE, et al. **Comparison of pressure-controlled provocation discography using automated versus manual syringe pump manometry in patients with chronic low back pain.** *Pain Med* 2011;12:18–26 CrossRef Medline
- Bartynski WS, Agarwal V, Khan AS, et al. **Motion characteristics of the functional spinal unit during lumbar disc injection (discography) including comparison between normal and degenerative levels.** *Pain Med* 2021;22:1735–42 CrossRef Medline
- Bartynski WS, Rothfus WE, Kurs-Lasky M. **Postdiskogram CT features of lidocaine-sensitive and lidocaine-insensitive severely painful disks at provocation lumbar diskography.** *AJNR Am J Neuroradiol* 2008;29:1455–60 CrossRef Medline
- Sachs BL, Vanharanta H, Spivey MA, et al. **Dallas discogram description: a new classification of CT/discography in low-back disorders.** *Spine (Phila Pa 1976)* 1987;12:287–94 CrossRef Medline
- Bartynski WS, Rothfus WE. **Peripheral disc margin shape and internal disc derangement: imaging correlation in significantly painful discs identified at provocation lumbar discography.** *Interv Neuroradiol* 2012;18:227–41 CrossRef Medline
- Coppes MH, Marani E, Thomeer RT, et al. **Innervation of “painful” lumbar discs.** *Spine (Phila Pa 1976)* 1997;22:2342–49; discussion 2349–50 CrossRef Medline
- Fagan AB, Sarvestani G, Moore RJ, et al. **Innervation of annulus tears: an experimental animal study.** *Spine (Phila Pa 1976)* 2010;35:1200–05 CrossRef Medline
- Munter FM, Wasserman BA, Wu HM, et al. **Serial MR imaging of annular tears in lumbar intervertebral disks.** *AJNR Am J Neuroradiol* 2002;23:1105–09 Medline
- Derby R, Lee JE, Lee SH. **Analgesic discography: effect of adding a local anesthetic to routine lumbar provocation discography.** *Pain Med* 2010;11:1335–42 CrossRef Medline
- Derby R, Aprill CN, Lee JE, et al. **Comparison of four different analgesic discogram protocols comparing the incidence of reported pain relief following local anesthetic injection into concordantly painful lumbar intervertebral discs.** *Pain Med* 2012;13:1547–53 CrossRef Medline
- Hirsch C, Schajowicz F. **Studies on structural changes in the lumbar annulus fibrosus.** *Acta Orthop Scand* 1952;22:184–231 CrossRef Medline
- McCarron RF, Wimpee MW, Hudkins PG, et al. **The inflammatory effect of nucleus pulposus: a possible element in the pathogenesis of low-back pain.** *Spine (Phila Pa 1976)* 1987;12:760–64 CrossRef Medline
- Ross JS, Modic MT, Masaryk TJ, et al. **Assessment of extradural degenerative disease with Gd-DTPA-enhanced MR imaging: correlation with surgical and pathologic findings.** *AJR Am J Roentgenol* 1990;154:151–57 CrossRef Medline
- Boos N, Semmer N, Elfering A, et al. **Natural history of individuals with asymptomatic disc abnormalities in magnetic resonance imaging: predictors of low back pain-related medical consultation and work incapacity.** *Spine (Phila Pa 1976)* 2000;25:1484–92 CrossRef Medline
- Avramov AI, Cavanaugh JM, Ozaktay CA, et al. **The effects of controlled mechanical loading on group-II, III, and IV afferent units from the lumbar facet joint and surrounding tissue: an in vitro study.** *J Bone Joint Surg Am* 1992;74:1464–71 Medline
- Yamashita T, Cavanaugh JM, Ozaktay AC, et al. **Effect of substance P on mechanosensitive units of tissues around and in the lumbar facet joint.** *J Orthop Res* 1993;11:205–14 CrossRef Medline
- Ohtori S, Takahashi K, Chiba T, et al. **Phenotypic inflammation switch in rats shown by calcitonin gene-related peptide immunoreactive dorsal root ganglion neurons innervating the lumbar facet joints.** *Spine (Phila Pa 1976)* 2001;26:1009–13 CrossRef Medline
- Siddall PJ, Cousins MJ. **Introduction to pain mechanisms: implications for neural blockade.** In: Cousins MJ, Horlocker TT, Bridenbaugh PO. *Neural Blockade In Clinical Anesthesia and Pain Medicine*. Fourth Edition. Lippincott Williams & Wilkins; 2009:661–692. <https://aneskey.com/introduction-to-pain-mechanisms-implications-for-neural-blockade/>. Accessed December 11, 2022
- Woolf CJ. **Central sensitization: implications for the diagnosis and treatment of pain.** *Pain* 2011;152:S2–15 CrossRef Medline

Spinal Cord Sarcoidosis Occurring at Sites of Spondylotic Stenosis, Mimicking Spondylotic Myelopathy: A Case Series and Review of the Literature

R.M. Kurtz, V.D. Babatunde, J.E. Schmitt, J.R. Berger, and S. Mohan



ABSTRACT

Sarcoidosis is a multisystem granulomatous disease, with intramedullary spinal cord involvement seen in <1% of cases. This case series illustrates the clinical presentations and imaging findings of 5 patients with intramedullary spinal neurosarcoidosis occurring at sites of spondylotic spinal canal stenosis, which can be indistinguishable from spondylotic myelopathy with cord enhancement. Both entities are most common in middle-aged men and present with weeks to months of motor and sensory symptoms. On imaging, both can have focal spinal cord enhancement and longitudinally extensive signal abnormality centered at or just below the level of spinal canal stenosis. On the basis of our experience, we suggest that in patients with cord enhancement centered at or just below a site of spinal canal stenosis, consideration should be given to chest imaging and lymph node biopsy when applicable, to assess for the possibility of underlying sarcoidosis before surgical decompression.

ABBREVIATIONS: ACE = angiotensin converting enzyme; WBC = white blood cell

Sarcoidosis is a chronic multisystem granulomatous disease characterized by the accumulation of noncaseating epithelioid granulomas.¹ Sarcoidosis involving the spine is rare and may include extradural, intradural, or intramedullary lesions, with intramedullary spinal cord involvement seen in <1% of cases.^{2,3} However, when spinal cord involvement is part of the disease course, it is frequently the first manifestation of the disease.^{1,4} These patients will often have asymptomatic disease elsewhere, such as hilar adenopathy.¹ Patients with intramedullary spinal neurosarcoidosis typically present with progressive paresthesia, proprioceptive disturbances, weakness, and/or sphincter dysfunction, with symptoms often occurring for months before the diagnosis is made.¹

Spondylotic myelopathy is a more common cause of spinal cord dysfunction. When involving the cervical spine, the term “spondylotic myelopathy” has recently been replaced with “degenerative cervical myelopathy,” which is now the recognized terminology in practice guidelines by AO Spine (<https://www.aofoundation.org/spine>) and has been accepted by multistakeholder evaluation.⁵

Nevertheless, the term “spondylotic myelopathy” has persisted throughout the literature, and we will use the term spondylotic myelopathy in this article for consistency and because some of our cases involve the thoracic spine. There are reports in the literature of a subset of cases of spondylotic myelopathy in which prominent spinal cord edema and focal enhancement of the cord are seen.⁶ The mechanism for the edema and enhancement has been speculated to be disturbed venous circulation caused by spinal cord compression resulting in venous hypertension at the affected level and a breakdown of the blood-cord barrier.⁷ Most of these patients initially present with motor weakness and sensory disturbance, gait disturbance, and exaggerated deep tendon reflexes, with symptoms usually present for several months before diagnosis.⁶

Intramedullary spinal neurosarcoidosis occurring in association with spondylotic spinal stenosis has not, to our knowledge, been specifically described in the radiology literature, with a few cases previously described in the neurosurgery and neurology literature.⁸⁻¹⁰ In some reported cases of presumed spondylotic myelopathy, the intramedullary abnormality of neurosarcoidosis was initially incorrectly ascribed to spondylosis, leading to ineffective decompressive surgery and subsequent progression of neurosarcoidosis owing to lack of appropriate treatment.

We report a series of 5 patients who presented to our institution from 2018 to 2019 and were diagnosed with intramedullary spinal neurosarcoidosis at the level of mass effect on the spinal cord due to either a disc herniation or spondylotic spinal canal stenosis. Four of these patients did not have a previous diagnosis of sarcoidosis, with cord involvement being the initial symptomatic

Received September 12, 2022; accepted after revision October 21.

From the Departments of Radiology (R.M.K., V.D.B., J.E.S., S.M.) and Neurology (J.R.B.), Hospital of the University of Pennsylvania, Philadelphia, Pennsylvania.

Please address correspondence to Robert M. Kurtz, MD, Hospital of the University of Pennsylvania, Department of Radiology, 3400 Spruce St, Silverstein 1, Philadelphia, PA 19104; e-mail: Robert.kurtz@penmedicine.upenn.edu; @RobertMKurtzMD

Indicates open access to non-subscribers at www.ajnr.org

Indicates article with online supplemental data.

<http://dx.doi.org/10.3174/ajnr.A7724>

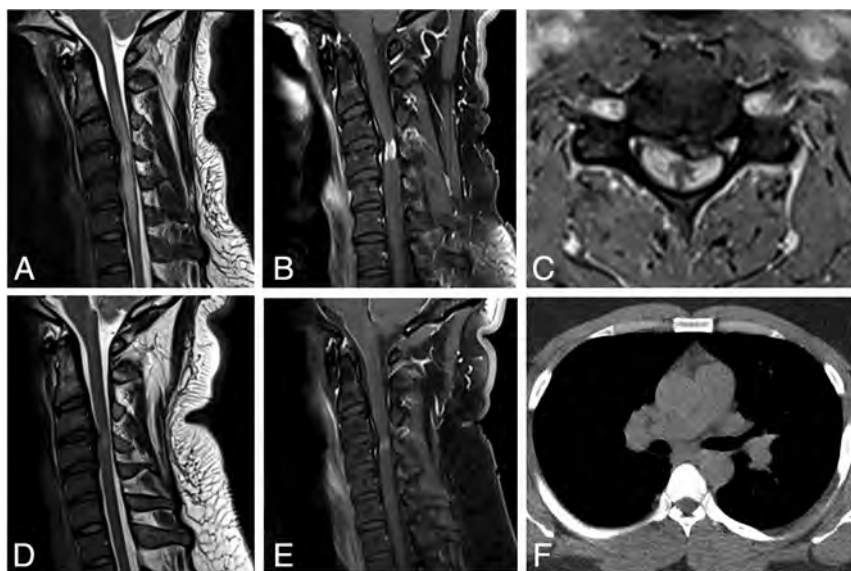


FIG 1. A 31-year-old man with 6 months of progressively worsening bilateral arm and leg weakness and numbness. Sagittal T2-weighted (A) image shows a prominent disc osteophyte complex at C3–4 with spinal canal stenosis and long-segment cord signal abnormality. There is focal cord enhancement centered just below the level of compression on postcontrast sagittal (B) and axial T1-weighted (C) sequences, with involvement of the peripheral cord and relative sparing of the central GM. There is persistent-but-decreased cord signal abnormality and enhancement at the 23-month follow-up on sagittal T2-weighted (D) and postcontrast T1-weighted (E) sequences. Noncontrast chest CT at presentation (F) shows bilateral hilar adenopathy.

lesion. Most interesting, the imaging appearance of our patients is strikingly similar to that in reported cases of spondylotic myelopathy. Spondylotic myelopathy was initially considered as a diagnostic possibility for most of our patients before we arrived at the diagnosis of sarcoidosis based on an intrathoracic lymph node biopsy.

This retrospective study was approved by our institutional review board.

CASE SERIES

Case 1

A 31-year-old man presented with 6 months of progressively worsening bilateral arm and leg weakness and numbness. On examination, his strength was 4/5 proximally and 3/5 distally in both his arms and legs. He had absent sensation to light touch and temperature in the bilateral upper extremities. Reflexes were 2+ in the upper extremities and 4+ in the lower extremities.

CSF analysis showed a white blood cell (WBC) count of $24/\mu\text{L}$ with lymphocytic pleocytosis, an elevated protein level of 54 mg/dL (reference range, 15–45 mg/dL) and an elevated glucose level of 114 mg/dL (reference range, 40–70 mg/dL). The serum angiotensin converting enzyme (ACE) level was normal at 53 U/L (reference range, 9–67 U/L). MR imaging of the cervical spine showed a prominent disc osteophyte complex at C3–4. There was long-segment cord edema extending from C2 through C7, with focal enhancement just inferior to the C3–4 intervertebral disc (Fig 1A–C). Findings were thought to be most consistent with spondylotic myelopathy. Due to the cord enhancement, a chest CT was obtained to assess for sarcoidosis. The chest CT

showed micronodularity in a perilymphatic distribution and hilar adenopathy, favoring sarcoidosis (Fig 1F). A transbronchial lymph node biopsy was performed, showing lymphocytes and non-necrotizing granulomas.

A steroid pulse was started after the biopsy, and the patient had rapid improvement in symptoms. He was then treated with prednisone, 60 mg daily, with a prolonged taper and adalimumab; he was later transitioned to infliximab. At imaging follow-up, the cord signal abnormality and enhancement improved but persisted at last follow-up at 23 months (Fig 1D, -E).

Case 2

A 52-year-old woman presented with 5 months of gradually worsening numbness from the waist down, weakness of the right hand and lower extremities, and urinary incontinence. She had a known history of pulmonary sarcoidosis. On examination, right upper-extremity strength was 3/5; left upper-extremity, 4/5; right lower-extremity, 1/5; and left lower-extremity, 3/5. The Hoffman sign was positive.

CSF analysis showed 7 WBC/ μL , a mildly elevated protein level of 54 mg/dL, and normal glucose levels. The serum ACE level was normal (11 U/L). MR imaging of the cervical spine showed spondylotic changes with maximal canal stenosis at C6–7. There was spinal cord signal abnormality spanning C4 through T4, with associated enhancement at C6 and C7 (Online Supplemental Data). Diagnostic possibilities offered included neurosarcoidosis versus spondylotic myelopathy. Chest CT showed very mild hilar adenopathy, related to known sarcoidosis.

She was started on IV methylprednisolone sodium succinate, and the paresthesia and lower-extremity weakness significantly improved the following day. She was then treated with a combination of infliximab and prednisone. At 13-month imaging follow-up, there was improved-but-persistent cord signal abnormality and enhancement (Online Supplemental Data).

Case 3

A 51-year-old man presented with 4 months of progressively worsening subjective, bilateral, lower-extremity weakness and bowel/bladder dysfunction. On examination, strength was 5/5 in the upper and lower extremities. Sensation to light touch was intact in all 4 extremities, and gait and reflexes were normal.

CSF analysis showed a WBC count of $237/\mu\text{L}$, with lymphocytic pleocytosis. There was mild elevation of the CSF protein level at 59 mg/dL. Glucose level was normal. The serum ACE level was within normal limits at 54 U/L. MR imaging of the cervical and thoracic spine was performed and showed a disc protrusion at T7–8. There was cord signal abnormality spanning T4 to T11 and enhancement at T7 and T8 (Online Supplemental Data).

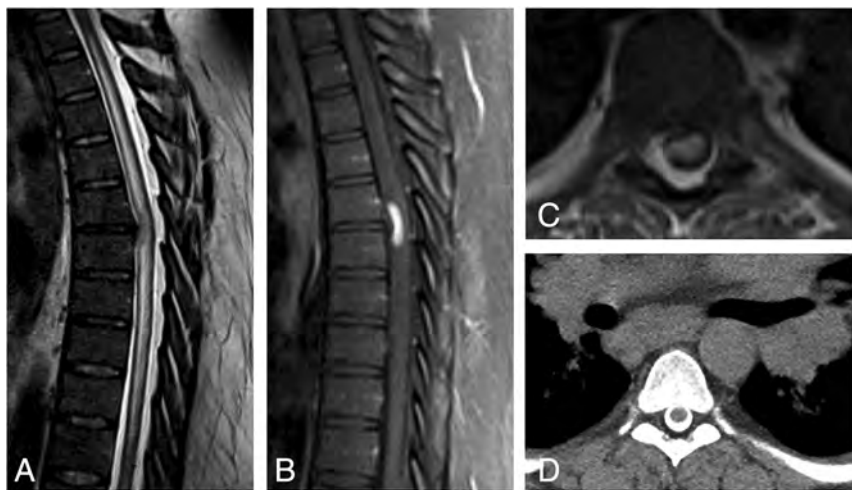


FIG 2. A 35-year-old man with 1 month of progressively worsening lower-extremity weakness, paresthesia, and difficulty with ambulation. Sagittal T2-weighted (A) image shows a disc extrusion at T6–7, with long-segment cord signal abnormality centered at this level. Postcontrast sagittal (B) and axial T1-weighted (C) sequences demonstrate focal cord enhancement at the level of the disc extrusion. CT myelogram (D) performed for further evaluation of the cord abnormality shows marked bilateral hilar adenopathy.

Differential considerations offered included demyelinating disease, sarcoidosis, and spondylotic myelopathy. A chest CT showed mild mediastinal and bilateral hilar adenopathy. An endobronchial biopsy of the lymph nodes showed non-necrotizing granulomas in a background of lymphocytes.

He was treated with a 5-day course of IV methylprednisolone with improvement in symptoms, then maintained on prednisone and methotrexate. Five-month imaging follow-up showed marked improvement in abnormal enhancement and expansion of the thoracic cord (Online Supplemental Data).

Case 4

A 35-year-old man presented with 1 month of progressively worsening lower-extremity weakness, paresthesia, and difficulty with ambulation. On examination, he had 3/5 strength in the bilateral lower extremities.

CSF analysis showed 32 WBC/ μ L with lymphocytic pleocytosis, a mildly elevated protein level at 51 mg/dL, and mildly elevated glucose level at 88 mg/dL. Serum ACE and CSF ACE levels were within normal limits at 63 and 1.8 U/L (reference range, 0.0–2.5 U/L), respectively. Thoracic spine MR imaging showed a right central disc extrusion at T6–7. There was cord signal abnormality from T3 to T11 and focal ventral cord enhancement at T6–7 (Fig 2A–C). The imaging differential diagnosis included neoplasm or sarcoidosis because hilar adenopathy was also noted on the MR imaging. Hilar and Mediastinal adenopathy were confirmed on a CT myelogram (Fig 2D). Endobronchial lymph node biopsy showed lymphocytes and granulomatous inflammation.

He was started on IV dexamethasone with improvement in symptoms. MR imaging of the thoracic spine performed after 4 days on steroid therapy showed a decrease in enhancement and edema. He was started on 30 mg of prednisone daily and has not received long-term follow-up at our institution.

Case 5

A 51-year-old man presented with 1–2 weeks of bilateral foot numbness that progressed up his legs, as well as urinary incontinence and saddle anesthesia. He was evaluated at an outside hospital where MR imaging showed cervical spondylosis, worst at C5–6 and C6–7, with disc osteophyte complexes causing moderate spinal canal stenosis at these levels. There was cord signal abnormality extending from C3 to T5, centered around enhancement in the dorsal and peripheral cord at C7 and T1 (Online Supplemental Data). A chest CT showed mediastinal and hilar adenopathy, and a biopsy was performed, with lymph nodes showing granulomatous inflammation. He was given dexamethasone with slight improvement in the numbness and urinary symptoms. Following a 2-week course of steroids, he presented to our institution with

worsening lower-extremity symptoms. On examination, he had decreased pinprick and temperature sensations over the back of his thighs and in his feet. Strength was normal in all 4 extremities. Reflexes were 2+ and symmetric.

No report of CSF analysis was available from the initial work-up. Following the initial course of therapy, a CSF examination at our institution demonstrated a mildly elevated glucose level at 72 mg/dL but was otherwise unremarkable. MR imaging of the cervical and thoracic spine showed improved-but-persistent cord signal abnormality and enhancement. Internal interpretation of the outside lymph node biopsy showed lymph nodes with numerous non-necrotizing granulomas, thought to be consistent with sarcoidosis.

He was treated with prednisone. At 4-month follow-up, the patient's symptoms of paresthesia in the lower extremities and right buttocks were unchanged. His examination findings had improved, with improved temperature sensation in the lower legs. Follow-up MR imaging at 5 months showed decreased-but-persistent enhancement in the cord (Online Supplemental Data).

DISCUSSION

This case series illustrates the clinical presentations and imaging findings of isolated intramedullary spinal neurosarcoidosis occurring at sites of spondylotic spinal canal stenosis. This entity can be indistinguishable both clinically and on imaging from spondylotic myelopathy. Both are most common in middle-aged men and present with weeks to months of motor and sensory symptoms. On imaging of both entities, there can be focal spinal cord enhancement and longitudinally extensive signal abnormality centered at or just below the level of spinal canal stenosis. We will also discuss a possible explanation for the coincidence of intramedullary spinal neurosarcoidosis occurring at the site of maximal spinal canal stenosis.

Intramedullary Spinal Neurosarcoidosis

Sarcoidosis is a systemic inflammatory disorder characterized by the development of noncaseating granulomas. The pathophysiology of sarcoidosis remains elusive. Granuloma formation is initiated by T lymphocytes responding to a specific-but-currently unknown antigen.¹¹ The most common sites of involvement are the lungs and lymph nodes; however, any part of the body can be affected. Although rare, when the spine is involved, it is most often in the form of neurosarcoidosis, with intramedullary and/or leptomeningeal involvement. Sarcoidosis can also involve the extradural spine, including the vertebrae or rarely the epidural space or discs.^{11,12} While the appearance is highly variable, the classic enhancement pattern of neurosarcoidosis in the cord is of dorsal-subpial enhancement, which, when present, in combination with central canal enhancement, can resemble a trident head on axial images.^{10,13} There is often more longitudinally extensive cord signal abnormality on the T2-weighted images,⁴ as seen in all our cases. The appearance is not specific for the disease, so in patients with intramedullary spinal neurosarcoidosis without systemic involvement, the correct diagnosis is often difficult and delayed.³ Correlation between symptom resolution and resolution of imaging findings in neurosarcoidosis is poor, especially with spinal cord lesions. Enhancement typically decreases with treatment but may persist for years. In our series, long-term follow-up scans revealed persistent, small amounts of enhancement in 3 of 4 cases.

For intramedullary spinal neurosarcoidosis, steroids can result in remarkable recovery, particularly if treatment is started early in the course of the disease.³ However, the disease may only partially resolve and may recur, especially if there is a delay in diagnosis and treatment.^{3,14} It is recommended that corticosteroid therapy be started as early as possible, before irreversible gliofibrosis occurs in the cord. Conditions of some patients may continue to deteriorate despite treatment, and they can end up with paraparesis. Therefore, patients with spinal cord sarcoidosis typically are committed to a long duration of therapy with gradual tapering of steroids,¹⁴ and they often require additional immunosuppressant therapy.¹⁵

In many cases of intramedullary spinal neurosarcoidosis, biopsy is not desirable due to the morbidities associated with biopsy of the spinal cord. A diagnosis of probable neurosarcoidosis can be based on clinical or imaging evidence of lesions, with evidence of systemic sarcoidosis obtained from a biopsy of another organ. Four of our patients had lymph node biopsies revealing granulomatous inflammation, and the fifth patient had a known history of pulmonary sarcoidosis. The diagnosis can be supported by ≥ 2 other findings, such as typical chest adenopathy or elevated serum ACE levels,¹¹ though ACE levels are only elevated in 5%–50% of cases. PET/CT can be more sensitive to systemic involvement and could be considered if chest CT findings are equivocal or negative,¹⁶ particularly if there is high clinical suspicion of sarcoidosis based on other factors such as family history or genetic predisposition. The CSF examination most often shows nonspecific elevation in protein levels and lymphocytosis. All our patients who had CSF laboratory values available before initiating therapy had elevated lymphocyte levels and mild elevation in protein levels. Two of our patients also had elevation of glucose levels.

Spondylotic Myelopathy

There are a number of case reports and publications in the literature that describe a pattern of spondylotic myelopathy with cord enhancement and T2 signal abnormality. One of the first case reports was in 2008 by Cabraja et al.¹⁷ They noted a case of a 36-year-old man with 3 months of slowly progressive symptoms who was found to have contrast enhancement localized directly at the site of greatest narrowing of the spinal canal.

In 2010, Kelley et al¹⁸ published a case series of 5 cases of suspected spondylotic myelopathy with cord edema and focal enhancement at the site of maximal stenosis. After decompression, none had recurrent myelopathy with a mean follow-up of 27 months.

In a case series by Nurboja et al¹⁹ in 2012 of 6 patients with cervical spondylotic myelopathy, 1 patient failed to improve following decompressive surgery and was later found to have neurosarcoidosis on the basis of chest x-ray, serum ACE levels, and chest mediastinoscopy. They suggested an algorithm for treating these patients, starting with a referral to a neurologist with further possible investigations including MR imaging of the brain, CSF analysis, hematologic and biochemical analysis, and nerve-conduction studies, to exclude other causes such as inflammatory, demyelinating diseases or neoplasms. If no neurologic cause is found, then spinal cord decompression should be considered. After satisfactory surgical decompression, regular follow-up should be arranged with serial MR imaging, with biopsy if there is further clinical or radiologic deterioration.¹⁹

In 2013, Flanagan et al²⁰ introduced a distinctive type of enhancement that can occur in spondylotic myelopathy, termed “pancake-like enhancement,” with the term referring to enhancement that is wider than tall when viewed in the sagittal plane. Flanagan et al²¹ later assigned 3 guidelines for the enhancement to be considered pancake-like: 1) a transverse band appearance, greater in transverse than in vertical extent on sagittal images, 2) location just below the site of maximal stenosis at the center of a spindle-shaped T2 hyperintensity, and 3) circumferential enhancement sparing GM on axial images. In this retrospective analysis, the characteristic pancake-like enhancement was seen in 41/56 patients (73%) with cord enhancement associated with spondylotic myelopathy.²¹ After the operation, 39 patients reported some improvement, 14 reported stable symptoms, and conditions of 3 continued to deteriorate despite the operation. Enhancement was found to persist in the cord in 100% at 3 months, 75% at 12 months, and 62% at last follow-up. Hilar adenopathy was seen in 2 of 33 chest CTs, and 3 patients had pathologic evidence of systemic sarcoidosis. Marked clinical and radiologic improvement after an operation without immunosuppressant treatment excluded neurosarcoidosis as the cause of the myelopathy in 1 of the 3 patients. In the other 2 patients, sarcoidosis may have contributed to the myelopathy, but spondylitis was considered more likely due to the pancake-like enhancement and improvement after the operation. They noted that while this pancake-like enhancement pattern is strongly indicative of spondylotic myelopathy, the exclusion of alternative causes of myelopathy associated with gadolinium enhancement is impossible with complete certainty.²¹

Intramedullary Spinal Neurosarcoidosis at the Level of Cervical Spondylosis

Regarding intramedullary spinal neurosarcoidosis occurring as isolated CNS involvement only at sites of spinal canal stenosis, it has long been postulated that other inflammatory lesions, specifically MS plaques, tend to occur at sites of cord trauma and degenerative stenosis, with close anatomic correspondence between mechanical stresses on the cord by spondylosis and spinal cord MS plaques.^{22,23}

The trauma could result in loss of blood-cord barrier impermeability, which could allow the entrance of the antigen responsible for sarcoidosis into the cord as well as the entrance of T lymphocytes to set off the inflammatory cascade. As stated by Hickey,²⁴ “any mechanism that physically destroys the components of the blood cord barrier will render the CNS open to the cellular and molecular constituents of the blood. The participants for inflammation can then be rapidly delivered to the site of injury in a gross, nonspecific fashion.” This explanation would fit very well with the pattern that we observed in our 5 cases, with no disease elsewhere along the neuroaxis aside from that centered at or just below the site of maximal spinal canal stenosis.

In 2011, Sakai et al⁹ reported a retrospective review of 12 patients with spinal cord sarcoidosis and concomitant cervical spondylosis. They noted the possibility that compressive cervical myelopathy could trigger the development of inflammatory granulomas in spinal cord sarcoidosis and that the MRIs showed that areas of enhancing sarcoid lesions coincided with the maximum compression levels. One-third of the patients in their study had temporary improvement in symptoms after decompressive surgery. They concluded that in spinal cord sarcoidosis accompanied by compressive myelopathy, decompressive surgery should not be the first choice of treatment. They also noted that the outcome was poorer in patients with neurosarcoidosis and compressive myelopathy compared with those without compressive myelopathy.⁹ More recently in a study of phenotypes of sarcoidosis-associated myelopathy, Murphy et al¹⁰ described a pattern of anterior thoracic myelitis associated with areas of disc degeneration and suggested that there may be a predilection for involvement of areas of the spinal cord susceptible to mechanical stress. They also suggested that in some cases, sarcoidosis and spondylosis may both be contributing to the clinical and imaging picture.

The differential diagnosis for intramedullary spinal cord enhancement with associated longitudinally extensive signal abnormality in the cord is broad and includes sarcoidosis, spondylotic myelopathy, neuromyelitis optica, spinal cord tumor, and dural arteriovenous fistula. Spondylosis is a common incidental finding in patients presenting with cord abnormalities. When the spinal cord enhancement and edema are centered at or just below the site of maximal spinal canal stenosis, the primary considerations should be intramedullary spinal neurosarcoidosis and spondylotic myelopathy. While our cases fulfilled some of the rules set forth by Flanagan et al,²¹ including location just below the site of maximal stenosis in the center of a spindle-shaped T2 hyperintensity and circumferential enhancement sparing GM on axial images, none of our cases had a band of enhancement that was greater in the transverse than in the vertical extent on sagittal images. This feature may be the most useful

finding to differentiate spondylotic myelopathy from intramedullary spinal neurosarcoidosis.

CONCLUSIONS

Intramedullary spinal neurosarcoidosis can have an identical imaging appearance and clinical presentation to spondylotic myelopathy, and intramedullary spinal neurosarcoidosis can be isolated only to sites of spondylotic spinal canal stenosis. We believe that in patients with cord enhancement centered at or just below a site of spinal canal stenosis, consideration should be given to chest imaging and lymph node biopsy if there is nodal enlargement. These recommendations are in addition to those previously put forth by others. A presurgical course of corticosteroids should be considered to see if there is improvement or resolution of symptoms without surgery. While urgent surgery may be warranted if a patient presents acutely, many of these patients present with subacute-to-chronic symptoms, allowing time for a trial of corticosteroids. It is also possible that some patients may ultimately benefit from surgical decompression in addition to medical management of sarcoidosis due to the coexistence of the 2 pathologies.

Disclosure forms provided by the authors are available with the full text and PDF of this article at www.ajnr.org.

REFERENCES

1. Durel CA, Marignier R, Maucourt-Boulch D, et al. **Clinical features and prognostic factors of spinal cord sarcoidosis: a multicenter observational study of 20 BIOPSY-PROVEN patients.** *J Neurol* 2016;263:981–90 CrossRef Medline
2. Joseph FG, Scolding NJ. **Sarcoidosis of the nervous system.** *Pract Neurol* 2007;7:234–44 CrossRef Medline
3. Koike H, Misu K, Yasui K, et al. **Differential response to corticosteroid therapy of MRI findings and clinical manifestations in spinal cord sarcoidosis.** *J Neurol* 2000;247:544–49 CrossRef Medline
4. Christoforidis GA, Spickler EM, Recio MV, et al. **MR of CNS sarcoidosis: correlation of imaging features to clinical symptoms and response to treatment.** *AJNR Am J Neuroradiol* 1999;20:655–69 Medline
5. Davies BM, Khan DZ, Barzangi K, et al. **We choose to call it ‘degenerative cervical myelopathy’: findings of AO spine recode-dcm, an international and multi-stakeholder partnership to agree a standard unifying term and definition for a disease.** *Global Spine J* 2022 June 29. [Epub ahead of print] CrossRef Medline
6. Sasamori T, Hida K, Yano S, et al. **Spinal cord swelling with abnormal gadolinium-enhancement mimicking intramedullary tumors in cervical spondylosis patients: three case reports and review of the literature.** *Asian J Neurosurg* 2010;5:1–9 Medline
7. Lee J, Koyanagi I, Hida K, et al. **Spinal cord edema: unusual magnetic resonance imaging findings in cervical spondylosis.** *J Neurosurg* 2003;99:8–13 CrossRef Medline
8. Tipper GA, Fareedi S, Harrison K, et al. **Neurosarcoidosis mimicking acute cervical disc prolapse.** *Br J Neurosurg* 2011;25:759–60 CrossRef Medline
9. Sakai Y, Matsuyama Y, Imagam S. **Spinal cord sarcoidosis accompanied with compressive cervical myelopathy.** In: Kalantar Motamed MH, ed. *Sarcoidosis Diagnosis and Management. InTech*; 2011
10. Murphy OC, Salazar-Camelo A, Jimenez JA, et al. **Clinical and MRI phenotypes of sarcoidosis-associated myelopathy.** *Neurol Neuroimmunol Neuroinflamm* 2020;7:e722 CrossRef Medline
11. Smith JK, Matheus MG, Castillo M. **Imaging manifestations of neurosarcoidosis.** *AJR Am J Roentgenol* 2004;182:289–95 CrossRef Medline

12. Paglia F, D'Angelo L, Armocida D, et al. **A rare case of spinal epidural sarcoidosis: case report and review of the literature.** *Acta Neurol Belg* 2021;121:415–20 CrossRef Medline
13. Zalewski NL, Krecke KN, Weinshenker BG, et al. **Central canal enhancement and the trident sign in spinal cord sarcoidosis.** *Neurology* 2016;87:743–44 CrossRef Medline
14. Hashmi M, Kyritsis AP. **Diagnosis and treatment of intramedullary spinal cord sarcoidosis.** *J Neurol* 1998;245:178–80 CrossRef Medline
15. Bradley DA, Lower EE, Baughman RP. **Diagnosis and management of spinal cord sarcoidosis.** *Sarcoidosis Vasc Diffuse Lung Dis* 2006;23:58–65 Medline
16. Fritz D, van de Beek D, Brouwer MC, et al. **Whole-body 18F-FDG PET-CT in the diagnosis of neurosarcoidosis.** *Mayo Clin Proc* 2020;95:1082–84 CrossRef Medline
17. Cabraja M, Abbushi A, Costa-Blechsmidt C, et al. **Atypical cervical spondylotic myelopathy mimicking intramedullary tumor.** *Spine (Phila Pa 1976)* 2008;33:E183–87 CrossRef Medline
18. Kelley BJ, Erickson BJ, Weinshenker BG. **Compressive myelopathy mimicking transverse myelitis.** *Neurologist* 2010;16:120–22 CrossRef Medline
19. Nurboja B, Chaudhuri A, David KM, et al. **Swelling and enhancement of the cervical spinal cord: when is a tumour not a tumour?** *Br J Neurosurg* 2012;26:450–55 CrossRef Medline
20. Flanagan EP, Marsh RW, Weinshenker BG. **Teaching neuroimages: “pancake-like” gadolinium enhancement suggests compressive myelopathy due to spondylosis.** *Neurology* 2013;80:e229 CrossRef Medline
21. Flanagan EP, Krecke KN, Marsh RW, et al. **Specific pattern of gadolinium enhancement in spondylotic myelopathy.** *Ann Neurol* 2014;76:54–65 CrossRef Medline
22. Poser CM. **Trauma to the central nervous system may result in formation or enlargement of multiple sclerosis plaques.** *Arch Neurol* 2000;57:1074–77, discussion 1078 CrossRef Medline
23. Gratch D, Do D, Khankhanian P, et al. **Impact of cervical stenosis on multiple sclerosis lesion distribution in the spinal cord.** *Mult Scler Relat Disord* 2020;45:102415 CrossRef Medline
24. Hickey WF. **Migration of hematogenous cells through the blood-brain barrier and the initiation of CNS inflammation.** *Brain Pathol* 1991;1:97–105 CrossRef Medline

The Dominant Anterior Thoracic Artery of the Spinal Cord

J.E. Small and V.H. Pérez Pérez

ABSTRACT

BACKGROUND AND PURPOSE: Dominant radiculomedullary arteries such as the artery of lumbar enlargement and the artery of cervical enlargement are well-documented. However, variability exists as to the size, number, and location of other radiculomedullary arteries contributing supply to the anterior spinal artery. The aim of this anatomic study was to document the prevalence and characteristics of the dominant anterior thoracic artery in cadaveric specimens.

MATERIALS AND METHODS: Microsurgical dissection of cadaveric human spinal cord specimens ($n = 50$) was conducted. The artery of lumbar enlargement was injected with colored latex until the small-caliber arterial vessels were filled. The dominant anterior thoracic artery was identified, injected, and filled with diluted industrial paint. The course, diameter, and location of the dominant anterior thoracic artery, artery of lumbar enlargement, and artery of cervical enlargement were documented.

RESULTS: The artery of lumbar enlargement was identified between T3 and L2 in all 50 specimens (100%), and the artery of cervical enlargement was identified in 84% of specimens (42/50). At least 1 dominant anterior thoracic artery distinct from the artery of lumbar enlargement and the artery of cervical enlargement was identified between T1 and T11 in 47 of the 50 specimens (94%). The most frequent origin of the dominant anterior thoracic artery was at the level of T4 on the left. The average size of the dominant anterior thoracic artery was 0.446 mm (range, 0.300–0.759 mm on the left and 0.270–0.569 mm on the right).

CONCLUSIONS: A dominant anterior thoracic artery is present in 94% of individuals. Variations of the arterial supply to the anterior thoracic cord are of great importance due to their implications for ischemic events as well as surgical and endovascular procedures.

ABBREVIATIONS: ACE = artery of cervical enlargement; ALE = artery of lumbar enlargement; ASA = anterior spinal artery; DATA = dominant anterior thoracic artery; RMA = radiculomedullary artery

Variations of the arterial supply to the anterior thoracic cord are important due to their implications for ischemic events as well as surgical and endovascular procedures. Radiculomedullary arteries (RMAs) represent the dominant arterial supply to the spinal cord and are the sole segmental supply to the anterior spinal artery (ASA) along the ventral cord.¹ The ASA ranges from 0.2 to 0.8 mm and has an inconsistent caliber along its length.^{2–4} The fluctuating size is related to the variable number of RMAs specifically providing arterial supply to the ventral cord.^{4,5} The number, caliber, and entrance level of the anterior RMAs have been previously studied^{6–8} and ranges in number from 2–14.²

Dominant radiculomedullary and radiculopial arteries such as the artery of lumbar enlargement (ALE),^{2–4} the artery of cervical enlargement (ACE),¹ and the great posterior radiculomedullary artery⁸ are well-documented. Historically, 2 RMAs have received the most consideration. In the lower thoracic or upper lumbar region, the dominant and most important radiculomedullary supply is the ALE, otherwise known as the arteria radiculomedullaris magna or, more commonly, the artery of Adamkiewicz.^{2–4} The ALE arises between T8 and L2 in 75% of individuals with a diameter ranging between 0.5 and 1.2 mm.^{2,3} The largest anterior cervical radiculomedullary branch is generally in the region of C5 through C6 and has been termed the ACE.¹ Although dominant RMAs such as the ALE and ACE are well-documented, variability exists as to the size, number, and location of other RMAs contributing supply to the ASA. Because RMAs other than the ALE have a considerably smaller diameter, they are difficult to identify on imaging, including angiography. Traditionally, RMAs arising from upper thoracic segmental arteries are generally regarded as branches only rarely present and therefore of little clinical

Received August 31, 2022; accepted after revision October 25.

From Lahey Hospital and Medical Center (J.E.S.), Burlington, Massachusetts; and Instituto de Ciencias Forenses (V.H.P.P.), TSJ Ciudad de México, Centro Medico Siglo XXI, Mexico City, Mexico.

Please address correspondence to Victor Hugo Pérez Pérez, MD, Instituto de Ciencias Forenses, TSJ Ciudad de México, Centro Medico Siglo XXI, Mexico City, Mexico; e-mail: victorhugo2perez@hotmail.com

<http://dx.doi.org/10.3174/ajnr.A7737>

significance. This notion has led to the commonly taught and widely held belief that the anterior thoracic arterial system represents a watershed territory.

A spinal angiography study conducted in 50 individuals identified a significant upper thoracic anterior RMA distinct from the ALE in 86% of patients.⁹ Due to the relatively constant nature of this artery, the author suggested naming this vessel the artery of von Haller. This was proposed in honor of Albrecht von Haller, who documented the arterial supply to the ASA including this vessel as well as the ALE in 1754,^{5,10} more than a century before Albert Adamkiewicz^{11,12} and Kadyi.¹³ However, instead of the artery of von Haller, we opted to refer to this vessel as the dominant anterior thoracic artery (DATA) so that the name could provide easy recognition and support more reliable terminology. The DATA has attracted little attention in the literature, and its importance is not widely known or taught. In addition, its angiographic identification is quite difficult due to its caliber as well as obscuration by overlying structures, including osseous and muscular arterial branches as well as the trachea.⁹ The aim of this anatomic study was to analyze the arterial supply to the ventral spinal cord and determine the prevalence of the DATA along with its morphometric characteristics in cadaveric specimens.

MATERIALS AND METHODS

We conducted an institutional review board–approved study of 50 (49 male and 1 female) cadaveric specimens at the Institute of Forensic Sciences of Mexico City (Instituto de Ciencias

Forenses de la Ciudad de Mexico). The cadavers ranged from 22 to 70 years of age, with a median age of 45 years. Spinal cord extraction was conducted after a posterior midline longitudinal incision from the occiput to the sacrum as well as laminectomies throughout the entirety of the cervical, thoracic, and lumbar spine. The spinal nerves were then cut with great care so as not to lesion the dura. Ventral and dorsal longitudinal midline durotomies were subsequently performed, and the spinal cord was irrigated with saline. To remove residual intravascular blood, the vascular system was irrigated with saline. After completing these steps, the ALE was identified, an angiocatheter of commensurate size was selected for cannulation, and injection of red natural latex was performed. Injection was conducted with close visual inspection and under moderate pressure in an attempt to prevent vessel rupture and contrast extravasation. The DATA was identified, and a microcatheter of commensurate size was selected to inject and fill this vessel with diluted industrial red paint. Diluted industrial paint was used in this step because natural latex was too viscous to fill vessels of this small caliber. We proceeded until latex and paint filled distal small-caliber arterial vessels. The specimens were then fixed in a 5% formaldehyde solution for 2 weeks. The spinal cord specimens were then studied with the aid of 5x surgical loupes. The ALE, the ACE, and any thoracic RMAs consistent with the DATA were identified and documented. Measurements were obtained with digital Vernier calipers. Digital photographic images were obtained including a measurement scale to corroborate caliper measurements with digital measurements.

RESULTS

No vascular malformations, fistulas, or other vascular abnormalities were identified in any of the specimens.

In only 3 specimens (3/50) was the DATA not identified. At least 1 DATA was evident in 94% of spinal cord specimens (47/50). A single DATA was present in 66% of the specimens (33/50) (Fig 1). Two DATAs were identified in 26% (13/50) (Fig 2). Three DATAs were identified in a single (1/50) specimen (2%), all arising on the left at the level of T3, T7, and T9. The laterality and spinal level of the DATA are summarized in Fig 3. A DATA was most frequently identified at the level of T4, with 15 left- and no right-sided specimens

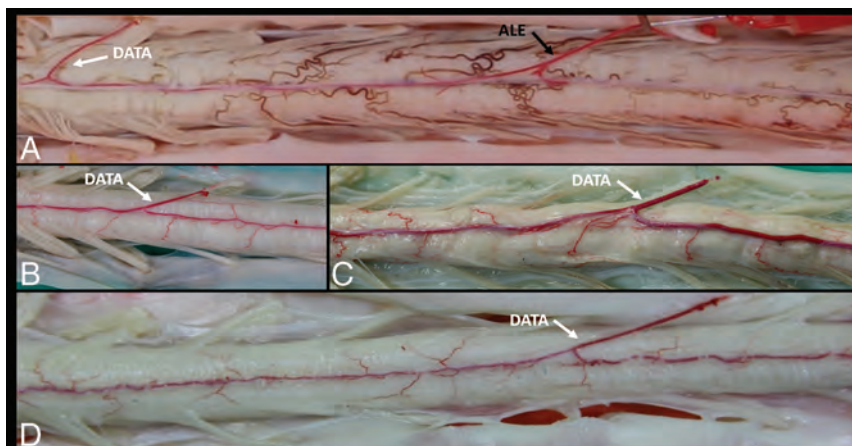


FIG 1. Single DATA. The anterior view of the spinal cord during arterial injection (A) clearly shows a T9 ALE (black arrow) as well as a single T4 DATA (white arrow), the most common level in our analysis. Three other specimens after fixation (B–D) clearly demonstrate a single dominant upper thoracic anterior RMA supplying the ASA, consistent with a DATA (white arrows).

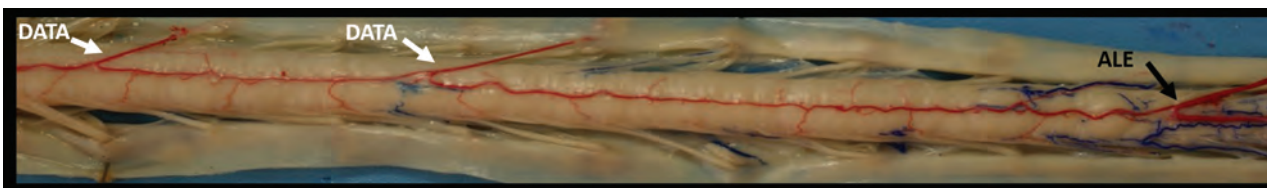


FIG 2. Two DATAs. The anterior view of the spinal cord clearly reveals evidence of the ALE (black arrow) as well as 2 left-sided DATAs consistent with 2 separate DATAs (white arrows) supplying the ASA.

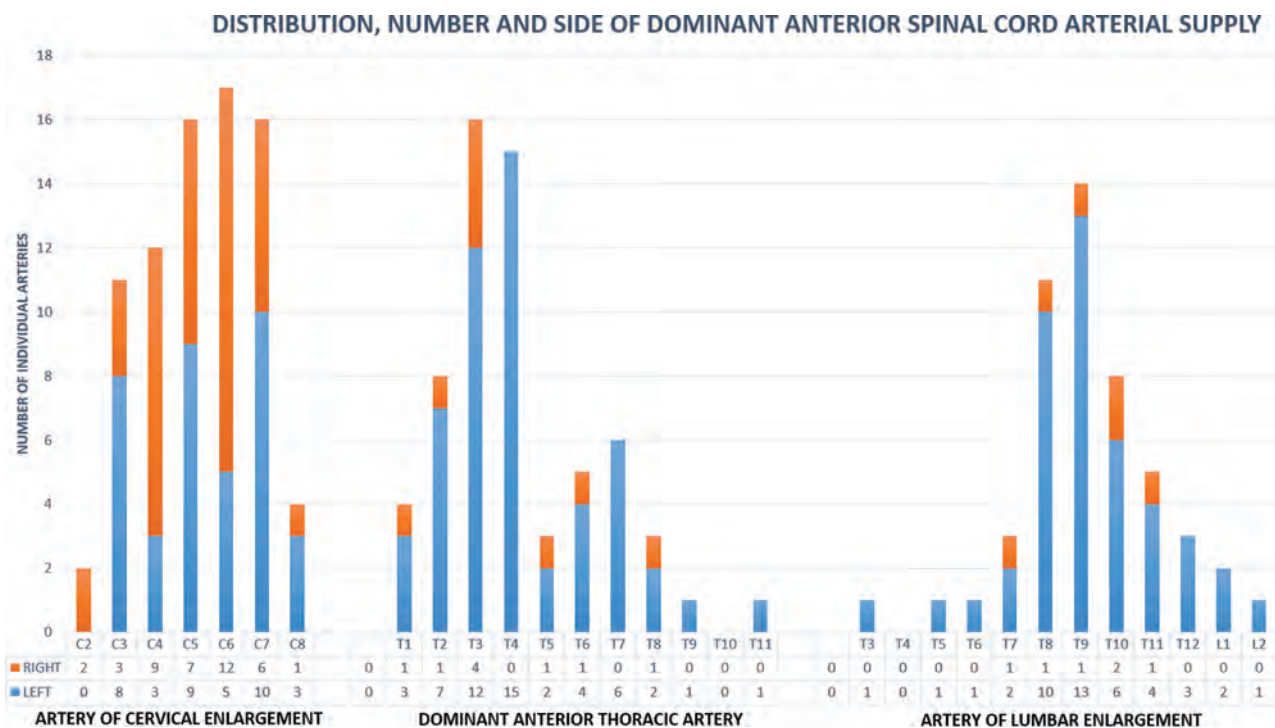


FIG 3. Distribution, number, and side of the ACE, DATA, and ALE.

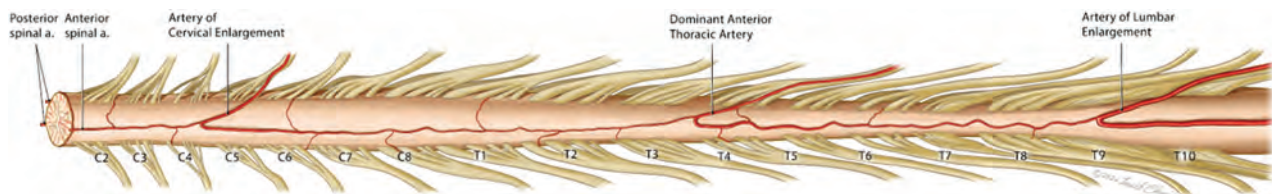


FIG 4. Dominant RMAs. In most individuals, at least 3 dominant RMAs exist and include the ALE, ACE, and DATA as illustrated and labeled above. The DATA is shown on the left at the level of T4, the most common side and level in our study. a. indicates artery.

identified at this level. The average DATA size was 0.446 mm, with a range of 0.300–0.759 mm on the left and 0.270–0.569 mm on the right.

The ALE was identified between T3 and L2 in all 50 spinal cords (100%). A left-sided ALE was present in 44 specimens, and a right-sided ALE was present in 6 specimens. The most proximal ALE was evident at the level of T3 on the left, and the most distal, at the level of L2 on the left. The side and spinal level of ALEs are summarized in Fig 3. On average, the diameter of the ALE was 0.83 mm, with the smallest caliber ALE measuring 0.49 mm and the largest measuring 1.21 mm.

The ACE was identified in 84% of specimens (42/50). A single ACE was present in 20 specimens; 2 separate ACEs, in 12 specimens; 3 ACEs, in 6 specimens; and 4 ACEs, in 4 specimens. A total of 78 ACEs were, therefore, documented, with 38 on the left and 40 on the right. The most proximal ACE was evident at the level of C2, and the most distal, at the level of C8. The side and spinal level of the ACEs are summarized in Fig 3. On average, the diameter of the ACE was 0.49 mm, with the smallest caliber ACE measuring 0.13 mm and the largest measuring 0.73 mm. In the 8 specimens in which no ACE was identified, the DATA originated

at T2 in 2 specimens, T3 in 3 specimens, T4 in 1 specimen, and T8 in 2 specimens.

DISCUSSION

Our results demonstrate that a DATA is present in most individuals (94%). Our findings are similar but more robust than those in the study of Gailloud,⁹ in 2013, in which a total of 43 of 50 patients (86%) had at least 1 RMA branch between T3 and T7, with a single anterior branch in 68% (34/50), 2 anterior branches in 18% (9/50), and none with 3 anterior branches. In contrast, we found a single DATA in 66% (33/50), 2 in 26% (13/50), and 3 in 2% (1/50). Improved detection in our cadaveric findings is likely due to increased sensitivity and accuracy because the upper thoracic RMAs may be obscured by overlying osseous or muscular branches on spinal angiography.

Although the caliber of the DATA did not approximate that of the ALE, the vessels were truly dominant and easily distinguished from the tiny caliber of the radicular arteries that accompany spinal nerves. Of note, no absolute cutoff measurement was used to establish the presence of a DATA because establishing the presence of a

dominant arterial feeder is a relative process specific to each individual. For instance, paucisegmental and plurisegmental ASA circulations are associated with markedly differing calibers of the ALE.

Although naming RMAs is necessarily arbitrary in nature, the presence of an ALE, ACE, and DATA in 42 of our specimens validates the naming of each of these vessels. In other words, the dominant upper thoracic RMA in a specimen clearly demonstrating an ALE and an ACE is best regarded as a DATA rather than a high-origin ALE or a low-origin ACE. Furthermore, in the 8 cases in which we did not identify an ACE, the DATA distribution from T2 through T8 did not demonstrate a high thoracic clustering, arguing against naming all these vessels as low-origin ACEs. In particular, it is difficult to justify the classification of the cases with no ACE and a DATA at either T4 or T8 as a low ACE variant instead.

These results are contrary to the notion that in most individuals, there is a thoracic spinal cord watershed zone at risk of ischemia. The presence of a DATA in most individuals counters the erroneous belief that there is a poorly arterialized thoracic segment. Instead, the concept that in most individuals there are at least 3 dominant RMAs such as the ALE, ACE, and DATA should be endorsed and taught during anatomic discussions (Fig 4). Our results have implications for reducing the risk of arterial spinal and aortic surgical and endovascular procedures. In particular, our findings are important for addressing vascular malformations of the spinal cord. The degree of involvement of the DATA in spinal cord pathology has yet to be studied, and we believe this would be a fruitful area for future research.

The number of specimens we examined supports the reliability of our vessel distribution, laterality, and diameter determinations. However, because most of our anatomic specimens were from male cadavers, we cannot exclude the unlikely possibility that sex differences exist. In addition, the possibility of racial variations cannot be excluded on the basis of this study.

CONCLUSIONS

A DATA is conclusively present in most individuals (94%). A more robust understanding of the intricate spinal arterial

anatomy and its variations is critical for endovascular procedures. A better appreciation of the spinal cord circulation will lead to a reduced risk of surgical and endovascular spinal and aortic procedures.

Disclosure forms provided by the authors are available with the full text and PDF of this article at www.ajnr.org.

REFERENCES

1. Lazorthes G. **Blood supply and vascular pathology of the spinal cord.** In: Pia HW, Djindjian R, eds. *Spinal Angiomas: Advances in Diagnosis and Therapy*. Springer-Verlag; 1978:1–17
2. Gregg L, Gailloud P, Gregg L. **Neurovascular anatomy: spine.** *Handb Clin Neurol* 2021;176:33–47 CrossRef Medline
3. Santillan A, Nacarino V, Greenberg E, et al. **Vascular anatomy of the spinal cord.** *J Neurointerv Surg* 2012;4:67–74 CrossRef Medline
4. Vargas MI, Gariani J, Sztajzel R, et al. **Spinal cord ischemia: practical imaging tips, pearls, and pitfalls.** *AJNR Am J Neuroradiol* 2015;36:825–30 CrossRef Medline
5. Kadyi H. *Über die Blutgefäße des menschlichen Rückenmarkes.* Gubrynowicz & Schmidt; 1889
6. Jellinger K. *Zur Orthologie und Pathologie der Rückenmarksdurchblutung.* Springer-Verlag; 1966
7. Pisco K. *Die Blutversorgung des Rückenmarks und ihre klinische Relevanz.* Springer-Verlag; 1972
8. Perez Perez VH, Hernesniemi J, Small JE. **Anatomy of the great posterior radiculomedullary artery.** *AJNR Am J Neuroradiol* 2019;40:2010–15 CrossRef Medline
9. Gailloud P. **The artery of von Haller: a constant anterior radiculomedullary artery at the upper thoracic level.** *Neurosurgery* 2013;73:1034–43 CrossRef Medline
10. von Haller A. *Iconum anatomicarum quibus aliquae partes Corporis Humani delineatae traduntur, Fasciculus VII, Arteriae cerebri medullae spinalis oculi.* 1782
11. Adamkiewicz A. **Die Blutgefäße des menschlichen Rückenmarkes. I. Theil. Die Gefäße der Rückenmarkssubstanz.** *Sitzungsberichten der Kaiserlichen Akademie der Wissenschaften, Mathematisch-naturwissenschaftliche Classe.* 1881;84:469–502
12. Adamkiewicz A. **Die Blutgefäße des menschlichen Rückenmarkes. II. Theil. Die Gefäße der Rückenmarks-Oberfläche.** *Sitzungsberichten der Kaiserlichen Akademie der Wissenschaften, Mathematisch-naturwissenschaftliche Classe.* 1882;85:101–30
13. Kadyi H. *Über die Blutgefäße des Menschlichen Rückenmarkes.* Gubrynowicz & Schmidt; 1889

Celebrating 35 Years of the AJNR

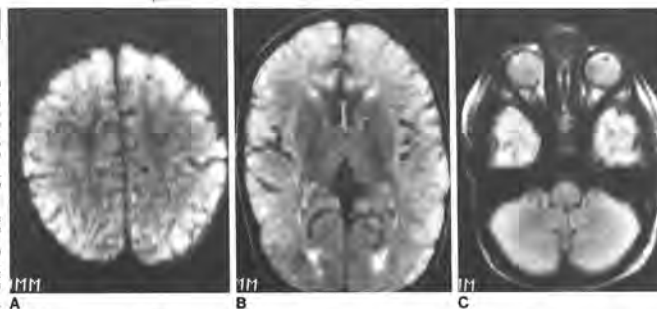
January 1988 edition

MR Evaluation of Early Myelination Patterns in Normal and Developmentally Delayed Infants

Rosalind B. Dietrich¹
William G. Bradley²
Edward J. Zarogova IV¹
Ronald J. Otto²
Ricki K. Tarr¹
Gabriel H. Wilson¹
Hoshsang Kargarloo¹

This study demonstrates the ability of MR imaging to show progress in 64 infants and young children (ages 4 days to 36 months). T2 pulse sequences, frequently used for routine screening of intracranial space, gray-white matter differentiation was seen in all patients, as well as age were documented. Three distinct patterns were seen, as established for each pattern in developmentally normal children: (1) normal (0-12 months), (2) intermediate (12-24 months), and (3) early adult (24 months or older). These data should be helpful for identifying and following up on clinically suspected developmental delay and those with dysmaturational disease.

Myelination is a dynamic process starting during intrauterine life and can thus be used as an index of brain maturation. In the first 2 years, when changes are occurring most frequently, when developmental delay is suspected clinically, opportunity to study myelination in vivo in normal and atypical sequentially and relative to a known standard. Such children are using combinations of long and short TR and long and short sequences. It is therefore imperative for the radiologist to be familiar with the normal appearance of the progression of myelination on these sequences if delay in myelination or abnormalities involving the white matter are to be detected and accurately diagnosed at the earliest possible time. It is also important that the



This article appears in the January 1988 issue of AJNR and the April 1988 issue.

Received January 21, 1987; revised July 13, 1987.

¹Department of Radiological Sciences, University of California, Los Angeles, CA. Address reprint requests to R. B. Dietrich.

²University Medical Research Institute, Los Angeles, CA.

AJNR 9:8-16, January/February 1988. 0195-9581/88/0001-0008.

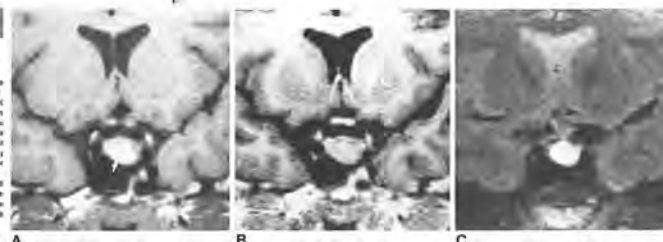
© American Society of Neuroradiology.

1.5-T MR Imaging of Pituitary Microadenomas: Technical Considerations and CT Correlation

Maden V. Kulkarni¹
K. Francis Lee¹
Craig B. McArthur¹
Joel W. Yeakley¹
Floyd L. Haar²

Thirty-seven patients with suspected pituitary tumors were imaged with 1.5-T MR. MR detected a microadenoma at eight patients who underwent transphenoidal surgery, while (1) in the correct location in only four of the eight patients clinically and endocrinologically considered to have a microadenoma. Pituitary signal abnormality in 83% and CT demonstrated microadenoma in 42%. Infundibular displacement, focal gland convexity, and asymmetry were seen equally well with CT and MR. MR imaging (T1-weighted spin-echo, coronal inversion-recovery, and coronal gated spin-echo images).

Although inversion-recovery images were superior in detecting microadenomas, better seen on T2-weighted images. MR images showed focal pituitary lesions better than CT. This technique demonstrates MR's superior sensitivity to CT in detecting microadenomas.



CT has been widely used as an imaging method in the detection of pituitary tumors. High-resolution CT with IV contrast material, sagittal and coronal reformatting, and direct coronal imaging have shown the utility of CT in the imaging of the pituitary gland and its lesions [1-11]. Although indirect signs for the diagnosis of a pituitary microadenoma such as sella floor erosion, focal convexity, and displacement of the infundibulum are well shown by CT, the detection of a focal hypo- or hyperdense lesion within the pituitary gland is the only statistically significant indicator of microadenoma [12]. However, microadenomas may reveal few or no abnormalities on CT [12, 13].

In recent years MR has also been useful in evaluating the pituitary gland [14-17]. High-resolution MR imaging has shown good results in the diagnosis of pituitary micro- and macroadenomas. However, in a recent comparative study, CT was found to be superior to MR in detecting microadenomas [18]. We prospectively evaluated patients with suspected pituitary tumors with MR and compared the results with available CT findings. The use of coronal gated spin-echo and inversion-recovery techniques in diagnosing pituitary microadenomas was also evaluated. The imaging data were subsequently compared with clinical, endocrinological, and surgical data.

Subjects and Methods

Thirty-seven patients with suspected pituitary tumors were examined. Six patients had pituitary lesions 12 mm or larger and were diagnosed as having pituitary macroadenomas. Of the 31 microadenoma patients (27 women, four men) 22 had increased prolactin and one had elevated adrenocorticotropic hormone. Amenorrhea, infertility, and/or galactorrhea were common symptoms in female patients. One male patient with impotence and three male patients with galactorrhea were found to have elevated prolactin levels (35-500 ng/mL). Two

Received May 27, 1987; accepted after revision August 12, 1987.

Presented at the annual meeting of the American Society of Neuroradiology, New York City, May 1987.

¹Department of Radiology, University of Texas Medical School at Houston and Hermann Hospital, 6431 Fannin, 2, 2A, MSB, Houston, TX 77030. Address reprint requests to M. V. Kulkarni.

²Department of Radiology, University of Texas Medical School at Houston and Hermann Hospital, Houston, TX 77030.

AJNR 9:8-16, January/February 1988. 0195-9581/88/0001-0008.

© American Society of Neuroradiology.

This is a correction to Yogananda CG, Shah BR, Nalawade SS, et al. **MRI-based deep-learning method for determining glioma MGMT promoter methylation status.** *AJNR Am J Neuroradiol* 2021;42:845–52 [10.3174/ajnr.A7029] [33664111]

There was an error in the Python code for the 3-fold cross-validation procedure. This resulted in the use of the training cases instead of the set-aside test cases for the testing procedure for molecular marker accuracy. This caused our reported accuracies from the TCIA/TCGA data set to be artificially inflated. The corrected accuracies for the Table (computed using nnU-Net¹), along with the updated receiver operating characteristic (ROC) curve for Fig 3 are provided here. The updated accuracies do not outperform other reported methods for MGMT molecular marker prediction using MR imaging.

Cross-validation results

Fold Description	MGMT-Net		
	% Accuracy	AUC	Dice Score
Fold no.			
Fold 1	59.75	0.4966	0.7906
Fold 2	73.49	0.6588	0.7725
Fold 3	64.63	0.5854	0.7874
Average	65.95 (SD, 0.06)	0.5802 (SD, 0.081)	0.7835 (SD, 0.009)

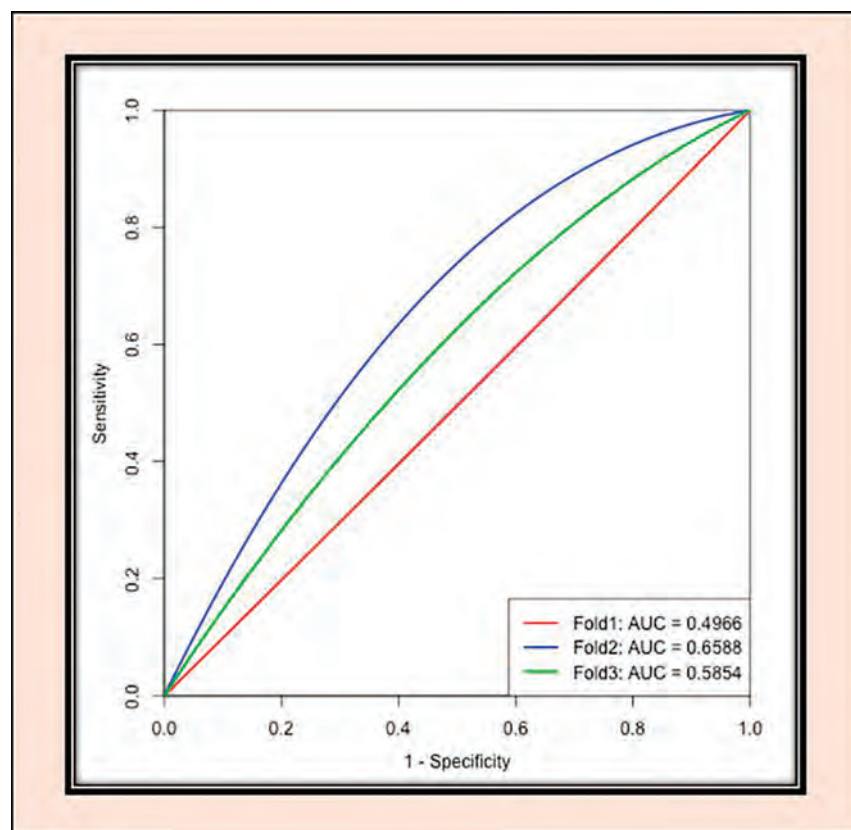


FIG 3. ROC analysis for MGMT-net. Separate curves are plotted for each cross-validation fold along with corresponding area under the curve (AUC) values.

REFERENCE

- Isensee F, Jaeger PF, Kohl SAA, et al. **nnU-Net: a self-configuring method for deep learning-based biomedical image segmentation.** *Nat Methods* 2021;18:203–11 CrossRef Medline

Regarding “Emergency Department Visits for Chronic Subdural Hematomas within 30 Days after Surgical Evacuation with and without Middle Meningeal Artery Embolization”

I read with great interest the retrospective clinical study by Catapano et al¹ on the evaluation of emergency department (ED) visits and re-admission within 30 days for patients with chronic subdural hematomas (cSDH) with and without adjunctive middle meningeal artery embolization. To address this issue, the aforementioned authors included 137 patients with cSDH based on the inclusion criteria. Patients were divided into 2 groups (the surgery-only group and the combined group) according to the presence or absence of middle meningeal artery embolization. The authors compared the ED visits and re-admission within 30 days for patients with cSDH between the 2 groups. The results concluded that there were fewer 30-day emergency department visits in the combined group compared with the surgery-only group.

I would like to understand more information about this excellent research work and would like to share my personal views according to previously published studies.

First, the authors did not disclose the preoperative and postoperative management of patients between the 2 groups, including anticoagulants or antiplatelet agent therapy and statin use. Statins may reduce inflammatory signaling and promote hematoma resorption by decreasing the expression of inflammatory mediators on the hematoma pseudomembrane in patients with cSDH. A prospective clinical trial on critical independent predictors of the success of atorvastatin monotherapy treatment suggested that higher total cholesterol, lower hematoma volume, and less midline shift in atorvastatin monotherapy are independent factors predictive of success.² Therefore, the authors should uncover the details of postoperative management between the 2 groups.

Second, the authors described ED visits and re-admission within 30 days as the primary outcomes. There were 34 patients with ED visits and 17 patients with re-admission within 30 days. I wonder whether follow-up recurrence of cSDH occurred in these patients and if these patients had been re-admitted to the hospital for any other reasons, which may be a potential source of bias.

In addition, the authors acknowledge the limitations of this study, including the single-center and retrospective design and all the procedures performed by the different operators and different surgical teams. Given that limitations are inevitable, even in high-quality studies, further large-scale prospective randomized controlled studies are required to validate the conclusions from this article. There are related clinical trials underway to make the current picture clearer.

Disclosure forms provided by the authors are available with the full text and PDF of this article at www.ajnr.org.

REFERENCES

1. Catapano JS, Scherschinski L, Rumalla K, et al. **Emergency department visits for chronic subdural hematomas within 30 days after surgical evacuation with and without middle meningeal artery embolization.** *AJNR Am J Neuroradiol* 2022;43:1148–51 CrossRef Medline
2. Wang D, Tian Y, Wei H, et al. **Risk factor analysis of the conservative treatment in chronic subdural hematomas: a substudy of the ATOCH Trial.** *Adv Ther* 2022;39:1630–41 CrossRef Medline

© L. Wang

Department of Neurosurgery
Zhongnan Hospital of Wuhan University
Wuhan, China

<http://dx.doi.org/10.3174/ajnr.A7654>

REPLY:

We thank Dr Wang¹ for the interest and careful review of our article “Emergency Department Visits for Chronic Subdural Hematomas within 30 Days after Surgical Evacuation with and without Middle Meningeal Artery Embolization.”² Middle meningeal artery (MMA) embolization is a promising treatment technique for chronic subdural hematomas (cSDHs) that is efficacious and safe.^{3–6} The goal of the aforementioned study was to evaluate the treatment efficacy of MMA embolization using standardized outcome measures as determined by emergency department visits and re-admissions within 30 days. Using a retrospective study design, we demonstrated that surgical evacuation combined with MMA embolization in patients with cSDH is associated with reduced 30-day emergency department use compared with surgical evacuation alone.

First, Dr Wang noted the potential impact on cSDH resolution and recurrence of postoperative medical management, including anticoagulation, antiplatelet, and statin therapy. Although we did not collect data on medical therapy, we provided data on comorbidities, including hypertension, diabetes, coronary artery disease, cerebrovascular events, and coagulopathy, among others, and we found no significant differences between the 2 treatment groups. While we agree that postoperative medical management may be implicated in the treatment outcome of cSDH, the potential influence of these drugs remains a subject of debate. For instance, Chang et al⁷ reported that antiplatelet therapy adversely affected hematoma resolution at 6 months—a finding that became nonsignificant on multivariate analysis. Other studies reporting similar findings have also expressed concern for an increased risk of thromboembolic events that must be weighed against the contentious risk of hematoma recurrence.^{8–10}

Likewise, there is controversy in the literature about whether statins are predictors of cSDH recurrence. In an institutional study, Housley et al¹¹ reported no differences in complete resolution and recurrence among patients with perioperative statin therapy versus those without statin therapy. In consideration of the ambiguity of postoperative medical management after cSDH treatment, we conclude that randomized controlled studies are needed to decipher the role of postoperative medical therapeutics as independent predictors of treatment outcome and disease recurrence.

Second, Dr Wang raised concern that readmissions unrelated to the index procedure may be a potential source of bias. As stated in the results, the readmission rate was largely higher among patients with an operation alone compared with combined therapy, and of those, most patients were re-admitted due to recurrence or a residual of cSDH. This finding stands in contrast to only 1 patient who was re-admitted for hematoma recurrence after adjuvant MMA embolization. Although we could not statistically compare these groups because of their small sample size, it is unlikely that miscellaneous reasons for re-admission introduced bias of any kind. We agree that longer follow-up of the groups would be of interest and merits future analysis.

Last, we agree with Dr Wang’s concluding remark that large-scale, prospective randomized controlled studies with predetermined outcome measures are required to validate the efficacy of MMA embolization as frontline-versus-adjuvant therapy for the treatment of cSDH.

Disclosures: Dr Ducruet is a consultant for Medtronic, PLC (Dublin, Ireland), Penumbra (Alameda, California), Stryker (Kalamazoo, Michigan), CERENOVUS (Johnson & Johnson Medical Devices Companies, Irvine, California), and Koswire (Flowery Branch, Georgia).

REFERENCES

1. Wang L. **Letter: Emergency department visits for chronic subdural hematomas within 30 days after surgical evacuation with and without middle meningeal artery embolization.** *J Neurointerv Surg* 2022. In press
2. Catapano JS, Scherschinski L, Rumalla K, et al. **Emergency department visits for chronic subdural hematomas within 30 days after surgical evacuation with and without middle meningeal artery embolization.** *AJNR Am J Neuroradiol* 2022;43:1148–51 CrossRef Medline
3. Kan P, Maragos GA, Srivatsan A, et al. **Middle meningeal artery embolization for chronic subdural hematoma: a multi-center experience of 154 consecutive embolizations.** *Neurosurgery* 2021;88:268–77 CrossRef Medline
4. Ng S, Derraz I, Boetto J, et al. **Middle meningeal artery embolization as an adjuvant treatment to surgery for symptomatic chronic subdural hematoma: a pilot study assessing hematoma volume resorption.** *J Neurointerv Surg* 2020;12:695–99 CrossRef Medline
5. Catapano JS, Ducruet AF, Nguyen CL, et al. **A propensity-adjusted comparison of middle meningeal artery embolization versus conventional therapy for chronic subdural hematomas.** *J Neurosurg* 2021 Feb 26. [Epub ahead of print] CrossRef Medline
6. Catapano JS, Koester SW, Srinivasan VM, et al. **Total 1-year hospital cost of middle meningeal artery embolization compared to surgery for chronic subdural hematomas: a propensity-adjusted analysis.** *J Neurointerv Surg* 2022;14:804–06 CrossRef Medline
7. Chang CL, Sim JL, Delgado MW, et al. **Predicting chronic subdural hematoma resolution and time to resolution following surgical evacuation.** *Front Neurol* 2020;11:677 CrossRef Medline
8. Guha D, Coyne S, Macdonald RL. **Timing of the resumption of anti-thrombotic agents following surgical evacuation of chronic subdural hematomas: a retrospective cohort study.** *J Neurosurg* 2016; 124:750–59 CrossRef Medline
9. Poon MT, Rea C, Kolas AG; et al; British Neurosurgical Trainee Research Collaborative (BNTRC). **Influence of antiplatelet and anticoagulant drug use on outcomes after chronic subdural hematoma drainage.** *J Neurotrauma* 2021;38:1177–84 CrossRef Medline
10. Scerrati A, Germano A, Trevisi G, et al. **Timing of low-dose aspirin discontinuation and the influence on clinical outcome of patients undergoing surgery for chronic subdural hematoma.** *World Neurosurg* 2019;129:e695–99 CrossRef Medline
11. Housley SB, Monteiro A, Donnelly BM, et al. **Statins versus nonstatin use in patients with chronic subdural hematomas treated with middle meningeal artery embolization alone: a single-center experience.** *World Neurosurg* 2022 Oct 15. [Epub ahead of print] CrossRef Medline

© L. Scherschinski

© J.S. Catapano

© A.P. Jadhav

© A.F. Ducruet

© F.C. Albuquerque

On behalf of all authors

Department of Neurosurgery

Barrow Neurological Institute, St. Joseph's Hospital and Medical Center

Phoenix, Arizona

MRI Monitoring of Anti-Alzheimer Therapy Amyloid-Related Imaging Abnormalities: Due Diligence or Overkill?

In a recent article in the *American Journal of Neuroradiology*, Cogswell et al¹ urged radiologists to learn about amyloid-related imaging abnormalities (ARIA) and their MR imaging appearance to be able to diagnose and monitor cerebral changes observed in patients with Alzheimer disease treated with amyloid-targeting monoclonal antibodies. These include aducanumab (marketed as Aduhelm; Biogen), approved by the FDA, and a number of similar treatments currently in clinical trials, eg, donanemab (Eli Lilly), lecanemab (Eisai), gantenerumab (Hoffmann-La Roche), and so forth.

Common to these drugs is the lack of convincing evidence for substantial clinical benefit. They are in no way curative, and multiple trials including thousands of patients have not provided clear, significant evidence of cognitive symptom reduction, let alone reversal. The claim of efficacy for these treatments is largely based on an alleged reduction in cerebral amyloid deposits, which is hypothesized to cause a delay of an inevitable cognitive decline. Surprisingly, therefore, the FDA made an accelerated approval of Aduhelm on June 7, 2021, not only contrary to the vote of its own expert panel but with reference exclusively to what was interpreted as a reduction in cerebral amyloid deposits assessed by serial amyloid PET scans. However, a reduction in PET signals due to treatment is also observed in the white matter, which is known not to have amyloid deposits, but in addition, the effect of therapy-related brain damage, including ARIAs, on the PET signal is inexplicably not taken into account.²⁻⁴ These effects are likely either off-target or a result of removing vascular amyloid.

We think that the FDA's approval conflicted with the core of the agency's mission to "protect and promote the public health," because the prevalent adverse effects of these ARIAs, also a consideration in the decision of the Centers for Medicare and Medicaid Services (CMS), cannot be ignored. The CMS's restrictive decision not to cover Aduhelm treatments, except for patients enrolled in future CMS-approved trials, is a welcomed initiative.

On that basis, the recommendation of Cogswell et al¹ can be seen as timely care, to the extent that it is becoming increasingly necessary to document the potential damage to patients caused

by these treatments. However, it raises the question of whether MR imaging is the right technique for the purpose. In the published drug trials, the significance of ARIAs is minimized and considered to be reversible, as assessed from MR imaging. However, this is not a gospel truth; instead, the ARIAs are severe adverse effects of the treatment, demanding a thorough investigation, including their long-term significance for patients.

What is necessary in this connection is to establish the functional impact of the treatment with the FDA/CMS-approved FDG-PET scans, demonstrating regional cortical glucose metabolism as a reliable expression of regional cerebral function. Using MR imaging as the sole indicator of diminishing or disappearing ARIAs is, in no way, a guarantee of diminishing or absent brain damage. We, therefore, recommend that the FDA put the approval of Aduhelm on hold, refrain from taking a position on other similar anti-amyloid treatments, and instead require regional brain function assessment by FDG-PET, before and after therapy, of patients who choose to enroll in the trials. Any indication of substantial regional and/or global reduction of brain function in treated patients would provide an indication that the trial should be discontinued.

We welcome radiologists learning about ARIAs and how they are best assessed with MR imaging but warn against introducing the method routinely for monitoring of patients with Alzheimer disease on amyloid-targeted immunotherapy, because diminishing or disappearing MR imaging abnormalities may create a false reassurance of the inertness of this kind of therapy.


Disclosure forms provided by the authors are available with the full text and PDF of this article at www.ajnr.org.


REFERENCES

- Cogswell PM, Barakos JA, Barkhof F, et al. **Amyloid-related imaging abnormalities with emerging Alzheimer disease therapeutics: detection and reporting recommendations for clinical practice.** *AJNR Am J Neuroradiol* 2022;43:E19–35 CrossRef Medline
- Sevigny J, Chiao P, Bussière T, et al. **The antibody aducanumab reduces A β plaques in Alzheimer's disease.** *Nature* 2016;537:50–56 CrossRef Medline
- Klein G, Delmar P, Voyle N, et al. **Gantenerumab reduces amyloid- β plaques in patients with prodromal to moderate Alzheimer's disease: a PET substudy interim analysis.** *Alzheimers Res Ther* 2019;11:101 CrossRef Medline


<http://dx.doi.org/10.3174/ajnr.A7702>

4. Høilund-Carlsen PF, Alavi A. **Aducanumab (marketed as Aduhelm) approval is likely based on misinterpretation of PET imaging data.** *J Alzheimers Dis* 2021;84:1457–60 CrossRef Medline

 **P.F. Høilund-Carlsen**
Department of Clinical Research
University of Southern Denmark
Odense, Denmark

 **A. Alavi**
Department of Radiology
Perelman School of Medicine
University of Pennsylvania
Philadelphia, Pennsylvania

 **G. Perry**
Department of Neuroscience, Developmental and Regenerative Biology
University of Texas at San Antonio
San Antonio, Texas

 **J.R. Barrio**
David Geffen UCLA School of Medicine at UCLA
Los Angeles, California

REPLY:

In the commentary “MRI Monitoring of Anti-Alzheimer Therapy Amyloid-Related Imaging Abnormalities: Due Diligence or Overkill?” Høiland-Carlsen et al provide their viewpoint on the efficacy of monoclonal antibody therapies (mAbs) targeting beta-amyloid and the appropriate imaging for treatment monitoring and assessment of outcomes. Drug efficacy and drug safety have been assessed via multiple metrics in clinical trials of anti-amyloid therapies. Assessment of drug efficacy is a matter of clinical trial design, which we did not address in our review.¹ Amyloid-related imaging abnormalities (ARIA) are one of the many safety metrics assessed and used to determine eligibility for continued dosing; their presence may require temporary suspension or permanent discontinuation of drug dosing.²

Regarding the appropriate imaging assessment of patients undergoing therapy, we limited the scope of our review to MR imaging assessment of patients before and during anti-amyloid mAb therapy. We did not address the role of PET in clinical trials or the potential role of PET in clinical practice. Further discussion of PET is warranted and may include amyloid PET for pre- or posttreatment evaluation, as has been used in clinical trials, and FDG-PET for assessment of functional outcomes, as proposed by Høiland-Carlsen et al. In the future, it may be helpful for individuals designing clinical trials to consider functional elements in the imaging assessment of patients before and during mAbs therapy. When mAbs targeting beta-amyloid become clinically available, it will be important for the community to consider the expanded use of PET in addition to MR for imaging assessment.

REFERENCES

1. Cogswell PM, Barakos JA, Barkhof F, et al. **Amyloid-related imaging abnormalities with emerging Alzheimer disease therapeutics: detection and reporting recommendations for clinical practice.** *AJNR Am J Neuroradiol* 2022;43:E19–E35 CrossRef Medline
2. Cummings J, Rabinovici GD, Atri A, et al. **Aducanumab: appropriate use recommendations update.** *J Prev Alzheimers Dis* 2021;8:398–410 CrossRef Medline

 **P.M. Cogswell**

 **C.R. Jack, Jr.**

Department of Radiology
Mayo Clinic
Rochester, Minnesota

 **J.A. Barakos**

Department of Radiology
California Pacific Medical Center
San Francisco, California

 **F. Barkhof**

Departments of Radiology and Nuclear Medicine
VU University Medical Center
Amsterdam, the Netherlands
Queen Square Institute of Neurology and Centre for Medical Image Computing
University College
London, UK

 **T.S. Benzinger**

Departments of Radiology and Neurosurgery
Washington University School of Medicine
St. Louis, Missouri

 **C.A. Raji**

Departments of Radiology and Neurology
Washington University School of Medicine
St. Louis, Missouri

 **T.Y. Poussaint**

Department of Radiology
Boston Children's Hospital
Boston, Massachusetts

 **V.K. Ramanan**

Department of Neurology
Mayo Clinic
Rochester, Minnesota

 **C.T. Whitlow**

Departments of Radiology and Biomedical Engineering
Wake Forest School of Medicine
Winston-Salem, North Carolina

<http://dx.doi.org/10.3174/ajnr.A7731>

Response to “Flow Diversion in the Treatment of Intracranial Aneurysms: A Pragmatic Randomized Care Trial”

With great interest, we read the article by Raymond et al,¹ which described the results of the Flow Diversion in the Treatment of Intracranial Aneurysms Trial. This parallel-group, pre-randomized, controlled, open-label, all-inclusive, pragmatic care trial included 278 patients from 3 centers in Canada during 10 years (2011–2020). In this study, patients who underwent flow diversion (FD) had significantly fewer poor outcomes than patients receiving alternative standard management options (ASMO; relative risk, 0.68; 95% CI, 0.50–0.92). The authors concluded, “For patients with mostly unruptured, large, anterior circulation (carotid) aneurysms, FD was more effective than the alternative standard management option in terms of angiographic outcome.” The authors conducted an all-inclusive care trial because previous trials lacked comparison with routine clinical practice and compared FD only with a specific alternative strategy. This all-inclusive policy is convenient because there is no widely supported consensus on which patients are suitable for FD, and stringent selection criteria may have limited center participation. Nevertheless, there is also a significant downside to this approach.

In this study, patients were eligible for inclusion if they had “an aneurysm for which FD was considered a promising treatment.”¹ Because of lacking clinical consensus, the study population was dependent on local practice and preferences. In such cases, it is too early to perform a randomized controlled trial (RCT) that will generate conclusions that will be supported by the community and implemented in routine practice. However, varying local treatment algorithms also have great potential to evaluate safety and efficacy outside the scope of an RCT. In comparative effectiveness research (CER), one uses varying center-specific treatment algorithms as an instrumental variable to evaluate clinical interventions on observational data.² Such research will facilitate clinical consensus on patient eligibility for FD treatment and works as a stepping stone for future RCTs.^{3,4} For now, without a clearly defined target population, it is difficult to assess the generalizability of the results of this study.

Furthermore, in the primary analysis, the authors found a significant difference in good outcome (a composite outcome of

mRS < 3 and complete or near-angiographic occlusion) between FD and ASMO therapies. This difference was driven by a higher rate of complete angiographic occlusion in the FD group. This is problematic because the patients in the ASMO group were allowed to be treated conservatively and were consequently scored with “incomplete occlusion.” This feature has created an imbalance between study groups and complicates the interpretation of the results. Alternatively, it would have been more informative to limit inclusion to patients who actually received aneurysm treatment.

Last, to investigate the heterogeneity of the treatment effect, the authors conducted a subgroup analysis by adding interactions to the model between baseline characteristics and treatment assignment. This approach requires a much larger sample size, and interactions are usually selected parsimoniously. The authors also conducted a conventional subgroup analysis by reporting the treatment effects stratified per subgroup. On the basis of these results, they concluded that FD was more effective than ASMO for each subgroup with a significantly different treatment effect. However, the study was underpowered to draw such specific conclusions. At best, these results can be interpreted as a motivation for future research.

In conclusion, the authors have conducted a challenging and ambitious trial, and even with its limitations, the higher rate of aneurysm occlusion is promising and mandates future research. We recommend first conducting a survey study to examine FD practice variability and afterward conducting CER as a stepping stone for future RCT development. This approach has the highest probability to generate conclusions that could lead to adoption of FD therapy in routine practice and thus aid in minimizing research waste.

Disclosure forms provided by the authors are available with the full text and PDF of this article at www.ajnr.org.

REFERENCES

1. Raymond J, Iancu D, Boisseau W, et al. **Flow diversion in the treatment of intracranial aneurysms: a pragmatic randomized care trial.** *AJNR Am J Neuroradiol* 2022;43:1244–51 CrossRef Medline
2. Ceyisakar IE, van Leeuwen N, Steyerberg EW, et al. **Instrumental variable analysis to estimate treatment effects: a simulation study showing potential benefits of conditioning on hospital.** *BMC Med Res Methodol* 2022;22:121 CrossRef Medline

3. van Essen TA, Lingsma HF, Pisica D, et al; CENTER-TBI Collaboration Group. **Surgery versus conservative treatment for traumatic acute subdural haematoma: a prospective, multicentre, observational, comparative effectiveness study.** *Lancet Neurol* 2022;21:620–31 CrossRef Medline
4. Wiegers EJA, Lingsma HF, Huijben JA, et al; OzENTER-TBI Collaboration Groups. **Fluid balance and outcome in critically ill patients with traumatic brain injury (CENTER-TBI and OzENTER-TBI): a prospective, multicentre, comparative effectiveness study.** *Lancet Neurol* 2021;20: 627–38 CrossRef Medline

 **J. de Winkel**

Department of Neurology
Department of Public Health
Erasmus MC University Medical Center Rotterdam
Rotterdam, the Netherlands

 **B. Roozenbeek**

Department of Neurology
Erasmus MC University Medical Center Rotterdam
Rotterdam, the Netherlands

REPLY:

We thank *AJNR* for sending us the letter of Drs de Winkel and Roozenbeek, which gives us an opportunity to emphasize the most important, patient-oriented motivation behind our approach.

Care trials such as Flow Diversion in Intracranial Aneurysm Treatment (FIAT) aim to use research methods for the benefit of patients. They are done not primarily to gain new knowledge but rather because they are the best, most ethical way to introduce new devices into endovascular practice. Trying a novel intervention in practice is a research context that requires specific methods to protect the medical interests of the patients. Thus, the trial was not conducted “because previous trials lacked comparison with routine clinical practice,” as the authors of the letter have suggested, but rather, as we wrote in the introduction of the article, “to introduce to endovascular practice a promising-but-unvalidated innovation for patients with difficult intracranial aneurysms.”

If we keep in mind the patients’ interests first, the all-inclusive policy was necessary because we are asked to care for all of these patients for whom flow diversion may be a good option. It was not chosen because it was thought “convenient because there is no widely supported consensus on which patients are suitable for FD and stringent selection criteria may have limited center participation.” Our policy is that promising new (but risky) innovations should be used only in the context of a trial. The main idea is to use clinical trial methodology to protect patients from unvalidated care.^{1,2} Moreover, protecting patients is not a concern that applies to only a small selected group of patients; it applies to all patients considered for the innovative treatment, here flow diversion.

The purpose of randomized controlled trial (RCT) methodology is to transparently reveal to patients that we are entering unknown territory and to use human intelligence to anticipate and control the potential risks of using an innovative treatment. Risks for each patient are mitigated by only offering the innovation as a 50% chance, balanced by a 50% chance of being treated by the better known, more standard therapy. This procedure is continued until the new treatment is shown to be better than standard therapy, at which time it can be safely used by the community. Alternatively, if the innovation is shown harmful, it is abandoned before too many patients have been harmed, as with the Stenting and Aggressive Medical Management for Preventing Recurrent Stroke in Intracranial Stenosis (SAMMPRIS) trial.³ This process is how trials can work in the interests of patients.

We can now contrast this approach with the aim of the authors of the letter: Let the innovation be used just as if it were standard care and without warning patients that they are being used as research subjects. The haphazard resulting practices will vary widely, of course, because no one really knows what to do. However, this diversity, with large numbers, will serve “as an instrumental variable to evaluate clinical interventions on observational data.” However, this objective is exactly what we all want to prevent! This is experimenting by using novel interventions without methods within the context of care. If it is ever possible

to learn from this method, it is only after errors have been committed on a large scale. Haphazard clinical practices and patients should not serve as “instrumental variables” for research.

The idea that observational studies will “facilitate clinical consensus on patient eligibility for FD treatment and works [sic] as a stepping stone for future RCTs” is a naïve illusion that is contradicted by decades of clinical experience. Everybody knows (but few will admit) that observational studies only serve to evade the necessity of doing RCTs. The authors’ claim that “It is too early to perform an RCT” is a well-known trap (it is always too early until it is too late). The proposal is directly responsible for the dearth of good clinical research in our field.

By claiming that “Without a clearly defined target population, it is difficult to assess the generalizability of the results of this study,” the authors show their poor understanding of generalizability, a subject that has previously been discussed at length.⁴ More important, we are not targeting populations with flow diversion but are treating our patients, one at a time. The central concern of the trial is to offer a way to protect the patient who could benefit from flow diversion but who could also potentially be harmed by an unproven new technology. This is why conservative management had to be included as a potential option to patients because observation rather than treatment is a genuine clinical option that can prevent iatrogenic morbidity. While FIAT included mostly large aneurysms, flow diversion is currently much more frequently used to treat patients with small aneurysms, and the central question remains as to whether these patients should even be treated at all.⁵

Thus, the remarks that follow are rather bizarre, unless they betray the authors’ dedication to data for data’s sake: “Patients were allowed to be treated conservatively....This has created an imbalance between study groups and complicates the interpretation of the results. Alternatively, it would have been more informative to limit inclusion to patients that actually received aneurysm treatment.” We strain to understand what “balance” the authors want to see between groups; treatments were randomly allocated. The results are not complicated to understand, for they are transparently shown in Fig 2. We also have a hard time understanding how the authors can believe that excluding patients could render a trial “more informative.”

The multiplicity of comparators was an essential feature for FIAT to reach its goal of protecting all patients considered for flow diversion. Multiple comparators are not uncommon in pragmatic trials.⁶ Consequently, various types of patients treated in various ways were all included. There is no need “to investigate the heterogeneity of treatment effect” as the authors propose, for the heterogeneity is obviously there; they criticized it earlier in the letter. This is, of course, why we provided subgroup details, as promised by protocol, regardless of the tests for interaction. While the authors rehearse the prevalent statistical dogmas regarding interaction tests and subgroup analyses, the idea of a single treatment effect does not make sense here, where treatments as varied as parent vessel occlusion and conservative management were used. However, the authors are right that the trial remains small and that a lot of work remains to be done.

The authors end their letter with their recommendations. They recommend the same old observational approach wrapped


up in a fashionable new guise (comparative effectiveness research). It has been attempted without success for decades, with the consequence that we all practice risky opinion-based surgical care. If no evidence is needed to adopt a new intervention into routine practice on a large scale, why would an RCT be needed 20 years later? How much damage will have been done in the meantime? Their final concern, “to minimize research waste,” says it all. However, this is just plain wrong: Of all methods, the observational approach is the least efficient. The authors see patients and surgical practices as opportunities for observational research. Clinical research should instead be designed to minimize harm to patients, and preventing needless morbidity by using RCTs is anything but a “waste.”¹

REFERENCES

1. Darsaut TE, Raymond J. **Ethical care requires pragmatic care research to guide medical practice under uncertainty.** *Trials* 2021;22:143 CrossRef Medline
2. Raymond J, Fahed R, Darsaut TE. **Randomize the first patient.** *J Neuroradiol* 2017;44:291–94 CrossRef Medline
3. Darsaut T, Raymond J, Lanthier S. **In TIA or stroke patients with intracranial arterial stenosis, aggressive medical therapy was superior to percutaneous transluminal angioplasty and stenting for 30-day risk of further stroke or death.** *Evid Based Med* 2012;17:115–16 CrossRef Medline
4. Fahed R, Darsaut TE, Raymond J. **The introduction of innovations in neurovascular care: patient selection and randomized allocation.** *World Neurosurg* 2018;118:e98–104
5. Darsaut TE, Desal H, Cognard C, et al. **Comprehensive Aneurysm Management (CAM): an all-inclusive care trial for unruptured intracranial aneurysms.** *World Neurosurg* 2020;141:e770–e7 CrossRef Medline
6. Zuidgeest MG, Welsing PMJ, van Thiel G, et al; WP3 of the GetReal Consortium. **Series: pragmatic trials and real world evidence: Paper 5. Usual care and real life comparators.** *J Clin Epidemiol* 2017;90:92–98 CrossRef Medline

 **T.E. Darsaut**

Department of Surgery, Division of Neurosurgery
Mackenzie Health Sciences Centre
University of Alberta Hospital
Edmonton, Alberta, Canada

 **M. Chagnon**

Department of Mathematics and Statistics
Université de Montréal
Montreal, Quebec, Canada

 **J. Raymond**

Department of Radiology, Service of Interventional Neuroradiology
Centre Hospitalier de l'Université de Montréal
Montreal, Quebec, Canada